

# **Nanoparticle Mediated Strategies Towards Stable Neural Electrode Tissue Interfaces**

by

**Kevin Michael Woeppe**

B.S. of Biomedical Engineering, University of Pittsburgh, 2016

Submitted to the Graduate Faculty of the  
Swanson School of Engineering in partial fulfillment  
of the requirements for the degree of  
Doctor of Philosophy

University of Pittsburgh

2022

UNIVERSITY OF PITTSBURGH

SWANSON SCHOOL OF ENGINEERING

This dissertation was presented

by

**Kevin Michael Woepfel**

It was defended on

March 25, 2022

and approved by

Alberto Vazquez, PhD, Associate Professor, Departments of Radiology and Bioengineering

Kacey Marra, PhD, Professor, Department of Plastic Surgery

Xiaoming Hu, PhD, Associate Professor, Department of Neurology

Dissertation Director: Xinyan Tracy Cui, PhD, William Kepler Whiteford Professor, Department  
of Bioengineering

Copyright © by Kevin Michael Woepfel

2022

# **Nanoparticle Mediated Strategies Towards Stable Neural Electrode Tissue Interfaces**

Kevin Michael Woeppele, PhD.

University of Pittsburgh, 2022

Interfacing with electrically excitable tissues via electronic devices has unlocked countless therapies and scientific discoveries, but the chronic stability and long-term clinical viability of these devices is greatly limited by the host tissues response to the implant. For example, chronic neural recording devices experience low recording yield, signal drift and degradation over time as the host inflammatory responses cause neuronal death and degeneration, microglia activation, scar tissue formation, and electrode material degradation. Previous research efforts have shown promising results from protein based biomimetic coating and conducting polymer-based drug release coatings in mitigating these adverse tissue responses. In this dissertation, we have utilized silica nanoparticles (SNP) to greatly enhance the efficacy of these coatings in different manners. The first is to enhance protein surface immobilization by the pre-deposition of a nanotopographical coating of silica nanoparticles. This nanotopographical coating elevated the protein binding, bioactivity, and stability, enhancing the tissue integration and long-term recording performance of neural electrodes. Further, the nanotopographical coating enabled the drying and storage of the biofunctionalized electrodes without loss of bioactivities, allowing for practical distribution of the protein modified devices to users. The second strategy is a novel mesoporous silica nanoparticle dopant for conducting polymers. These mesoporous particles can be loaded with pharmaceuticals and then used as drug carriers to bring the compounds into electropolymerized conducting polymer polyethylenedioxythiophene (PEDOT) coating. The resulting PEDOT/SNP films were able to increase drug release by a factor of 16 compared to traditional conducting polymer-based drug

delivery systems and enabled the loading and delivery of positively charge and electroactive compounds, as well as the co-loading and release of multiple compounds from the same film. *In vivo*, we demonstrate that the bioactivity of the released compounds is maintained by temporally modulating neural activity and vascular dynamics. We may make use of *in vivo* drug delivery to reduce the effects of injury driven excitotoxicity which are observed following implantation or to expediate re-perfusion of the tissues around the electrode after injury induced damage to cortical vasculature.

## Table of Contents

Preface.....	xvii
<b>1.0 Introduction to Neural Electrodes and Drug Delivery .....</b>	<b>1</b>
<b>1.1 Current Understanding of Failure Mechanisms .....</b>	<b>2</b>
1.1.1 Mechanical and Material Failure .....	4
1.1.2 Biological Tissue Response .....	7
1.1.3 Interplay Between Material Response and Biological Response .....	12
<b>1.2 Methods of Investigating the Electrode Tissue Interface and Recording performance .....</b>	<b>13</b>
1.2.1 Electrophysiology .....	13
1.2.1.1 Local Field Potentials .....	13
1.2.1.2 Single and Multi-unit Activity .....	14
1.2.2 Electrochemical Impedance Spectroscopy.....	15
1.2.3 <i>In Vitro</i> Methods.....	16
1.2.4 <i>In Vivo</i> Two Photon Microscopy.....	17
1.2.5 Postmortem Histology.....	17
<b>1.3 Strategies For Improving the Long-Term Performance of Electrodes .....</b>	<b>18</b>
1.3.1 Geometry.....	19
1.3.1.1 Textural Modifications.....	20
1.3.2 Mechanical Properties .....	21
1.3.3 Bioactive Coatings.....	22
1.3.4 Drug Delivery .....	23

1.3.4.1 Controlled Drug Delivery.....	25
1.3.4.2 Drugs Utilized In Neural Engineering .....	26
1.3.4.3 Microfluidics .....	27
1.3.4.4 Degradable Polymers.....	31
1.3.4.5 Hydrogels.....	33
1.3.4.6 Nanoparticle Based Drug Delivery.....	34
1.3.4.7 Silica Nanoparticles .....	35
1.3.4.8 Conducting Polymers for Drug Delivery .....	36
1.4 Final Introductory Remarks .....	42
<b>2.0 Enhancing Surface Immobilization of Bioactive Molecule via Silica Nanoparticle</b>	
Base Coating .....	44
2.1 Introduction .....	45
2.2 Methods .....	47
2.2.1 Materials and Characterization.....	47
2.2.2 Nanoparticle Fabrication .....	48
2.2.3 Nanoparticle Characterization .....	49
2.2.4 Surface Functionalization.....	49
2.2.5 Evaluation of Antioxidant Coatings .....	52
2.2.6 Surface Protein Concentration .....	53
2.2.7 Surface Characterization.....	53
2.2.8 Cell Culture .....	54
2.2.9 Cell Staining and Imaging.....	55
2.2.10 Statistics .....	55

<b>2.3 Results and Discussion .....</b>	<b>56</b>
<b>2.3.1 Nanoparticle Fabrication .....</b>	<b>56</b>
<b>2.3.2 Surface Modification.....</b>	<b>57</b>
<b>2.3.3 Antioxidant Immobilization .....</b>	<b>60</b>
<b>2.3.4 Surface Density of Immobilized Proteins.....</b>	<b>62</b>
<b>2.3.5 Bioactivity of the Immobilized Proteins.....</b>	<b>65</b>
<b>2.4 Conclusions .....</b>	<b>72</b>
<b>3.0 Nanoparticle Modified Substrates Enhance Biomimetic Coatings .....</b>	<b>74</b>
<b>3.1 Chapter Introduction .....</b>	<b>75</b>
<b>3.2 Materials and Methods .....</b>	<b>77</b>
<b>3.2.1 Materials and Reagents .....</b>	<b>77</b>
<b>3.2.2 Nanoparticle Synthesis .....</b>	<b>78</b>
<b>3.2.2.1 Nanoparticle Characterization .....</b>	<b>78</b>
<b>3.2.3 Particle Immobilization .....</b>	<b>79</b>
<b>3.2.4 L1 Isolation .....</b>	<b>79</b>
<b>3.2.5 Protein Immobilization.....</b>	<b>80</b>
<b>3.2.6 Antioxidant Immobilization .....</b>	<b>80</b>
<b>3.2.6.1 Evaluation of Surface Antioxidants .....</b>	<b>80</b>
<b>3.2.7 <i>In Vitro</i> Experiments.....</b>	<b>81</b>
<b>3.2.7.1 Neuron Culture and Staining .....</b>	<b>81</b>
<b>3.2.8 Surgery and Implantation .....</b>	<b>82</b>
<b>3.2.9 Chronic Electrophysiology .....</b>	<b>83</b>
<b>3.2.10 Perfusion .....</b>	<b>84</b>

3.2.11 Immunostaining and Histology .....	84
3.3 Results.....	85
3.3.1 Nanoparticle Characterization and Deposition.....	85
3.3.2 Protein Binding and Binding Lifetime .....	87
3.3.3 Bioactivity of L1 and Bioactive Lifetime.....	87
3.3.4 Electrical Properties and Electrophysiology Performance of Modified Electrodes.....	90
3.3.5 Post-Mortem Histology .....	92
3.3.6 Explant Analysis.....	102
3.4 Discussion .....	104
3.5 Conclusions .....	111
4.0 Chronic Recording from TNP+L1 Modified Electrodes Following Dry Storage .....	113
4.1 Chapter Introduction .....	114
4.2 Methods .....	117
4.2.1 Chemicals and Materials .....	117
4.2.2 Nanoparticle Fabrication .....	117
4.2.3 Sample Preparation .....	117
4.2.4 Protein Isolation and Deposition .....	118
4.2.5 Neuron Culture .....	118
4.2.6 Surgeries and Recording .....	119
4.2.7 Statistics .....	121
4.3 Results.....	121
4.4 Discussion .....	133

<b>4.5 Conclusions .....</b>	<b>136</b>
<b>5.0 Chronic Neural Recordings from TNP+L1 Electrodes Modified 28 Days Prior to</b>	
<b>Implantation .....</b>	<b>137</b>
<b>5.1 Chapter Introduction .....</b>	<b>138</b>
<b>5.2 Methods .....</b>	<b>140</b>
<b>5.2.1 Chemicals and Reagents .....</b>	<b>140</b>
<b>5.2.2 Nanoparticle Synthesis and Deposition .....</b>	<b>140</b>
<b>5.2.3 L1 Isolation .....</b>	<b>140</b>
<b>5.2.4 Electrode Modification .....</b>	<b>141</b>
<b>5.2.5 Surgery .....</b>	<b>142</b>
<b>5.2.6 Electrophysiology .....</b>	<b>143</b>
<b>5.2.7 Postmortem Histology .....</b>	<b>144</b>
<b>5.2.8 Explant Analysis .....</b>	<b>144</b>
<b>5.3 Results and Discussion .....</b>	<b>145</b>
<b>5.3.1 Electrophysiology .....</b>	<b>145</b>
<b>5.3.2 Depth Wise Impedance and Yield .....</b>	<b>149</b>
<b>5.3.3 Histology .....</b>	<b>151</b>
<b>5.3.4 Explant Analysis .....</b>	<b>156</b>
<b>5.4 Conclusions .....</b>	<b>158</b>
<b>6.0 Silica Nanoparticles as Dopants for Conducting Polymers .....</b>	<b>159</b>
<b>6.1 Chapter Introduction .....</b>	<b>160</b>
<b>6.2 Methods .....</b>	<b>164</b>
<b>6.2.1 Materials and Characterization .....</b>	<b>164</b>

6.2.2 Thiolated Silica-Nanoparticle Synthesis .....	164
6.2.3 Oxidation of Thiol to Sulfonate.....	165
6.2.4 Electropolymerization .....	165
6.2.5 Electrochemical Characterization .....	165
6.2.6 Biocompatibility .....	166
6.2.7 Drug loading .....	167
6.2.8 Electropolymerization and Drug Release .....	167
6.2.9 <i>In Vitro</i> Activity .....	168
6.2.10 <i>In Vivo</i> Drug Release.....	168
6.2.11 Statistics .....	169
6.2.12 Acknowledgements and Conflicts of Interests.....	170
<b>6.3 Results and Discussions.....</b>	<b>171</b>
6.3.1 Synthesis of Nanoparticle Dopants .....	171
6.3.2 Electropolymerization and Electrochemical Properties of the PEDOT/SNP .....	174
6.3.3 Electrically Controlled Drug Release .....	181
6.3.4 Bioactivity of the Released Drug.....	184
6.3.5 <i>In Vivo</i> Proof of Concept Drug Release Demonstration.....	188
<b>6.4 Conclusions .....</b>	<b>190</b>
<b>7.0 Controlled Delivery of Vasodilators from PEDOT/SNP.....</b>	<b>192</b>
7.1 Chapter Introduction .....	193
7.2 Methods .....	195
7.2.1 Materials and Reagents .....	195

7.2.2 Nanoparticle Synthesis .....	195
7.2.3 Drug loading and Electropolymerization.....	195
7.2.4 Drug Release and Detection .....	196
7.2.5 Animal Experiments with 2 Photon Microscopy.....	196
7.2.6 Statistics .....	197
7.3 Results.....	198
7.4 Discussion .....	205
7.5 Conclusions .....	207
8.0 Conclusions.....	209
8.1 Summary of Findings .....	209
8.2 Future Directions.....	211
8.2.1 Topographical Modification of Electrodes .....	211
8.2.1.1 Modification of Additional Substrates.....	212
8.2.1.2 Potential Molecular Modifications.....	212
8.2.2 PEDOT/SNP Drug Delivery .....	213
8.2.2.1 Drug Selection .....	213
8.2.2.2 Timing and Method of Release.....	214
Bibliography .....	216

## List of Tables

<b>Table 1. Histological Markers.....</b>	<b>18</b>
---	-----------

## List of Figures

<b>Figure 1. Comparison of traditional and selected advanced electrodes. ....</b>	<b>3</b>
<b>Figure 2. Material degradation observed on an explanted human Utah array used for stimulation. ....</b>	<b>6</b>
<b>Figure 3. Explanted Utah style arrays from a human participant after 182 days.....</b>	<b>8</b>
<b>Figure 4. Sample poor and good waveform shapes. ....</b>	<b>15</b>
<b>Figure 5. Microfluidic devices.....</b>	<b>30</b>
<b>Figure 6 Select conducting polymers utilized for neural applications and drug delivery. ..</b>	<b>37</b>
<b>Figure 7 Drug loading and release from conducting polymers. ....</b>	<b>40</b>
<b>Figure 8 Scheme of surface modification.....</b>	<b>51</b>
<b>Figure 9 Surface modification and stability of nanoparticle coatings. ....</b>	<b>58</b>
<b>Figure 10. Antioxidant Immobilization .....</b>	<b>61</b>
<b>Figure 11. Roughness of TNP Substrates .....</b>	<b>64</b>
<b>Figure 12. Neurite Outgrowth. ....</b>	<b>66</b>
<b>Figure 13 SEM images of neurons grown of TNP roughened surfaces. ....</b>	<b>69</b>
<b>Figure 14. Astrocyte Outgrowth.....</b>	<b>70</b>
<b>Figure 15. Nanoparticle immobilization. ....</b>	<b>86</b>
<b>Figure 16. Characterization of TNP modified substrates .....</b>	<b>86</b>
<b>Figure 17 Protein binding and bioactive lifetime.....</b>	<b>89</b>
<b>Figure 18 Recording performance. ....</b>	<b>91</b>
<b>Figure 19. Quantification of neural cell bodies. ....</b>	<b>93</b>
<b>Figure 20. Quantification of axons. ....</b>	<b>95</b>

<b>Figure 21. Quantification of microglia.....</b>	<b>97</b>
<b>Figure 22 Quantification of astrocytes.....</b>	<b>99</b>
<b>Figure 23. Examination of the origin of local neurons. ....</b>	<b>101</b>
<b>Figure 24. Explant analysis.....</b>	<b>103</b>
<b>Figure 25. L1 bound to TNP retains its bioactivity when stored dry and at room temperature. .....</b>	<b>123</b>
<b>Figure 26. <i>In vivo</i> impedance and recording performance. ....</b>	<b>126</b>
<b>Figure 27. NeuN, and DAPI.....</b>	<b>128</b>
<b>Figure 28. GFAP and NF200.....</b>	<b>130</b>
<b>Figure 29 Nestin and DCX Staining.....</b>	<b>132</b>
<b>Figure 30. Electrophysiology from 32Ch electrodes.....</b>	<b>148</b>
<b>Figure 31. Depth Wise Impedance and Recording Yields.....</b>	<b>150</b>
<b>Figure 32. NF200, GFAP, and Lectin staining. ....</b>	<b>153</b>
<b>Figure 33. NeuN staining and Quantification. ....</b>	<b>155</b>
<b>Figure 34 Explant analysis of TNP+L1 with SEM.....</b>	<b>157</b>
<b>Figure 35 Particle synthesis and polymerization of PEDOT/SNP.....</b>	<b>170</b>
<b>Figure 36. Particle Characterization.....</b>	<b>173</b>
<b>Figure 37. PEDOT/SNP Characterization.....</b>	<b>175</b>
<b>Figure 38 Charge injection and stimulation stability.....</b>	<b>178</b>
<b>Figure 39 Drug loading into SNP and Drug Release. ....</b>	<b>180</b>
<b>Figure 40. Dye Release.....</b>	<b>182</b>
<b>Figure 41. <i>in vitro</i> activity of released compounds.....</b>	<b>186</b>
<b>Figure 42. <i>In vivo</i> release from PEDOT/SNP polymer.....</b>	<b>189</b>

**Figure 43. *In Vitro* release of NaNP..... 199**

**Figure 44. Characterization of NaNP loaded PEDOT/SNP coated CFE..... 201**

**Figure 45. Vessel dynamics after NaNP release. .... 203**

**Figure 46 Changes in vessel diameter grouped by vessel size..... 205**

## Preface

Throughout my studies at the university of Pittsburgh, I have been blessed to be surrounded by so many outstanding people. Many have helped me along the way and without them, this work would not have been possible. First and foremost, I must thank and acknowledge my loving wife, Deanna Walsh, who has put up with my highs and lows for nearly six years. Her emotional support was unparalleled and cannot be understated, even while having her own med school course load. Secondly, I want to thank my advisor, Dr. Tracy Cui, for her countless hours of guidance and coaching me through my entire graduate tenure. In addition, my committee members including Drs. Xiaoming Hu, Kacey Marra, and Alberto Vazquez have each been instrumental in the design and analysis of the experiments and research performed in this work. In addition to his participation as a member of my committee, Dr. Vazquez was an invaluable source of knowledge and expertise regarding two photon imaging and analysis in addition to training and use of the microscope, and this work would certainly not have been possible without his input and advice.

My fellow lab members at the NTE lab have been critical to the research performed in this dissertation, and I want to express my gratitude to them. Namely Dr. Sally Zheng, who trained and guided me through most of my *in vivo* work when I started at the lab. Qianru Yang, who has been invaluable in providing information and guidance on two photon microscopy. Vaishnavi Dhawan, who assisted in recordings and ensured that the lab maintained its social aspects during the Covid pandemic. Daniela Krahe, who has worked with me for over 3 years and aided in my drug delivery experiments. Further, this work would not have been possible without input from every member of the lab during my time at the NTE lab, including Drs James Eles, Mitch Taylor, Elisa Castagnola, Asiyeh Golabchi, Neetu Kushwah, and Elaine Robbins, and the lab members yet to

receive their doctorates, including Bingchen Wu, Delin Shi, and Mary Pwint. Finally, I wanted to thank our wonderful lab manager, Dr Xia Li

## **1.0 Introduction to Neural Electrodes and Drug Delivery**

Works from this section were previously published[1]. Neurotechnology is facing an exponential growth in the recent decades thanks to the advances demonstrated by brain machine interface human trials and clinical successes in neuromodulation therapies. A core component of neurotechnology involves invasive electrode devices interfacing directly with neural tissue for recording and/or stimulation. While satisfactory long-term performance was demonstrated in some applications, such as cochlear implants and deep brain stimulators, more advanced neural interfacing devices requiring higher resolution for single unit recording or microstimulation still face significant challenges in reliability and longevity. The most significant challenge lies in the neural electrode-tissue interface, where a man-made device is brought in contact with biological neural tissue and electrical voltages or currents are being transmitted across the electrode-tissue interface. Like any implantable devices, the highly corrosive and dynamic environment of the host tissue is hostile to implants, among which micro-electronic devices are especially vulnerable. The implantation and presence of an artificial device elicits acute injury and chronic inflammatory reactions that lead to tissue remodeling, degeneration and regeneration that alter the microenvironment with which the device is interfacing. Dynamic changes in the neural tissue around the implants affect the quality and stability of the neural electrode recording and/or stimulation performance. This introductory section intends to 1) review the most recent findings that contribute to our current understanding of the unsatisfactory quality, stability and longevity of neural recording or stimulation, 2) summarize the strategies that have been applied to improve the interface, and 3) discuss the challenges and opportunities in improving the interface and achieving seamless integration between the implanted electrodes and neural tissue both anatomically and

functionally. This section provides an overview of nervous system electrodes, but puts emphasis on central nervous system recording electrodes.

### **1.1 Current Understanding of Failure Mechanisms**

Recording the highest quality single neuron activity in the brain requires penetrating electrodes [2]. While many designs have been utilized for electrode devices implanted in the brain parenchyma, almost all electrodes have certain basic features: electrode sites of a conductive material, conducting leads connecting the electrode sites and external electrical components, and an insulating layer defining the electrode site areas and protecting the connection from electrical shunting. While microwire arrays (bundles of insulated metal wires), Michigan electrodes (planar arrays), and Utah Arrays (bed of needles) are some of the more well-known and studied designs, many new designs and materials have been proposed for neural interfacing (Figure 1). While neural electrodes have advanced greatly over the past few decades, recording and stimulation performance is highly variable and most devices show failure after chronic implantation ranging from weeks to months and a few years. The causes of variability and long-term failure have been attributed to mechanical/material and biological factors.

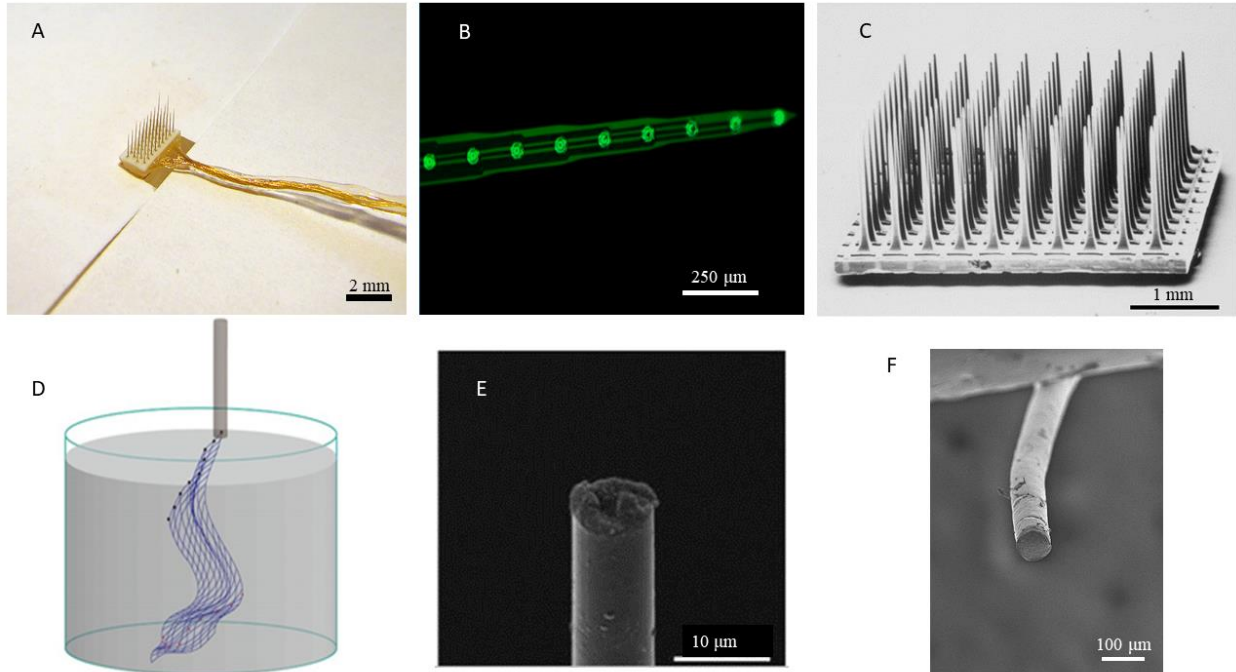


**Figure 1. Comparison of traditional and selected advanced electrodes.**

**(A) Microwire array, reproduced with permission from Microprobes for Life Sciences Inc. (B) Planar (Michigan) electrode. (C) Bed of needles (Utah) array [112], copyright 1998 Elsevier. (D) Syringe injectable mesh electrode [80], copyright 2017 National Academy of Sciences. (E) Carbon fiber electrode [47], copyright 2012 Nature Publishing. (F) Elastic wire electrode.**

### 1.1.1 Mechanical and Material Failure

Despite decades of research and development, mechanical and material failures are still a major contributor of performance failure for neural electrode devices. In a non-human primate study examining chronic recording performance of the Utah array (Blackrock Microsystems), mechanical and material failure have been reported to be the greatest cause of failure, accounting for upwards of 48% of all failure in the first year [3]. While many failures occurred at the percutaneous connectors and wire bundles, further difficulties arise with de-insulation, corrosion, and cracking of the electrodes directly interfacing with the neural tissue.

Several recent studies characterized different types of material failures and their recording/stimulation consequences [4, 5]. One potential cause of material failure is de-insulation along the electrode or at the electrode tip. De-insulation at the electrode site increases the surface area exposed, decreasing the impedance of the electrode but also decreasing the recording quality [6]. Another notable observation is that failure is variable from animal to animal, with some electrode arrays recording on 80% of channels while others produced no recording [4]. One interesting study focused on the mechanical and material failure mode analysis on chronically implanted planar microelectrode arrays (Michigan probes, NeuroNexus) with multiple electrode sites along the shanks [5]. By correlating neural recordings, electrochemical impedance spectroscopy, and scanning electron microscopy of the explanted probes with Finite Element Modeling (FEM), several modes of material failure were identified that resulted in degradation and/or loss of recording, including loss of the metal site, delamination and cracking. Interestingly, cracking and delamination of conducting traces *in vivo* after long term implantation were most frequently observed near the electrode sites where the strain is most concentrated as determined by FEM, due to the mechanical mismatch between the iridium and silicon layers. This study points

out the regions of the planar devices most vulnerable to mechanical stress induced failure, and can be used as a guide to design more robust planar arrays in the future. While this study focused on planar brain electrodes, the results are likely applicable to any electrode in the central or peripheral nervous system whose components have clashing mechanical properties.

Material corrosion/degradation can occur naturally or be accelerated through electrical stimulation. Material degradation following stimulation has been observed even in human participants (Figure 2). Corrosion products have concerns of toxicity [7], but the greatest difficulty lies in loss of the structural stability and electrical functionality of the device. Implanted tungsten recording electrode exhibited a high degree of corrosion and subsequent delamination of their insulation [4]. The common electrode material silicon dioxide may dissolve away in aqueous environments at the rate of 3.7-43.5 pm h<sup>-1</sup> [8, 9]. Smaller devices are more susceptible to degradation, as such nanowires fabricated from silicon or assorted semi-conductors will degrade away in a few weeks unless protected [10].

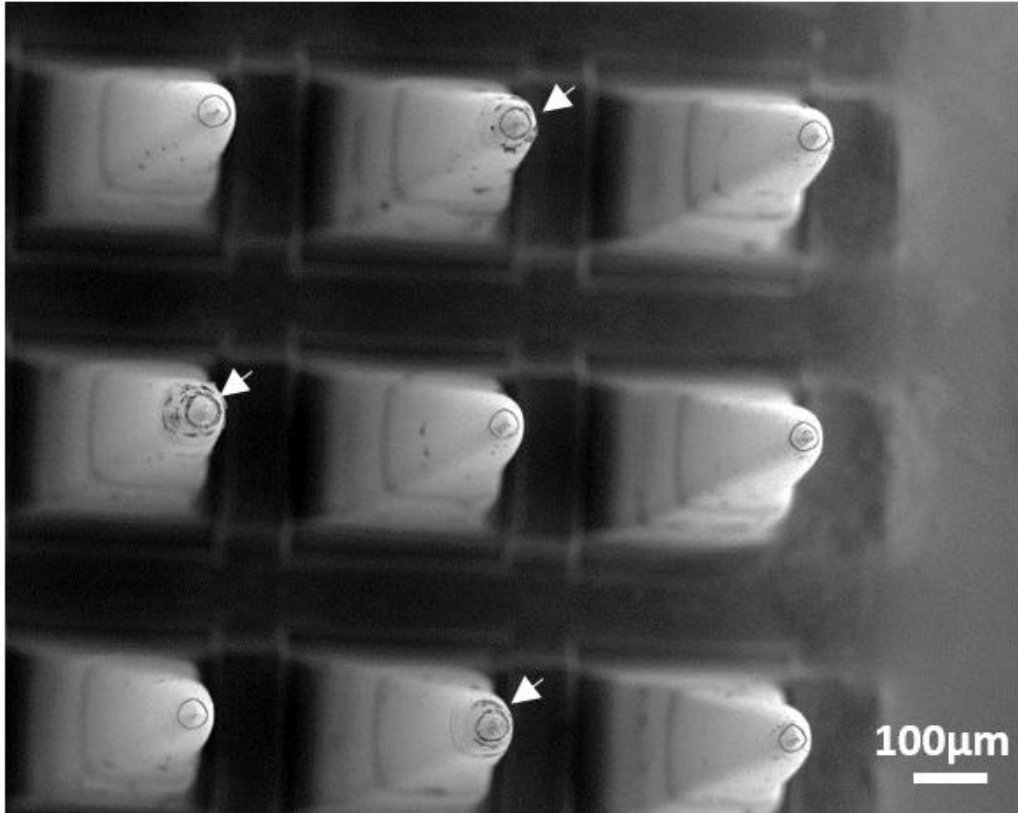


**Figure 2. Material degradation observed on an explanted human Utah array used for stimulation.**

**The 60 channel array was stimulated on 28 of the sites in a grid pattern, stimulated sites are denoted by the white arrows. Of the 28 stimulated sites, 21 showed signs of significant material damage.**

Stimulations pose additional harsh conditions to the electrodes. Improper stimulation can lead to electrode damage (metal corrosion, metal site detachment and insulation failure) and tissue inflammation due to electrolysis of water [11], local pH shifts [11], generation of free radicals, and release of metal ions [12]. Even some of the more electrochemically stable carbon electrodes can be oxidatively etched by stimulation [13]. As such, materials capable of withstanding high degrees of repetitive electrical stimulation and have a large charge injection capacity continue to be investigated [14, 15]. Using a combination of experimental data and theoretical analysis, Cogan et al. demonstrated that for microstimulation utilizing microelectrodes, the previously defined tissue damage limit using charge density and charge per phase by Shannon's equation, no longer applies [12, 16-18]. This study calls for new considerations and tests in order to establish and validate safe stimulation limit for microelectrodes.

### **1.1.2 Biological Tissue Response**

Regardless of implant location, biological tissue response against the implants is a major cause of electrode failure. On the macro scale, meningeal fibroblasts may migrate down the electrode shanks from the brain surface, contribute to the scar formation [19]. In more severe cases, the dural undergrowth may even encapsulate the whole device, resulting in ejection of the probes and signal loss[20]. This dural undergrowth has been seen even in human patients with implanted intracortical electrodes (Figure 3),[21] and may represent a significant hurdle for chronic electrode implantation.

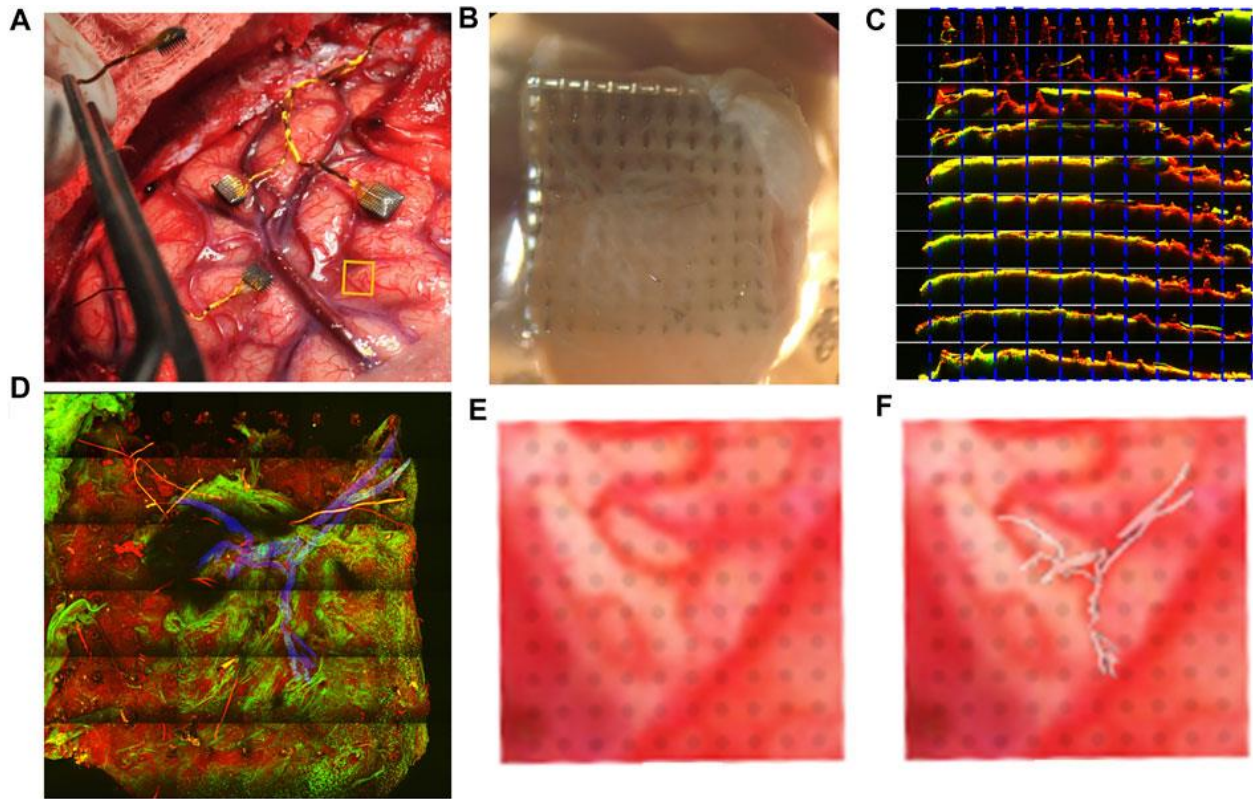


**Figure 3. Explanted Utah style arrays from a human participant after 182 days.**

(A) implant locations are shown for the electrode on the day of surgery. The yellow box denotes the location of the 4<sup>th</sup> electrode prior to implant. (B) Following explantation of the electrode, a thick fibrotic encapsulation is visible under light microscopy. The nature of the fibrotic scar was examined with two-photon microscopy (C,D), green denoting the second harmonic imaging from collagen fibers and red the autofluorescent signal from the device. (C) individual shanks are imaged, with each row corresponding to a row of shanks from the implant. (D) A blood vessel identified due to the second harmonic signal is highlighted in blue. (E,F) The location of the device shanks are overlaid with the implant location from (A), and the vasculature from (D) is highlighted in (F).

On the micro scale, several types of cells are involved in the inflammatory response to the implants, known as the foreign body response (FBR) [22, 23]. Microglia are the first inflammatory cells to respond to the implant, and microglial cells were immediately activated upon implantation [24] and release various inflammatory factors to recruit monocytes and astrocytes [25]. Following the injury, microglia investigate the site by extending their processes towards the device. Once the glia contact the device, the cells determine whether the device is a foreign object of host tissues. The glia then proceed to encapsulate the device, transitioning into their activated amoeboid phenotype and migrating their cell bodies towards the implant. The activated microglia begin to upregulate the production of inflammatory cytokines and free radical production. Molecules such as tumor necrosis factor alpha (TNF- $\alpha$ ), interleukin-1 (IL-1), and interleukin-6 (IL-6) are rapidly produced and released, enhancing the inflammatory cascade, recruiting additional immune cells, and even directly damaging nearby neurons[26].

These activated microglia/macrophages remain at the vicinity over long-term implantations, and are surrounded by a dense layer of astrocytes, often referred to as glial the scar. Glial encapsulation insulates electrodes from nearby neurons, increasing the impedance and the distance between electrodes and viable neurons [27]. Meanwhile, neurons (cell body and processes) may be damaged during insertion, pushed away by the glia scar, or degenerated by reactive oxygen species and proinflammatory or cytotoxic factors released from the chronic inflammation and/or become less active due to mechanical strain or disconnect from the rest of the network. It is assumed that these biological effects will result in recording or stimulation failure, but the contribution of each mechanism to device function has not been clearly understood.

An additional trigger of cellular responses and high degree of variability is vascular damage or breach of blood brain barrier (BBB). Electrode implantations inevitably break vasculature to

various degrees. BBB leakage leads to release of blood cells, clotting factors and neurotoxic plasma proteins, and monocytes recruitment. A two-photon imaging study demonstrated that inflammatory tissue response may be minimized by reducing the vascular damage during insertion [28]. BBB damage does not stop at the insertion injury, more data have shown persistent BBB leakage during chronic implantation time, which is inversely related to electrode performance [29].

Mechanical mismatch between the biological tissue and electrode devices may be of concern for chronic implantation. Conventional neural electrode devices are made of metal and silicon having mechanical modulus several orders of magnitude higher than the brain or peripheral nervous tissue. During breathing or movement of the animal, micromotion between the brain tissue and the inserted electrodes pose strain to the surrounding tissue, which lead to neural apoptosis [30]. Based on this, various mechanically soft and flexible electrode devices have been developed and when compared to the stiff devices, reduced inflammatory tissue responses have indeed been observed [31-33]. The mechanical strain may be aggravated by tethering the electrodes on the skull as opposed to free floating ones. Tethering increases the relative movement between implanted electrodes and the brain tissue and prevents the healing of the BBB, both of which may worsen the inflammation and cause neuronal degeneration or demyelination [34, 35].

Another mechanism for the implant to cause persistent inflammation is thought to be the accumulation of inflammatory cells and their inflammatory products. This is supported by two studies. In the first study, lattice probes were compared to solid probes of the same dimension and materials [36]. The lattice probes were designed with a low surface area and an open architecture to allow inflammatory products to freely diffuse away from the electrode. The study found that the lattice devices resulted in reduced inflammatory response when compared to solid probes. In the

second study, diffusion sinks were created on the electrode using a thick hydrogel coating, and significantly reduced foreign body response was also observed [37].

Surface chemistry of the implant has been hypothesized to play a role on host tissue response, because plasma protein adsorption and inflammatory cell attachment occur on the surface are the earliest events after implantation. No differences in glial and neuronal responses have been found between Parylene C and silicon dioxide surfaces, two commonly used insulation materials [35], and polyethylene glycol based hydrogel coatings did not show any benefit [38]. These results suggest that physical chemistry alone may not be sufficient to alter the host tissue response. Bioactive coatings [39, 40] that interact with the host tissue via biologics or therapeutics may be necessary to actively modulate the tissue response.

In order to find the right bioactive intervention, it is important to identify the molecular pathways critical to the host tissue responses. Several studies utilizing knockout animals or RNA array analysis have shed new light on the relevant molecular pathways. For example, Caspase-1 knock out (KO) mice implanted with the Michigan probes have shown improved electrophysiological recording performance, indicating that caspase-1 mediated inflammation and/or apoptosis pathways are playing an important role [41]. In another study, foreign body response to intracortical silicon implants in MCP-1(also CCL-2) KO mice was reduced [42], possibly through inhibiting the TNF induction and NF $\kappa$ B pathway [43]. These studies appear to indicate that molecular pathways are suitable targets for improving the long-term performance of these electrodes.

In sum, the biological tissue response to the implants involves a cascade of reactions in multiple types of cells. While it is clear that the biological response to implants contributes to the devices performance, the contributions of different mechanisms (glial scar, neuronal degeneration

and loss, inflammation etc.) to the failure of implanted devices remains to be determined. Furthermore, multiple triggers of these biological responses have been proposed but the challenge is to separate the impact of many biological factors and physicochemical triggers. To date, no single mechanism or factor has been found to predominate the performance of electrodes.

### **1.1.3 Interplay Between Material Response and Biological Response**

Implantations of artificial devices cause tissue injury and inflammation, which may lead to release of free radicals, reactive oxygen and nitrogen species. These species may not only damage the tissue, but also accelerate the degradation of the electrode materials. In an *in vitro* study, tungsten electrodes exhibit a heightened degree of corrosion when exposed to common reactive oxygen species and H<sub>2</sub>O<sub>2</sub> [44, 45]. This correlates with *in vivo* findings, where tungsten wires exhibit the greatest degree of degeneration immediately after implantation, likely due to the increased free radical concentration and comparatively harsh environment around the implant post-surgery [4]. In addition to tungsten, reactive oxygen species showed corrosive effects on Pt/Ir, Pt, Ir, Au, Silicon Nitride, Polyimide, and Parylene-C [45]. Depending on the type of degrading material, degradation products may worsen the inflammation. This leads to more reactive species, which in turn accelerates the material failure. Therefore, *in vitro* testing protocols and *in vivo* evaluations need to take into account these important interplays.

## **1.2 Methods of Investigating the Electrode Tissue Interface and Recording performance**

### **1.2.1 Electrophysiology**

Once implanted into the CNS, neural electrodes are designed to detect the small- and large-scale changes in ionic fluctuations in the CNS tissues. These fluctuations result in measurable changes in the voltage experienced at the electrode site. These fluctuations can be characterized by their speed and frequency, as well as their relative strength. The largest of these fluctuations occur on the largest time scales, and selective filtering methods are used to differentiate between large scale multi-cellular activity and the much smaller changes caused by the firing of individual neurons. Certain slow oscillations can be detected from electrodes that are placed outside of the skull through electroencephalography (EEG). However, penetrating neural electrodes are able to gather data inaccessible to these external devices such as local field potentials (LFP), multi-unit activity (MU), and even single unit spiking (SU).

#### **1.2.1.1 Local Field Potentials**

LFP data is acquired by filtering the data to remove high frequency events, generally setting an upper limit between 150Hz and 300Hz. Changes in local field potentials do not immediately correlate to cellular firing, but instead to the averaged activity of the brain region. This can be useful in demonstrating how brain regions connect with each other, as subsequent depolarizations in nearby brain regions are believed to indicate the transfer of information between regions. An application of this is to perform an analysis referred to as current source density (CSD) mapping. If the mapping between brain regions is already well understood, CSD can become a useful tool for tracking the locations of certain electrodes over time[46].

### 1.2.1.2 Single and Multi-unit Activity

Neural spiking activity takes place in the higher frequency ranges and can be separated from LFP data by selectively filtering between 300Hz and 5000Hz using a band pass filter. The electrophysiological data in this regime is inherently noisy, and extra analysis must be performed to isolate the signals of interest. The first method of extracting useful data is to perform a thresholding algorithm. A common method of thresholding the data is to calculate the standard deviation of the data stream and select a cut-off, events that cross this cut-off are reported and further examined for potential spiking activity. An example cut-off is 3.5SD, eliminating 99.98% of the data. These so-called threshold crossing events are then documented, and a window of time before and after the event are developed for waveform analysis. The data from this window is often referred to as a snippet.

The potentials created by neuron firings have very characteristic shapes. Not all threshold crossing events translate to neural activity and separating the noise from the spiking activity is performed by examining the shape of the snippets. Principle component analysis (PCA) is used to group similar snippets based on their shapes, and then manual spike sorting is performed to identify how many units a particular electrode is able to record. The characteristic shape should include an initial decrease in potential as the cell fires, followed by a longer repolarization phase, all taking place within 2ms (Figure 4). The percentage of electrodes able to record at least one unit is referred to as the electrode site yield.

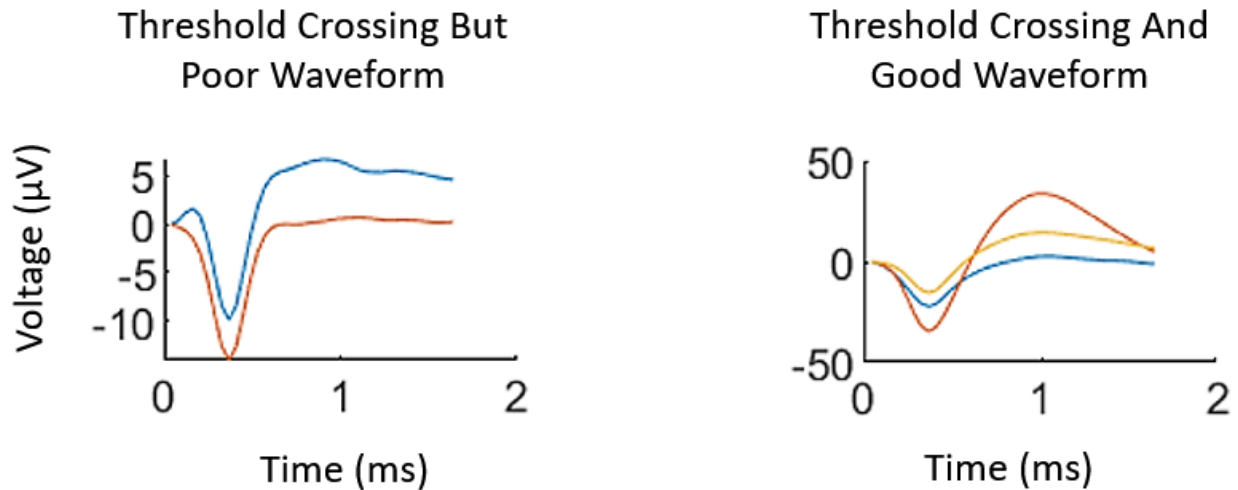


**Figure 4. Sample poor and good waveform shapes.**

Additionally, the signal strength can be measured by taking the average voltage difference from the lowest and highest values for the grouped waveform. This peak-to-peak voltage ( $V_{pp}$ ) is often compared to the background signal intensity and reported as the signal to noise ratio (SNR) as calculated in equation 1.

**Equation 1-1**

$$SNR = \frac{V_{pp}}{Noise}$$

Noise is defined as the intensity of the background signal. In order to prevent the value of the noise from being affected by the neural spiking events, the noise is calculated after removal of the snippets from the data stream. The noise is then calculated as 2SD of the remaining data.

### **1.2.2 Electrochemical Impedance Spectroscopy**

While the electrode is implanted, it is difficult to directly observe the electrode sites or the surrounding tissues. Electrochemical impedance spectroscopy (EIS) offers a method of

investigating this interface in a non-invasive manner. EIS measures the current response of an electrode in solution when a sinusoidal voltage is applied. This response is the electrode impedance and is directly related to ohm's law. The frequency of this sinusoid is adjusted, and the changes in electrochemical impedance provide useful information on the nature of the electrode tissue interface in addition to the health of the device. For example, inflammatory reactions to an electrode result in tissue encapsulation, increasing impedance magnitude over the first weeks of implantation. A sudden drop in electrode impedance may be due to loss of electrode insulation, indicating that the electrode may be close to failing or has failed already. A similar observation would be a rapid rise in impedance, often of over an order of magnitude, indicating that a disconnect has occurred and that data is no longer able to be acquired from that site.

### **1.2.3 *In Vitro* Methods**

The bioactivity and potential toxicity of a coating or material must be extensively examined *in vitro* prior to *in vivo* experimentation. Toxicity testing is performed with cell culture to ensure that the material does not produce any unforeseen adverse reactions within biological systems. This may include producing toxic leachable compounds or degrading into toxic components. Standard procedure for biocompatibility testing can be found in ISO-10993. These tests use cells of interest (fibroblasts, primary neurons, and glia) and measure their response to potential toxic components with cellular viability assays such as MTT and XTT, or examine the ratio viable to non-viable cells with co-staining of Calcein-AM (live) and Propidium Iodide (dead).

Bioactivity testing is more applicable to surface modifications. Surfaces that are designed to directly interact with cells through known mechanisms can be examined by the culture of cells directly on the substrate. The bioactivity of the neural adhesion molecule L1-CAM be examined

by immobilizing the L1 to glass substrates and culturing primary neurons or primary glia on these samples[47, 48]. Subsequent fixation and staining can reveal the interactions between the cells and the substrate and can be used to track any changes in bioactivity that may occur over time.

#### **1.2.4 *In Vivo* Two Photon Microscopy**

Although it is often impractical or impossible to directly observe the tissue reactions to an implant in wild-type mice with conventional microscopy, specialized transgenic breeds of mice have been developed for use with two photon microscopy which allows for direct examination of cellular responses in real time and in alive animals. The mice have been designed to express fluorescent markers which can be monitored by the incredibly sensitive detectors of the microscope. These markers can be expressed selectively in microglia, neurons, oligodendrocyte precursor cells, and some markers are only fluorescent when neurons fire. This data can then be analyzed to examine a plethora of CNS responses to an implanted device, including: microglial activation and encapsulation[49, 50], vascular remodeling[51], changes in pericytes and oligodendrocyte precursor cells,[52] and neural firing[53-55].

#### **1.2.5 Postmortem Histology**

Postmortem histology is an endpoint analysis technique that examines the cellular and subcellular responses in the tissues around the implant. Postmortem histology has the advantage of being able to stain for a far greater number of cellular markers than two photon microscopy in addition to enhanced resolution of the stain. Thin sections of CNS tissue are treated with antibodies

or dyes that specifically label certain cells, proteins, organelles, or phenotypes. A list of many common stains used for postmortem histology are included in table 1.

**Table 1. Histological Markers**

Marker	Expressed by:
DAPI	Cell Nuclei
Glial Fibrillary Acidic Protein (GFAP)	Activated Astrocytes
Iba-1	Microglia
NeuN	Neural Nuclei
NF-200	Neuron Axons
ED-1	Activated Microglia
Inos	M1 Microglia
Arg-1	M2 microglia
Caspase-3	Apoptotic cell death
4-HNE	Lipid peroxidation
Nestin	Neural stem and progenitor cells
DCX	Immature Neurons
Lectin	Blood Vessels and Microglia

### **1.3 Strategies For Improving the Long-Term Performance of Electrodes**

Strategies to improve the chronic performance of the electrodes are widely varied in the field including altering implant dimensions and mechanical properties, improving material stability and functionalities, surface coatings, and drug delivery to minimize the FBR.

### 1.3.1 Geometry

As discussed before, size of implants contributes to FBR via multiple mechanisms. Smaller sizes reduce the magnitude of BBB damage and tissue displacement, reduce surface area and may also decrease the device stiffness by decreasing the cross-sectional area. For these reasons, reducing the size of implanted electrode devices to subcellular level i.e. below several microns [10, 56-62] has been actively pursued by many groups. One study pioneered the use of carbon fiber (7 mm in diameter) for chronic neural recording and demonstrated negligible gliosis and neuron loss [63]. This study motivated several groups to fabricate arrays of carbon fiber for multisite recording/stimulation [64, 65]. However, making carbon fiber arrays is a labor intensive and largely manual operation, and the array configuration is limited to one electrode site per fiber. Lieber's lab has been successful in developing SU-8 based 3D macroporous mesh electrode arrays using micro/nanofabrication technology with features sizes less than 10 $\mu$ m and exceptionally low bending forces, resulting in minimum foreign body responses and intimate neuron-device interaction [60]. Chronic recording with such mesh electrodes was demonstrated for at least 8 months [66].

As devices are made smaller and more flexible, more advanced and robust materials are required. Ultrasmall and flexible devices are more prone to mechanical and material failure by the nature of their geometry. In addition, these devices often require very thin insulation. However, almost all thin (<1  $\mu$ m) insulating materials have problems with long term stability and reliability [67], indicating the need for greatly improved insulation materials/methods. Xie et al. has improved the insulation by first depositing a 52 nm adhesive layer of Al<sub>2</sub>O<sub>3</sub> via atomic layer deposition before the Parylene C coating [68], however, results seem to vary between positive results for planar electrodes [103] and potentially detrimental results for bed of needle style

electrodes [104]. Thermally deposited silicon dioxide (100 nm) on silicon wafers has shown exceptionally good resistance to water penetration as well as highly uniform corrosion [67]. For flexible electronics, materials not only need to present sufficient flexibility, but also need to maintain the conductivity upon flexing/stretching. A notable development in elastic conductors has been produced through the nanoconfinement effect. These promising materials have yet to be introduced into neural devices.

Device size reduction also leads to necessary decrease in the size of the electrode sites, increasing the site impedance. While the small size of electrode sites may improve single neuron discrimination, very high impedances can increase the noise of recording or prevent effective stimulation. A potential solution may be found in conducting polymers. Conducting polymer coatings are known to dramatically decrease electrode impedance and increase charge injection limit [18, 69], and have been used to enable recording from ultrasmall electrode sites [63, 70]. New advances in conducting polymers may be found in novel dopants [58, 71], drug delivery [71], and novel monomers and crosslinkers for ease of functionalization or improved stability [72-75]. These novel polymer coatings may allow for further decreased size of both recording and stimulating electrodes for central and peripheral nervous system applications.

### **1.3.1.1 Textural Modifications**

The natural topography of tissues is inherently heterogeneous, with subcellular features sizes. In contrast, even the smallest neural electrodes are comparatively smooth. Cells are able to differentiate between surfaces at nanometer scales, and changes in the topography of substrates that cells are cultured on can have dramatic effects on the morphology and phenotype of the cells themselves.[76-85] This topographical mismatch may contribute to the recognition of foreign bodies by host cells.

One method of imparting topography to a substrate is to deposit a substrate directly onto the electrode. Imparting nanoscale topography to neural electrodes without altering the surface chemistry is often achieved through destructive means such as chemical[86] or ion etching[85, 87]. This may cause concerns for researchers handling delicate and expensive neural electrodes. However, a novel method of imparting topography in a non-destructive manner have been developed using silica nanoparticles. Silica nanoparticle, discussed later in terms of the applications for drug delivery, are particularly attractive topographical modifications due to their highly controlled size and surface chemistry.

### **1.3.2 Mechanical Properties**

Biological tissues, particularly those found in the CNS, have very low mechanical moduli. However, traditional electrode materials such as silicon and metals are exceptionally stiff and have young's moduli of up to 5 orders of magnitude higher than the surrounding tissues. This is useful for device insertion, but the different responses of the tissue to stresses causes constant motion of the device relative to the surrounding tissues. These micromotions may be present even during physiological changes such as fluctuations in blood pressure and are a constant source of irritation for the sensitive tissues.

In efforts to reduce mechanical mismatch between the electrode and the nervous tissue, electrodes constructed to be soft and flexible [60, 88-90] or stretchable [31, 91-93] continues to be a hot topic of research. Increasing flexibility can be achieved via reducing the cross sectional area [94] or increasing the length of the device, without changing the material properties [95]. Alternatively, novel soft and/or elastic conducting materials may be developed. Many of these flexible and elastic electrodes have demonstrated reduced FBR chronically, but rigorous and direct

comparisons in chronic recording performance between soft electrode and traditional silicon/metal electrodes remain to be seen.

Creating soft and flexible electrodes presents difficulties with insertion. Many of these difficulties are handled by coatings such as silk [96, 97] and carboxymethyl cellulose [98], or shuttles [88, 99, 100], syringe injection [101] and magnetic insertion [102]. Materials that are stiff at room temperature and soften after implantation in the brain are another interesting strategy [103, 104], however, these materials tend to absorb water *in vivo*, which challenges the insulation. Functional devices with these mechanically adaptive materials have yet to be demonstrated.

Mechanical mismatch can also be minimized by removing the tether. Note “tether” here means the interconnect between the device that is in the brain tissue and the connector that is usually mounted on the skull. This may be accomplished by implanting the entire device below the meninges [105], and using ultrasonic [106, 107] or induction [108] based power supplies for signal and/or power communication. While currently limited in ability to gather and transmit high quality information, the potential benefits of wireless devices are tremendous.

### **1.3.3 Bioactive Coatings**

After implantation, host glial cells investigate the injury site by extending their processes towards the electrode. Once in contact with the electrode, the cells recognize the foreign body and proceed to encapsulate the device. The glial cells also release inflammatory signaling molecules which recruit additional cells and result in an inflammatory cascade and greatly elevated tissue reactions. Preventing the recognition of the device as a foreign body could have dramatic downstream benefits towards minimizing inflammation and improving the long-term performance of neural electrodes.

Bioactive coatings work by directly modulating the cellular activity around the electrode via bioactive molecules immobilized on the implant surface or released from coatings [39, 71, 109, 110]. One strategy is to promote neuron-electrode integration by surface-immobilizing biomolecules that encourage neuronal attachment and growth. Extracellular matrix protein laminin has been applied to the surface of neural probes as “neuro-integrative” coating. Interestingly, no improvement on neuronal growth was found but the coating appears to increase the initial inflammatory response, while attenuating the activation of microglia and astrocytes after 4 weeks [91]. This burst in proinflammatory signaling may aid in acute wound healing and minimize long term tissue damage around the electrode. On the other hand, use of L1, a neuron specific cell adhesion molecule, has resulted in increased neuronal attachment along with decreased gliosis around the implants [40, 49, 111, 112]. More recently an *in vivo* TPM study revealed that microglia cells send processes to probes coated with L1 immediately after implantation at a similar speed as they do to uncoated controls. However upon arriving at the probe surface, the spreading of microglia processes was significantly reduced by the surface immobilized L1 [49]. This study suggests that there is a window of opportunity to modulate the initial cellular behavior via bioactive surface cues.

#### **1.3.4 Drug Delivery**

Alternatively, drug delivery can be effective at reducing the implantation trauma and decreasing inflammation and degeneration around the site of implantation [109, 113]. While systemic administration bears the risk of side effects [114], local delivery from coatings faces the challenge of drug exhaustion after long-term implantation [71, 109, 110]. For sustained release, drug delivery channels may be incorporated into the electrode device [115-117]. Due to the

electrical nature on neural implants, electrically driven drug release may be beneficial in delivering drug locally on demand [71, 118, 119].

*The following section was previously published in the Springer Handbook of Neuroengineering and is reused with permission. [120]*

Drug administration has been explored as means to manage the inflammatory tissue response and neuronal death for maintaining a healthy and stable device tissue interface. Indeed, we observe that interventions in the brain are promising, and when possible have been highly successful. Daily intraperitoneal (i.p.) injection of melatonin, an anti-inflammatory, anti-apoptotic, and anti-oxidant molecule, has shown to decrease oxidative stress, inflammation and neuronal death around implanted electrodes and improve chronic recording quality for 16 weeks.[121] Another antioxidant, resveratrol, and anti-inflammatory minocycline injections have also shown beneficial effects for neural electrodes.[122-124] Additionally, dexamethasone retro-dialysis in the brain tissues greatly attenuates acute microglial activity in response to electrode insertion,[125] and reduces gliosis and improve blood flow near the dialysis probe, resulting in less disturbed analyte sampling over 1 week.[126] It is important to point out that such interventions may have benefits beyond the health of the tissues, as minimizing inflammation lowers concentrations of corrosive free radicals, potentially increasing the material lifetime of the probe.[127, 128]

However, systemic administration has a number of limitations. First, the blood brain barrier (BBB) prevents the entry of many potential candidate drugs into the brain, with only a select few compounds demonstrating bioavailability in the brain parenchyma. Secondly, systemic administration may cause unwanted side effects[122]. Thirdly, for the micro-device and the small inflammation zone involved, majority of the drug dose will be wasted if systemically delivered, either being destroyed by organs such as the liver, being excrete prior to performing its desired

function, or binding outside of the tissues of interest. All these challenges call for highly controlled drug delivery technologies.

#### **1.3.4.1 Controlled Drug Delivery**

Controlled drug delivery is a field where materials science, engineering, and medicine are used to tailor a chemical's release to a desired location, timing, quantity, or any combination of the three. The Journal of Controlled Release discusses three generations of controlled delivery. The first controlled delivery devices (CDD) aimed to provide sustained release via oral or transdermal administration. The 2<sup>nd</sup> generation CDD focuses on zero order release, stimulus responsive or targeted delivery using advanced polymers and nanoparticle designs. The 3<sup>rd</sup> generation include methods and treatments yet to be fully utilized, such as targeted gene expression, closed-loop mechanisms, and chronic delivery platforms[129]

Controlled drug delivery platforms employed by neural engineers are widely varied. Outside of oral administrations, the first developed methods of controlled drug delivery are based around the controllable and predictable degradation of certain polymers. Similar to these degradable polymers, hydrogel-based methods which control the diffusion of the compounds into the tissues have been explored. Another commonly employed method which has been gaining interest in the last few decades is the use of nanoparticle-based systems, or their lipid analogs, liposomes and micelles. Infusion pumps and microfluidics can also fall into the category of controlled drug delivery. Finally, electrochemical methods of drug delivery have been developed based on intrinsically conductive polymers, causing ejection of compounds into the soundings when appropriate electrical potentials have been applied.

#### 1.3.4.2 Drugs Utilized In Neural Engineering

As previously stated, drug delivery has already shown promise in addressing inflammation, modulating neural activity, and treating disease. Anti-inflammatory compounds are perhaps the most widely utilized drugs for neural engineering applications. These compounds address the innate immune reactions caused by device implantation. Dexamethasone[119, 125, 130, 131] is one of the most commonly utilized compounds, in part due to its efficacy at low dosages and partly due to its low cost. Compounds with similar effects include melatonin[121], resveratrol,[122] curcumin,[132] and superoxide dismutase mimics.[133] These compounds have often shown outstanding *in vivo* results, minimizing neuron death or glial activation, but often lack access to the brain from the vasculature and require a controlled delivery platform.

Neural modulating compounds may aid in disease treatment, device tissue integration, and neurological investigations. Acetylcholine and gamma-aminobutyric acid (GABA) has been released under controlled methods for induction and control of seizures,[134] and glutamate channel blockers like 6,7-dinitroquinoxaline-2,3-dione (DNQX) are compatible with electrochemically controlled delivery.[135] Without listing every compound capable of chemically controlling neural signals and activity, it is obvious that administration of neurological compounds can greatly benefit from controlled drug delivery.

Gene and RNA delivery into the brain is also important to mention. Viral vectors have been used to produce localized gene expression in animals without need for transgenic lines. Virally transfected GCaMP animals have been used for investigation of neuron firing[136] and calcium signaling in astrocytes.[137] RNA delivery in the brain can knock-down gene expression[138, 139] at exceedingly low concentrations in the picomolar range, demonstrating great therapeutic potential.

### **1.3.4.3 Microfluidics**

The most direct method of crossing the blood brain barrier is physically breaking into the CNS tissues. It is no surprise then that direct injection into the CNS has been well explored by the medical field. Multiple procedures of differing levels of invasiveness have been developed to directly deliver compounds to a region of interest. One particular advantage to these methods is that there is next to no limitations on the compatible compounds, and no degradation products or material debris is left behind once the device is removed. However, the invasiveness of an intracranial injection cannot be ignored, especially if the injection device must be present for an extended period of time. Constant surgical treatments are impractical, and insertion can cause discomfort and irreplaceable tissue damage. Minimizing the size of the device can aid in lowering inflammation, potentially allowing a device to remain implanted chronically. Further, if the fluid channel is small enough, the channel may even be incorporated directly into the design of a neural electrode. This brings about the field of microfluidics as a mechanism for drug delivery.

As the name implies, microfluidics are devices with small channels, which enable a solution of drug to be injected into a region of interest over time. The channels can be fabricated on the scale of microns, with the limiting factor being the pressure required to pass fluid through progressively smaller passages, as well as the stability of the material from which the device is created. These devices can be fabricated from many materials, from conventional silicon and glass, to newer materials such as silicone (PDMS), polymethyl-methacrylate, polystyrene, and polytetrafluoroethylene. These newer materials offer flexibility or anti-fouling characteristics, and can be easily incorporated into the designs of current neural electrode materials. One potential advantage of microfluidics as a drug delivery mechanism for neural engineering is the vast amount research in their design and implementation in other fields.

Drawbacks of microfluidic designs often stem from their complex fabrication. In order to incorporate this method of drug delivery, microfabrication experience, equipment, and facilities are a strict requirement. Similarly, issues with mass production of these devices may limit adoption. Further, the fluidic devices require volume injections, which may have detrimental effects to the highly sensitive neural tissues[140]. Another issue is backflow up the device due to fluid pressure separating the tissue and device.[141]

From a neural interface technology perspective, microfluidics are most often incorporated as a component of an interface device. Due to the small required size of microfluidics, design and implementation of a channel often does not substantially impact the footprint of an electrode. Direct incorporation of microfluidics into implantable neural electrodes has been demonstrated for spinal surface electrodes[142] and cortical electrodes (Figure 5).[143, 144] Designs have been proposed for a wide variety of materials, include silicon[145], glass,[146] polydimethylsiloxane (PDMS),[142] parylene,[143] and polyimide.[147] An interesting deviation from common microfabrication techniques has been demonstrated, where-in a microfluidic channel is incorporated into a macrofiber, which is then drawn into a microfiber under heat to produce a microelectrode with a fluid channel (Figure 5C-E).[148] Direct evidence for the efficacy of drug delivery through microfluidics has been demonstrated by the induction of seizure-like activity following baclofen injections.[149] Another example, dopamine infusion is capable of triggering activity in the hippocampus.[146] The Langer lab manufactured a steel based microfluidic device, capable of delivering the GABAergic compound muscimol, and successfully controlled the behavior of awake mice through administration while simultaneously recording neural activity from an incorporated tungsten electrode.[150] When applicable, microfluidic designs have been

consistently successful at delivery compounds directly into the CNS tissues while maintaining their activity.

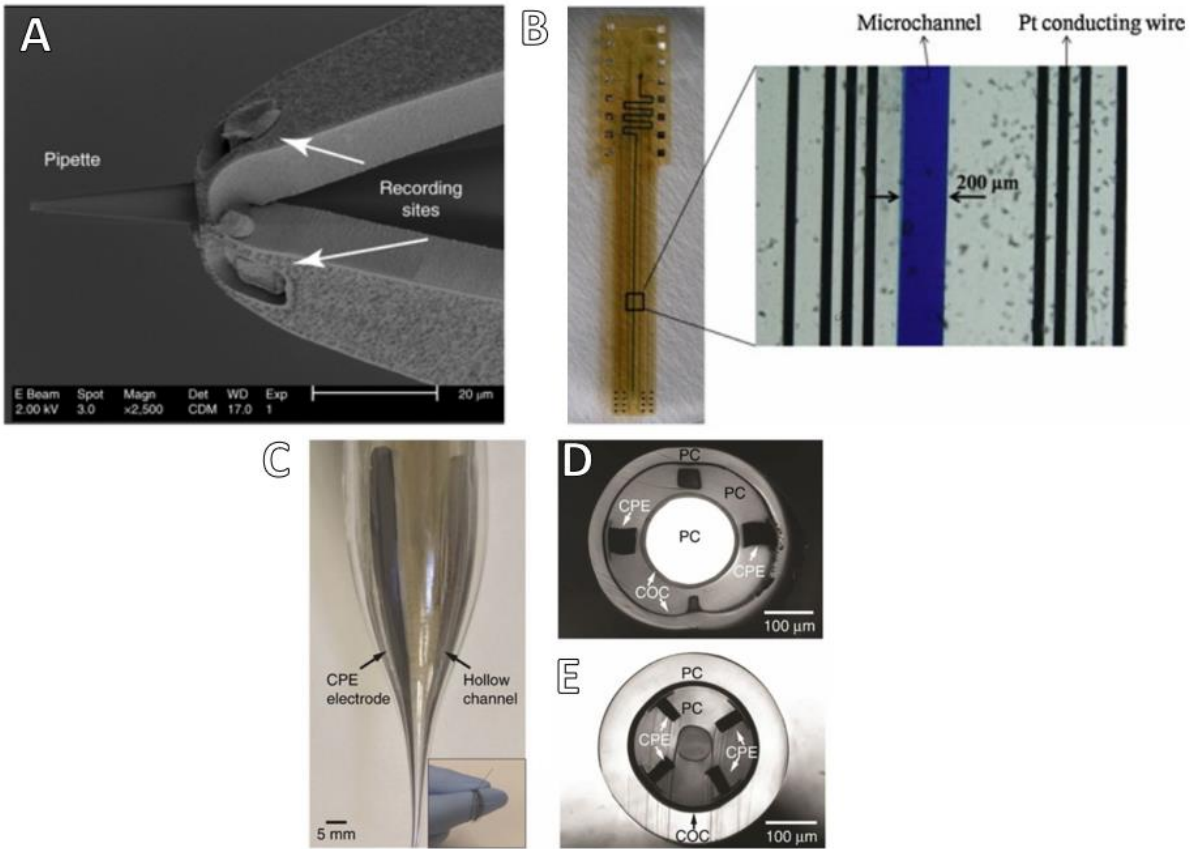


Figure 5. Microfluidic devices.

(A) SEM image of a glass based device microfluidic device, adapted by permission from Springer; Nature Biomaterials[146] copyright 2019. (B) Light images of a polyimide based electrode with microfabricated fluidic channel, reused with permission from “Fabrication of flexible microelectrode arrays integrated with microfluidic channels for stable neural interfaces”. *Sensors and Actuators A: Physical* 2013, 197, 9-14 with permission from Elsevier. (C-E) Pulled fiber electrode with recording sites, optogenetic stimulation, and microfluidic channels, reused with permission from Springer: Nature biomaterials[148] copyright 2015. (A) SEM image of a glass based device microfluidic device, adapted by permission from Springer; Nature Biomaterials[146] copyright 2019. (B) Light images of a polyimide based electrode with microfabricated fluidic channel, reused with permission from “Fabrication of flexible microelectrode arrays integrated with microfluidic channels for stable neural interfaces”. *Sensors and Actuators A: Physical* 2013, 197, 9-14 with permission from Elsevier. (C-E) Pulled fiber electrode with recording sites, optogenetic stimulation, and microfluidic channels, reused with permission from Springer: Nature biomaterials[148] copyright 2015.

#### 1.3.4.4 Degradable Polymers

Controlled release from many polymeric systems of drug release is predicated on their predictable degradation rates, most typically by hydrolysis. In a general sense, the compound of interest is trapped inside of the polymer matrix. This compound will be released slowly as the polymer degrades away, resulting in a controlled release of the compound localized to the site of implantation. As an interesting alternative, some degradable polymers don't contain any loaded compounds, because the polymer itself degrades into the drug of choice. In one example, the polymer takes the form of a pro-drug, which becomes active upon degradation into salicylic acid.[151]

Because the polymer must degrade under physiologic conditions, this method of drug delivery is dependent on the polymer itself being somewhat unstable. The method and time of degradation is directly linked to the drug release abilities. Most often, these polymers will have hydrolysable bonds in the backbone or in the crosslinking, such as anhydride and ester bonds. Carbon-carbon bonds are generally viewed as non-hydrolysable, making the inclusion of heteroatom groups necessary. Somewhat less common is the deterioration of the polymer through a second factor, potentially enzymatically driven or in response to oxidative stress.

When designing a drug delivery platform, it is best to understand factors that control the rates of degradation of your materials. Fortunately, factors affecting hydrolytic degradation are well understood. The first factor is the type of degradable bond. In general, anhydride bonds are the most reactive and rapidly degraded, followed by ester bonds.[152] Amide bonds are slower[152] and may require a secondary factor to speed up the degradation. The second factor impacting the degradation rate of the polymer is the hydrophilicity of the backbone. Polymers with backbones and sidechains that attract water are more likely to degrade faster, while hydrophobic

groups slow down degradation.[153] As an example, PLA and PGA are very similar in structure, differing by only a hydrophobic methyl group, but this small difference is enough to prolong the life of PLA relative to PGA. The third factor is the crystallinity; polymers of greater crystallinity degrade slower than amorphous polymers.[152, 153] Degradable polymers are generally amorphous to semi-crystalline,[154] and the degree of crystallinity is affected by the arrangement and size of the side chains and processing conditions. In general, bulky side-groups produce low crystallinity while processing conditions such as annealing and pulling result in higher crystallinity. Finally, a regular and repeating pattern of side groups tends towards higher crystallinity. Understanding these trends may aid in tweaking the polymer to the appropriate half-life.

Degradable polymers have a history of usage within the CNS for controlled drug delivery. The Gliadel Wafer® is one of the most successful examples, used to combat glioma after surgical removal of the tumor. This drug delivery platform utilizes a degradable polymer disk, which releases its payload and degrades away. After resection of a tumor, the wafer is placed in the cavity, where the degradable bonds control the release of carmustine.[155] The Gliadel Wafer® has shown to increase both life expectancy and quality of life for patients with malignant gliomas.[155, 156] Some degradable polymers (i.e. PLA, PLGA, PCL, and many others) are compatible with electrospinning.[79, 157] Electrospun polymers can be directly applied to many surfaces, and possess exceptionally high surface areas to volume ratios, presenting an attractive drug delivery platform.[79, 157] Similarly, degradable polymers can form micro/nanoparticles, or serve as gating mechanisms for other nanoparticles to control delivery of compounds[154, 158]. These polymeric particles can even be designed to target CNS tissues after intravenous administration, as discussed later in the nanoparticle-based methods of drug delivery.

#### **1.3.4.5 Hydrogels**

Hydrogels present a second form of polymeric drug release. As the name implies, a hydrogel is a crosslinked (physically or chemically) hydrophilic polymer where a substantial portion of its mass is water. Changing the water content and the rate of diffusion of the polymer are therefore the major factors in modulating the release of compounds from the matrix. The hydrogel itself can then be stable or degradable, depending on the application. Hydrogels themselves have many unique and interesting properties which make them ideal materials for using in neural engineering, even when not accounting for the potential for drug delivery. First, they are soft, even approaching the mechanical modulus of the neural tissues and may minimize mechanically driven inflammation over long implantations[159]. Second, many hydrogels possess anti-fouling properties, which may aid in controlling the release of drug into the tissue or decreasing cellular response to the implant. Outside of drug delivery, this has led to hydrogels being utilized to control tissues reactions to implanted devices, as well as masking foreign bodies from the host immune system. Hydrogels can serve as regeneration scaffold in the spinal cord[160] or throughout the body, even conforming to the shape of the wound after injection.[160] Finally, many biologically derived materials, such as collagen, alginate, and extracellular matrix create outstanding hydrogels, while also imparting their own useful characteristics and often being biodegradable.

Since the implantation of the electrode devices already breach the BBB, drug delivery coatings do not need to include design strategies for BBB crossing. Polymer coatings can be applied to an electrode by dip-coating, spin coatings, or direct polymerization at the electrode surface, allowing for drug delivery local to the neural implants.

Frequently, degradable polymers and hydrogels are combined for controlled release of drugs or proteins. Kim and Martin loaded dexamethasone into degradable PLGA particles which were then bound to an electrode in an alginate hydrogel for sustained release over two weeks.[161] PLGA fibers were also encased in alginate on a neural electrode for controlled release of dexamethasone for over 5 weeks.[162] Another experiment released dexamethasone from nitrocellulose coatings on silicon neural electrodes, significantly reducing microglial activity at 4 weeks post implantation.[163] Dexamethasone loaded PLGA fibers have also been used for peripheral nerve cuff electrodes to minimize inflammation.[164] A similar setup was used by loading cyclosporin A into PLGA particles which are immobilized in a PEG based hydrogel coating of a cuff electrode, to increase axonal regeneration and lower fibrous tissue formation.[165] HEMA based hydrogels coated electrodes have also demonstrated controlled release of nerve growth factor.[166]

#### **1.3.4.6 Nanoparticle Based Drug Delivery**

As the name suggests, nanoparticle-based drug delivery is centered around the idea that synthesized materials with dimensions below 500nm may be loaded with pharmacological compounds for targeted and controlled release. These particles are often designed such that the drug payload is released under certain conditions, e.g. oxidative stress, changes in pH, or outside stimulation. Nanoparticles can be designed from many materials, but the most commonly used for biological applications are silica (SiO<sub>2</sub>), gold, ferric Oxide (Fe<sub>3</sub>O<sub>4</sub> and related iron oxides), and polymers. While this is not nearly an exhaustive list of compounds capable of creating nanoparticles, special care must be taken such that the particle itself and any decomposition components are not toxic.

Nanoparticle-based drug delivery systems (along with several other systems to be discussed here) have a distinct advantage over pure pharmacological interventions. The nanoparticles themselves can be modified without impacting the activity of the drug payload. Through use of signaling peptides or other surface modifications, researchers are examining ways to overcome the issues presented by the blood brain barrier. When successful, nanoparticles which have been appropriately modified can deliver compounds into the CNS tissues. This may lead to ground breaking treatments for patients of neurological disorders. Further this is relevant to neural engineers working on device tissue integration or regenerations, as new therapeutics and treatments can be investigated.

#### **1.3.4.7 Silica Nanoparticles**

Perhaps the most studied nanoparticle for drug delivery applications is the silica nanoparticle, or more specifically, the mesoporous silica nanoparticle. The characteristic feature of mesoporous silica is the highly porous structure, imparting both a high surface area and high drug loading volume. A slight alteration to these particles is the mesoporous shell, where the internal structure of the silica particle is empty. Multiple synthesis paradigms have been presented for mesoporous silica, varying in surfactant and pH. In one example, by combining a silica precursor (tetraethyl orthosilicate) and a surfactant template (cetyl trimethylammonium chloride) under basic conditions, the silica precursor condensed around the template, forming a highly ordered, porous particle.[167] Slight alterations in the reaction temperature and basic catalyst can change the order and size of the particles.[168] The resulting mesoporous silica particles can range in diameter from 10s to 100s of nanometers. Silica particles slowly degrade when exposed to simulated body fluid, with unmodified particles lasting about 4 weeks[169]. *In vivo*, mesoporous silica nanoparticles accumulate mainly in the liver and spleen, with no noticeable toxicity 1 month

after administration.[170] Finally, the surface of silica particles can be covalently functionalized via a wide range of modified silanes.[171] Modification via silane chemistry can produce amine, thiol, epoxide, alkyl, PEG, and many other functional groups, thereby tuning the properties of silica nanoparticles for niche uses. In particular, thiol and amine functional groups can be further modified to include bioactive coatings,[172] tumor targeting sequences,[173] and even BBB crossing peptide sequences.[174]

#### **1.3.4.8 Conducting Polymers for Drug Delivery**

Conducting polymers offer an interesting drug delivery platform. A conducting polymer is an intrinsically conductive macromolecule, where charge transport down a chain of alternating pi-bonded atoms proceeds with minimal resistance. The most common examples of conducting polymers for biological applications are polypyrrole (PPy), polyaniline, and polyethylenedioxythiophene (PEDOT), along with some functionalized derivatives of these compounds (Figure 6).[175-180] These polymers can be formed directly on the electrode site by electropolymerization, where the electrode is submerged in a solution of monomer and counterion. The application of an oxidizing voltage drives the polymerization of the polymer, which carries positive charges along the backbone. Charge balance is then achieved by incorporation of negatively charged species present in the polymerization solution.

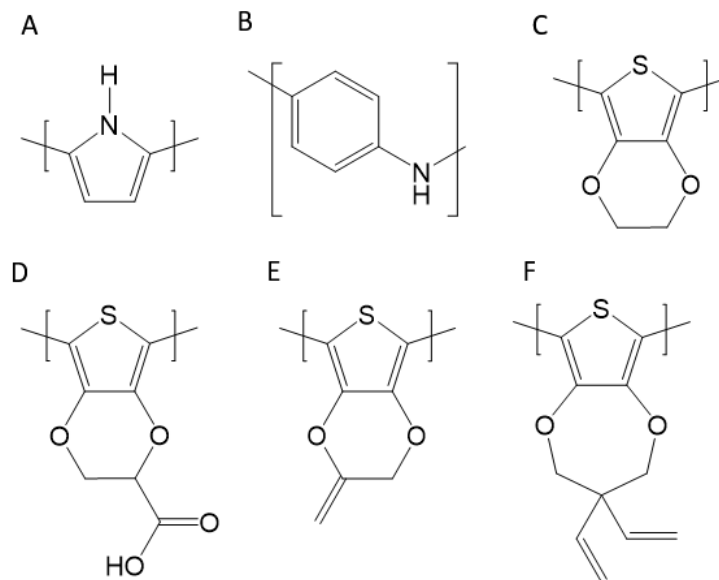


**Figure 6 Select conducting polymers utilized for neural applications and drug delivery.**

**(A) polypyrrole, (B) Polyaniline, (C) Polyethylenedioxythiophene, (D) Polyethylenedioxythiophene-Acid, (E) Polyethylenedioxythiophene-Exomethylene, and (F) Polypropylenedioxythiophene-diene. Functionalized conducting polymers (D-F) are included due to their ability to be post-modified, often to increase adhesion or impart bioactivity to the coating.**

Conducting polymers have a prolific presence in neural engineering due to their exceptional electrochemical properties. Surface coatings of conducting polymers are capable of greatly reducing the impedance of the electrode, minimizing noise and increasing the signal to noise ratio.[181] Secondly, these materials have applications for stimulating electrodes, increasing the amount of charge which can be passed from the electrode into the tissue without causing dangerous and irreversible reactions at the electrode site.[182] However, a completely different application of conducting polymers relates to their ability to undergo a reversible redox reaction upon electrochemical control, transitioning its positively charged matrix to a neutral film and vice versa. Researchers investigating this transition have developed highly controlled methods of drug delivery which are localized to the electrode surface.

Conducting polymer based drug delivery is summarized quite well by Svirskis et al.[183] For negatively charged drugs, they can be loaded into a conducting polymer film during electropolymerization as dopants. [183] Nearly any negatively charged and electrochemically stable compound can be loaded via this process and the resulting polymer contains the positively charged conducting polymer backbone electrostatically bound to the negatively charged drug. Following a reduction voltage, the polymer backbone loses the positive charge. The absence of the charge-based interaction allows for diffusion of the negative drug out of the film, creating an electrochemically controlled drug release mechanism (Figure 7). Additional mechanisms come into play for loading and release of positively charged compounds. Positively charged compounds can be loaded by physical entrapment in the film, or interactions with larger negatively charged dopants (Figure 7). Changes in the swelling of the polymer occurs between the oxidized and reduced states. When a large anionic dopant is present, as in the cationic drug release example, the reduction of the film causes the influx of positive ions to counteract the negative charge. Similarly,

the lack of charge-based interaction between the polymer and dopants causes the film to be much more porous. Water enters the film, driven by osmotic gradients. This water is then expelled during the subsequent oxidation, further encouraging drug release.[183]

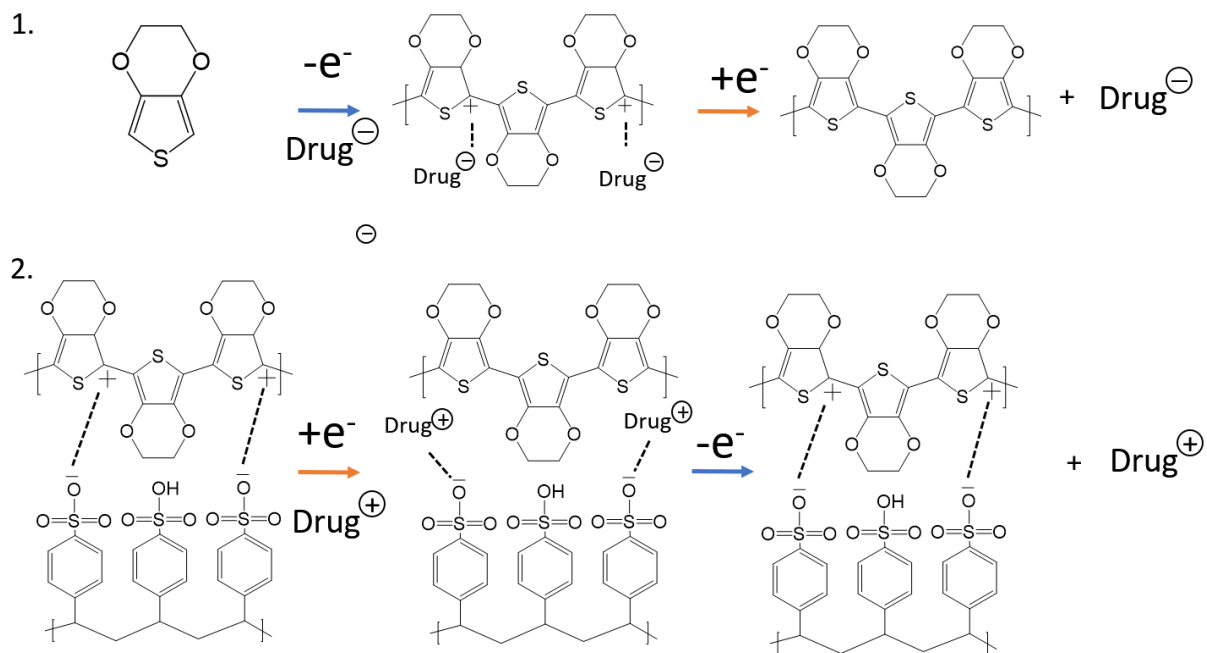


Figure 7 Drug loading and release from conducting polymers.

After polymerization, the drug interacts with either the positively charged film (1) or polyanionic dopant (2).

1. For anionic drug, loading is achieved through doping during e-polymerization, and release is via the application of a reducing voltage causes ejection of some of the drug from the matrix. This negative charge is recovered by negatively charged compounds in the solution during re-oxidation. This redox cycling can be repeated until the drug is exhausted. 2. Cationic drug release occurs under a separate mechanism. Loading is achieved by applying a reduction potential to release some of the negatively charged groups from the polyanion dopants which bind the positively charged drug. An oxidation current causes expulsion of positively charged drug.

The conducting polymer drug delivery platform provides highly controlled release in both the spatial and temporal domains. For example, while polymeric coatings are capable of localizing release almost entirely to the site of implantation, the diffusive or degradation-based trigger has minimal control after implantation. Conducting polymers on neural electrodes have a direct electrical connection to the outside of the host, allowing a researcher to stimulate the polymer at any point to trigger release. Many stimuli have been used for drug delivery, including cyclic voltage, mono and biphasic voltage/current pulses, and sinusoidal waveforms, each resulting in unique drug delivery profiles.[184] Another level of control is the amount of drug release, which can be tuned by the strength and duration of the stimulation. [184] The total amount of drug loaded into the film is also controllable by adjusting the concentration of dopant during polymerization and increasing the polymerization time.[184]

As a notable example, one study by Du et al has shown that a -1V 100ms cosine stimulus produced a small, predictable release, while -1.5V and -2V stimuli caused the release an amount over six times greater. All of these stimuli were then modeled and used to accurately predict drug release for 90 cycles. Secondly, this conducting polymer drug release platform was able to control neural activity by releasing DNQX, constrained to 1s and 446 $\mu$ m from the point of release over multiple trials.[135]

One group even released directly from the electrode in attempt to modulate the tissue reactions[185]. Other anti-inflammatory compounds such as ibuprofen have been investigated.[186] Loading and release of neurotropic factors is also feasible. Biotin has been loaded into PPy films, following which streptavidin bound nerve growth factor was immobilized and released while maintaining activity *in vitro*. [187] Similarly, many peptides and neurotrophic

factors can be directly doped into conducting polymer films,[188, 189] [190] and even be released from the film.[191, 192]

Due to the constraints of loadable quantities, methods have been developed to increase drug loading into conducting polymer films, either by modifying the structure of the film or incorporating large dopants as drug reservoirs. By polymerizing around and subsequently dissolving polystyrene beads, Luo et al was able to make a highly porous PPy film, greatly increasing the drug loading.[193] Functionalized graphene oxide[71] and carbon nanotubes are also great reservoirs for drug loading.[118] The release of 6,7-dinitroquinoxaline-2,3-dione (DNQX) from PPy/CNT films was able to repeatably and reversibly silence neuron activity in the barrel cortex.[135] , while the dexamethasone containing PEDOT/CNT improved neuronal survival around neural stimulation electrode in dorsal root ganglion. [194]

Further, ion pumps have been developed for *in vivo* delivery of compounds to the CNS tissues. Ion pumps utilize a microfluidic channel as a drug reservoir, while employing conducting polymers as a gating mechanism. Reduction and oxidation of the conducting polymer pulls charged particles from the channel (or solution) into the films, then ejects them into the tissues with virtually no volume change. By controlling ion concentrations, ion pumps are capable of modulating neural activity at the single cell level[195] and *in vivo* neurotransmitter delivery.[196] These devices have been successful at delivering GABA for seizure control.[197]

## 1.4 Final Introductory Remarks

Electroactive tissues are the key components to many of our bodies most important organs. Interfacing with muscles, central and peripheral nervous systems, and cardiac tissues have all

produced clinically approved medical devices. The central nervous system is of particular interest in its complexity, unique immune system, and resistance to drug uptake due to the blood brain barrier. Despite certain challenges, the ability to interface with the brain has unlocked countless scientific and medical advancements. Through recording ionic fluctuations and the resulting voltages, researchers have even been able to decipher the complex signaling of the human brain and translate this data into movement of mechanical extremities.[2] This has enabled brain machine interfaces capable of restoring a great degree of motion to patients with quadriplegia.[198]

In this dissertation, we enhance the device tissue integration by addressing the issues of biomimetic coatings and anti-inflammatory drug administration. We have demonstrated that thiolated silica nanoparticles (TNP) immobilized on smooth substrates dramatically increase the concentration of protein bound to the surface. The increase in binding increases the bioactivity of both immobilized proteins and catalytic antioxidants.[172] In chapters 2-5, we investigate a method of altering the surface topography to increase protein binding and stability.

Conducting polymer coatings on neural electrodes lower impedance, lower noise, and raise the signal to noise ratio during *in vivo* recording.[181, 199] Additionally, localized drug release through conducting polymers is well documented.[183]. In chapters 6 and 7, we will use a sulfonate modified silica nanoparticle to load melatonin into a poly(3,4-ethylenedioxythiophene) (PEDOT) film on the electrode site for controlled release after implantation. Through localized delivery directly to the site of injury, we will extract the advantages of drug administration while minimizing or eliminating concerns of downstream and systemic side effects.

## 2.0 Enhancing Surface Immobilization of Bioactive Molecule via Silica Nanoparticle Base Coating

*This chapter has been published in [172].* Surface modification is of significant interest in biomaterials, biosensors, and device biocompatibility. Immobilization of bioactive or biomimetic molecules is a common method of disguising a foreign body as host tissue to decrease the foreign body response (FBR) and/or increase device–tissue integration. For example, in neural interfacing devices, immobilization of L1, a neuron-specific adhesion molecule, has been shown to increase neuron adhesion and reduce inflammatory gliosis on and around the implants. However, the activity of modified surfaces is limited by the relatively low concentration of the immobilized component, in part due to the low surface area of flat surfaces available for modification. In this work, we demonstrate a novel method for increasing the device surface area by attaching a layer of thiolated silica nanoparticles (TNPs). This coating method results in an almost two-fold increase in the immobilized L1 protein. L1 immobilized nanotextured surfaces showed a 100% increase in neurite outgrowth than smooth L1 immobilized surfaces without increasing the adhesion of astrocytes *in vitro*. The increased bioactivity observed in the cell assay was determined to be mainly due to the higher protein surface density, not the increase in surface roughness. In addition, we tested immobilization of a superoxide dismutase mimic (SODm) on smooth and roughened substrates. The SODm immobilized rough surfaces demonstrated an increase of 145% in superoxide scavenging activity compared to chemically matched smooth surfaces. These results not only show promise in improving biomimetic coating for neural implants, but may also improve surface immobilization efficacy in other fields such as catalysts, protein purification, sensors, and tissue engineering devices.

## 2.1 Introduction

Surface modification plays a major role in solid state catalyst design, corrosion resistance, wear resistance, and biocompatibility. For implantable medical devices, bioactive and biomimetic coatings are of particular interest for biochemical sensing, promoting host tissue integration, and reducing foreign body responses (FBR). For example, Heparin coatings have been shown to decrease restenosis of vascular stents.[200] Incorporation of biological molecules such as brain derived neurotropic factor (BDNF)[201] increases the tissue regeneration when applied to regenerative scaffolds for tissue engineering. Biosensors incorporate bio-recognition molecules such as aptamers,[202] enzymes,[203, 204] and antibodies [205] onto their surface. Immobilized enzymes may aid in CO<sub>2</sub> removal for artificial lungs.[206, 207] In neural devices, immobilized proteins, anti-inflammatory peptides, and antioxidants may decrease FBR and increase tissue integration for the peripheral[208] and central nervous system.[40, 209]

However, surface immobilization of functional molecules is limited by the availability of binding sites and surface area presented by the pristine substrate. 2D surface coatings such as immobilized catalysts or proteins are only capable of being bound at a relatively low density to the surface of the substrate. The activity of these coatings may be increased if the surface area was increased. A simple mathematical calculation reveals that by using the hexagonal sphere packing method, we can convert a smooth surface to a sphere coated surface, which nearly doubles the available surface area, with hexagonal sphere packing increasing area by a factor of 1.9, or up to 4.1 if the underside of the sphere can still be accessed. As such, nanoparticle immobilization to the surface of a substrate offers a promising method of increasing the surface available without damaging the substrate, as is a potential in surface etching. Silica nanoparticles are commonly employed for drug delivery[210] and have been well characterized as biocompatible.[211, 212] In

addition, the surface properties can be easily modified via direct functionalization[213] or through incorporating different monomers into the reaction solution,[213, 214] producing nanoparticles with active thiol[214, 215] or amine[213] groups. Together, these properties make silica nanoparticles attractive candidates for surface modification when biocompatibility is a concern.

Implanted neural electrodes are one example where surface modification has shown benefit in promoting device-tissue integration. The potential for neural interfacing devices to restore neurological function to patients is profound, but most neural electrodes suffer from a chronic degradation in recording quality. Biologically, this long-term degradation is often attributed to the host inflammatory response to the implant, of which the native glial cells (notably astrocytes and microglia) play a critical role.[216] In response, increasing the biocompatibility of these devices has become an extensive field of research. Nanopatterned surface ridges on silicon implants have been showed to reduce the activity of astrocytes *in vitro*,[87] while surface topographic features can guide neurite outgrowth and alignment.[78, 217] Meanwhile, superoxide dismutase mimics such as Mn(III)tetrakis(4-benzoic acid)porphyrin[133, 218] and amine functionalized meso-tetra (2-pyridyl) porphine (referred to as iSODm)[133, 218] have been covalently bound to the surface of neural implants to reduce harmful reactive oxygen species (ROS) released both acutely after insertion injury and chronically as a component of the inflammatory tissue responses. Biomimetic coatings utilizing peptides[188, 189] and proteins[40, 47, 219] have pronounced effects in reducing the inflammatory response and/or encouraging neurite attachment as well as decreasing activation of glia. Laminin coated surfaces can modulate the inflammation around the implant, increasing the microglia activation acutely but decreasing the glial scar after 4 weeks.[209] Neural electrodes modified with the neuron specific adhesion protein L1 have shown attenuated microglia

activation immediately after implantation,[219] as well as increased neuron attachment, neuron health, and reduced glial encapsulation over many weeks of implantation.[40]

Here we describe a novel surface modification technique utilizing thiol functionalized silica nanoparticles to increase the available surface area for protein and antioxidant catalyst binding (Figure 8). We utilize neural electrodes as a model system, which may benefit from an increase in the density of bioactive molecules at the surface. Through nanoparticle surface roughening, we can increase the area of a flat neural probe, proportionally increasing the number of active sites for crosslinking and bioactive molecule attachment, thereby increasing the effectiveness of surface immobilization. We test three immobilizable molecules: iSODm, L1, and laminin. First, we show that increased antioxidant attachment (iSODm) on textured surface is more effective at eliminating reactive oxygen species (ROS), in comparison to the smooth surface control. Second, we demonstrate that increased protein attachment (L1 and laminin) results in increased neurite outgrowth of primary neurons cultured on nanotextured substrate compared to protein bound smooth controls. Third, increasing surface area alone does not lead to increased cell attachment.

## **2.2 Methods**

### **2.2.1 Materials and Characterization**

All chemicals were purchased from Sigma-Aldrich and used as received unless otherwise noted. Ultrapure di-water was used for all experiments (18.2M $\Omega$ , Milli-Q). Glass Coverslips (8mm diameter) were purchased from Electron Microscopy Sciences. Silicon wafer was ordered from

University Wafer. Pregnant and post-natal rats were ordered from Taconic. All animal procedures were performed in compliance with the United States Department of Agriculture and were approved by the University of Pittsburgh Institutional Animal Care and Use Committee.

Transmission electron microscopy (TEM) images were taken on Joel 2100F TEM microscope. For TEM, nanoparticles were collected from suspension via centrifuge and resuspended in 100% ethanol to form a dilute suspension. To produce reduced particles, 15mg of Tris(2-carboxyethyl)phosphine (TCEP) was added to 2ml of suspension for 10 minutes prior to collection by centrifuge. 1ul drops were added over TEM grids (400 mesh carbon on copper, Ted Pella). Scanning electron microscopy (SEM) was performed by JSM6335. SEM samples were made conductive by sputter coating a 3.5nm thick layer of Au/Pd alloy (108Auto, Cressington). Atomic Force Microscopy (AFM) was performed by asylum MFP3D with silicon probes (HQ-300-Au, Oxford Instruments) on dehydrated samples on silicon substrates. Dynamic Light Scattering (DLS) was taken in Malvern ZS90 Zetasizer. All spectrophotometry measurements were performed by SpectraMax i3x, Molecular Devices. Water contact angle (WCA) and ellipsometry were performed by AST Products VCA Optima and J.A. Woollam  $\alpha$ -SE, respectively. Ellipsometry data was fitted with a Cauchy model, using a silica refractive index of 1.46. Fluorescence microscopy images were taken by Leica DMI4000b.

### **2.2.2 Nanoparticle Fabrication**

Thiol functionalized nanoparticles were prepared via a sol-gel process. 50mL of 0.014M NaOH in H<sub>2</sub>O was heated to 70°C. While vigorously stirring, 500 $\mu$ l of tetraethyl orthosilicate (TEOS) was quickly pipetted into the flask. After 5 minutes, 100 $\mu$ L of mercaptopropyl

trimethoxysilane (MTS) was added and the solution reacted for 2h to form a slightly cloudy nanoparticle suspension. Nanoparticles were collected by centrifugation.

### **2.2.3 Nanoparticle Characterization**

For Dynamic Light Scattering, 0.5 mg of nanoparticles were re-suspended in 50mg TCEP dissolved in 2mL of water to break any di-sulphide bonds between particles and sonicated for 5 minutes. The particles were again collected, suspended in 2mL of water, pipetted into a disposable polystyrene cuvette, and analysed. Note that TCEP was only used for nanoparticle size characterization with DLS and TEM.

Thiol concentration was measured with Ellman's reagent. A calibration curve was established by dissolving MTS in pH 7.4 phosphate buffered saline (PBS), and reacting with equal volumes of Ellman's reagent (2mg/mL) in PBS. 0.2mg of TNPs was suspended in 1mL of PBS and reacted with 1mL of Ellman's reagent solution for 15 minutes. Particles were spun out of solution prior to measuring absorbance. Colour change was measured by spectrophotometry at 420 nm.

### **2.2.4 Surface Functionalization**

Surface modification routes of experimental and control surfaces are described in Figure 8. Prior to functionalization, glass coverslips or silicon wafers were cleaned by sonicating in acetone for 3x15 minutes and isopropyl alcohol for 3x15 minutes. Substrates were then submerged in piranha solution (3:1 H<sub>2</sub>SO<sub>4</sub>: 30% H<sub>2</sub>O<sub>2</sub>) for 30 minutes to remove any surface contamination. Cleaned substrates were dried under nitrogen, and placed into a 48 well plate. 500µl of 0.1M NaOH

was added to each well for 1 hour followed by 20 minutes of sonication. Substrates were washed thoroughly in water followed by ethanol and dried under nitrogen. 500 $\mu$ l of 2.5% (3-glycidyloxypropyl) trimethoxysilane (GTS) in ethanol and 0.1M acetic acid was added to each well and allowed to react for 1 hour. Wells were washed with ethanol and dried under nitrogen stream. To some of these GTS functionalized samples, thiolated nanoparticles were added to create the textured surface. Nanoparticle suspensions were created by centrifuging 2mL of the prepared TNPs solutions and resuspending the TNPs with sodium carbonate (100mg/ml) aqueous solution. 300 $\mu$ L of nanoparticle suspension was added to each well containing GTS functionalized coverslips and incubated at 80°C for 30 minutes to form the TNP coated coverslips. To other GTS functionalized samples, iSODm or proteins were later added directly to form the GTS smooth surface controls.

Additionally, smooth MTS coated substrates were prepared as surface chemistry matched controls to examine the effect of surface texturization. NaOH treated substrates were added to 25mL anhydrous toluene which was then degassed under N<sub>2</sub>, then kept under nitrogen atmosphere. 625 $\mu$ L of MTS was syringed into the flask, and allowed to react for 1 hour. Samples were washed with ample toluene then dried under N<sub>2</sub>.

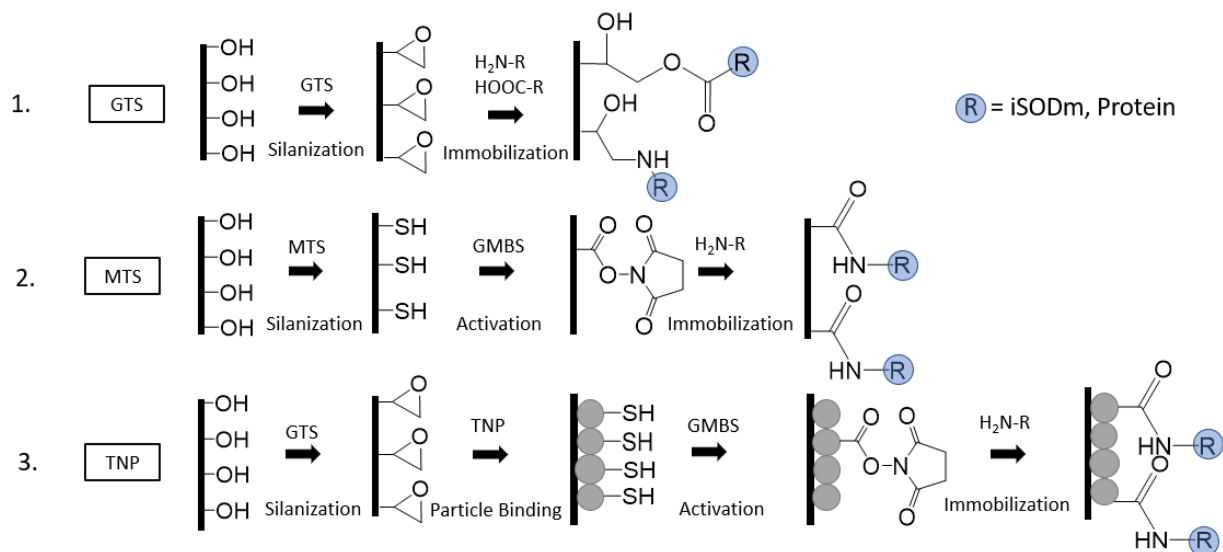


**Figure 8 Scheme of surface modification.**

1) **GTS surfaces.** Smooth silicon and glass substrates are first activated then coated by a layer of epoxide containing silane. Epoxide modified surfaces are linked to amine/carboxyl containing antioxidant or protein via nucleophilic ring opening (GTS surfaces). 2) **MTS surfaces.** Smooth silicon and glass substrates are activated then coated with a thiol containing silane. Thiol groups are linked to amine containing molecules by a N-Malaimidobutyryl-oxysuccinimide ester (GMBS) crosslinker. 3) **TNP surfaces.** Thiol coated nanoparticles are linked to the GTS modified substrate by carbonate catalysed ring opening to produce a roughened surface with thiol groups which can link to amine containing molecules via GMBS

L1 protein was isolated from P4 postnatal rat pup brains using affinity column as previously described.[220] Laminin was purchased from Invitrogen. 1mg of sulfo-GMBS was dissolved in the minimum amount of dimethyl formamide, then brought to a final concentration of 0.2mg/ml in absolute ethanol. 200 $\mu$ L of GMBS solution was added over MTS and TNP functionalised coverslips in dried wells for 1 hour followed by ethanol and PBS washing. Protein immobilization occurred by reacting protein amine groups with epoxides on the GTS surface, or oxy-succinimide esters present on GMBS that are coupled to MTS and TNP modified coverslips, respectively. 100 $\mu$ l 20 $\mu$ g/ml protein solution was added over the functionalised coverslips (GTS, MTS + GMBS, and TNP+GMBS) and incubated for 1.5 hours at 37 $^{\circ}$ C followed by 30 minutes at 23 $^{\circ}$ C.

Superoxide dismutase mimics (SODm) based on a reactive metal centre coordinated to a porphyrin are well characterized in their ability to reduce the presence of free radicals.[221] To produce the immobilizable form of SODm (iSODm), meso-tetra (2-pyridyl) porphine (Frontier Scientific) was reacted with excess 3-bromo-propylamine to form amine side groups, followed by MgCl<sub>2</sub> to create the reactive centre as previously described.[218] To immobilize, iSODm was dissolved in water (4mg/ml), and 350 $\mu$ L was plated over GTS, MTS + GMBS, or TNP + GMBS modified coverslips for 1 hour at 23 $^{\circ}$ C.

### **2.2.5 Evaluation of Antioxidant Coatings**

Cytochrome-C assay was performed to determine the catalytic superoxide scavenging property of the immobilized iSODm using different surface modification methods. Specifically, Superoxide (O<sub>2</sub><sup>•-</sup>) was generated by reacting xanthine oxidase (0.1 mg/ml) and xanthine (0.1 mg/ml) in the presence of cytochrome-C (2mg/ml) in 1 x PBS. To prevent interference from H<sub>2</sub>O<sub>2</sub>,

catalase (1mg/ml) was added to the reaction. The assay was conducted in a 48-well tissue culture polystyrene dish at room temperature, and each well received 100  $\mu$ L reagent solutions. After 30 minutes, the reaction product from the 48-well plate was transferred to a 96-well half area plate for absorbance measurement of the oxidized cytochrome C at 550 nm.

### **2.2.6 Surface Protein Concentration**

Protein coated samples were washed by 1% Tween-20 in PBS to remove any non-covalently bound protein then moved to a glass vial. 400 $\mu$ L of 6M HCl was added to the vials, which were then placed in an 80°C incubator for 36 hours to digest the amide bonds. The solution containing the digested amino acids was analysed by spectrophotometry for absorbance at 280nm.

### **2.2.7 Surface Characterization**

Five samples were prepared as described above, each sample was measured at 2 separate points for WCA and ellipsometry. Stepwise reactions were monitored by WCA. Prior to contact angle measurement, samples were washed with water and dried. Thickness and surface roughness were measured by ellipsometry. Prior to measurement, samples were dried by compressed gas to remove any dust from the surface. Nanoparticle distribution was visualized by SEM. Nanoparticle adhesion was qualitatively examined by a scotch tape assay, described further in the supplemental material.

### 2.2.8 Cell Culture

*In vitro* neuron and astrocyte cultures were used to assess the biocompatibility and bioactivity of the surface. Neurons were collected from E18 rat fetuses. E18 pregnant Sprague-Dawley rats were euthanized under CO<sub>2</sub> followed by decapitation. Rat pups were removed and washed with 70% ethanol solution, followed by removal of the foetal pup brain. Brains were homogenized by soaking in 0.25% trypsin/EDTA for 15 minutes then mechanically dispersed by repeated trituration with a fire polished Pasteur pipette. 10µL aliquots of cell suspension were added to 10µL of trypan blue solution prior to counting by haemocytometer. Only cells deemed viable were counted. Three coverslips per condition were prepared as described above and placed in a 48 well plate (TCPS, Falcon). Neurons were plated at a density of 25,000 cells/well in B27/GlutiMax/PenStrep supplemented Neurobasal Media and grown for 36 hours. Cultures were repeated 3 times to ensure validity of the results.

Astrocytes were isolated from E18 Rat fetuses. E18 pup brains were collected as described above. 6 pup brains were homogenized by soaking in 0.05% trypsin/EDTA for 25 minutes followed by mechanical dispersion by trituration. Cells were resuspended in astrocyte culture media (10% FBS, 1% PenStrep in DMEM) and plated over a poly-lysine coated 75cm<sup>2</sup> cell culture flask (Corning) for 10 days, replacing the media every third day. Once the astrocyte layer was confluent, microglia and oligodendrocytes were removed by vigorously shaking the culture flask, followed by 3 successive washes with PBS. Purified astrocytes were split between two culture dishes. For culture, astrocytes were suspended by 0.05% trypsin/EDTA and collected by centrifuge. Three coverslips per condition were prepared as described above and placed into a 48 well plate (TCPS, Falcon). Astrocytes were plated at a density of 5,000 cells/well in astrocyte culture media for 36 hours. Cultures were repeated 3 times.

### **2.2.9 Cell Staining and Imaging**

After growth, cells were fixed with 4% PFA, followed by permeabilizing with 0.2% Triton-X. Primary antibodies Beta-III-Tubulin (Neurons) and Glial Fibrillary Acidic Protein (GFAP, Astrocytes) (Invitrogen) were introduced at 1:1000 concentration in 5% Goat serum in PBS for 2 hours at 37°C. After PBS wash, secondary antibodies were introduced at 1:1000 concentration in 5% Goat serum in PBS for 45 minutes at room temperature. Nuclei were stained with Hoechst stain (Invitrogen) at 1:1000 in PBS for 10 minutes at 37°C. Each sample was imaged 3 times by fluorescence microscopy at 100x magnification, for a total of 9 samples per experimental group. Neuron culture images were analysed by NeuriteTracer ImageJ plugin.[222] Astrocyte cultures were analysed by a custom MATLAB script. Astrocyte images were treated by a binary threshold to determine area coverage. Nuclei were counted manually.

### **2.2.10 Statistics**

Unless otherwise stated, statistical significance was determined by analysis of variance (ANOVA) followed by Tukey's post hoc. Statistical significance of WCA was determined by two-way students t-test of unequal variance. Ellipsometry roughness was compared using paired t-test. The threshold of statistical significance was set to  $p < 0.05$ .

## 2.3 Results and Discussion

### 2.3.1 Nanoparticle Fabrication

Surface modification using nanoparticles may greatly increase the surface area available for surface immobilization of protein and other bioactive compounds. Ideally, the nanoparticles used for modification should be able to bind strongly to both the substrate and the desired immobilizable compound. For biologically interfacing devices, the particles must not produce toxic degradation products or present other biocompatibility issues. Thiol modified silica nanoparticles were chosen due to their ability to be easily crosslinked to amine containing compounds through a GMBS linker, to attack epoxides present on the substrate surface, and to bind to each other through disulphide bonds. Further, silica nanoparticles are non-toxic, commonly being employed in drug delivery applications.[210] The resulting surface modification from TNPs is a biocompatible and complex 3-Dimensional structure.

Thiol functionalized nanoparticles were synthesized by a sol-gel process and characterized by TEM and DLS. Determining individual nanoparticle diameters by DLS was performed in the presence of TCEP, a reducing agent that can react with disulphides and keep the nanoparticles from aggregating. Synthesized TNPs have a peak hydrodynamic diameter of approximately 50nm, with a median hydrodynamic diameter approaching 60nm. The polydispersity index of 0.161 indicates a narrow particle size distribution. In the absence of TCEP, the thiol groups are free to form di-sulphide bonds, and the particle aggregate together into large clusters, as shown in the unreduced TEM images and DLS. Unreduced TNP have a greater peak diameter of 164nm as well as a larger range of diameter values. Ellman's reagent was used to measure the surface thiol concentration of the TNP. A 0.2mg sample of nanoparticles resulted in an equivalent colour change

to 12.4 nmol of MTS, which was used in combination with the size and surface area data from DLS to calculate and determine the surface thiol concentration of one thiol per 2.8 nm<sup>2</sup>. Assuming uniformity, this high thiol density should result in more than sufficient binding sites for L1 and Laminin.

### **2.3.2 Surface Modification**

Surface modification was tracked stepwise by water contact angle (Figure 9A). GTS was chosen as a base silane because of its ability to directly interact with proteins and the TNP. This should form an active base layer, where any portion of the surface not modified by TNP can still be used for immobilization. As expected, both NaOH treatment and GTS functionalization produced a drop in the water contact angle. Direct binding of hydrophobic laminin to the GTS modified surface increased the water contact angle, indicating that proteins can bind to the epoxide modified surface. Protein binding to the surface of the GTS modified substrates is likely to occur due to combination of slower amine-epoxide interactions, and faster carboxylic acid-epoxide interactions.[223]

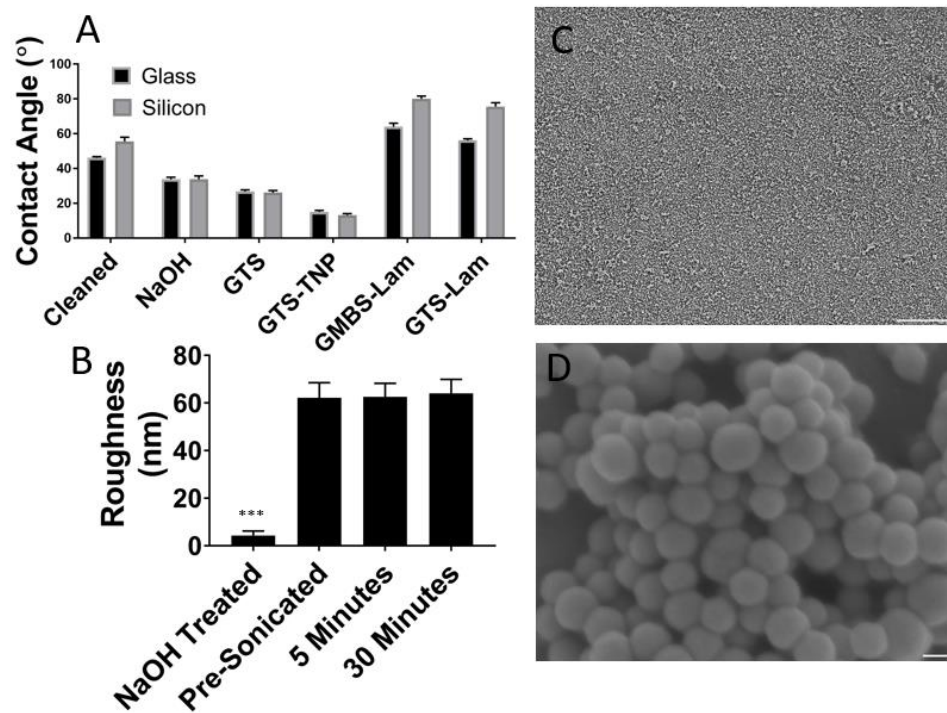


Figure 9 Surface modification and stability of nanoparticle coatings.

(A) WCA demonstrating the stepwise reaction on glass and silicon substrates. All changes are significant ( $p < 0.05$ ). (B) Surface roughness of the NaOH cleaned silicon substrate measured by ellipsometry in comparison to TNP coated surface both before and after sonication. (C) SEM of TNP coated substrates before and after sonication, scale bar  $100\mu\text{m}$ . (D) Magnified image of (C). Large clusters of nanoparticles are visible on the surface, scale bar =  $50\text{nm}$ . (\*\*\*) $p < 0.001$

TNP were bound to the GTS modified surface through sodium carbonate catalysed epoxide ring opening by the thiols presented on the TNP. Binding of TNP to the surface of the GTS modified glass further decreased the contact angle. This decrease may be attributed to changes in surface roughness and/or potentially further etching of the glass/silicon by the sodium carbonate catalyst. Finally, laminin immobilization on the surface of the GMBS linked TNP modified surface increased the water contact angle. All changes were significant ( $p < 0.05$ ) compared to the prior measurement. Changes in surface roughness were tracked with ellipsometry (Figure 9B). Substrates were limited to silicon with native oxide to minimize the initial roughness. A large increase in surface roughness was observed after the immobilization of TNPs to the surface, indicating an increase in surface features and resulting surface area. The roughness for TNP surface was also measured by AFM (Figure 11E) with a value of 58 nm with a standard deviation of 6nm, similar to the ellipsometry results. To investigate the stability of the TNP coating, samples were subjected to 5 and 30 minutes of sonication. Examining the surfaces through ellipsometry (Figure 9B) and SEM, no substantial changes in surface roughness were observed after sonication, displaying the strong adhesion between the TNP and the GTS modified surface. For chronic neural implant applications, adhesion of coatings is of great importance. Sonication has been used to test the adhesion of neural electrode coating such as Pt black.[224] The fact that the TNP coating is capable of withstanding sonication is a promising result. Surface adhesion of TNP was further characterized by a scotch tape assay. Precleaned TNP coated silicon did not leave a detectable residue on the scotch tape, again showing the strong interaction between the TNP and the epoxide coating at forces larger than those experienced during implantation. However, to fully understand the chronic stability, future in vivo studies will be conducted to examine the mechanical and chemical stability of the immobilized nanoparticles during extended implantation periods.

### 2.3.3 Antioxidant Immobilization

Previous reports have suggested that both free[122, 125] and immobilized[133] antioxidants decrease inflammation and improve neuronal health at the site of implantation. Increasing the surface antioxidant concentration and antioxidant activity may allow for a greater effect of immobilized antioxidant coatings. To examine the effect of surface roughening on antioxidant attachment, the antioxidant iSODm was bound to the surface of GTS, MTS and TNP modified substrates. As expected, all iSODm modified substrates demonstrated superoxide scavenging capacity, with control bare glass samples serving as a 0% reference (Figure 10). The superoxide scavenging activity of the iSODm bound to roughened TNP modified substrates is approximately 145% and 113% greater than that bound to MTS and GTS smooth substrates respectively (Figure 10). This large increase in antioxidant activity is likely due to a respective increase in the amount of the bound iSODm, as the small size of the iSODm allows the antioxidant to take full advantage of the surface features presented by nanoparticle roughening. The observed increase in activity from immobilized antioxidant on roughened surfaces will likely further decrease the reactive oxygen and nitrogen species released in response to an implanted neural device, thereby reducing the damage to both the host tissues and the device itself. Additionally, these results may likely translate to applications where catalyst immobilization is involved such as blood deoxygenation and chemical sensing.

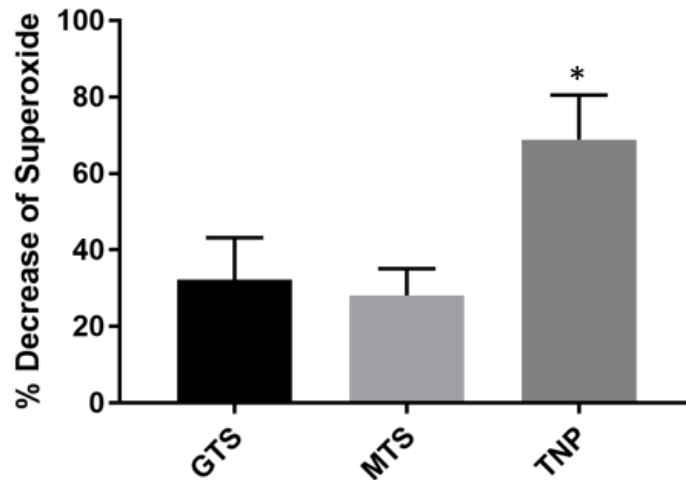


**Figure 10. Antioxidant Immobilization**

Relative decrease in superoxide level determined by the oxidation of cytochrome-c, measured at 550nm. Superoxide was produced by xanthine oxidase in the presence xanthine over GTS, MTS and TNP modified glass coverslips with immobilized antioxidant iSODm. Percent decrease of superoxide from control where cytochrome-c was oxidized over bare glass is shown (\* $p < 0.05$ ).

### 2.3.4 Surface Density of Immobilized Proteins

We hypothesized that nanoparticle surface modification increases protein quantity bound to the surface of TNP modified substrates compared to the smooth controls. Protein attachment was quantified by digesting the protein off the surfaces and analysing the absorbance of the digested solution at 280nm (Figure 11A). Absorbance values are normalized to the control GTS surface without the protein. The digested solution from the nanoparticle coated surface produced significantly higher absorbance compared to either smooth surfaces (GTS and MTS), indicating the surface density of the immobilized protein was significantly higher on the TNP coated substrates for both laminin and L1. Notably, there was a substantial difference in the percent increase in protein attachment of laminin and L1 to TNP roughened surfaces, with L1 concentrations increasing by 90% while laminin concentrations increase by 30%. This discrepancy may be due to the differences in relative size of the proteins. Where L1 is a protein with a mass of 220 kDa,[225] laminin is a much larger molecule composed of 3 separate chains with total molar mass of 810 kDa.[226] Being the larger protein, laminin occupies a greater area and volume, likely decreasing its ability to take advantage of the smaller features of the nanoparticle modified surface. Laminin also tends to form polymerized structures,[227] further increasing its relative size. As such, the relationship between the size of the immobilized molecule and the textural features has a large impact on the efficacy of roughening prior to immobilization.

AFM was used to examine changes in surface roughness after protein immobilization (Figure 11B-E). Three TNP modified samples: bare, with laminin, or with L1, were examined. The surface of the bare TNP sample and the laminin coated sample has stark differences in surface topography, with a quantifiable decrease in the surface roughness after laminin immobilization from 58nm to 41nm (Figure 11E). The L1 coated surface did not appear to be significantly altered,

and the decrease in surface roughness was not significant. These results support the previous finding that laminin is less capable of utilizing the increased surface area presented by nanoparticle immobilization, potentially due to larger scale polymerization of the protein over the surface.

Given these findings, it is reasonable to assume that decreasing the diameter of these particles would likely exaggerate these differences until particles become so small that neither protein is able to make effective use of the textural features. In addition, there is a direct relationship between the size of the immobilized particle and the resulting footprint of the device upon implantation. For neural interfacing devices, small changes in the width of the device may have pronounced effects on the resulting inflammatory response, while other applications are likely more robust to changes in device/particle size. While not directly investigated in this work, there may be value in optimizing the size of the nanoparticle base layer to best fit the application and protein of choice.

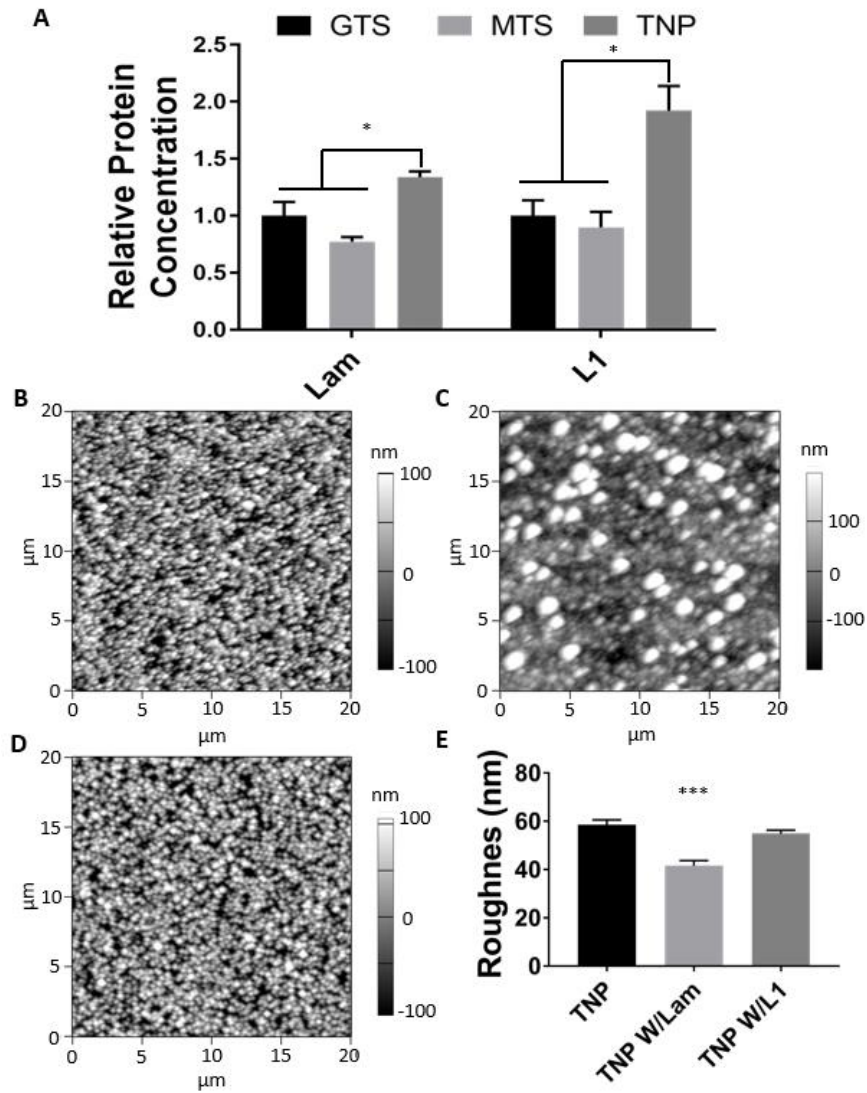


**Figure 11. Roughness of TNP Substrates**

(A) Relative protein concentration bound to substrates as determined by UV spectroscopy of the digested solution measure at 280nm. (B-D) AFM images of Bare, Laminin, and L1 modified TNP coated substrates, respectively. Left and bottom scaled in  $\mu\text{m}$ , height scaled in nm. (E) Surface roughness as determined by AFM. ( $*p < 0.05$ ,  $***p < 0.001$ )

### 2.3.5 Bioactivity of the Immobilized Proteins

Neuronal loss and glia scarring around a neural implant is one of the most common responses to neural interfacing devices. A protein coating which is capable of inhibiting the formation of this scar, either by promoting neural health or minimizing astrocyte activation and spreading has potential to increased chronic recording viability. Laminin and L1 are two proteins that have been shown to promote neurite outgrowth *in vitro* and have been used to reduce the inflammatory response to implantation *in vivo*. [40, 209] The biological effects of the surface roughening and protein immobilization were examined with cultures of primary neurons and astrocytes. Figure 12 displays the outgrowth of neuron cultures on bare and protein modified substrates. Two smooth surfaces (GTS and MTS) and a nanoparticle modified surface (TNP) were used to evaluate the bioactivity of laminin and L1 immobilized to roughened substrates. Both laminin and L1 bound to the GTS modified surfaces show an increase in the neurite outgrowth when compared to bare controls (Figure 12J), indicating that the GTS modified surface is capable of coupling to proteins while retaining their bioactivity. GTS is used to modify the surface prior to TNP attachment (Figure 8), and the ability of GTS modified substrates to increase neurite outgrowth with immobilized protein allows any substrate area that is not covered by the TNP modification to produce a bioactive coating. This may fill in any holes resulting from incomplete nanoparticle coverage, as well as produce an active base layer where small molecules may be able to bind.

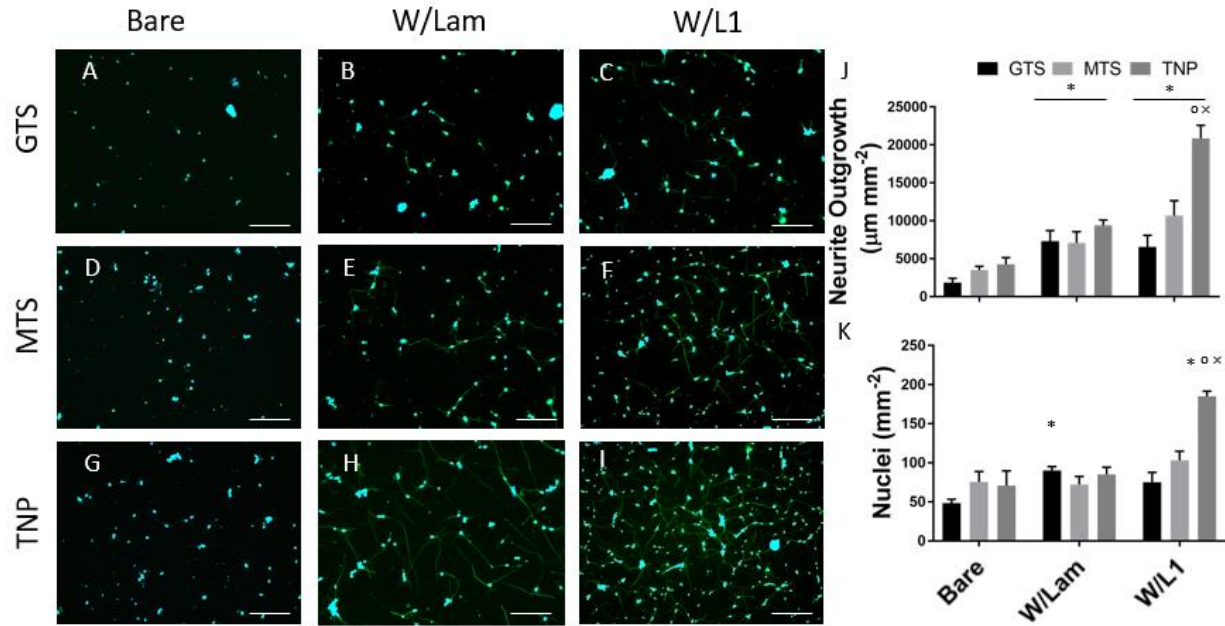


Figure 12. Neurite Outgrowth.

(A)-(I) Representative images of neurons grown on different substrates. Stained for Beta-III-Tubulin (green) and DAPI (blue), scale bar = 100µm. (J) Total neurite outgrowth per mm<sup>2</sup>. (K) Nuclei counts per mm<sup>2</sup>. (\**p*<0.05 compared to bare, <sup>o</sup>*p*<0.05 compared to laminin, ×*p*<0.05 compared to respective protein coated smooth surface)

MTS and TNP surfaces present the same reactive thiol group at the surface and utilize the same chemistry for immobilization on a smooth and nanoparticle roughened surface, respectively. After protein immobilization, smooth GTS and MTS surfaces with immobilized laminin and L1 both demonstrated significant increases in neurite outgrowth when compared to their respective bare samples. Consistent with previous findings, L1 and laminin retained their bioactivity after immobilization.[47] We expect that by increasing the concentration of protein bound to the surface, there will be a resulting increase in neurite outgrowth, and nanoparticle modified substrates have shown to increase the amount of bound protein (Figure 11A). Consequently, TNP modified surfaces show a significant increase in neurite outgrowth compared to the smooth MTS modified substrates (Figure 12J). Further, TNP W/L1 surfaces showed the highest number of neuronal nuclei among all groups. Increases in number of neurons attached may be attributed to 1) improved neuronal survival and/or 2) increased neurite extension resulting in a more stable attachment capable of surviving the multiple washing steps involved in cell staining because of the higher surface density of L1 for cells to interact with.

Examining the SEM images of the primary neuron cultures (Figure 13A-F) reveal differences in surface topography and neuron morphology. Magnified images in figure 13 (D-F) appear to show a decrease in the roughness after protein immobilization, as shown by AFM (Figure 11B-E). Respective AFM determined roughness and standard deviation of bare, laminin and L1 coated TNP samples were 58 (5.9), 41 (6.4), and 54 (4.2) nm, with laminin being significantly lower than the other samples. As previously stated, this may be attributed to the smaller size of the L1 in comparison to laminin, as well as the nature of laminin to form large superstructures. The shape of the neurites is also noticeably different on laminin and L1 coated TNP substrates. Qualitatively, cells grown on laminin coated TNP substrates show flattened neurites, whereas cells

grown on L1 coated TNP substrates showed more 3-dimensional shape for neurites. In addition, there appears to be a heightened degree of neurite sprouting off the larger processes of neurons grown on L1 adhered substrates.

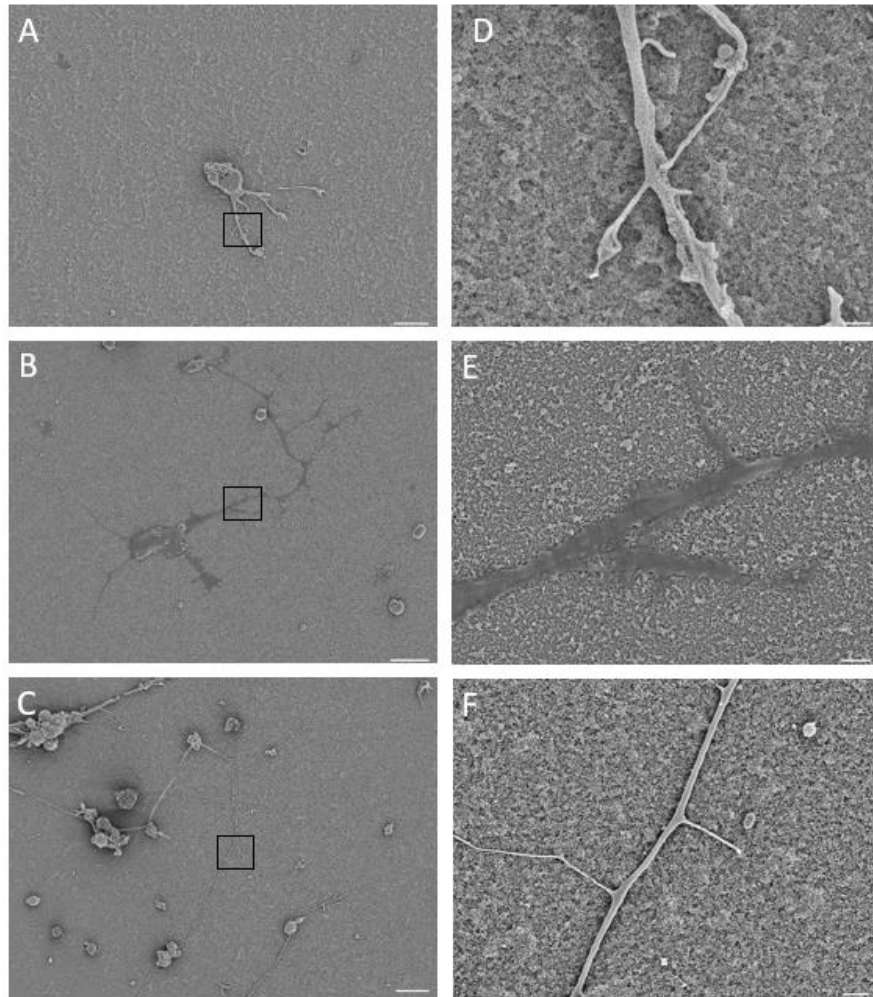


**Figure 13 SEM images of neurons grown of TNP roughened surfaces.**

**(A-C) are Bare, Laminin, and L1 modified TNP coated substrates, respectively, scale bar = 10 μm. (D-F) and are magnified regions of A-C, respectively, scale bar = 1 μm**

Astrocyte activation and adhesion may be indicative of *in vivo* astrocytic scar formation. Here we test the effect of two different protein coatings and roughening on the spreading of primary astrocyte cells. As in the primary neuron cultures, astrocytes were grown on bare or protein modified substrates, with two smooth (GTS and MTS) and 1 roughened (TNP) surface. Regardless of roughening, astrocyte outgrowth was significantly higher for groups coated with laminin compared to bare or L1 coated samples (Figure 14J).

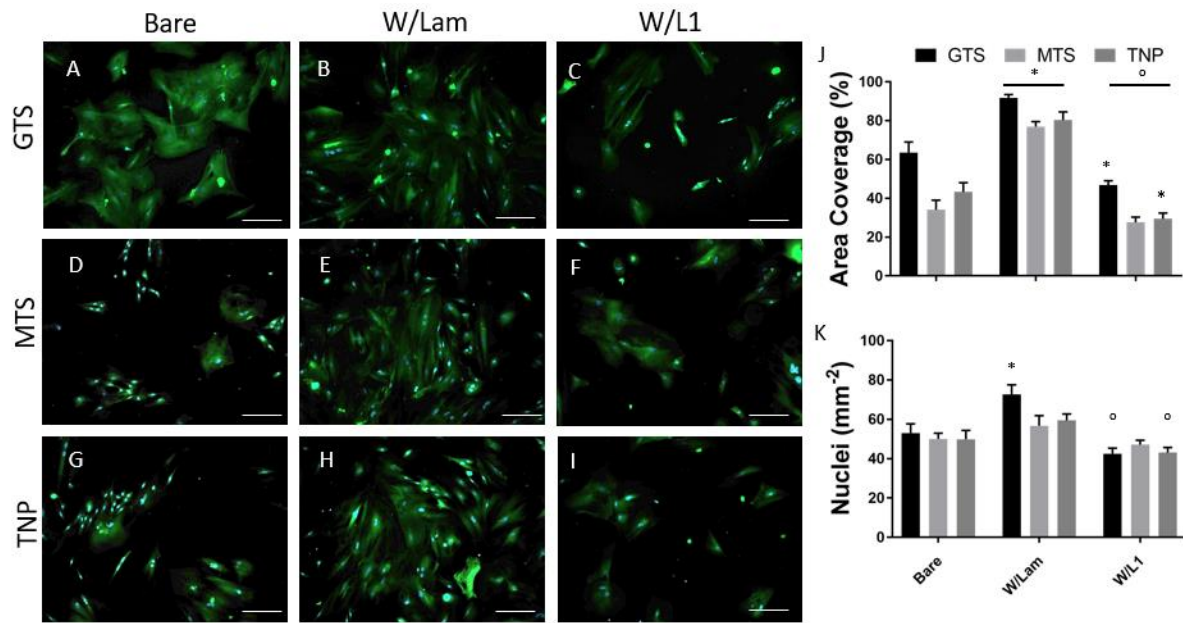


**Figure 14. Astrocyte Outgrowth.**

(A)-(I) Representative images of astrocytes grown on different substrates. Stained for GFAP (green) and DAPI (blue), scale bar = 100µm. (J) Area covered. (K) Nuclei counts per mm<sup>2</sup>. (\*p<0.05 compared to bare, °p<0.05 compared to laminin)

L1 modified groups show the opposite trend, as all L1 modified substrates show significantly lower astrocyte spreading compared to laminin groups, and both GTS and TNP groups with L1 exhibiting lower astrocyte spreading than their respective bare samples. This is consistent with previous findings for L1 and laminin coated smooth surfaces.[47, 228] Laminin is a non-specific extracellular matrix protein that promotes attachment of multiple cell types

including astrocytes, while L1 selectively promotes neurons[228] and inhibits astrocyte proliferation and astrocytic differentiation from neural stem cells.[229] The behaviors of neurons and astrocytes on L1 vs. laminin immobilized TNP surfaces are consistent with their known biological properties, which is an important criterion for surface immobilization. Likewise, astrocyte nuclei counts were significantly lower in 2 groups where L1 was coupled to the surface compared to laminin, while being higher in one of the laminin coated groups (Fig. 14K).

Compared to surface chemistry matched MTS, TNP surfaces did not produce a significant change in astrocyte spreading and adhesion, with or without bound L1. This suggests that the modified surface roughness does not increase glial attachment to the substrate. This result is different from previous reports that silicon with nano-scale etched ridges reduced astrocyte proliferation and GFAP expression *in vitro* when compared to smooth substrates,[87] but it is difficult to compare different methods of topographical surface modification directly without accounting for geometry of the texture or changes in surface chemistry. [87] but it is difficult to compare different methods of topographical surface modification directly without accounting for geometry of the texture or changes in surface chemistry. We find that the roughening prior to protein adhesion is most promising for L1 coated samples. Importantly, the ability of TNP W/L1 surfaces to further increase neuron outgrowth without increasing astrocyte activation is a promising property for *in vivo* implementation, where the beneficial survival signaling, and neural attachment may increase without negatively impacting glial activation.

## 2.4 Conclusions

Thiolated nanoparticles were successfully immobilized onto glass and silicon substrates via silane chemistry. This coating was stable under mechanical perturbation. Binding a small molecule antioxidant to the TNP functionalized surface increased the antioxidant activity by approximately 145% compared to the surface chemistry matched smooth surfaces. Roughening the surface with TNP also increased the surface density of proteins. The L1 protein binding was increased by 90% and laminin by 30%; this discrepancy may be due to the size of the bound molecules relative to the size of the surface features. L1 bound TNP surfaces greatly increased the neurite outgrowth compared to L1 bound smooth surfaces, while TNP roughening was less effective at increasing the neuronal response to laminin. Further, L1 bound TNP surfaces inhibited the astrocyte attachment and growth, an effect observed previously for L1 smooth surfaces. On the other hand, laminin increases the astrocyte attachment and growth, due to its non-specific cell adhesion promoting nature. These results confirm that the surface immobilization of bioactive molecules on TNP surface preserved their specific biological function. Taken together, roughening surfaces with TNP effectively increased the surface density and effect of bound molecules of different size. These results are not limited to neural devices. Surface modifications implemented in chemical sensing, device/tissue integration, and catalytic coatings may also benefit from this strategy.

**Conflicts of interest:** The authors declare no conflict of interest.

**Acknowledgements:** This project was financially supported by National Institute of Health NINDS (Grant 5R01NS062019 and 1R01NS089688). We thank Professor Lei Li in the

Chemical Engineering Department at the University of Pittsburgh for the use of WCA and Ellipsometry.

### 3.0 Nanoparticle Modified Substrates Enhance Biomimetic Coatings

Due to their ability to interface with neural tissues, neural electrodes are the key tool used for neurophysiological studies, electrochemical detection, brain computer interfacing, and countless neuromodulation therapies and diagnostic procedures. However, the long-term applications of neural electrodes are limited by the inflammatory host tissue response, decreasing detectable electrical signals, and insulating the device from the native environment. Surface modification methods are proposed to limit these detrimental responses but each has their own limitations. Here, a combinatorial approach is presented toward creating a stable interface between the electrode and host tissues. First, a thiolated nanoparticle (TNP) coating is utilized to increase the surface area and roughness. Next, the neural adhesion molecule L1 is immobilized to the nanoparticle modified substrate. *In vitro*, the combined nanotopographical and bioactive modifications (TNP+L1) elevate the bioactivity of L1, which is maintained for 28 d. *In vivo*, TNP+L1 modification improves the recording performance of the neural electrode arrays compared to TNP or L1 modification alone. Postmortem histology reveals greater neural cell density around the TNP+L1 coating while eliminating any inflammatory microglial encapsulation after 4 weeks. These results demonstrate that nanotopographical and bioactive modifications synergistically produce a seamless neural tissue interface for chronic neural implants.

### 3.1 Chapter Introduction

*Work presented in this chapter has been published previously in [1, 172, 230, 231].*

Biomimetic coatings are one of the most promising methods of controlling the inflammatory host tissue reactions following implantation. At its core, biomimetic coatings are specialized surface modifications that disguise foreign materials as native tissues, masking the device from immune cells and limiting their activation. The molecules chosen for these coatings are often proteins (L1, Laminin, extracellular matrix), peptides (P20), or other biological molecules such as polysaccharides. These molecules are often, but not always, chemically linked to the electrode through some form of surface modification. For example, silicon and silicon dioxide, two of the most commonly employed electrode materials, surface modification is readily performed through silanes. Chemicals such as aminopropyltriethoxysilane (ATS) and mercaptopropyltrimethoxysilane (MTS) are common examples which form high quality modifications of activated silicon surfaces. These silanes also present novel organic functional groups, which are utilized in subsequent steps to ensure a strong bond between the biomimetic molecule and the underlying electrode.

Biomimetic coatings produced in this manner have been consistently successful *in vitro* and *in vivo*, however they do suffer from limitations. First, the binding of bioactive molecules is limited to the available surface area. Neural electrodes, which have dimensions on the scales of 10s to 100s of micrometers, therefore would never be able to present the same density of bioactive molecules that exist on host cells with topographies on the scales of microns. Secondly, bioactive molecules themselves are often fragile. The function of proteins is highly dependent on their 3D conformation, and changes to this confirmation caused by improper handling, drying, or simply over time can result in a complete loss of function. It is therefore evident that new strategies which

increase the binding and stability of immobilized molecules are paramount to the long-term success of biomimetic coatings.

Another surface modification strategy for encouraging a healthy integration of the electrode and the host tissues is to tailor the surface micro and nano topography via different means of topographical modification and patterning. The effects of topographic modifications *in vitro* have been extensively studied. Neurons grown on topographically modified substrates were more viable[232], and had greater neurite outgrowth[76, 86, 172, 233]. Neuron differentiation and outgrowth can be affected by micro to nano geometries such as nanopillars,[78, 234] nanofibers,[80, 235] and nanopores.[236, 237] Topography can also vary in organization, with aligned features encouraging more directional neuron outgrowth than random features.[80, 235] Further, micro-topographical changes alter glial cell phenotypes[83] with rougher surfaces decreasing glial cell activation *in vitro*. [87, 236] However, topographic modifications alone have not been shown to be sufficient at halting inflammation in response to neural electrode implantation *in vivo*. [238] In addition, while certain topographical modifications are non-damaging,[172] many require that the surface be etched or eroded,[76, 86, 87, 238] treatments that are likely to be incompatible with thinly insulated microelectrode devices.

The potential of synergistic effects of bioactive coatings and topographical modifications in producing stable chronic neural electrodes has been less explored. Topographical modifications can increase the surface area for modification, effectively increasing the number of binding sites. Others have shown that proteins immobilized to nano-topographical surfaces are more stable than their soluble counterparts. [239]

Herein we developed and validated a nano-topographical bioactive neural electrode coating. First, we created a topographical modification by immobilizing thiol-functionalized silica

nanoparticles (TNP) to the surface of silicon and glass substrates. Next, the TNP surface was covalently coated with the neural adhesion protein L1. We examined the bioactivity and stability of the coating *in vitro* with comparisons made to the L1 coated smooth surface without TNP. Finally, the TNP+L1 coating was applied to silicon based single shank electrode arrays to evaluate the synergistic effects of TNP and L1 on neural recording performance and tissue reactions *in vivo*.

## 3.2 Materials and Methods

### 3.2.1 Materials and Reagents

All reagents were purchased through Acros Organics (Fair Lawn, NJ) and used as purchased unless otherwise stated. Tetraethyl orthosilicate (TEOS) was purchased from Millipore-Sigma (Burlington, MA). Silicon wafer was purchased through University Wafer (Boston, MA), glass coverslips through Electron Microscopy Sciences (Hatfield, PA), and silicon electrodes were supplied by NeuroNexus (Ann Arbor, MI). Functional electrodes were model A1x16-3mm-100-703, with a total length of 3mm, and electrode diameter of 30 $\mu$ m, and 1kHz impedances between 200k $\Omega$  and 400k $\Omega$ , and dummy electrodes were matched to this geometry but without the functional connector attached. Fluorescence imaging was performed on a Leica DMI4000b. Brain slicing was performed with a Leica CM 1950 cryostat. Confocal images were taken by Olympus Fluoview 1000. Scanning electron microscopy (SEM) images were taken by JSM6335. Particle sizes were measured with ImageJ. Water contact angle (WCA) measurements were performed with AST Products VCA Optima. Ellipsometry measurements were performed on J. A. Woollam  $\alpha$ -SE, data were analyzed with a Cauchy model, assigning a refractive index of 1.45.

### **3.2.2 Nanoparticle Synthesis**

Thiol modified nanoparticles were fabricated as previously described. [167] In brief, a solution of water (36mL), ethanol (5mL), and triethanolamine (6.18mL) was heated to 60°C. Under vigorous stirring, TEOS (3mL) was added dropwise. The reaction was allowed to proceed for 5 minutes, at which point mercaptopropyl trimethoxysilane (MTS, 1mL) was added. The reaction continued under stirring for 1 hour, then additional MTS (250µl) was added and the reaction continued for 1 additional hour. Particles were collected from suspension via centrifuge and washed with ethanol and water.

#### **3.2.2.1 Nanoparticle Characterization**

For Dynamic Light Scattering, 0.5 mg of nanoparticles was re-suspended in 50 mg of TCEP dissolved in 2 mL of water to break any disulphide bonds between particles and sonicated for 5 minutes. The particles were again collected, suspended in 2 mL of water, pipetted into a disposable polystyrene cuvette, and analyzed. Note that TCEP was only used for nanoparticle size characterization by DLS and TEM

Thiol concentration was measured using Ellman's reagent. A calibration curve was established by dissolving MTS in pH 7.4 phosphate buffered saline (PBS), and reacting with equal volumes of Ellman's reagent (2 mg mL<sup>-1</sup>) in PBS. 0.2 mg of TNPs was suspended in 1 mL of PBS and was allowed to react with 1 mL of Ellman's reagent solution for 15 minutes. Particles were spun out of the solution prior to measuring absorbance. The colour change was measured by spectrophotometry at 420 nm.

### **3.2.3 Particle Immobilization**

Substrates (silicon wafer, glass coverslips, or silicon probes) were washed with acetone and isopropanol, followed by activation under oxygen plasma for 5 minutes. Functional electrodes were grasped with a stereotaxic frame by the tab, while dummy probes were secured to a plastic tab which was secured to a stereotaxic frame. The activated substrates were immersed in aminopropyl triethoxysilane (APTES) or MTS at 2.5v/v% in ethanol for 1 hour then washed thoroughly with ethanol followed by water. MTS coated substrates were removed at this point to serve as chemistry matched smooth control compared to TNP electrodes. APTES modified substrates were immersed in GMBS solution (2mg mL<sup>-1</sup> in phosphate-buffered saline (PBS)) for 30 minutes, then washed with water. A nanoparticle suspension was made by sonicating TNP (10mg) in 0.1x PBS (10mL), diluted with double DI-water. APTES-GMBS modified substrates were immersed in the nanoparticle suspension for 1 hour at 37°C, with constant agitation provided by either an orbital shaker (for glass/silicon) or a small stir bar (probes).

### **3.2.4 L1 Isolation**

L1 was isolated from rat brain tissues as previously described.[220] In brief, brains were isolated from p16-20 rat pups and the membrane was isolated and solubilized in CHAPs buffer. The solubilized membrane was then passed through an antibody affinity column and L1 protein was eluted by the addition of diethylamine solution at pH 11.5. L1 samples were collected, combined, and stored at -80°C. Before use, L1 solutions were thawed and dialyzed to remove diethylamine.

### **3.2.5 Protein Immobilization**

Protein immobilization was performed on either smooth MTS modified substrates or TNP modified substrates. Substrates were re-immersed in GMBS solution ( $2\text{mg mL}^{-1}$ ), followed by washing and submerging of the substrates in L1 solution ( $50\mu\text{g mL}^{-1}$ ) for 1 hour at  $37^\circ\text{C}$ . L1 was immobilized to 18mm glass coverslip pre-modified with TNP or MTS and the slides were placed into 12 well plates. Half of the modified coverslips were dried thoroughly, and the remaining submerged in PBS (2mL). The plate was then incubated for one or four weeks, after which all samples were washed with DI water. L1 was digested off the samples with 6N HCl for 24H at  $80^\circ\text{C}$  in sealed containers. The peptide concentration was measured by UV-absorbance of the sample at 280nm.

### **3.2.6 Antioxidant Immobilization**

Immobilizable superoxide dismutase mimic (iSODm) was synthesized as described in Zheng et al. [240]. iSODm was immobilized in the same manner as the L1 protein. TNP or MTS modified substrates were submerged in GMBS solution ( $2\text{mg mL}^{-1}$ ) for 30m then submerged in iSODm solution ( $4\text{mg mL}^{-1}$ ) for 1 hour. The samples were then removed and washed with excess DI water.

#### **3.2.6.1 Evaluation of Surface Antioxidants**

Cytochrome-*c* assay was performed to determine the catalytic superoxide scavenging properties of the immobilized iSODm using different surface modification methods. Specifically, superoxide ( $\text{O}_2^-$ ) was generated upon reaction of xanthine oxidase ( $0.1\text{ mg mL}^{-1}$ ) and xanthine

(0.1 mg mL<sup>-1</sup>) in the presence of cytochrome-*c* (2 mg mL<sup>-1</sup>) in 1 × PBS. To prevent interference from H<sub>2</sub>O<sub>2</sub>, catalase (1 mg mL<sup>-1</sup>) was added to the reaction. The assay was conducted in a 48-well tissue culture polystyrene dish at room temperature, and each well received 100 μL of reagent solutions. After 30 minutes, the reaction product from the 48-well plate was transferred to a 96-well half area plate for absorbance measurement of the oxidized cytochrome *c* at 550 nm.

### **3.2.7 *In Vitro* Experiments**

To examine the long-term bioactivity of L1 after immobilization, coverslips were created and split between TNP modified coverslips and smooth MTS modified coverslips, with at least 5 samples per condition and 3 experimental repeats. 4 weeks before cell culture, 1 group of smooth and TNP modified glass was immersed in GMBS solution followed by L1 immobilization as described above. The samples were then washed and stored in PBS in a cell culture incubator. This procedure was repeated at 7 and 3 days before cell culture, as well as the day of culture.

#### **3.2.7.1 Neuron Culture and Staining**

Primary neurons were isolated from rat E18 fetuses. The mother rat was euthanized under CO<sub>2</sub> followed by cervical dislocation, at which point the pups were removed and placed in ice-cold Hanks balanced salt solution (HBSS). Individually, a pup was isolated, decapitated, and the brain removed. The cortex was isolated and submerged in .15% trypsin solution for 15 minutes at 37°C. The brain was washed with HBSS and dissociated via trituration. The supernatant was collected and cells concentrated via centrifuge. Cells were resuspended in Neurobasal media, supplemented with B27, GlutaMAX, and Pen/Strep, then counted and plated at a density of 25,000 cells cm<sup>-2</sup>. Cells were grown for 36 hours, then fixed with 4% paraformaldehyde (PFA). Fixed

cells were permeabilized with 0.2% Triton-X in PBS, followed by immuno-staining for  $\beta$ (III)-tubulin and DAPI.

### **3.2.8 Surgery and Implantation**

All animal work was performed under the guidelines of the University of Pittsburgh Institutional Animal Care and Use Committee (IACUC). A mouse model was chosen to examine the effects of topographical and bioactive modification *in vivo*, (Figure 15). Four experimental conditions were chosen to elucidate the individual and combinatorial effects of topography and proteins: control (MTS modified), L1 (MTS modified with immobilized L1), TNP (TNP modified), and TNP+L1 (TNP modified with immobilized L1). The control condition is included to assess the baseline histological responses to the implants. For acute (1 week) and chronic (4 week) histology, mice (C57-BL6) were anesthetized under isoflurane gas (1.5%) and the surgical area sterilized with iodine solution and 70% ethanol. The scalp was removed, and 4 probe holes spaced 2mm apart in a square configuration were made in the left skull, between lambda and bregma. An additional hole was made for an anchor screw to be attached. Into each animal, 1 dummy probe of each condition was implanted 2mm deep with a stereotaxic manipulator, with the order randomized. Probe holes were then sealed with silicone-epoxy. A skull cap was then formed with UV-curable dental cement, and the wound was closed by suturing around the skull cap. Four animals were implanted for each time-point, each with four electrodes, one of each experimental condition.

### 3.2.9 Chronic Electrophysiology

For electrophysiology assessment, functional electrodes were implanted in the same manner as above but were limited to one electrode per animal and electrodes were inserted into the left visual cortex. Three bone screws were placed into the skull, two anterior to the electrode, and 1 on the adjacent hemisphere to stabilize the headcap. The visual cortex was located by measuring 1mm anterior to the lambda, and 1.5mm from the midline. A small hole was drilled and the electrode was inserted with a stereotaxic manipulator such that all electrode sites were in the cortex. The hole was then sealed with silicone epoxy and the omnnetic connector was stabilized by a headcap created from UV-curable dental acrylic. Chronic data was gathered from six animals per condition.

Impedance measurements were performed on an AutoLab potentiostat, sampled between 32kHz and 10Hz. Electrophysiological recordings were performed under 1% isoflurane anesthesia. The resulting data was sampled at 24,414Hz (RX7, Tucker-Davis Technologies) prior to being analyzed under a custom MATLAB script. The data stream was filtered between 300 and 5000Hz for identification of single units. Single unit snippets (1.2ms) were isolated by threshold crossing events greater than 3.5 standard deviations of the noise, then manually sorted based on waveform and spike timing. Snippets were removed from the data prior to the calculation of the peak-to-peak noise.<sup>[65]</sup> Signal to noise ratio (SNR) was calculated as the mean peak to peak voltage of the greatest single unit waveform divided by two standard deviations of the noise.

### **3.2.10 Perfusion**

At the experimental end points, mice were deeply anesthetized with a ketamine/xylazine cocktail and perfused with 100mL PBS followed by 100 mL 4% PFA. The bottom of the skull was then removed and the brains, still attached to the upper skull, were post fixed in 4% PFA for 4 hours. The brains were then removed from the skull, sucrose protected, frozen, and cryosectioned. The electrodes remained attached to the skull and were therefor removed from the brain when the brain was separated from the upper skull. Brain slices were rehydrated and immunostained.

### **3.2.11 Immunostaining and Histology**

Brain slices were rehydrated with PBS then blocked with 10% goat serum, following which the brain slices were treated with 0.1% Triton-x for 45 minutes. Staining of the brains was performed in groups consisting of NeuN (Millipore mouse 1:250), NF200 (Abcam rabbit 1:500), Iba-1 (Millipore mouse 1:500), GFAP (DAKO rabbit 1:500), nestin (Millipore mouse 1:200), and DCX (Abcam rabbit 1:1000). The probes, which remained connected to the skull after removal of the brain, were then gathered by snapping the shank proximal to the skull. Finally, the probes were dehydrated with ethanol and hexamethyldisilazane for SEM imaging.

### 3.3 Results

#### 3.3.1 Nanoparticle Characterization and Deposition

Particle deposition is predicated on the interaction between thiols, amines, and the hetero-crosslinker gamma-maleimidobutyryl-oxysuccinimide ester (GMBS), as shown in figure 15. The deposition was monitored stepwise via water contact angle (WCA) and ellipsometry (Figure 16A), measuring changes in hydrophilicity and roughness respectively between steps. Substrates were first cleaned with acetone and isopropanol to remove larger contaminants, then activated under O<sub>2</sub> plasma. O<sub>2</sub> plasma treatment eliminated any organic contamination on these substrates, and also dramatically increased the hydrophilicity of the substrate with WCA decreased from  $65.0^{\circ} \pm 5.3^{\circ}$  to  $11.3^{\circ} \pm 2.3^{\circ}$  (mean  $\pm$  SD). Next, aminopropyl triethoxysilane (APTES) was then reacted with the activated substrate, which was verified by the increase in WCA ( $61.9^{\circ} \pm 1.6^{\circ}$ ). The amine groups were then linked to the GMBS crosslinker, reducing the contact angle ( $40.6^{\circ} \pm 3.5^{\circ}$ ). Finally, the maleimide group on GMBS reacted with the TNP to covalently link the nanoparticles to the silicon or glass. The WCA significantly decreased after particle immobilization ( $13.1^{\circ} \pm 2.3^{\circ}$ ), while the RMS roughness of the substrate increased ( $78.6\text{nm} \pm 0.2\text{nm}$ ). Nanoparticle distribution was then visualized under SEM (Figure 16B). Modification of the silicon substrate with TNP occurred uniformly across the substrate. TNP bound to each other, producing larger interconnected features with even greater roughness and surface area than would be expected from a single monolayer of nanoparticles.

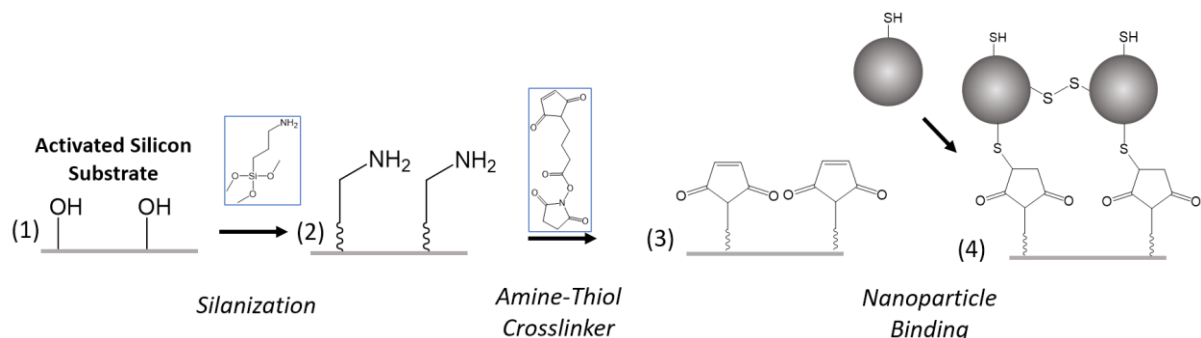


Figure 15. Nanoparticle immobilization.

1) Silicon substrates were first cleaned then activated with O<sub>2</sub> plasma. 2) The activated substrate was then silanized with APTES, producing an amine functionalized surface. 3) The amine groups were then reacted with GMBS, displacing the oxy-succinimide group, leaving the maleimide group. 4) TNP were then bound to the maleimide group via thiol-ene click chemistry. Additional bonds between TNP may form via disulfide bridging.

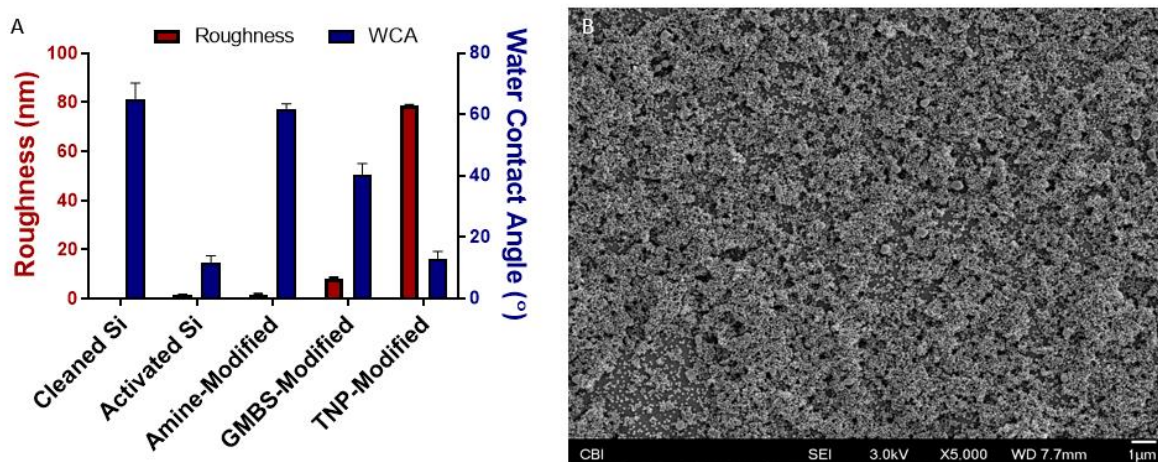


Figure 16. Characterization of TNP modified substrates

(A) water contact angle measurement changes during nanoparticle immobilization and surface roughness and changes in coating thickness of the modified silicon substrate measured by ellipsometry. Values represent change in thickness between steps. (B) SEM image of nanoparticle modified surface. Data presented as the mean  $\pm$  standard error from nine trials.

### **3.3.2 Protein Binding and Binding Lifetime**

The effect of surface topography on increasing protein bioactivity and stability was assessed via culture of primary cortical neurons (Figure 17). Glass coverslips were modified to display either thiol groups (smooth substrates) or nanoparticles (rough substrates). Smooth thiol modified substrates were produced by reacting activated glass substrates with MTS, mimicking the surface chemistry of rough substrates. Both smooth and rough samples were then reacted with GMBS followed by immobilization of L1 (see scheme in Figure 17A,B). Smooth and nanoparticle modified coverslips were coated with L1 and incubated in PBS at 37°C to examine the relative amounts of bound L1 and whether the L1 will detach from the substrate over time. We observed that there was a 75% increase in the amount of L1 bound to the TNP modified surface relative to the smooth surface prior to the incubation, indicating that more L1 was able to bind to the TNP modified surface. After incubation, the amount of L1 bound to the smooth surface decreased by 59.05% and 64.56% after one and four weeks, respectively. Conversely, the amount of L1 bound to the TNP modified surfaces was better retained, decreasing by 3.53% after one week and 15.23% after four weeks (Figure 17C).

### **3.3.3 Bioactivity of L1 and Bioactive Lifetime**

Next, we examined the long-term bioactivity of L1 bound to smooth or rough substrates. Sets of L1 modified samples were soaked in PBS at 37°C for 3 days, 7 days, or 28 days to determine if the bioactivity of immobilized L1 decreases under physiologic conditions. Additional modified coverslips were created without protein modification to examine the effect of topography on neurite outgrowth. Primary neurons were cultured directly onto the substrates for 36 hours,

followed by fixation and staining for  $\beta$ (III)-tubulin (neurons) and DAPI (nuclei). Topographical modification had a significant effect on neurite outgrowth, with an increase in the overall length of projections compared to a smooth surface without subsequent protein modification (Figure 17E). Meanwhile, L1 immobilization was advantageous regardless of surface topography, with significant increases in neurite outgrowth apparent on both smooth and rough substrates at early time points (Figure 17E). Overall, L1 modified rough substrates produced the highest neurite outgrowth of the test conditions. Furthermore, L1 was not stable on smooth substrates, with significant decreases in total neurite projections observed between the fresh and 4-week timepoints. On the other hand, there was no observed decrease in neurite outgrowth for L1 modified rough substrates, regardless of incubation time (Figure 17F).

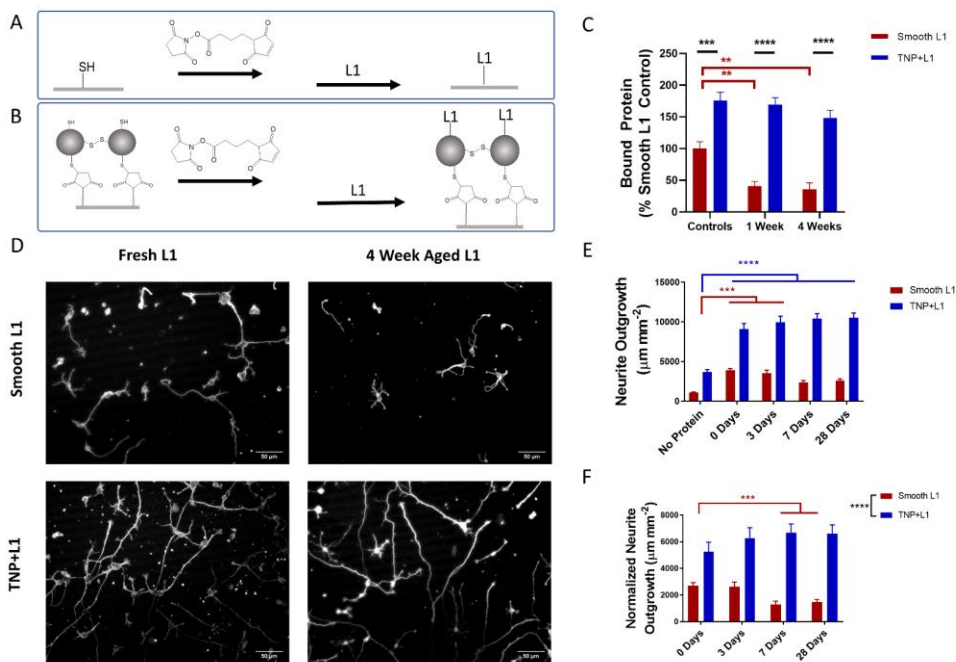


Figure 17 Protein binding and bioactive lifetime.

A) Immobilization of L1 on MTS modified substrates via GMBS crosslinking. (B) Immobilization of L1 on TNP via GMBS crosslinking. Note that the binding mechanism of both MTS and TNP is identical. (C) Relative amounts of L1 bound to glass substrates after incubating for 7 or 28 days at 37°C in PBS, n=9 with significance between timepoints determined with one-way ANOVA with Tukey's post hoc. Significance between groups was determined with Student's t-test with a Bonferroni correction. (D) fluorescence images of b(III)-tubulin stained neuron cultures grown on freshly prepared L1 modified substrates and L1 modified substrates aged for 28 days. (E) Neurite outgrowth on smooth, rough, and protein modified substrates. (F) Quantified neurite outgrowth normalized to their respective non-protein modified surfaces. Data presented as the mean  $\pm$  standard error from n=12 trials. Statistical significance was determined with a two-way ANOVA and Tukey's post hoc \*\*p<0.01 \*\*\*p<0.001 \*\*\*\*p<0.0001

### **3.3.4 Electrical Properties and Electrophysiology Performance of Modified Electrodes**

To ensure that the non-conductive coatings do not interfere with the electrophysiology recording, a set of functional electrodes was used to examine the effects of TNP+L1 coatings on the electrical property and recording capability over time (Figure 18). Impedance measurements were taken prior to surface modification (pristine) and all subsequent impedance modulus values were scaled to the pristine impedance. Following modification there was a slight increase in the impedances for the TNP and TNP+L1 electrodes, while the smooth L1 electrodes decreased slightly in impedance (Figure 18A). Impedances on all electrodes increased after implantation, but the increase in impedance was significantly lower for the TNP+L1 modified electrode at two, three, and four weeks (Figure 18A). TNP+L1 single unit yield was greatest at all time points and was significantly higher than all conditions when compared across timepoints (Figure 18B,  $p < 0.001$ ). The TNP+L1 coating did not appear to affect the SNR (Figure 18C), however, the TNP+L1 coating did produce a significant decrease in the recording noise at three and four weeks (Figure 18D).

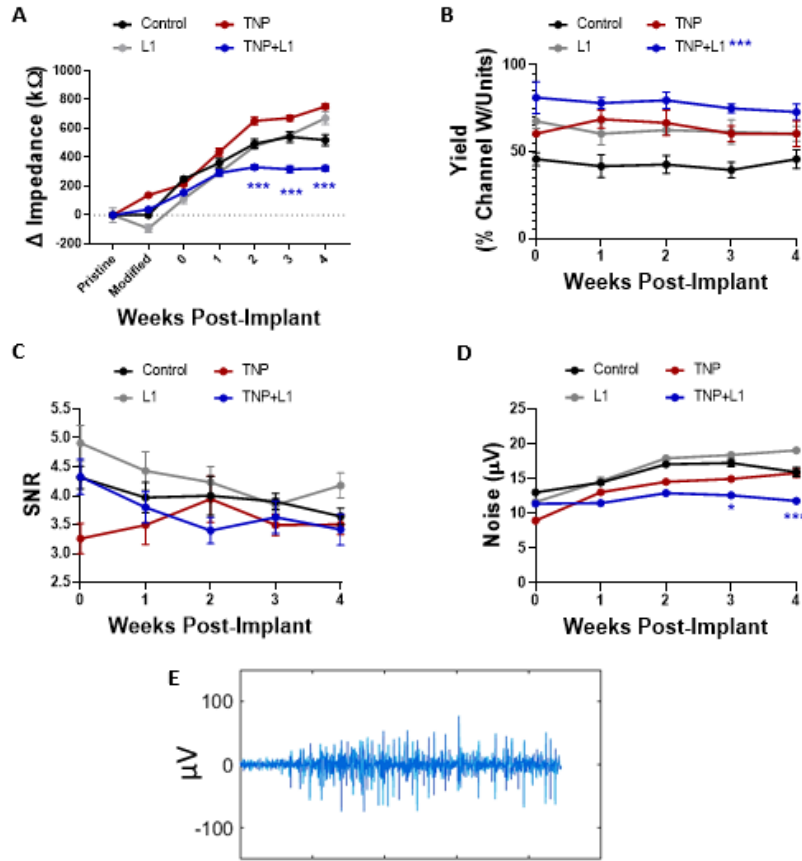


Figure 18 Recording performance.

(A) Impedance measurements normalized to the pristine electrode (before surface modification). The second data point indicates the change in impedance after modification. (B) Single unit yield (C) SNR, and (D) noise measured over the first four weeks of recording. When compared across all time points, yield (B) was significantly higher for the TNP+L1 modified electrodes. Data presented as the mean  $\pm$  standard error from six animals (one probe with 16 electrode sites per animal) Significance was determined with two-way ANOVA with Tukey's post hoc \* $p < 0.05$ , \*\* $p < 0.01$ , \*\*\* $p < 0.001$ . (E) Sample neural recording traces from a TNP+L1 electrode after 4 weeks, filtered between 300 and 5,000Hz.

### **3.3.5 Post-Mortem Histology**

Neural nuclei were stained with NeuN (Figure 19A,D), and cell counts were quantified and normalized to control images (Figure 19B,E). Quantifying cell counts immediately adjacent to the electrode at 1-week post implantation revealed that control electrodes had significantly lower cell counts within the 100 $\mu$ m zone of implants than any other condition, while L1 and TNP+L1 electrodes showed the highest cell density. All electrodes exhibited a decrease in cell counts in the vicinity of the electrode compared to undisturbed regions of the brain, with relative cell counts approaching control tissues after 150 $\mu$ m from the implant surface (Figure 19C). The observed decrease in neurons adjacent to the electrode was no longer universally present after four weeks. At four weeks, neuron density was greatest adjacent to TNP+L1 electrodes, significantly higher than any other condition (Figure 19E). This result is even more interesting due to the neural cell density being greater than the control brain regions.

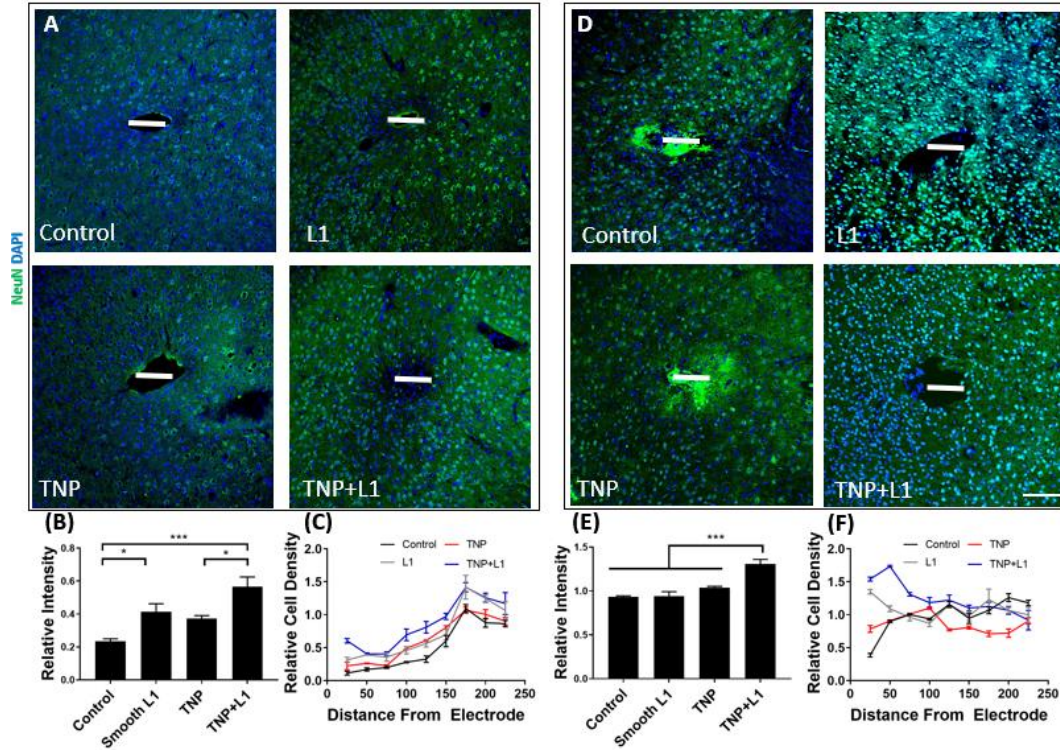
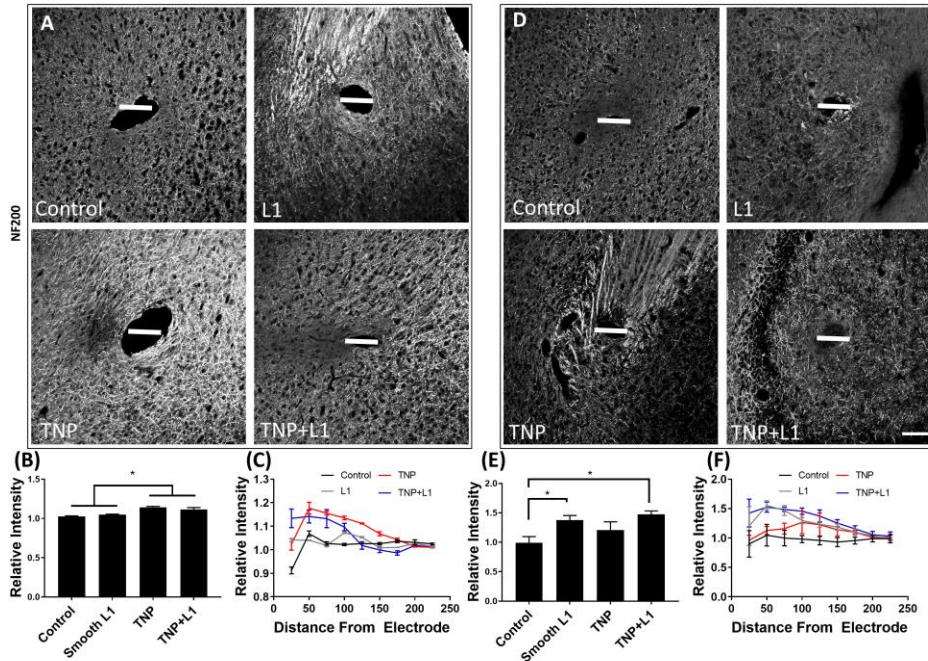


Figure 19. Quantification of neural cell bodies.

Values are scaled to contralateral tissues, where the relative intensity is 1. (A,D) Representative images of NeuN stained tissue slices after 1 week or 4 weeks of implantation, respectively. (B,E) Quantification of NeuN positive cells up to 100µm from the implant surface for 1- and 4-week implantation, respectively. (C,F) Relative cell density as a function of distance from the electrode for 1- and 4-week implants, respectively. Data presented as the mean  $\pm$  standard error from four animals per timepoint. Significance was determined with one-way ANOVA with Tukey's post hoc \* $p < 0.05$  \*\* $p < 0.01$ . Scale bar is 100µm. Large white bars at the center of the image denote the electrode location.

NF-200 staining was performed to examine the axonal growth after implantation (Figure 20A,D). At 1-week post implantation, a significant increase in NF-200 staining was observed for both nanoparticle-modified conditions within the 100 $\mu$ m zone (Figure 20B). By contrast at 4-weeks, the most intense staining was adjacent to the TNP+L1 electrode. The NF-200 intensity in the 100 $\mu$ m region adjacent to the TNP+L1 electrode was significantly higher than the region adjacent to the control electrode as well as the baseline value calculated from the control images. NF-200 intensity was also elevated near L1 modified electrodes, with the mean intensity higher than control images (intensity > 1) but not significantly different than the tissue proximal to the control electrode (Figure 20E). Regardless of experimental condition or timepoint, relative NF-200 staining intensity returned to baseline prior to the 225 $\mu$ m measurement (Figure 20C,F).



**Figure 20. Quantification of axons.**

Values are scaled to contralateral tissues, where the relative intensity is 1 (A,D) Representative images of NF-200 stained tissue slices after 1 week or 4 weeks of implantation, respectively. (B,E) Quantification of NF200 staining intensity up to 100 $\mu$ m from the implant surface for 1- and 4-week implantation, respectively. (C,F) Relative intensity as a function of distance from the electrode for 1- and 4-week implants, respectively. Data presented as the mean  $\pm$  standard error from four animals per timepoint Significance was determined with one-way ANOVA with Tukey's post hoc  $*p < 0.05$ . Scale bar is 100 $\mu$ m. Large white bars at the center of the image denote the electrode location.

Host microglia were stained with Iba-1 (Figure 21A,D). At the 1-week timepoint, Iba-1 expression appeared to trend upwards after nanoparticle modification, however these results were not deemed significant ( $p>0.05$ , one-way ANOVA) (Figure 21B). After one week, the staining intensity versus distance was similar for all test conditions, with a peak staining intensity adjacent to the electrode followed by a decrease to baseline values after 100-150 $\mu\text{m}$  from the implant (Figure 21C). After four weeks, this trend was no longer apparent. The TNP modification produced the greatest increase in Iba-1 staining, while the TNP+L1 modification eliminated microglial encapsulation after 4 weeks (Figure 21E). Smooth conditions were nestled between the TNP modified conditions, with L1 modified probes exhibiting lower Iba-1 expression than smooth controls. The TNP intensity versus distance shows an interesting peak at 50 $\mu\text{m}$  from the implant (Figure 21F). The peak was attributed to low sample sizes for the 25 $\mu\text{m}$  bin due to tissue loss during brain removal.

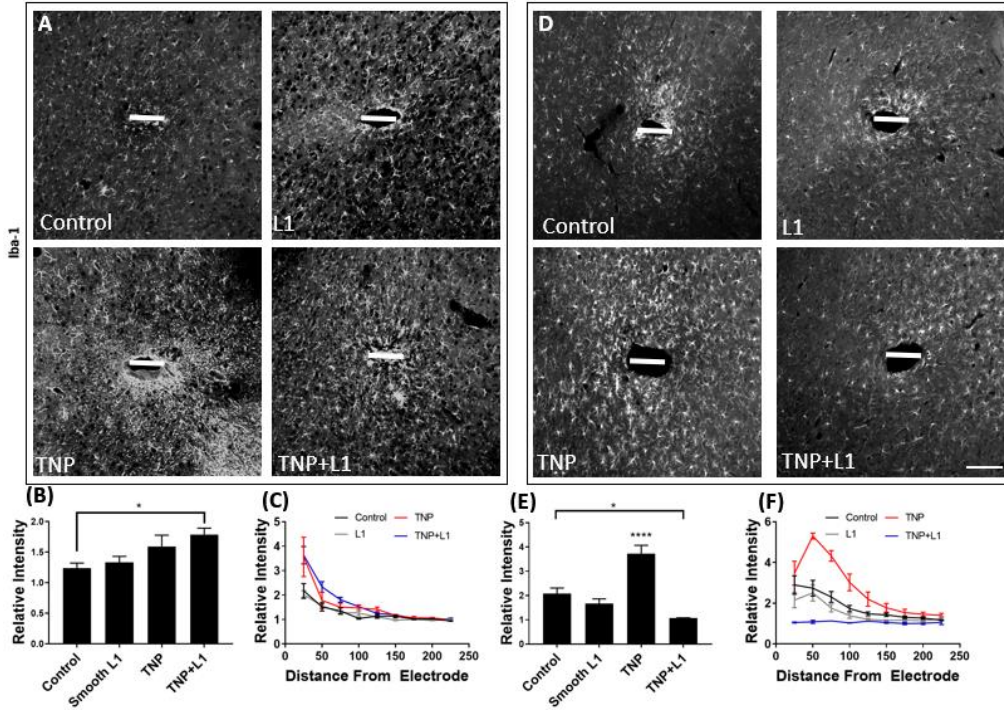


**Figure 21. Quantification of microglia.**

Values are scaled to contralateral tissues, where the relative intensity is 1 (A,D) Representative images of Iba-1 stained tissue slices after 1 week or 4 weeks of implantation, respectively. (B,E) Quantification of Iba-1 staining intensity up to 100 $\mu$ m from the implant surface for 1- and 4-week implantation, respectively. (C,F) Relative intensity as a function of distance from the electrode for 1- and 4-week implants, respectively. Data presented as the mean  $\pm$  standard error from four animals per timepoint. Significance was determined with one-way ANOVA with Tukey's post hoc \* $p < 0.05$ , \*\*\*\* $p < 0.0001$ . Scale bar is 100 $\mu$ m. Large white bars at the center of the image denote the electrode location.

Astrocytic activation was visualized by staining for GFAP (Figure 22A,D). At 1-week, GFAP staining was significantly higher in the control group than any of the experimental conditions (Figure 22B). The intensity versus distance graphs demonstrate the expected trend, with the highest GFAP staining being closest to the electrode and decreasing towards baseline. At 4-weeks post implantation, the L1 and TNP+L1 groups had significantly lower GFAP expression adjacent to the electrode compared to the control electrodes (Figure 22E).

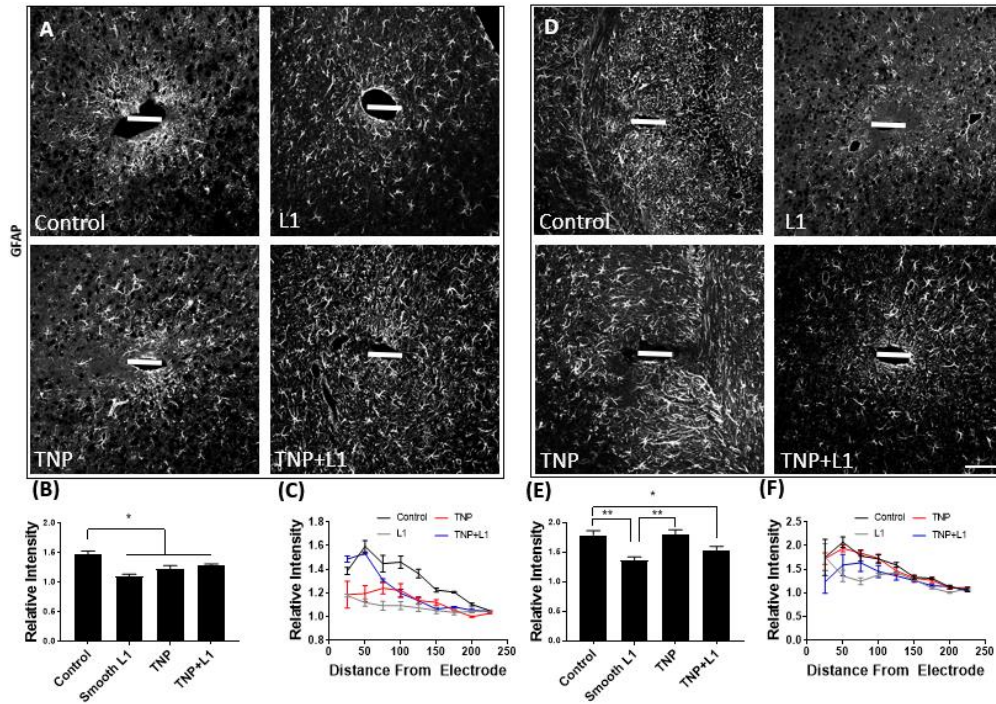


**Figure 22 Quantification of astrocytes.**

Values are scaled to contralateral tissues, where the relative intensity is 1 (A,D) Representative images of GFAP stained tissue slices after 1 week or 4 weeks of implantation, respectively. (B,E) Quantification of GFAP staining intensity up to 100 $\mu$ m from the implant surface for 1- and 4-week implantation, respectively. (C,F) Relative intensity as a function of distance from the electrode for 1- and 4-week implants, respectively. Data presented as the mean  $\pm$  standard error from four animals per timepoint. Significance was determined with one-way ANOVA with Tukey's post hoc \* $p < 0.05$  \*\* $p < 0.01$ . Scale bar is 100 $\mu$ m. Large white bars at the center of the image denote the electrode location.

The observed increase in neurons adjacent to the TNP+L1 electrode prompted investigation into the origin of these cells. Nestin (green) and DCX (red) stains were performed on the one and four week tissues (Figure 23A,D). At 1-week, an increase in nestin positive cells was observed for the TNP+L1 and TNP electrodes relative to the control (Figure 23B). Similarly, an increase in DCX positive cells was observed for all conditions relative to control at 1-week with TNP+L1 having the highest number of DCX positive cells (Figure 23C). The nestin and DCX staining dropped dramatically at four weeks. At the later time point, only the L1 modified smooth probe produced significant differences in nestin and DCX positive cells relative to the other probes (Figure 23E,F).

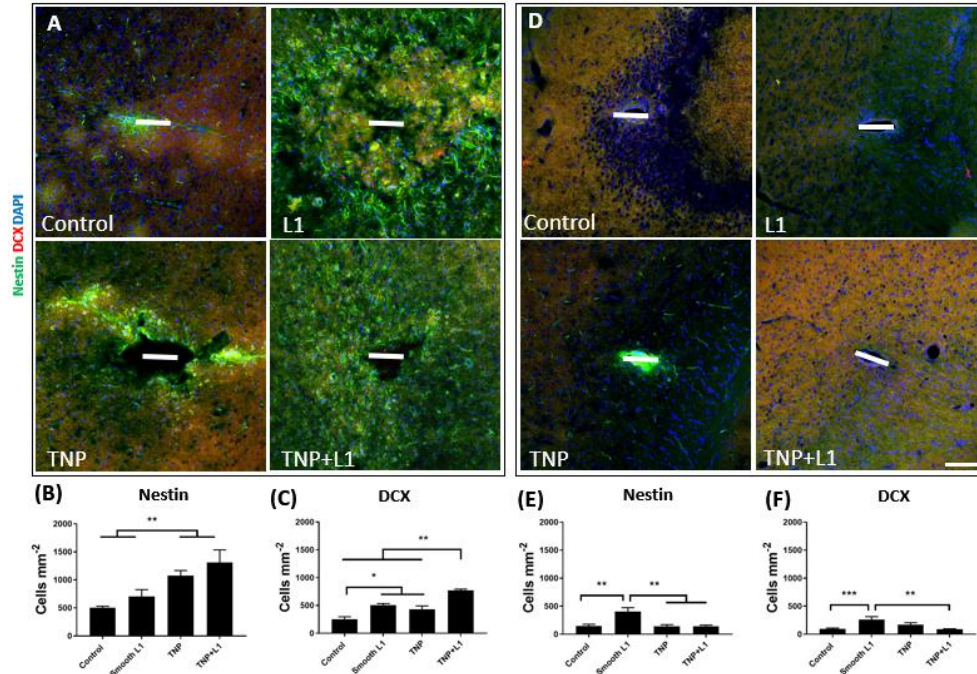


**Figure 23. Examination of the origin of local neurons.**

(A,D) Representative images of nestin (green) and DCX (red) stained tissue slices after 1 week or 4 weeks of implantation, respectively. (B,E) Quantification of nestin staining intensity up to 100µm from the implant surface for 1- and 4-week implantation, respectively. (C,F) Quantification of NDCX staining intensity up to 100µm from the implant surface for 1- and 4-week implantation, respectively. Data presented as the mean  $\pm$  standard error from four animals per timepoint. Significance was determined with one-way ANOVA with Tukey's post hoc \* $p < 0.05$  \*\* $p < 0.01$ , \*\*\* $p < 0.001$ . Scale bar is 100µm. Large white bars at the center of the image denote the electrode location.

### 3.3.6 Explant Analysis

Explanted electrodes were examined under SEM to confirm the stability of the nanoparticle deposition *in vivo* (Figure 24). Regions adjacent to the skull were less tissue-encapsulated, and the particle modification was clearly visible (Figure 24A). Distal regions of the electrode were well coated with biological materials, and nanoparticles were not able to be directly observed by SEM. However, deformations in the biological tissue (diameter  $147\text{nm} \pm 17\text{nm}$ , mean  $\pm$  SD) coincided well with the dimensions of the nanoparticles, suggesting their presence below the biological layer (Figure 24B,D). The biological encapsulation was also present on electrodes without TNP modifications, but the lack of underlying textural modification produced a smooth coating (Figure 24C).

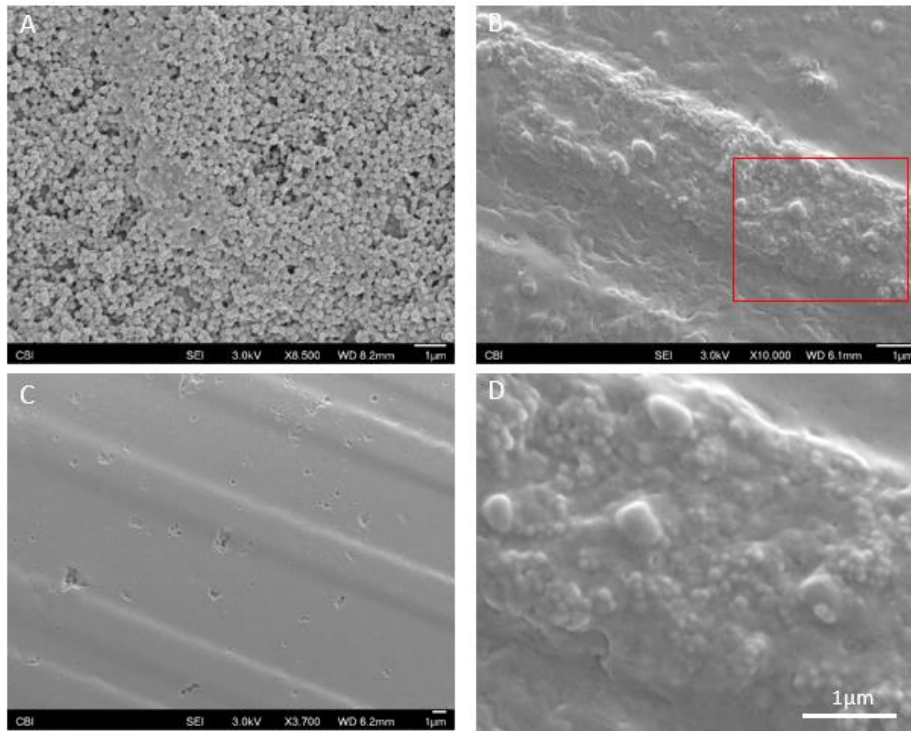


**Figure 24. Explant analysis.**

**(A) SEM image of explanted nanoparticle modified electrode taken near the skull. (B) Nanoparticle modified electrode with biological materials attached. Nanoparticle topography can still be observed underneath the biological film. (C) Biofouling was also present on electrodes without TNP. (D) Enlarged region indicated by the red box in (B).**

### 3.4 Discussion

Silica nanoparticles are an ideal candidate for surface topographical modification. A thiol modified silica nanoparticle was synthesized such that the particles would be covalently linked to GMBS modified substrates of either silica or silicon. The methods detailed here allow for precise tailoring of the chemical and morphological properties of silicon surfaces. The binding mechanism can be altered by changing the base silane, the crosslinking agent, or even the functionalization of the nanoparticles. The surface chemistry of the fully modified substrate is directly related to the surface chemistry of the silica nanoparticles. Exchanging the silane used during nanoparticle synthesis may allow for alkene, alkyne, amine, amide, epoxide, sulfonate, and many other surface functional groups. The topography may be readily tailored by changing the size of the nanoparticles, their concentration, or changing the amount of interaction between particles to increase or reduce stacking. Unlike etching or focused ion beam milling, TNP modification can change the topography with minimal damage to the underlying substrate, which would otherwise be a concern when working with costly neural electrodes or other medical devices. Finally, the nanoparticle binding is stable both *in vitro* and *in vivo*, making the surface modification ideal for biologically interfacing devices.

One of the primary findings was that significantly more L1 bind to the roughened surface and this higher surface density translated to higher bioactivity manifested as longer neurite extension. We specifically examined the longevity of the protein coating by soaking samples at physiological conditions for extended periods of time to simulate the *in vivo* application and examined the amount of bound proteins and their bioactivity. First, we observed an increase in the amount of protein bound to the TNP modified substrates. In addition, TNP modified substrates

maintained their bound protein better under physiological conditions. The increase in bound protein translated to enhanced bioactivity of the substrates.

The increase in stability may be attributed to a few factors, including an increase in the amount of bound protein, a decrease in deterioration of the protein,[241] complementary interactions of topography and protein modifications, and stronger binding of the protein to the TNP substrate compared to the smooth substrate. The increase in stability may be attributed to a few factors, including an increase in the amount of bound protein, a decrease in deterioration of the protein,[241] complementary interactions of topography and protein modifications, and stronger binding of the protein to the TNP substrate compared to the smooth substrate. TNP surface modification has demonstrated to increase the amount of protein bound to the surface by increasing the available binding locations. If the surface bound concentration of L1 is greater than the concentration detectable by neurons, then loss of a small portion of the bound L1 should not affect the neurite outgrowth. Conversely, the L1 binding may be below the highest effective level but capable of maintaining its bioactivity for longer when bound to the TNP substrate. Binding of the L1 to multiple locations may increase the bioactive lifetime. L1 bound to a single location on the surface would be removed by breaking any chemical bond in the protein backbone or crosslinker, making the binding mechanism precarious. L1 scaffolded to the TNP modified surface may have a greater number of binding sites with the surface and be far less likely to de-couple during the incubation period.

In addition to maintaining the bioactivity of the L1, the possibility of a cooperative effect between the protein and topographical modifications should not be ignored. This idea is supported by the observation that the TNP modification was sufficient to increase neurite outgrowth compared to smooth chemistry-matched samples, and that the L1 maintained a small degree of

activity on smooth surfaces after 28 days. The synergistic effect of the TNP+L1 coating may be sufficient to maintain the neurite outgrowth even as the L1 itself decreases in activity.

Rough substrates have previously been shown to enhance neurite outgrowth and attachment,[76, 233, 242, 243] with the maximum outgrowth seen for surface roughness between 20nm and 70nm.[76] These findings are further supported by this work, with the calculated roughness of the TNP modified substrates ( $78.6\text{nm} \pm 0.2\text{nm}$ ) just above the upper limit. with the maximum outgrowth seen for surface roughness between 20nm and 70nm.[76] These findings are further supported by this work, with the calculated roughness of the TNP modified substrates ( $78.6\text{nm} \pm 0.2\text{nm}$ ) just above the upper limit. The discrepancy may be explained by the mathematical representation of roughness. Roughness calculations are imperfect representations of surface topography, most often relying on deviations from the mean height of the sample and not the size/shape of the surface features. The aforementioned ideal roughness was measured on etched silicon, producing a more jagged surface topography than TNP immobilization. The smoother TNP coating may have a different ideal roughness, and further examination of neurite outgrowth on nanoparticle modified surfaces may provide invaluable information regarding the interplay of roughness, particle size, and neurite extension.

We observed that the NPs not only cover the silicon oxide portion of the neural probe, but also the electrode sites. One valid concern is whether the non-conductive NP coating will block signal transduction and consequently compromising the recording capability. The impedance of the electrodes was increased by  $<150\text{k}\Omega$  after the TNP and TNP+L1 coatings, a change which is unlikely to affect recording performance. The TNP+L1 electrodes had the lowest *in vivo* impedances at three and four weeks, negating any initial impedance increases due to modification. Interestingly, a slight decrease in the impedance of the L1 modified electrodes was observed,

which was attributed to additional cleaning of the electrode site during modification. However, bound proteins can affect the charge exchange at the electrode,[244] and L1 itself may have contributed to the observed impedance change. The implanted TNP+L1 electrodes maintained the lowest *in vivo* impedances of the tested conditions, potentially indicating that the modification could minimize glial encapsulation at the electrode site. Additionally, the TNP+L1 modification increased the single unit yield of the modified electrodes compared to the other conditions, further confirming the functionality of the electrode was not compromised by the non-conductive coating. The increased recording yield could be a result of higher neuron density at the vicinity of the probe with the TNP-L1 showing the highest yield and highest neuron density among all groups. Noise was also lowered by the TNP+L1 modification due to the decreased impedances. Johnson noise was calculated by the equation:

$$V_{noise} = \sqrt{4k_BRT\Delta f} \quad (3-1)$$

Where  $k_B$  is the Boltzman Constant ( $1.38 \times 10^{-23}$  J K<sup>-1</sup>),  $R$  is the real impedance,  $T$  is temperature in Kelvin, and  $\Delta f$  is the sampling frequency. The calculated values of  $V_{noise}$  for the TNP+L1 and TNP electrodes at week four are  $9.57 \mu V$  and  $14.72 \mu V$ , respectively. The measured noise values of  $11.28 \mu V$  and  $15.81 \mu V$  align well with the calculated values. With lower noise, additional low amplitude units may be captured which can lead to higher yield but lower average peak to peak amplitude.

Neural electrodes rely on the proximity of the electrode sites and neural somas to be within  $140 \mu m$ [245] and closer distances are heavily preferred.[245] and closer distances are heavily preferred. The neuron cell density at the vicinity of the implant was higher for the L1 modified electrodes compared to control and TNP modified groups, but overall cell density was dramatically

lower than control tissues at the 1-week time point. The general decrease in neuron cell density is likely due to insertion injury and the strong acute response to the implant. Neuron density adjacent to the electrode was recovered at four weeks and was even elevated above control tissue for the L1 and TNP+L1 modified conditions. Such increase in neuronal density is likely to contribute to the elevated single unit yield. The increased presence of neuron somas adjacent to the electrode could be due to a number of reasons: 1) tissue compression after electrode insertion along with the lack of cellular death around the L1 coated probes due to the anti-inflammatory and neuroadhesive effect L1 and 2) migration of neurons to the site of injury and neurogenesis.

Nestin and DCX staining was performed to examine the origin of the neurons around the implanted electrodes. Nestin is expressed in neural stem and progenitor cells and endothelial cells during angiogenesis.[246] The increase in nestin staining at 1-week post implantation indicates that tissue healing has commenced, and new cells and vessels are present adjacent to the probe. [246] The increase in nestin staining at 1-week post implantation indicates that tissue healing has commenced, and new cells and vessels are present adjacent to the probe. This response appears to be most prominent adjacent to the TNP+L1 electrode. This expression decreases at the four-week timepoint for all conditions, possibly indicating that the new tissues around the electrode have begun maturing. DCX is used as a marker of immature neurons[247] and increases in DCX staining may indicate that immature neurons are present adjacent to the electrode after injury. DCX positive cells have been observed following implantation of mesh electrodes, potentially due to migration of neurons to the site of implantation.[248] At 1-week post implantation, a significant increase in the DCX positive cells was observed in both L1 and L1+TNP groups, further suggesting that neurons in the area may have formed recently. [248] Similar to the nestin staining, the number of DCX positive cells decreased at the 4-week timepoint as the cells mature. The increase in nestin

and DCX staining for the L1, TNP, and TNP+L1 is a promising indication of the beneficial effects of both topographical and bioactive modifications. The positive nestin and DCX staining are very promising, but a more intensive characterization is required to confirm the origin and age of the neurons and whether these cells can contribute to the recording yield.

The axonal densities were similar between all groups at 1-week post implantation, however there was a small but significant increase in the NF-200 staining directly adjacent to the TNP and TNP+L1 modified electrodes relative to the control and L1 groups. At 4 weeks, the two L1 modified conditions exhibited significantly increased NF-200 staining relative to control and TNP groups. Unlike somas, regeneration is more commonly observed in axons. The increase in NF-200 staining is attributed to a combination of axonal regeneration, adhesion to the L1-modified electrode, and tissue compression/remodeling after insertion. L1 is a potent promoter of neurite extension *in vitro* and axonal regeneration *in vivo*. [220, 249-251] The axonal promoting effect of L1 coating on neural probe has been previously reported by our group. [48, 230, 252] The result here is consistent with the previous finding.

Staining microglia and astrocytes allowed for the examination of non-neural cell responses to the implanted foreign body. Contrary to expectations, at the 1-week time point there was an elevated, yet not significant, iba-1 expression adjacent to the TNP+L1 electrodes. This result reversed itself at the 4-week timepoint, with the TNP+L1 modified electrodes performing significantly better than all other treatments. Previous experiments have concluded that L1 minimized microglial activation after contact, such that the cells still respond to the implant but after examining the surface do not continue forward to traditional encapsulation. [219] Here, we see that at the early time point the microglia are still in the process of examining the implant. At 4-weeks, the TNP+L1 electrodes exhibited no microglial encapsulation. The complete lack of

microglial activation for TNP+L1 electrodes is attributed to the increased stability of the L1 coating, remaining active throughout the initial inflammation and allowing for the formation of a healthier electrode-tissue interface. TNP modification itself did not lead to decreased immune response, instead increasing microglial encapsulation at 4-weeks. The increase in glial response may be caused by the increased binding of blood proteins to the TNP surface, or detachment of a small number of particles which then caused an additional immune response. Rosengren et al. found that encapsulation of smooth electrodes increased between 6 and 12 weeks, while encapsulation of porous surfaces decreased or remained constant.[253] Therefore, it remains to be important to investigate how inflammatory responses evolve over longer implantation time for the TNP surface.

Increased expression of GFAP in astrocytes is often observed after brain injury as the tissue forms a scar around the damaged area.[126] At the one-week timepoint, differences in astrocytic encapsulation were observable between the control electrodes and all three experimental conditions. Astrocytic encapsulation occurs after microglial,[216] and was expected to be more predominant at the 4-week time point. At this time point, L1 and TNP+L1 electrodes elicited significantly lower encapsulation than the control electrodes. Notably, the TNP modification alone was not able to affect the astrocytic encapsulation at four weeks. While previous work has demonstrated that topographical modifications are sufficient to limit astrocytic spreading *in vitro*, the presence of L1 appears to be required to translate these findings *in vivo*.

Finally, it is necessary to confirm the attachment of the nanoparticles after explantation. The adhesion of the particle to the electrode must be maintained throughout the study for the L1 coating to maintain its function. Furthermore, unbound nanoparticles may increase inflammation as phagocytic cells try to remove them from the implant vicinity. The binding of the nanoparticles

to the surface was confirmed by SEM after explanting the electrodes, verifying that the TNP and TNP+L1 modifications are stable throughout the 4-week experiment. SEM is not capable of confirming that no nanoparticles detached *in vivo*, and removal of a small percentage of the nanoparticles may have occurred without being detected. While not performed in this study, more direct measurements of the nanoparticle layer (surface area and roughness) before implantation and after explantation would provide a more quantitative assessment of nanoparticle layer stability. However, the bulk of the coating remained intact after explantation and maintained its bioactivity throughout the time course of this study. Together with previous studies which have examined the adhesion of the nanoparticles and silicon substrates, there is sufficient evidence to indicate the maintenance of nanoparticle adhesion for at least 4-weeks *in vivo*.

### 3.5 Conclusions

In this work we have explored the combined use of nano topographical and bioactive surface modifications for use on neural implants. *In vitro* we observed that the nanoparticle modification was successful at both increasing the bioactivity of the L1 surface modification, as well as maintaining that activity for up to four weeks at 37°C in PBS. *In vivo*, the L1+TNP modification outperformed both individual modifications (TNP and L1 respectively) by demonstrating the highest single unit recording yield, highest number of neural somas adjacent to the electrode, and eliminated microglial reactions after four weeks. Elevated expression of DCX and nestin adjacent to the TNP+L1 electrode may indicate that neural stem/progenitor cells may have migrated to the electrode site after implantation and some of them underwent neuronal differentiation. Additionally, the nanoparticle modification was stable for the course of the

experiment. Together, we have found that the combined nanoparticle and bioactive L1 surface modifications offer an opportune method of increasing chronic electrophysiologic recording performance by enhancing both the bioactivity and lifetime of protein surface modifications, without risk of damage to the device.

#### 4.0 Chronic Recording from TNP+L1 Modified Electrodes Following Dry Storage

Rapid advancements in neural engineering have enabled incredible therapeutic and scientific impact. The question now is not whether neural electrodes are viable, but instead for how long. Indeed, there is a characteristic decay in the recording quality of neural electrodes, which can result in the ultimate failure of the device prior to its desired endpoint. Strategies to mitigate this chronic recording degradation are vast, and one of the most exciting and successful methods has been to employ biomimetic coatings derived from proteins and other biological molecules. These coatings are highly effective, albeit fragile and the application of these coatings can be technically challenging and time consuming. Further, the necessity of these coatings to be applied on site, immediately prior to implantation, make the large-scale manufacture of modified electrode infeasible without further advancements in the coating stability. Herein we have developed a method of increasing both the efficacy and longevity of biomimetic coating for neural electrodes through a preliminary topographical modification that stabilizes the subsequently bound protein. *In vitro* characterization suggests a coating lifetime of at least 8 weeks when stored dry and at room temperature, and *in vivo* recording performed with electrodes which were fabricated days prior to implantation was equivalent to electrodes coated the day of implantation. These findings serve to demonstrate that biomimetic coatings do not need to be limited to the lab, and topographical modifications can serve as an invaluable tool for the widespread adoption of biomimetic neural electrodes.

## 4.1 Chapter Introduction

Proteins and other biomolecules manufactured by cells are used as key components of biosensors for chemical detection,[203, 204, 254] blood oxygenation [206, 207], purification[255, 256], biotechnology and pharmaceutical industry as well as surface modifications of bio-interface devices [1, 172, 230, 231]. Despite their utility, the use of biomolecules is hindered by their operational lifetime, resulting in long term losses in bioactivity under physiological conditions. For example, glucose detection with glucose oxidase decays over time, likely due to damage to the protein itself.[257-259] Carbonic anhydrase used for CO<sub>2</sub> capture rapidly lost activity when in its soluble form,[260] and a separate study observed that carbonic anhydrase lost 60% of its catalytic activity when aged for 20 days in saline at 25°C.[261] This instability also impacts the ability of biofunctionalized surfaces to be stored and transported, and maintaining bioactivity is a common challenge for immunoassays, protein arrays, enzyme-based biosensors, and peptide functionalized medical implants [262-266].

A particularly interesting example of surface modification improving device function is biofunctionalization of neural electrodes. Chronic neural recoding is often limited by a gradual degradation in electrode site yield.[2] This is in part due to the inflammatory reactions which occur after the electrode array is implanted.[1, 2] These inflammatory reactions result in acute and long-term damage to the blood brain barrier (BBB)[29], activation and migration of host glial cells to the site of the implant, and loss of viable neurons near the electrode sites.[29], activation and migration of host glial cells to the site of the implant, and loss of viable neurons near the electrode sites.[1, 216] It is not surprising then that substantial research effort has been invested into controlling and minimizing this inflammation. Fortunately, these reactions can be controlled and mitigated by disguising the electrode as host tissue, a technique referred to as biomimetic

coatings.[1, 40, 48, 209, 231, 267] Biomimetic coatings are composed of biological molecules bound to the surface of the electrode. Of particular interest are coatings derived from L1, a protein found on neuronal axons and synapses.[220, 250] L1 elicits unique reactions from multiple CNS cell types, both *in vitro* and *in vivo*. Glia are less likely to bind to L1 modified surfaces *in vitro*,[47, 172] and host immune cells that contact L1 modified electrodes do not proceed to encapsulate the device as would otherwise be observed.[219] Neurons can interact directly with L1, resulting in elevated neurite outgrowth on L1 modified substrate *in vitro* [47, 172, 231]. *In vivo*, it has been observed tissues surrounding L1 modified electrodes have elevated axonal density and great counts of neuronal cell bodies.[48, 230, 231] The interactions between the host tissues and L1 result in greatly improved chronic recording performance,[230] and may be crucial for developing stable electrode tissue interfaces.

However, these coatings have some limitations which have stalled the widespread adoption of biomimetic surfaces in neural engineering. First, the bioactivity of a coating is tied to both the amount of bound biomolecules and their stability. Further, immobilized protein tends to denature in non-physiological conditions, necessitating the application of these coatings occur on-site and immediately prior to use. These limitations greatly hindered the dissemination of the biomimetic coating technology and motivated us towards developing a biomimetic coating that is stable enough to be prepared off-site and transported to users prior to use. Attempts to stabilize these molecules include encasing the protein in polyethylene glycol gel, [268] and topographical modifications to the substrate to which the protein is bound [231, 239, 260].

We have previously investigated the use of nano-textured surfaces on the stability and bioactivity of neural electrodes.[172, 231] Silica nanoparticles functionalized with thiol groups (TNP) on the surface were immobilized to silicon substrates prior to the deposition of the L1

coating. The nanotextured TNP surface was able to bind more proteins and demonstrated higher bioactivity than smooth surfaces[172, 231]. Further, the protein coating was stable for four weeks in buffered saline at 37°C. We hypothesized that enhanced stability of the L1 may be due to the microenvironment inside the porous structure of the nanotopographical modification maintaining the hydrated state of the protein; alternatively, there may be stronger attachment and a greater degree of anchoring of the protein to the nanotopographical surface compared to a smooth surface. These findings were promising but requiring electrodes to be stored in liquid greatly complicates the ability to distribute pre-modified electrodes. The presence of water also increases the chance of hydrolytic degradation of the molecules and even the underlying substrate. In order to enable transportation of modified devices, dry storage is preferred over wet because it makes packaging and delivery of delicate microdevices easier.

To facilitate distribution and adoption of biomimetic coatings, we have investigated the stability of the TNP+L1 coating after drying. *In vitro*, we examine the stability of dried TNP+L1 surfaces for eight weeks with primary neuron cell cultures. We then implanted electrodes modified with freshly prepared TNP+L1 in addition to TNP+L1 modified electrodes which was dried and stored for 3 days prior to the surgery. 3 days will be a sufficient amount of time for the delivery of the coated probes to most laboratories worldwide. The electrophysiological performance of the devices was measured for 16 weeks, and subsequent postmortem histology was used to investigate the interface between the electrode and the host tissues.

## 4.2 Methods

### 4.2.1 Chemicals and Materials

All reagents were purchased from Sigma Aldrich unless otherwise specified. Neural probes (A16x1) were purchased from NeuroNexus (Ann Arbor, MI), and consisted of 16 electrode sites of 30 $\mu$ m diameter, separated by 100 $\mu$ m from center to center. Glass coverslips were purchased from Electron Microscopy Sciences.

### 4.2.2 Nanoparticle Fabrication

Nanoparticles were fabricated as previously described[231] from tetraethyl orthosilicate (TEOS) and mercaptopropyl trimethoxysilane (MTS). Following formation, the nanoparticles were collected by centrifuge and washed with water and absolute ethanol, then stored dry. Before use, thiolated nanoparticles (TNP) were resuspended in an aqueous solution of tris-carboxyethylphosphine (TCEP, 1mg ml<sup>-1</sup>) to reduce any disulfide bonds and then centrifuged and washed with water.

### 4.2.3 Sample Preparation

Modified substrates consisted of glass (coverslips) or silicon dioxide (probes). Samples were first cleaned with acetone and isopropyl alcohol then the surface was activated using O<sub>2</sub> plasma for 5 minutes, then submerged in 2.5% silane solution in absolute ethanol for one hour. The silane was either MTS for control samples, or aminopropyltriethoxysilane (ATS) for

nanoparticle immobilized samples. Samples destined to have immobilized nanoparticles were then submerged in an aqueous solution of the hetero-bifunctional crosslinker gamma-maleimidobutyryl-oxysuccinimide (GMBS,  $2\text{mg ml}^{-1}$ ) for 30 minutes. Following which the samples were washed with water and exposed to a suspension of TNP in water ( $10\text{mg ml}^{-1}$ ) for one hour with gentle agitation of the solution performed every 15 minutes to prevent clumping of the particles.

#### **4.2.4 Protein Isolation and Deposition**

L1 was isolated from post-natal rat pups using an affinity column as previously described[220]. Prior to deposition, samples were treated with GMBS for 30 minutes then washed with water. Samples were then exposed to L1 solution ( $2\mu\text{g ml}^{-1}$  in saline) for one hour followed by washing with saline. Select samples were then dried by removing the saline with an aspirator until completely dry. Dried samples were stored at room temperature in the absence of light.

#### **4.2.5 Neuron Culture**

Primary neurons were isolated from E18 rat fetuses. The mother rat was euthanized with  $\text{CO}_2$  and the embryos removed and submerged in ice-cold Hank's buffered salt solution (HBSS, Gibco). The pup brains were removed and the cortex isolated and washed with HBSS. The cortex was then digested with trypsin solution (0.05wt%, Gibco) for 15m at  $37^\circ\text{C}$ . The trypsin was then removed and the cortex was broken-up by gently trituration. Finally, cells were isolated, resuspended in neurobasal media (Gibco) supplemented with 2% B27, 1% GlutiMax, and 1% Penicillin/Streptomycin, and counted prior to plating at a density of  $25,000\text{ cells cm}^{-2}$ . Cells were

grown for 48 hours at 37°C in 5% CO<sub>2</sub> then fixed with 4% paraformaldehyde. Cells were stained with B(III)-Tubulin and DAPI as previously described.[172] Images were taken on a Leica DMI 4000b and neurite outgrowth was quantified with the Neurite Tracer ImageJ plugin.[222]

#### **4.2.6 Surgeries and Recording**

All animal experiments were approved by the University of Pittsburgh Institutional animal Care and Use Committee. Mice (8-week-old, C57-BL6) were purchased from Jackson Labs. 15 mice, 5 per condition, we implanted with either TNP modified electrodes, TNP+L1 modified electrodes, or 3-Day Dried TNP+L1 electrodes. Control recording data from 6 animals was used from previous experiments[230] and reanalyzed with the same script to examine the performance of the TNP and TNP+L1 modified electrodes to unmodified electrodes. Animals were anesthetized under 1.5% isoflurane in O<sub>2</sub> at a flow rate of 1L min<sup>-1</sup> and anesthesia was maintained with 1.3% isoflurane. The scalp hair was removed, and the scalp sterilized with iodine solution and 70% ethanol. The scalp was then removed, and a hole was drilled in the animal skull above the visual cortex. The hole was covered with a sterile gelatin sponge to prevent the brain from drying, and three bone screws (Fine Science Tools) were secured to the skull. The gelatin sponge was then removed, and the electrode was inserted into the brain with a stereotactic manipulator. A small amount of medical grade silicone epoxy (Kwik-Sil) was then used to fill the hole around the probe. The reference and ground wires were wrapped around the bone screws, then the probe was secured to the skull with UV-curable dental acrylic. A small amount of triple antibiotic ointment was applied to the injury site following surgery to minimize the risk of infection. Following the operation, the animal received analgesic Ketofen injections for 3 days (5mg kg<sup>-1</sup>).

Impedance measurements were taken with a Potentiostat (Metrohm PGSAT128N). Neural recordings were taken with an RX7 acquisition system (Tucker Davis Technologies) and a Medusa Pre-amplifier (Tucker Davis Technologies). Animals were anesthetized during measurement with 1% isoflurane. Electrophysiology data was analyzed with a custom MATLAB script. Data was filtered between 300 and 3000Hz and a threshold of 3.5 standard deviations of the data stream was applied to isolate potential spiking activity. The threshold crossing events were then subjected to principal component analysis and visual inspection prior to being counted as a single unit. The noise was then calculated as 2 standard deviations of the data stream after subtracting the spiking events, and the signal to noise ratio was the peak-to-peak amplitude of the spiking event divided by the noise.

Following the 16w experiment, animals were anesthetized with Ketamine ( $90\text{mg kg}^{-1}$ ) and Xylazine ( $9\text{mg kg}^{-1}$ ) and perfused with 100ml of PBS followed by 100ml 4% paraformaldehyde (PFA) in PBS. The bottom of the animal skull was removed and post-fixed in 4% PFA for 2 hours. The brain was then removed from the skull, dehydrated in 15% and 30% sucrose, and frozen prior to sectioning. Sections were taken on a Leica CM 1950 cryostat with a thickness of  $10\mu\text{m}$ . Sections were stored frozen until staining.

Staining was performed by rehydrating the slices in citrate buffer then blocking with 10% goat serum, following which the brain slices were treated with 0.1% Triton-x for 45 minutes. Staining of the brains was performed in groups consisting of NeuN (Millipore mouse 1:250), NF200 (Abcam rabbit 1:500), Iba-1 (Millipore mouse 1:500), GFAP (DAKO rabbit 1:500), nestin (Millipore mouse 1:200), and DCX (Abcam rabbit 1:1000). Images were taken on a confocal microscope (Olympus Fluoview 1000) and analyzed with a custom MATLAB script. Bins of 10 or  $25\mu\text{m}$  were created concentrically around the probe implant and the intensity of the stain or

number of cells labeled per bin was measured. Intensities and counts were scaled to control regions at the corners of the images.

#### **4.2.7 Statistics**

Cell culture experiments are the combined results of 3 separate culture preparations, each culture with 3 samples and 3 image per sample and normalized to the TNP group. Samples were compared across groups with ANOVA followed by Tukey's post hoc. Electrophysiological data was collected from six mice per condition and compared with 2-way ANOVA followed by Tukey's post hoc. Histological staining was performed on eight brain sections per animal, and intensity of cell counts were compared with 2-way ANOVA followed by Tukey's post hoc. Data is plotted as the mean  $\pm$  standard error.

### **4.3 Results**

The immobilization of nanoparticles onto silicon and glass substrates has previously demonstrated to increase protein immobilization and bioactivity.[172, 231] In addition, the proteins bound to these substrates were stable for at least 8 weeks under aqueous conditions at 37°C. However, transportation of electrodes in liquid could prove difficult and it is desirable to develop a coating that is stable under ambient conditions after drying. To test the bioactivity of the TNP+L1 coating after drying and storage, samples were prepared up to eight weeks prior to culture and dried thoroughly with an aspirator vacuum, then stored at room temperature away from light

for 1,2,4,6 and 8 weeks. A second set of samples was prepared to examine the bioactivity of smooth L1 modified samples and the ability of the smooth L1 samples to be dried and stored prior to use.

Primary neurons plated over the dried TNP+L1 samples along with the controls for 48 days prior to fixation and staining with B(III)-Tubulin to visualize the neuron outgrowth. Neurites were visible on all TNP modified substrates but were notably longer and denser on TNP+L1 modified samples (Figure 25A-D). The lowest outgrowth was observed on the smooth sample without L1, while freshly prepared smooth-L1 samples performed far better ( $p < 0.0001$ ). However, the smooth L1 samples were not able to be created and dried prior to use, and after only three days we observed a significant reduction in neurite outgrowth on smooth-L1 samples ( $p < 0.0001$ ). This trend was not observed for the TNP modified samples. All TNP+L1 modified samples performed better than the TNP modified sample (Figure 25E,  $p < 0.001$  ANOVA). In addition, the duration of the dry storage from 1 to 8 weeks did not affect the neurite outgrowth.

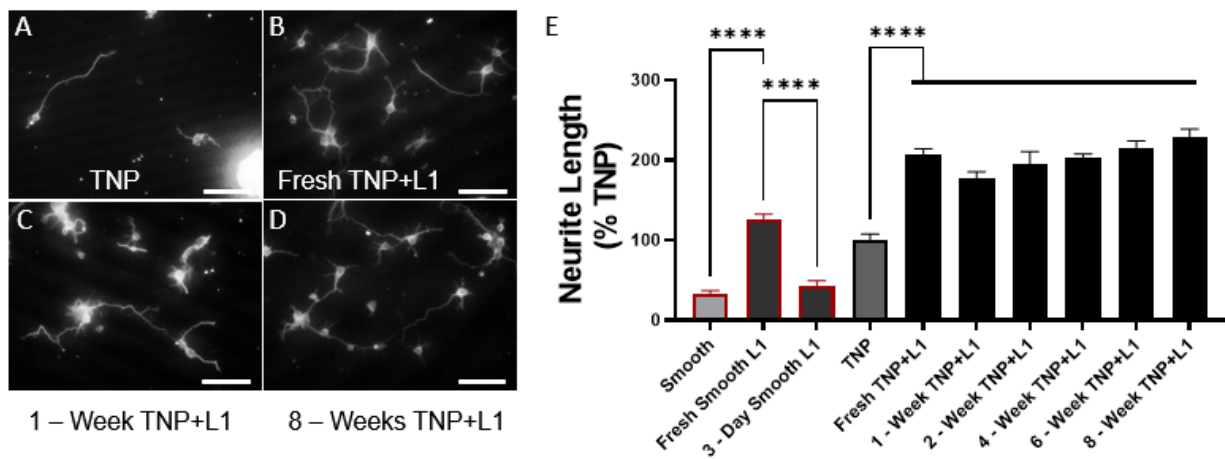


Figure 25. L1 bound to TNP retains its bioactivity when stored dry and at room temperature.

(A-D) Representative images of neurons grown on TNP and TNP+L1 substrates after aging. (E) Neurite outgrowth on glass coverslips with only silane modification (smooth), with L1 but without topographical modification prepared the day of culture and 3 days prior to culture (Fresh and 3-day Smooth L1), modified with TNP or TNP+L1. \*\*\*\* $p < 0.0001$ , ANOVA with Tukey's post hoc.  $n=9$  for smooth, fresh smooth L1, and 3-day smooth L1,  $n=27$  for the TNP modified samples.

After confirming that the bioactivity of the TNP+L1 surface, as accessed by L1's neurite extension promoting property, was not diminished after drying and storage, we examined how the dried coatings would perform *in vivo*. Mice were implanted with 16 channel linear NeuroNexus electrode arrays modified with one of three conditions: TNP only, TNP+L1 prepared the day of surgery, and TNP+L1 dried and stored at ambient temperature in air for three days prior to implantation. These findings were compared to control data previously published by our lab. Following implantation, neural activity and impedance were recorded every week for 16 weeks, followed by sacrificing the animal and performing post-mortem histology. We compared the impedance and electrophysiologic recording performance over the course of the recording period, in addition to performing an endpoint analysis at the final week of recording.

Impedance measurements taken just prior to electrophysiology show a characteristic increase over the first weeks of implantation but level off after approximately 2-4 weeks (Figure 26A). Impedances of the TNP only group were significantly higher than the other conditions between weeks 5-16 ( $p < 0.001$ , two way ANOVA), potentially indicating gliosis around the implant. The application of L1, both in the TNP+L1 and the 3-day dried samples, resulted in lower and more stable impedances than the TNP modification alone, with no significant difference between the L1 treated groups. Interestingly, control electrodes did not significantly differ from the TNP+L1 or 3-day dried groups throughout the majority of the experiment. However, there was a significant difference in the impedances between the control and TNP+L1 and 3-day dried electrodes at the 16 week timepoint (Figure 26E).

Although impedance can allow for investigation of the nature of the electrode tissue interface, it is often poorly correlated with recording performance. To examine the effect of the TNP+L1 coatings on electrophysiology, we performed weekly recordings for 16 weeks. Electrode

site yield was defined as the number of channels recording single units/16 for each array (Figure 26B). Recording yield was highest for the TNP+L1 and 3-day dried groups, and the yield from these electrodes was maintained between 60-80% for the entire 16-week experiment. The elevated yield was significantly greater than the TNP modified electrode and the control electrodes when compared across the entire recording period ( $p < 0.0001$  for TNP compared to TNP+L1,  $p < 0.0001$  for TNP compared to 3-day dried,  $p < 0.0001$  for control compared to TNP+L1,  $p < 0.0001$  for control compared to 3-day dried, ANOVA). In addition, when limiting our examination to only the last week of recording, the TNP+L1 and 3-day dried electrodes did produce significantly greater recording yield compared to the control electrodes (Figure 26F). The TNP modified electrodes outperformed the control electrodes, produced higher recording yields than the control electrodes when examined across all weeks ( $p < 0.0001$ , ANOVA).

We then examined the noise and signal to noise ratio of the electrodes. The noise floor was significantly lower for the TNP+L1 and 3-day dried electrode groups of the course of the recording compared to TNP and control electrodes throughout the recording period ( $p < 0.0001$ , ANOVA, Figure 26 C) and on the final week of recording ( $p < 0.001$  for 3day dried compared to TNP and control electrodes,  $p < 0.05$  for the TNP+L1 compared to TNP electrodes, ANOVA with Tukey's post hoc, Figure 26G). It was further observed that the signal to noise ratio was highest when L1 was immobilized to the electrode (Figure 26D) when compared across all weeks, but there was no significant differences observed at week 16 (Figure 26H).

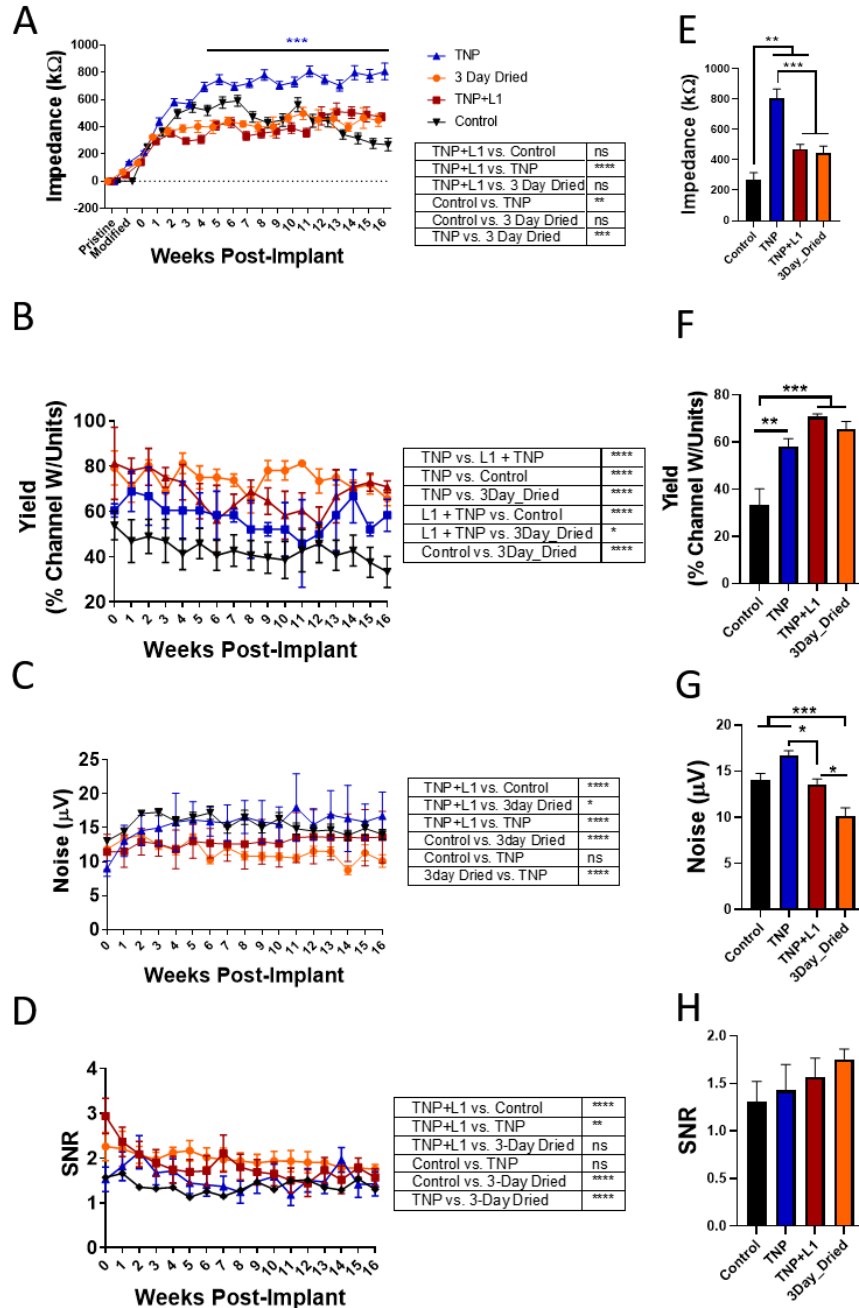


Figure 26. *In vivo* impedance and recording performance.

(A) impedance measurements were performed prior to each recording session, in addition to before modification and immediately prior to implantation. (B) Single unit yield was evaluated for each electrode. (C) Signal to noise ratio (SNR) and (D) the noise floor for electrodes throughout the 16 week recording period. (E-H) Analysis of the impedance, yield, noise, and SNR was repeated for the 16<sup>th</sup> week of recording. \*\*\* $p < 0.001$  comparing TNP to control, TNP+L1, and 3-Day Dried, two-way ANOVA.

Extracellular recordings predominately detect the spiking activity of neuron cell bodies, and the recorded potentials are expected to diminish with the square of distance to the soma. We visualized the neuronal soma with NeuN while co-labeling with caspase 3, which is a marker for the apoptotic cell death (Figure 27A). In all conditions, there was a decrease in the relative NeuN density directly adjacent to the electrode, but there was a quicker return to baseline in the TNP+L1 and 3-day dried samples (Figure 27B). We quantified the number of neurons present in the first 50 $\mu$ m from the implant and observed that there was a significant elevation in the number of neuron cell bodies adjacent to the freshly prepared and 3-day dried TNP+L1 modified electrodes compared to the TNP modified electrode. Caspase-3 staining did not indicate a difference in the number of apoptotic cells among any of the experimental groups (Figure 27D). In the same manner as the quantification of the neural cell bodies, we examined the number of co-labeled cells over the first 50 $\mu$ m. However, we again did not observe any significant differences between the groups (Figure 27E).

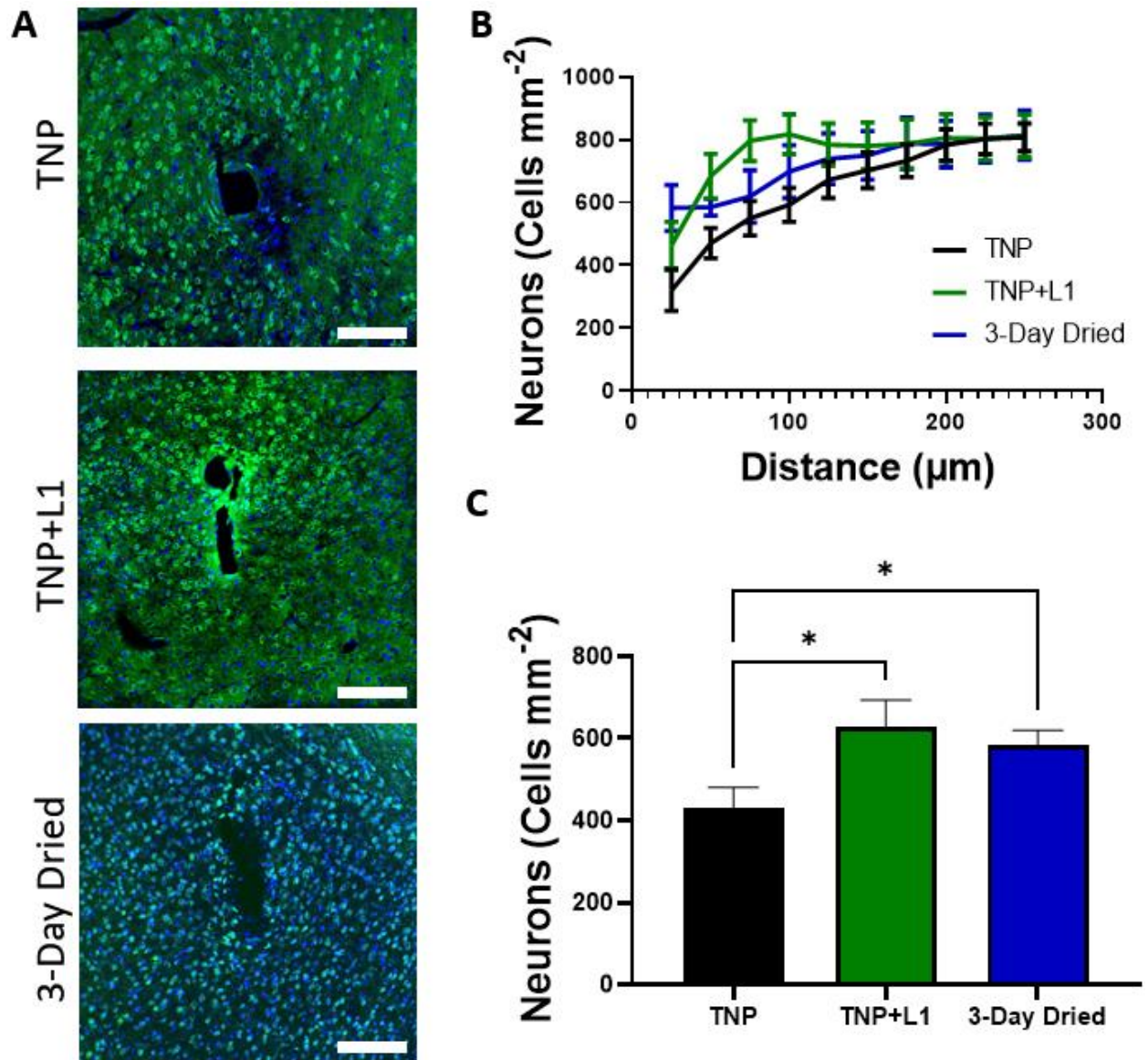


Figure 27. NeuN, and DAPI.

NeuN (neuron cell bodies) and Dapi (cell nuclei) staining of cortical tissues after 16 weeks of recording. (A) Representative images of cortical tissues stained with NeuN (green) and Dapi (blue) for tissues implanted with TNP (top), TNP+L1 (middle), and TNP+L1 which was dried for three days prior to implantation (bottom). (B) Relative NeuN counts as a function of distance from the electrode surface. (C) Quantification of neuron cell bodies over the first 50 $\mu\text{m}$  from the implant surface. \* $p < 0.05$  ANOVA with Tukey's Post Hoc. Scale bars are 100 $\mu\text{m}$ .

Postmortem histology was used to examine the nature and extent of inflammation in the brain following the electrode implantation and to gauge the health of the neural tissues near the implants. Reactive astrocytes were visualized with Glial Fibrillary Acidic Protein (GFAP) while axons were stained with NF200 (Figure 28A). Quantification of the GFAP stain revealed elevated astrocytic activity around the TNP modified electrode relative to the TNP+L1 electrode (Figure 28B). Significant differences in GFAP staining were observed between the TNP+L1 and TNP groups between 20 and 90 $\mu$ m from the electrode, and an overall statistical significance was found between groups across all time points (two-way ANOVA,  $p < 0.01$ ). There were no significant differences observed at any individual binned distance for the 3-day dried electrodes compared to the TNP electrodes, but there was an overall significant decrease in GFAP expression between these groups across all binned distances ( $p < 0.05$ , ANOVA). Axons were minimally affected by the electrode insertion in all experimental groups (Figure 28C). There does appear to be an elevated expression of NF200 directly adjacent to the TNP+L1 modified electrodes compared to TNP modified electrodes, but this only resulted in statistically significant differences for the first 10 $\mu$ m bin ( $p < 0.05$ , two way ANOVA).

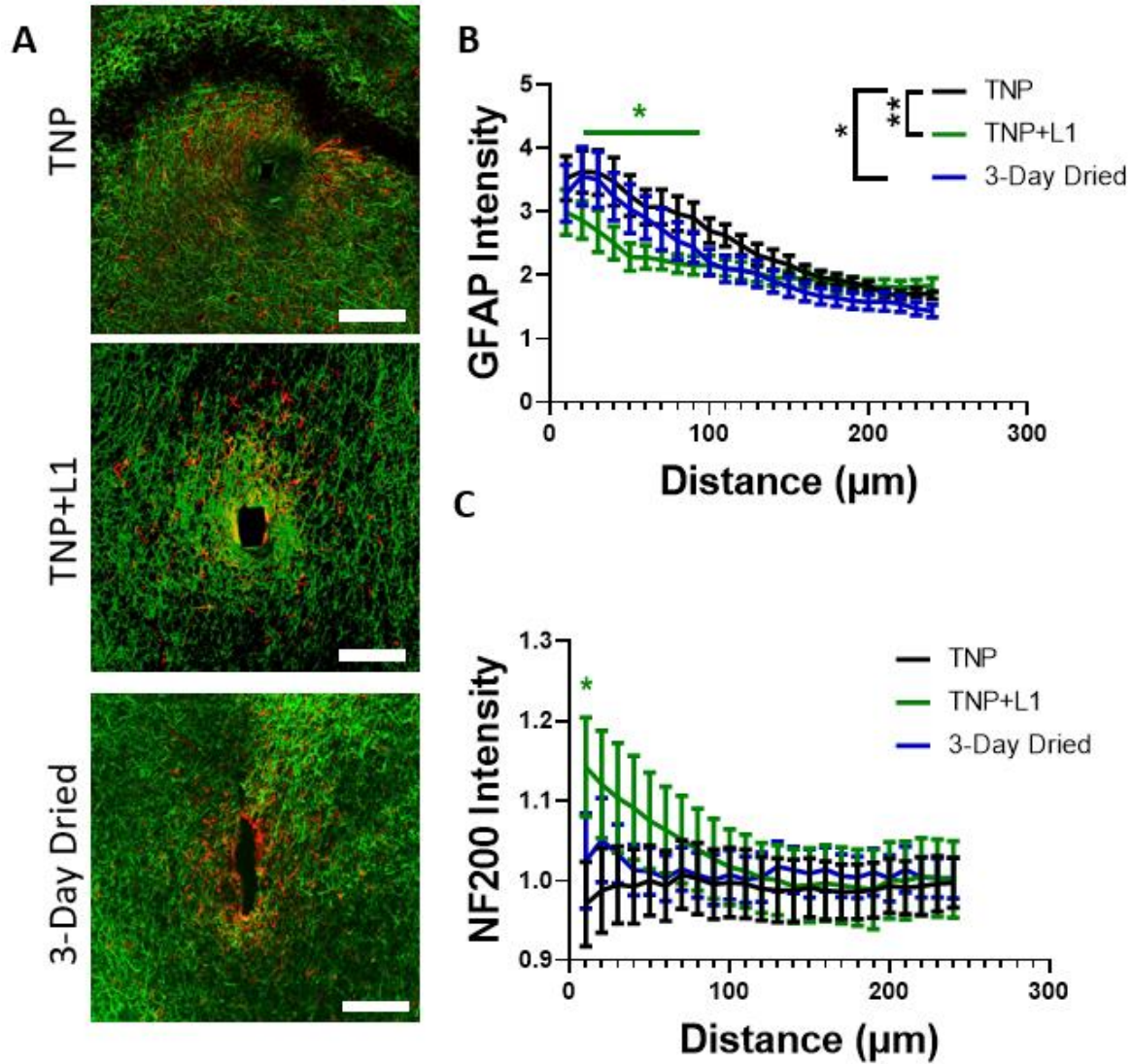


Figure 28. GFAP and NF200.

GFAP (activated astrocytes) and NF200 (neuron axons) staining of cortical tissues following 16 weeks of recording. (A) Representative images of NF200 (green) and GFAP (red) for tissues implanted with TNP (top), TNP+L1 (middle), and TNP+L1 which was dried for three days prior to implantation (bottom). (B) GFAP intensity vs distance from the electrode surface. GFAP intensity is highest nearer to the electrode and drops towards baseline in all cases. (C) NF200 intensity vs distance from the electrode surface. \* $p < 0.05$  \*\* $p < 0.01$ , green asterix signifies TNP+L1 significantly differs from other groups, scale bars are  $100\mu\text{m}$

Our previous investigations revealed elevated expression of nestin and DCX in the tissues surrounding TNP+L1 modified electrodes compared to control and TNP after one or four weeks of implantation. [231] We performed the same staining on the 16-week tissue samples to investigate if the observed elevation of nestin and DCX staining continued beyond the four-week time point. Indeed, we did observe a qualitative trend of elevated nestin staining around the TNP+L1 and 3-Day Dried conditions vs. the TNP (Figure 29A), but this was limited only to the regions directly adjacent to the electrode (Figure 29B). Examining only the first 20 $\mu$ m from the electrode surface (Figure 29C) did not reveal a statistically significant difference in the intensity of nestin staining. The number of DCX positive cells was quantified for the first 100 $\mu$ m from the electrode. Significant differences in DCX staining were observed between the 3-Day Dried samples and the TNP modified samples (Figure 29D).

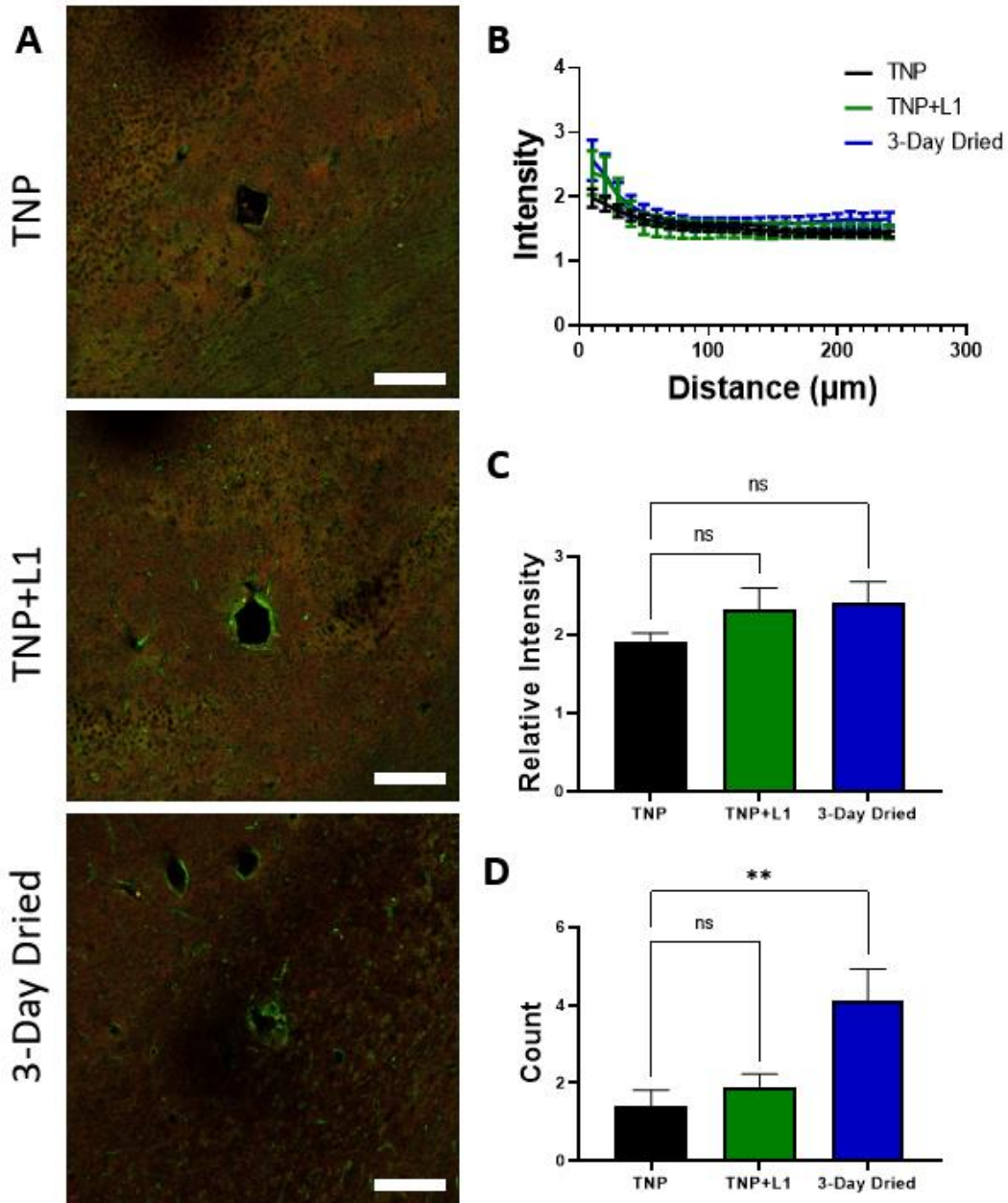


Figure 29 Nestin and DCX Staining.

(A) representative images of TNP, TNP+L1, and TNP+L1 which was dried for three days prior to implantation stained with nestin (green) and DCX (red). (B) quantification of the nesting staining intensity over distance from the electrode surface. (C) Nestin staining was then quantified over the first 20µm from the implant. (D) DCX positive cells counted over the first 100µm from the implant surface. Scale bars are 100µm. \*\*p<0.01 One-way ANOVA with Tukey's post hoc.

## 4.4 Discussion

Biomimetic coatings are one of the most promising methods of controlling undesired tissue response, promoting neuron health and density, and improving recording quality and longevity. Despite their promise, challenges in maintaining coating stability in use and storage prevented their widespread adoption. In this work, we have examined the effects of TNP pre-modification on stabilizing the L1 protein in dry storage. We then examined the electrophysiological performance of the electrodes with TNP+L1 coating that has been dried in air for 3 days to verify that the coating maintains their function.

The L1 coating was first subjected to dry-storage conditions to examine the long-term stability of the protein modified surface. Our results indicated that there was no loss of L1's neurite promoting properties for at least 8 weeks under these conditions. Our results further suggest that the immobilization of the L1 to the nano-textured surface greatly increases the stability of the coating.[239] Other studies have observed similar increases in protein stability when bound to nanotopographical surfaces[260, 269]. The elevated stability of L1 bound to the TNP surface is hypothesized to be due to multiple potential factors. The first is that the nanotopographical coating may be able to support a controlled microenvironment within the porous structure, reducing the interactions between the protein and damaging external species. The second may be due to a scaffolding effect, where the protein is bound to multiple locations within the porous structure. The result of this scaffolding effect is an increase in the strength of the interactions between the protein and the surface, reducing the potential for the protein to be cleaved off, as well as encouraging the protein to maintain its active tertiary structure. This finding is particularly interesting in its potential applications outside of neural engineering. Many devices that employ

biologically derived modifications such as artificial lungs[206, 207] and biosensors[204, 205, 270] may benefit from enhanced stability and bioactivity.

Following these *in vitro* experiments, we transitioned into the *in vivo* model to examine how the enhanced coating effect electrophysiological performance over 16 weeks. The TNP modified electrode, without L1, performed remarkably well considering there was no modification to the surface other than textural. Although impedances measured on TNP modified electrodes were significantly higher than control or L1 modified electrodes, this does not seem to have impacted the recording performance of the devices. The weekly yield from TNP modified electrodes was on par or greater than unmodified control electrodes, at minimum indicating that the modification did not produce any adverse reactions in the tissues. These findings are further corroborated by the postmortem histology. Although we observed many characteristic signs of inflammation, including elevated astrocytic encapsulation and decreased neuron density adjacent to the electrode, these responses were not out of line with previously reported literature examining unmodified electrodes.[230] Changes to the topography of substrates has previously been shown to change cellular responses and differentiation *in vitro*. [77, 81, 82, 87, 236, 271] This is believed to be partly due to the natural topography of biological environments,[84] where cells are interacting with a web of extracellular matrix, surrounding cells, and vessels.

The TNP+L1 modification has previously been examined for up to four weeks of recording[231]. The electrodes modified with TNP+L1 had lower impedances, higher recording yield, greater neuron density, and lower expression of inflammatory cells than the unmodified or TNP modified electrodes. In this longer-term study, we again observe decreased impedances for the TNP+L1 electrode relative to the TNP electrode, potentially indicating decreased scarring and improved device/tissue integration. The recording yield of the TNP+L1 modified electrode was

significantly higher than our previously reported control electrodes,[230] and outperformed the TNP modified electrode. Drying and storing the electrode for 3 days prior to implantation did not negatively affect the recording performance of the device, and the 3-day dried electrodes were able to produce the same reduced impedances and elevated yields that were observed on the TNP+L1 devices.

Postmortem histology further elaborated on tissue reactions to the implant. A degree of astrocytic encapsulation was expected to occur for all samples, and we observed only a slight elevation of activated astrocytes adjacent to the TNP+L1 implants. Histological analysis of the tissues surrounding the implants revealed that certain markers were more greatly affected by the TNP+L1 coatings. Notably, the number of NeuN positive cells was elevated for both of the protein modified conditions, which can be directly related to the number of cells able to be recorded from in the immediate vicinity of the electrode. L1 is known to interact directly with both inflammatory cells and neurons. These interactions likely encourage neurons and their axons to bind directly to the electrode and enhancing the number of cells proximal to the surface. A second potential interaction may be a survival cue for these cells, preventing the cells from undergoing apoptosis following electrode implantation or during the chronic inflammation phase.

Nestin and DCX staining were chosen as markers for neural progenitor/stem cells and immature neurons, respectively. Our previous study had observed elevated expression of both of these markers surrounding L1 modified implants, suggesting L1 promoted tissue healing following implantation.[231] Additionally, we observed that there was a decrease in the expression of these markers at four weeks compared to one week post implantation. In this work, we examined the expression of these two markers after 16 weeks but were only able to observe a significant increase in the number of DCX positive cells for the 3-day dried group compared to the TNP group. This

may indicate that the wound healing response posited in our previous work predominantly takes place over the first few weeks of implantation, and by 16 weeks this response was greatly reduced.

#### 4.5 Conclusions

The use of L1 as a surface modification for neural electrodes can greatly increase the short and long term recording performance of these devices while maintaining the health of the neural tissues. We have investigated an enhancement to the standard L1 coating which employs a nanotopographical base layer derived from the immobilization of silica nanoparticles to the electrode surface. The resulting TNP+L1 surface was superior to smooth L1 substrates *in vitro* and was even able stabilize the protein such that it could be dried and stored prior to use *in vivo*. We have demonstrated that the TNP+L1 surface can be prepared and stored under favorable conditions for distribution for at least 3 days. In combination with our *in vitro* studies, these results indicate that the device is compatible with off-site modification followed by transportation between facilities and enables a new tool for enhancing long term recording performance from neural electrodes.

## **5.0 Chronic Neural Recordings from TNP+L1 Electrodes Modified 28 Days Prior to Implantation**

In order to chronically interface with the central nervous system, it is paramount that the inflammatory biological reactions to the implanted electrode be controlled. Many advanced bio-functional coatings have been developed to modulate these reactions, yet these coatings themselves are limited by the inherent instability of the immobilized molecules. The result is that these coatings must be applied on-site, immediately prior to implantation, and has greatly limited the widespread adoption and implementation biomimetic coatings. We have developed a method of enhancing the stability of these coatings, enabling biomimetic electrodes to be created up to 28 days prior to use. These electrodes were implanted in mice and produced stable recording yield for at least 16 weeks and performed significantly better than the control unmodified electrodes. Subsequent histological staining of the tissues revealed elevated neuron density and reduced astrogliosis around the electrodes modified with the TNP+L1 coating, while explant analysis showed the presence of neuron-like tissues on the nanoparticle modified electrodes.

## 5.1 Chapter Introduction

Brain computer interfacing offers outstanding therapeutic potential but is limited by the innate inflammatory reactions elicited by neural electrodes following implantation. These reactions result in activation of host glial cells[2], generation of reactive oxygen species[238], and insulation of the device from the surrounding neurons[3, 34, 272, 273]. Further, these inflammatory reactions can be damaging to both the device[128] and the sensitive neural tissue which are being recorded from[238, 274]. The result in a constant decrease in recording quality proportional to the length of implantation.[272] It is evident that methods of controlling or eliminating these inflammatory reactions are required to produce stable chronic neural interfaces.

One of the most promising methods of improving long term electrode performance and maintaining the health of the tissues following implantation is the use of biomimetic coatings. These coatings, derived from proteins, peptides, and other biologically derived molecules, directly interact with host immune cells and neurons, modulating their responses to the implanted electrodes. Laminin modified electrodes were able to increase tissue integration after an initial burst in inflammation following implantation. [209] Similarly, small peptides derived from laminin or secreted by astrocytes have been successful at encouraging neuron attachment and electrode performance [188, 267, 275]. Binding of the interleukin-1 receptor antagonist was more effective than laminin at reducing astrocytic encapsulation.[276] One particularly successful coating has is derived from L1, a neuron adhesion molecule found in neuron axons and synapses.[220, 250, 251, 277, 278] Glial encapsulation around L1 modified electrodes is significantly reduced on the scale of hours, [49] to weeks[48, 230, 231], and which occurs alongside elevated neurite extension, axon density, and an increased number of neuron cell bodies adjacent to the electrode[47, 48, 172, 230, 231]. The coating has also demonstrated to preserve the

recording quality of implanted neural electrodes for at least 16 week in the mouse visual cortex.[230]

Key limitations to the widespread adoption of biomimetic coatings for neural electrodes are the technical challenges to applying the coatings and the necessity for the coatings to be prepared immediately prior to implantation. These coatings must be applied in a sterile environment, with chemicals and equipment that are not ubiquitous to neural engineering laboratories. Biological molecules are often fragile and sensitive to their environment, making offsite application of the coatings impractical without a method of stabilizing the protein during transportation.

We have previously examined a nanotopographical modification that can be applied to neural electrodes to enhance the bioactivity and stability of the subsequent biomimetic coating. By employing silica nanoparticles as a topographical agent, we can build up from the surface with an exceptional degree of control over the surface chemistry. Here we examine the ability of these coatings to be applied to electrodes and stored dry for up to 28 days prior to implantation. 32 channel single shank electrodes were modified and stored for one month prior to implantation in the mouse visual cortex. Subsequent electrophysiology was recorded for 16 weeks, following which histological examination of the tissue was performed to examine the cellular responses to the implant. Finally, the integrity of the electrodes and the nanoparticle modification was examined under scanning electron microscopy.

## **5.2 Methods**

### **5.2.1 Chemicals and Reagents**

All chemicals were purchased from Sigma Aldrich unless otherwise stated. Absolute ethanol and double deionized water were used in all experiments.

### **5.2.2 Nanoparticle Synthesis and Deposition**

Nanoparticle synthesis was performed as previously described.[231] In Brief, the nanoparticles were formed under a base catalyzed reaction from a solution of water (36mL), ethanol (5mL), and triethanolamine (6.18mL). The solution was heated to 60°C and stirred for 30 minutes following which 3ml of the silica precursor tetraethyl orthosilicate (TEOS) was added dropwise. The reaction was then continued for 5 minutes, at which point 1ml of mercaptopropyl trimethoxysilane (MTS) was added. After an hour, an additional 250µl of MTS was added to ensure the particle surface was coated with the thiol functional groups. The reaction progressed for an additional hour, after which the solution was allowed to cool to room temperature. The particles (TNP) were collected by centrifuge and washed with water and ethanol, then dried and stored at 4°C until used.

### **5.2.3 L1 Isolation**

L1 was isolated from postnatal rat pup brains as previously described.[220] The rat pups were anesthetized and sacrificed, then the brains removed and cooled in centrifuge tubes in an ice

bath. The brains were then homogenized and the membrane was isolated by centrifuging against a sucrose gradient. The membranes were collected and treated with CHAPS detergent. The membranes were stored in the CHAPS detergent at  $-80^{\circ}\text{C}$  until further use. Once required, the membrane was thawed and passed through an antibody affinity column to collect the L1 protein, which was then eluted by increasing the pH with diethylamine. Collected samples were then buffered with HEPES to return the pH to 7. The elution media was removed with a centrifugal protein concentrator with a 10kDa cut-off. The L1 was washed with phosphate buffered saline (PBS) and resuspended in PBS for immobilization

#### **5.2.4 Electrode Modification**

Electrodes were purchased from NeuroNexus (Ann Arbor, MI). Electrode modification was performed with sterilized electrodes in a laminar flow hood, using sterile reagents and practices. Electrodes possessed a silicon dioxide insulation layer that was activated by  $\text{O}_2$  plasma. The activated electrodes were submerged in a 2.5wt% solution of aminopropyl triethoxysilane (ATS) for 1 hour to silanize the surface. Following which the electrodes were washed with ethanol and water and then submerged in a solution of the crosslinker gamma maleimidobutyryloxysuccinimide ester (GMBS) for 30 minutes. The electrodes were washed again with water then immersed in a suspension of TNP in water ( $10\text{mg ml}^{-1}$ ) for 1 hour with gentle agitation provide every 10 minutes to prevent particles from clumping. Electrodes were then removed, washed with water, and again submerged in GMBS for an additional 30 minutes. Finally, the electrodes were washed and immersed in the L1 solution ( $2\mu\text{g ml}^{-1}$ ) for 30 minutes to immobilize the protein to the surface. The electrodes were then removed, dried under an aspirator vacuum, and stored in a sterile housing for 28 days at room temperature and in the dark prior to implantation.

### 5.2.5 Surgery

All animal procedures were approved by the university of Pittsburgh institutional animal care and use committee. Surgical procedures were performed under isoflurane anesthesia, 1.5% in O<sub>2</sub> for induction and maintained at 1.35% throughout the operation. Anesthesia was confirmed by the lack of a response to toe pinch, and heartrate and breathing were monitored throughout the operation. Once the animal was under anesthesia, the animal was placed in a stereotaxic frame with a nose cone and ear-bars stabilizing the head. The scalp fur was removed with clippers and the head sanitized by 3 successive washings with iodine solution (Betadine) and 70% ethanol. A sterile drape was then placed over the animal and the head exposed by cutting a hole through the drape. The scale was then removed and a hole drilled above the primary visual cortex, located by measuring 1mm from lambda and 1.5mm from the midline. Three bone screws (Fine Science Tools, 19010-00) were placed in the skull to anchor the electrode and serves as the counter electrodes. Once the screws were in place, the sterile drape was removed and the electrode inserted into the cortex with a stereotaxic manipulator until all electrode sites were visibly in the cortex. The hole above the cortex was sealed with medical grade silicone epoxy (Kwik-Sil) and the probe was secured to the skull with dental acrylic. The ground and reference wires were tightly wrapped around the bone screws, and additional dental acrylic was applied to further stabilize the probe and the wires. The probe was then removed from the manipulator and triple antibiotic ointment was applied to the wound area. Finally, day 0 recording was performed then the animal was allowed to wake up and was monitored to ensure a full recover following the surgery. Analgesic Ketofen (5mg kg<sup>-1</sup>) was given to the animal on the day of surgery and 2 day following.

### 5.2.6 Electrophysiology

Electrophysiology and impedance measurements were performed and lightly anesthetized animals. Animals were kept under 1% isoflurane anesthesia to prevent movement but to allow for the animal to receive visual input. Impedance measurements were performed with an Autolab potentiostat. (PGSTAT128N), measured between 32kHz and 10Hz. Electrophysiology data was gathered through a Medusa RA16 Preamplifier (Tucker Davis Technologies) and then processed by an RX7 base station. Data was gathered at 24.14kHz. Visual stimuli were provided by a custom MATLAB script, producing a series of moving bars to the contralateral eye.

Electrophysiology was processed with a custom MATLAB script. Data was separated based on frequency, and spike data was filtered between 300 and 3000Hz. Potential spiking activity was identified by threshold crossing events that exceeded 3.5 standard deviations of the filtered data stream. A window was created around the threshold crossing events, and these snippets were further analyzed by principal component analysis followed by visual inspection of the units. Yield was defined as the number of sites with units divided by the total number of sites. A peak to peak voltage was calculated as the difference between the lowest and highest values within the grouped snippet. The noise floor was calculated as 2 standard deviations of the data stream after removing the snippets. Finally, the signal to noise ratio (SNR) was found by dividing the peak to peak voltage by the noise floor. SNR of channels without identifiable units was set to 0.

### **5.2.7 Postmortem Histology**

Following the endpoint of recording the animals were sacrificed and perfused to preserve the histology of the brain. Animals were given a heavy dose of ketamine ( $65\text{mg kg}^{-1}$ ) and xylazine ( $7\text{mg kg}^{-1}$ ), and the animals were perfused by pumping 100ml of PBS followed by 100ml 4% paraformaldehyde (PFA) through the aorta. The animal head was removed and the bottom of the brain exposed and then post-fixed in 4% PFA for 4 hours at  $4^{\circ}\text{C}$ . The brain was then removed from the skull leaving the probe in the skull. The brains were sucrose protected with 15% and 30% sucrose, frozen, and sectioned at  $25\mu\text{m}$  on a cryostat (Leica CM 1950).

Prior to staining, brain slices were rehydrated with PBS then blocked with 10% goat serum. The brain slices were then permeabilized with 0.1% Triton-x for 45 minutes. Staining of the brains was performed in groups consisting of NeuN (Millipore mouse 1:250), NF200 (Abcam rabbit 1:500), Lectin (Vector Labs 1:250), GFAP (DAKO rabbit 1:500). Images were taken with a confocal microscope (Olympus Flouview 1000) then analyzed with MATLAB. Concentric bins were created around the electrode, and the intensity or cell count within the bins was measured.

### **5.2.8 Explant Analysis**

After the brains were removed from the skull, the majority of the organic material was carefully removed. The skull cap was then dehydrated in a stepwise gradient of ethanol and then desiccated for 1-week over  $\text{CaSO}_4$ . The probes and skull cap were made conductive by sputter coatings with 6nm of Au/Pd. Finally, the samples were imaged with SEM (Zeiss Sigma500-VP).

## 5.3 Results and Discussion

### 5.3.1 Electrophysiology

A primary limitation of bioactive coatings is their poor stability under ambient conditions, which necessitates their application be performed on site and immediately prior to implantation. We have previously observed that topographical modification of the base substrate with silica nanoparticles followed by immobilization of the protein L1 was able to impart sufficient stability that the coatings could be stored dry and under ambient conditions for at least 8 weeks without loss of bioactivity *in vitro* and for at least 3 days *in vivo*. We look to expand upon these findings by extending the storage time prior to implantation to 28 days. In addition, we have increased the electrode site density by nearly a factor of 2, enhancing the resolution of the recorded signals and increasing the amount of data recoverable by the devices. These 32 channel NeuroNexus electrodes were inserted into the mouse visual cortex and electrochemical characterization and electrophysiological recordings were performed for 16 weeks.

EIS offers a method of non-invasively investigating the electrode tissue interface and can be used to identify potential damage to the electrode and insulation, or encapsulation by host tissues. We observed a temporary increase in the device impedances following insertion (Figure 30A), as is expected after implanting into the tissue. Initially, impedances were lower for the protein modified device, but a gradual decrease in the impedance measured on the control device resulted in the impedance magnitudes nearing each other after eight weeks. This decrease in impedance on the control electrode may indicate that damage occurred to the insulation or electrode sites, increasing their electrochemical surface area. This damage may be due to elevated production of reactive oxygen species around the control electrodes [128] from activated glia. The

stability of the impedance measurements from the TNP+L1 devices may in turn be due to their surface bioactivity, preventing the activation of the microglial cells after insertion and maintaining the health of both the electrode and the surrounding tissues.

Electrophysiology was recorded throughout the 16-week implantation period. Data gathered from electrophysiologic measurements was filtered between 300 and 3000Hz to prior to isolation of single unit action potentials. The action potentials were identified through a combination of threshold crossing events, principal component analysis, and visual inspections prior to being confirmed as a unit for that electrode site. For non-modified electrodes, the recording site yield is expected to decrease over time. The control electrodes did exhibit a decrease following the first week of recording and a more gradual decline in yield thereafter (Figure 30B). This trend was not observed on the TNP+L1 electrodes, which were able to maintain a recording site yield of approximately 60% for the duration of the implant. TNP+L1 electrodes performed significantly better than the control electrodes over the course of the experiment ( $p < 0.0001$ , two way ANOVA) in addition to being significantly greater at weeks 1, 7, 9, 12, and 15 ( $p < 0.05$ , two way ANOVA). Both electrodes exhibited similar trends for the recording noise floor, stabilizing at approximately  $7\mu\text{V}$ . The SNR factors in the strength of the recorded units, the background noise, and the number of sites actively recording units. We observed that the SNR was consistently higher for the TNP+L1 electrode over the course of the experiment, with significant differences occurring at 1, 7, 10, 12, and 13 weeks ( $p < 0.05$ , two way ANOVA) as well as an overall significant difference between groups over the course of the experiment ( $p < 0.0001$ , two way ANOVA).

These electrophysiological characterizations indicate that the TNP+L1 protein coating is capable of dramatically increasing electrode performance, increasing yield and SNR for at least 16

weeks following implantation. This result occurred even though the L1 coating was prepared a month in advance of the implantation.

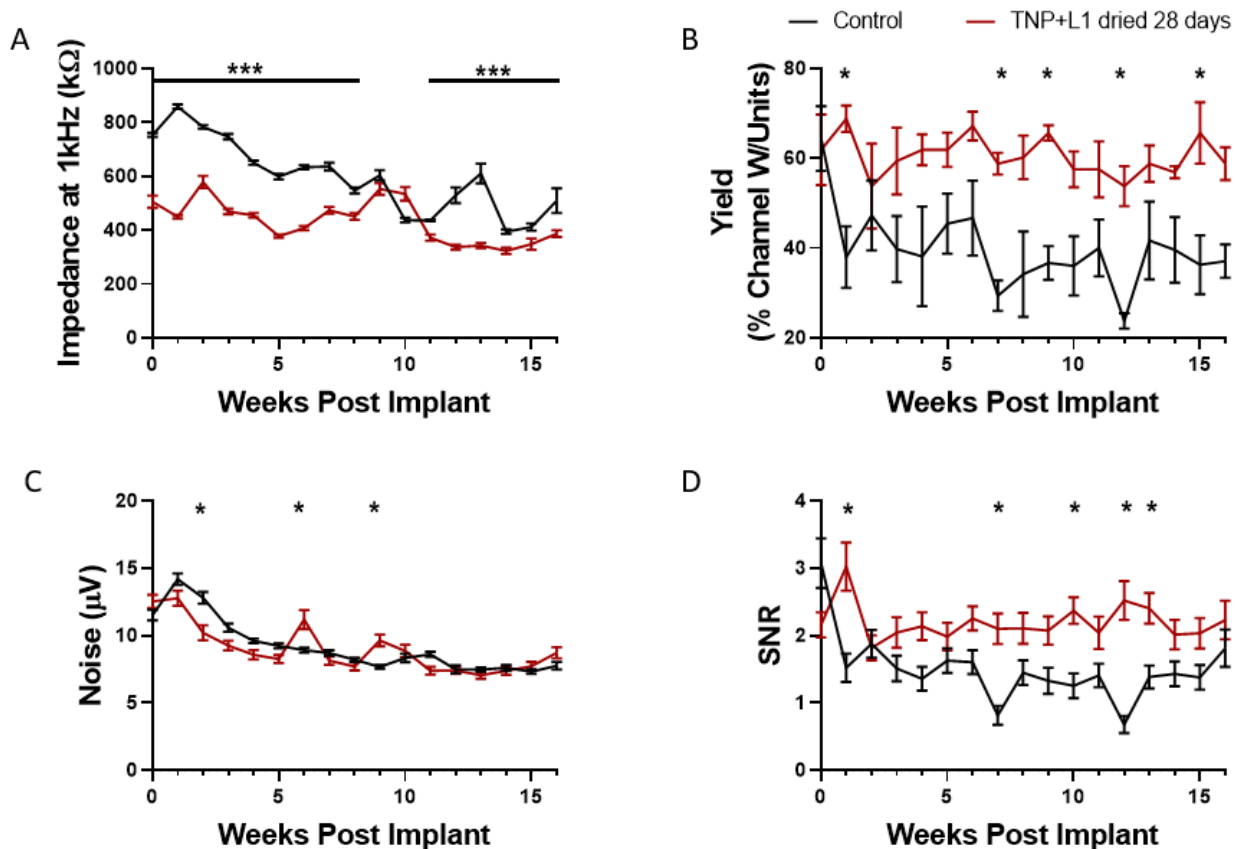
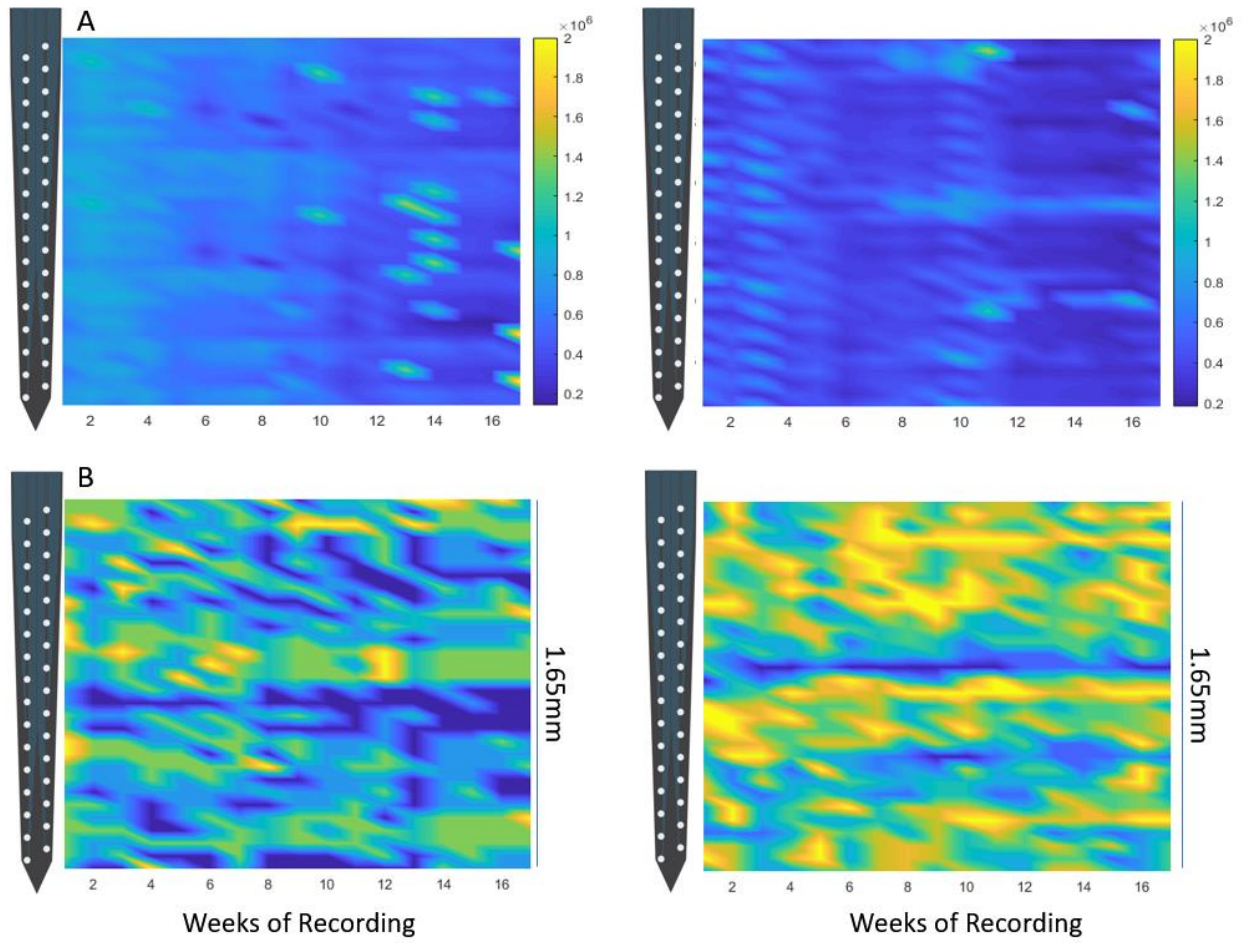


Figure 30. Electrophysiology from 32Ch electrodes.

(A) impedance measured over the 16 week experimtn reveals that the TNP+L1 electrode maintained a constant impedance following insertion. There is a characteristic drop in electrode impedances visible for the control electrode, potentially indicating damage to the insulation over time. (B) recording yield was elevated for the TNP+L1 electrode relative to the control for the 16 week experiment. The noise floor (C) was not different between electrodes except at select time points, and no overall trend was observed. (D) the signal to noise ratio was elevated for the 32 channel electrodes. \*p<0.05 \*\*\*p<0.001 two way ANOVA

### 5.3.2 Depth Wise Impedance and Yield

The brain is not homogenous, and we expect to see variations in the recording performance at different depths in the cortex. To understand how the depth of the electrode site affects the recording performance, we mapped the electrode EIS at 1kHz and the recording site yield based on the electrode position (Figure 31A,B). Due to the layout and limitations of our recording system, only 16 channels were able to be recorded from simultaneously, which may explain some of the banding visible on the impedance plots. Interestingly, there does appear to be some heterogeneity in the recording yield for both the control and TNP+L1 modified electrodes. Notably there is a band of low recording yield for both electrode conditions at approximately 800 $\mu$ m from the top-most electrode site. Previous examinations of recording yield mapped to electrode depth in the brain have found similar patterns[41, 230], and this has been attributed to these electrode sites sitting just beyond the end of the cortex, where electrodes would not be expected to produce recordings as there would not be any neurons present.



**Figure 31. Depth Wise Impedance and Recording Yields.**

Impedances (A) and yields (B) over time and depth are plotted for the unmodified electrode (left) and the TNP+L1 electrode (right). Impedances were measured at 1kHz.

### 5.3.3 Histology

Following the 16-week implantation period, the animals were sacrificed by perfusion and the brains sectioned and stained for markers of neuronal health (NeuN, Nf200) and inflammation (GFAP, Lectin, Iba-1). L1 exhibits direct interactions with both inflammatory cells and neurons and may function through a combination of these effects. We first stained for GFAP, NF200, and Lectin to examine the interactions between the implanted electrodes and the host astrocytes (GFAP), axons (NF200), and microglia and vasculature (Lectin) (Figure 32A,B). L1 is a homophilic binding protein present on axons and synapses[220, 250], and we would expect that active L1 would encourage axon at the electrode surface. Indeed, we observed that NF200 staining was diminished adjacent to the control electrodes but was maintained around the TNP+L1 modified electrodes (Figure 32C). Although there were no significant differences in the axon density around either electrode at any specific distance from the probe, there was an overall significant decrease in axon density around the control electrode that was not present on the TNP+L1 modified electrode.

GFAP and Lectin both mark inflammatory cells, while lectin also labels vasculature around the implant. GFAP was significantly elevated around the control electrodes compared to the TNP+L1 electrodes at binned distances between 10 and 60 $\mu$ m from the implant surface (Figure 32D). However, lectin staining did not reveal significant differences in intensity for any binned distance or overall between the control and TNP+L1 electrodes (Figure 32E). We have previously reported that the TNP+L1 modification was capable of increasing neurite extension and outgrowth while limiting astrocytic spreading *in vitro*[172] and *in vivo* after one and four weeks.[231] The findings reported here serve to demonstrate that the interactions between the TNP+L1 surface and

both neurite and astrocytes are maintained for at least 16 weeks *in vivo* and even after the surface has been stored for 28 days prior to implantation.

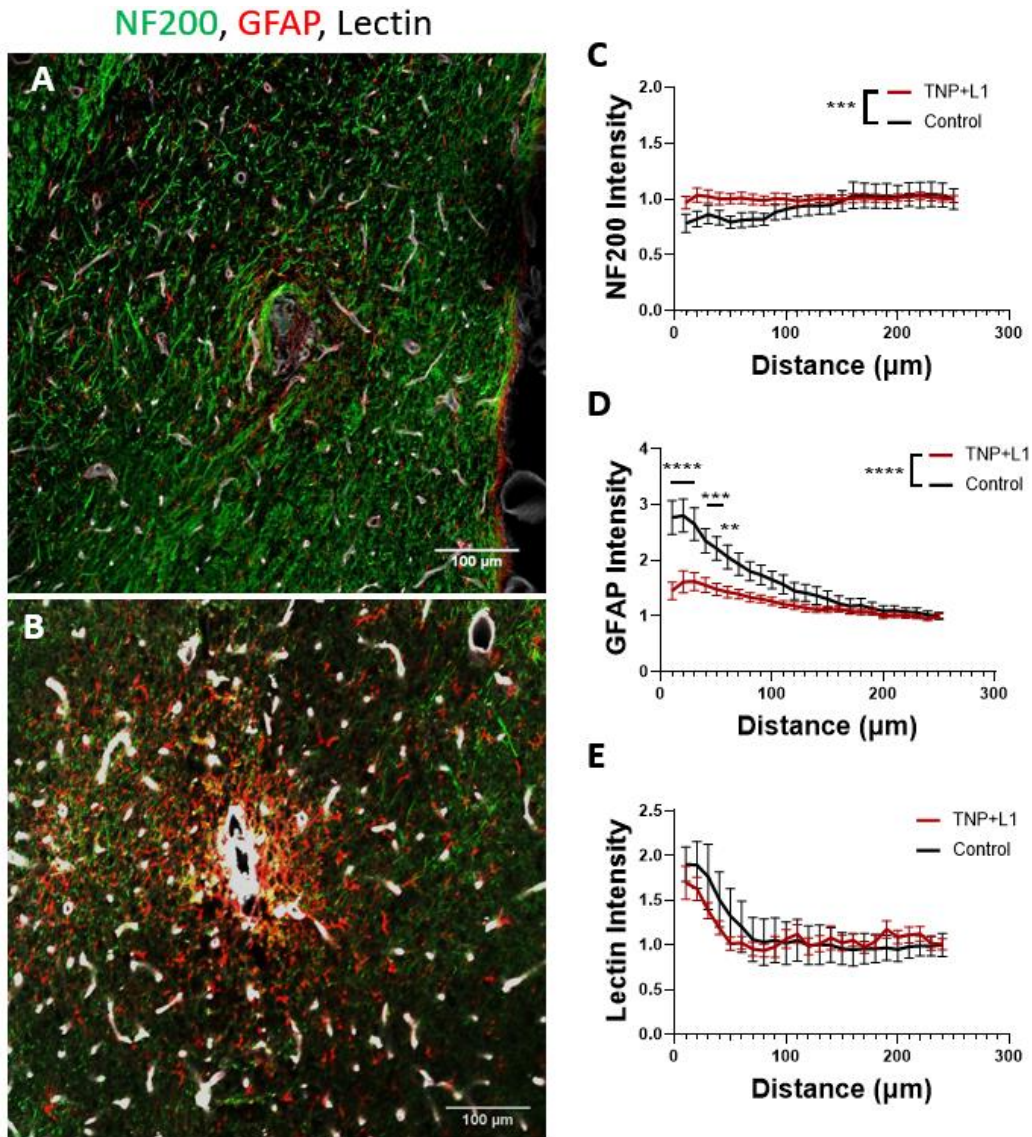


Figure 32. NF200, GFAP, and Lectin staining.

Tissue sections from TNP+L1 (A) and Control (B) animals were stained for NF200 (green), GFAP (red), and Lectin (White). (C) Quantification of the NF200 staining as a function of distance from the electrode surface. Significant differences were observed between the control and TNP+L1 groups when compared across all distances (two way ANOVA). (D) Quantification of the GFAP staining as a function of distance from the electrode surface. Significant differences were observed between the control and TNP+L1 groups when compared across all distances in addition to significant differences at 10 $\mu$ m-60 $\mu$ m from the implant (two way ANOVA with Tukey's post hoc). Quantification of the Lectin staining as a function of distance from the electrode surface. \*\*p<0.01 \*\*\*p<0.001 \*\*\*\*p<0.0001

Action potentials from the neuron cell body are believed to be the predominant signals measured during electrophysiologic recording. NeuN and Iba-1 staining were used to visualize the density of neuron cell bodies and microglial cells (Figure 33A,B). Neuron cell bodies were counted over 25 $\mu$ m bins, and we observed a significant increase in the number of neurons adjacent to the TNP+L1 modified electrode compared to the control ( $p < 0.05$ , Figure 33C). In addition, there was a significant increase across all bins for the TNP+L1 modified electrode ( $p < 0.001$ ). Iba-1 staining intensity was significantly lower for the TNP+L1 modified electrodes, but did not follow the same dramatic changes observed with other experiments examining the microglial encapsulation around L1 modified electrodes (Figure 33D). This finding may be attributed to inherent variability between animals, but is in agreement with the lectin staining.

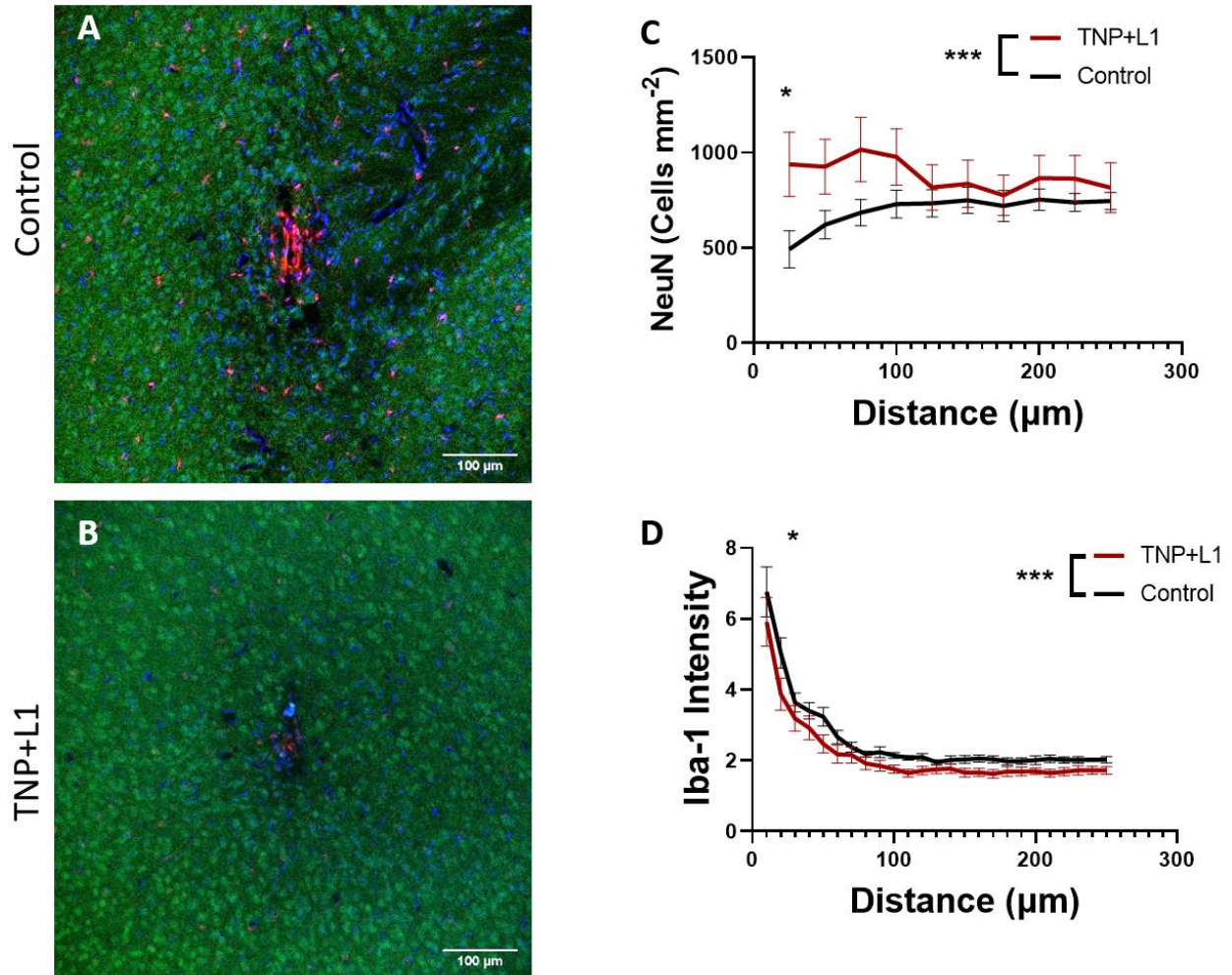
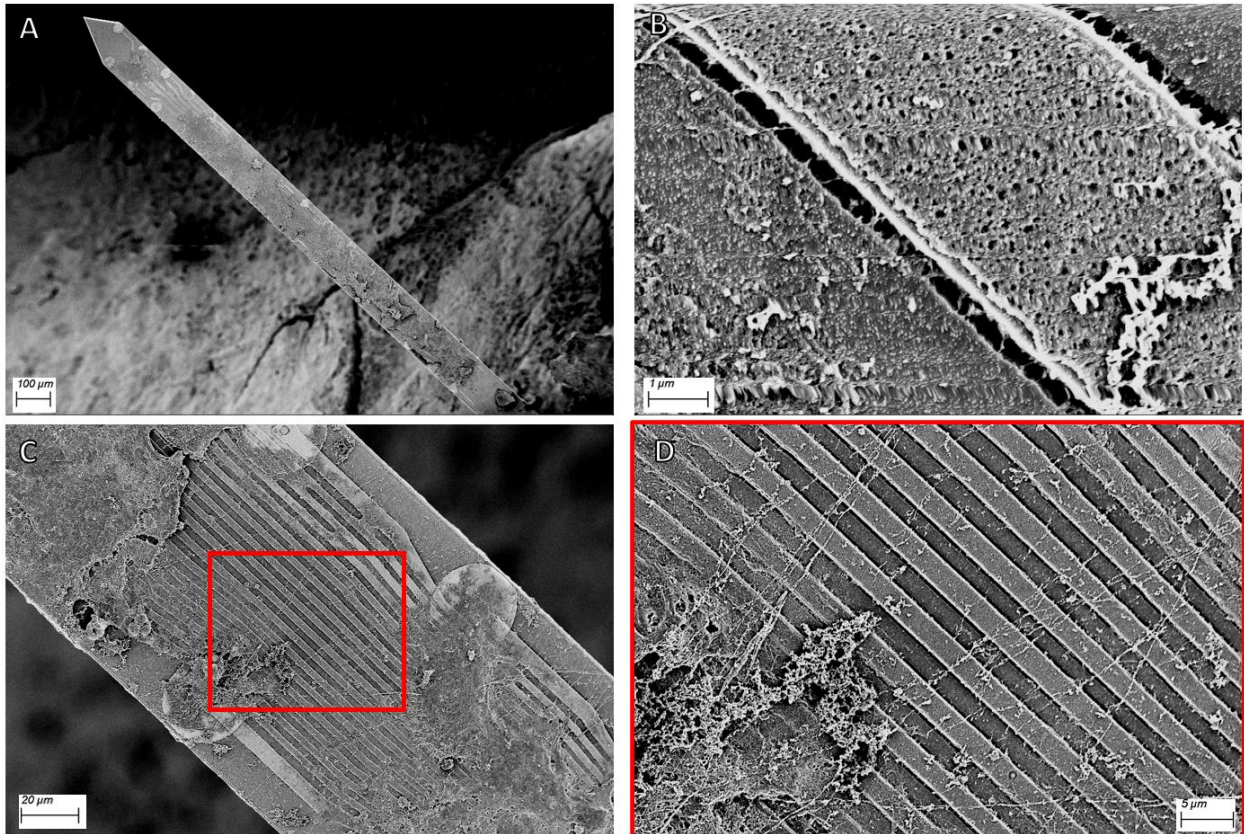


Figure 33. NeuN staining and Quantification.

Neurons were labeled with NeuN and apoptotic cells were labeled with caspase-3. (A,B) Representative images of the tissues adjacent to TNP+L1 (A) and control (B) electrodes. The number of neuron cell bodies was quantified in 25μm bins from the electrode surface (C). Further analysis was performed by examining the number of neuron only in the first 25μm (D).

### 5.3.4 Explant Analysis

Following the endpoint of recording and removal of the brains for postmortem histology, the underside of the skull which still contained the attached probe was prepared for and imaged with SEM (Figure 34A). The high magnification images revealed a porous structure present on the traces of the electrode, likely due to the immobilized TNP. There was also a substantial degree of biological material present on the device (Figure 34C), with what appear to be neurite projections originating from a cell or mass of cell located directly on top of an electrode. Increasing the magnification on the highlighted region, we can examine the morphology of these projections on the surface of the device. These projections are long and straight, and highly resemble the neurites that appear on L1 modified substrates *in vitro*. Further analysis will be required to confirm the nature of these biological features, but the results suggest that there continues to be intimate interactions between the electrode and the host neurons up until the point of sacrifice and explantation.



**Figure 34** Explant analysis of TNP+L1 with SEM.

SEM images were taken of the TNP+L1 electrode in the skull (A) and zoomed in to show the morphology of the surface (B). This image shows an electrode trace, with the underlying substrate on both sides. Biological material was observed on the electrode (C) and apparent neurites were seen extending from the cell bodies (D).

## 5.4 Conclusions

L1 has immense potential in the field of neural interfaces. However, the necessity of the protein to be immobilized on-site, immediately prior to implantation, are critical hurdle to the widespread adoption of L1 surface modifications. We have demonstrated that through the use of a topographical base layer formed by the immobilization of silica nanoparticles to the neural electrode, we are able to increase the stability of L1 to the point that the surface can be dried and stored for at least 28 days prior to use. These finding pave the way for distribution and adoption of TNP+L1 electrodes to labs worldwide. This will be a critical step in demonstrating the safety and efficacy of bioactive coatings, and crucial for the approval and adoption of these electrode coatings for use in human patients.

## 6.0 Silica Nanoparticles as Dopants for Conducting Polymers

In order to address the material limitations of biologically interfacing electrodes, modified silica nanoparticles are utilized as dopants for conducting polymers. Silica precursors are selected to form a thiol modified particle (TNP), following which the particles are oxidized to display sulfonate functional groups (SNP). The selective inclusion of hexadecyl trimethylammonium bromide (CTAB) allows for synthesis of both porous and non-porous SNPs. Non-porous nanoparticle doped polyethylenedioxythiophene (PEDOT) films possess low interfacial impedance, high charge injection ( $4.8\text{mC cm}^{-2}$ ), and improved stability under stimulation compared to PEDOT/poly(styrenesulfonate). Porous SNP dopants can serve as drug reservoirs and greatly enhance the capability of conducting polymer based, electrically-controlled drug release technology. Using the SNP dopants, drug loading and release is increased up to 16.8x, in addition to greatly expanding the range of drug candidates to include both cationic and electroactive compounds, all while maintaining their bioactivity. Finally, the PEDOT/SNP composite is capable of precisely modulating neural activity *in vivo* by timed release of a glutamate receptor antagonist from coated microelectrode sites. Together, this work demonstrates the feasibility and potential of doping conducting polymers with engineered nanoparticles, creating countless options to produce composite materials for enhanced electrical stimulation, neural recording, chemical sensing, and on demand drug delivery.

## 6.1 Chapter Introduction

*Work presented in this chapter has been previously published [53].* Biologically interfacing electrical devices are prominent components of *in vivo* bio-chemical sensors[53]. Biologically interfacing electrical devices are prominent components of *in vivo* bio-chemical sensors[254, 279], drug delivery platforms[183], and cardiac or neural recording/stimulating electrodes in humans[198, 280]. However, it has become increasingly apparent that material limitations are blocking progress in the development of next generation devices. While device and electrode miniaturization are desired for reducing invasiveness and increasing density of information flow, such designs pose significant challenges to the electrochemical properties and stability of the current materials, as both impedance and charge injection limits are inversely proportional to the surface area of the electrode. One potential solution is conducting polymer surface modifications. These intrinsically conductive coatings have the ability to greatly increase charge injection limits for safe and effective stimulation and maintain low impedances necessary to record bio-electrical activity.

Conducting polymers have gained substantial attention in recent years as an advanced coating for microelectrodes[1], with particular emphasis on the polypyrrole[135, 199, 281] and poly 3,4-ethylenedioxythiophene[135, 181, 182, 194, 282, 283] (PEDOT). Conducting polymer coatings can be applied to an electrode by immersing the electrode site in a solution of monomer alongside a negatively charge dopant. A positive potential applied to the electrode results in spontaneous oxidation and polymerization of the monomer into a polymer film. These oxidized conducting polymer films possess positive charges along the backbone, which is then balanced out by the anionic dopants. Further polymerization leads to thicker coating with a unique fractal pattern[181], increasing surface area by orders of magnitude and resulting in dramatically reduced

impedances of the electrode[181, 199]. In neural engineering, these coatings are notable for improving recordings from electrodes as small as 7 $\mu$ m in diameter[283], lowering thermal noise and increasing the signal to noise ratio of recorded neural action potentials[282]. Similarly, conducting polymer coating can greatly increase amount of charge which can be injected into tissues prior to the buildup of unsafe potentials[284-287]. These exceptional electrochemical properties have led conducting polymers to be at the forefront of microelectrode design.

Doping offers endless possibility for tuning the properties of conducting polymer as the dopants carries in their unique characteristics and functionality. Various dopants have been incorporated into conducting polymer from non-bioactive ions[288, 289], to peptides[188], proteins, to peptides[188], proteins[192, 290, 291], polysaccharide[292], and even cells[293]. Large biomolecules are immobilized this way to impart bioactivity to the conducting polymers[294], while smaller dopants can be released via ion exchange or electrochemical controls[183]. The electrochemically driven release provides a mechanism for on demand drug delivery systems with precise temporal and spatial control. In such a system, conducting polymers serve as a vehicle for drug delivery, with their oxidized state carrying positively charged matrix serving as a gating mechanism. Applying a sufficient negative potential removes this gating and enables release of the dopant. The result is a highly controlled release mechanism, which is entirely localized only to the site of implantation. Researchers have used conducting polymer-based drug delivery to release steroids, polysaccharide[292], and even cells[293]. Large biomolecules are immobilized this way to impart bioactivity to the conducting polymers[294], while smaller dopants can be released via ion exchange or electrochemical controls[183]. The electrochemically driven release provides a mechanism for on demand drug delivery systems with precise temporal and spatial control. In such a system, conducting polymers serve as a vehicle for drug delivery, with

their oxidized state carrying positively charged matrix serving as a gating mechanism. Applying a sufficient negative potential removes this gating and enables release of the dopant. The result is a highly controlled release mechanism, which is entirely localized only to the site of implantation. Researchers have used conducting polymer-based drug delivery to release steroids[71, 130, 295, 296], dyes[135, 193], and even as a gating mechanism for ion pumps[196, 197].

The primary limitations of conducting polymer-based drug delivery are the quantity of drug loaded and the compatibility of pharmacologic compounds. To address the issue of drug quantity, drug reservoirs have been incorporated into the polymer film. Examples including graphene oxide[71, 130] and functionalized carbon nanotubes[135] (CNT) have been successful in increasing the quantity of the drug payload. The ion pump approach can further circumvent this issue by incorporating a fluid channel and ion reservoir that can be refilled, but this requires extensive microfabrication and is not immediately compatible with many current electrically interfacing devices. When considering candidate drugs suitable for such drug delivery system, anionic compounds are more commonly utilized, as they can directly dope the polymer during polymerization and be released upon de-doping, while loading of neutral and cationic compounds relies on physical entrapment or interactions with the dopants[183]. Additionally, loaded compound needs to be electrochemically stable under the potentials required for polymerization or for triggering drug release. To the best of our knowledge, no viable options to load electroactive compounds have been presented.

We have designed sulfonated silica nanoparticles as dopants for conducting polymers. Silica nanoparticle dopants may provide a potential drug delivery reservoir while also maintaining the impressive electrochemical properties of PEDOT films. First, the size, porosity and surface chemistry of silica nanoparticles is modifiable[213, 214], and can be tuned to specific applications.

Incorporation of thiol containing silane mercaptopropyl trimethoxysilane (MTS) results in the presentation of thiol groups at the particle surface[172]. These thiol groups can be efficiently oxidized to sulfonates under relatively mild hydrogen peroxide oxidation[297]. The presence of negatively charged sulfonate groups allow the nanoparticles to be effectively doped in the PEDOT matrix. Secondly, mesoporous silica has been well studied as a drug delivery platform[298]. The highly porous structure of the mesoporous silica nanoparticles enables a large degree of drug loading[298], while the non-reactive nature of silica renders them biologically inert[298]. Further, the silica nanoparticle dopants are substantially larger than either CNT or graphene, potentially making them capable of more substantial drug loading. Finally, silica itself is non-conductive, possibly shielding the payload from the strong potentials during film polymerization or release triggers.

In this work, we first synthesize sulfonate modified silica nanoparticles (SNPs) with and without mesopores (scheme 1). We then present SNP-doped PEDOT composites, a biocompatible polymer with highly favorable electrochemical properties. Impedance of gold electrodes was dramatically reduced after coating with PEDOT/SNP, and charge injection limits exceed  $4\text{mC cm}^{-2}$ . The mesoporous SNP can carry a high drug payload into the polymer film. The drug can then be controllably released by cyclic voltage sweeps for over 13000 stimulations. We then show that the drug release with SNP is up to 16.8 times greater than without the SNP reservoir. The PEDOT/SNP can load and release not only negative drugs but also positive drugs. More importantly, the electroactive compound melatonin, that would otherwise be oxidized and lose antioxidant efficacy during the electropolymerization process, can be protected by the SNPs. Finally, we utilize our PEDOT/SNP coating to directly modulate neural activity by focal release of neurochemicals, demonstrating the proof of concept for *in vivo* applications.

## 6.2 Methods

### 6.2.1 Materials and Characterization

All materials were purchased from Sigma Aldrich and used as received unless otherwise stated. Transmission electron microscopy (TEM) images were taken by Joel JEM2100f. Scanning electron microscopy (SEM) were taken by JSM6355F. Dynamic light scattering and  $\zeta$ -potential measurements were performed with Malvern ZS90 Zetasizer. Electrochemical polymerization, analysis, and release were performed by Autolab (PGSTAT128N). Spectroscopic measurements were performed on Molecular Devices SpectraMax i3x. Fluorescence imaging was performed on Leica, DMI4000 B fluorescent scope. Two-photon imaging was performed on an Ultima IV, Prairie Technologies

### 6.2.2 Thiolated Silica-Nanoparticle Synthesis

Thiol modified silica nanoparticles synthesis was adapted from Moeller *et al.*[167] In brief, a solution comprising of 36mL of water, 5 mL of ethanol, 1.3g of hexadecyl trimethyl-ammonium bromide (CTAB), and 6.18mL of triethanolamine were mixed for 30 minutes and heated to 60°C. [167] In brief, a solution comprising of 36mL of water, 5 mL of ethanol, 1.3g of hexadecyl trimethyl-ammonium bromide (CTAB), and 6.18mL of triethanolamine were mixed for 30 minutes and heated to 60°C. CTAB was excluded from the synthesis of non-porous particles. To this mixture, 3mL of Tetraethyl orthosilicate was added dropwise, followed by 1mL of mercaptopropyl trimethoxysilane (MTS). A second 100 $\mu$ L aliquot of MTS was added after 1 hour. The reaction proceeded for 2 hours, then was cooled and the particles collected by centrifuge (20,000 rpm x 10

minutes). Surfactant template was removed by washing in water, ethanol, then by heating the particles in 100mL of 1:5 concentrated HCl in ethanol under reflux at 70°C for 10 hours. Particles were then collected and washed in water.

### **6.2.3 Oxidation of Thiol to Sulfonate**

Two grams of thiol modified particles were suspended in 25ml of 20% H<sub>2</sub>O<sub>2</sub> in water, followed by the addition of 20μL of H<sub>2</sub>SO<sub>4</sub>. After oxidation, particles were collected by centrifuge and washed with water. Resulting SNP were colloiddally stable and stored at 4°C until used.

### **6.2.4 Electropolymerization**

Polymerizations were carried out with a three-electrode set-up with a platinum foil counter and Ag/AgCl reference. 0.01M EDOT in DI-water was mixed with SNP (5mg ml<sup>-1</sup>) and sonicated for 5 minutes in a bath sonicator. Electrode materials varied by experiment, but all polymerizations were carried out under constant current at 320μA cm<sup>-2</sup>.

### **6.2.5 Electrochemical Characterization**

All electrochemical characterizations were performed in triplicate on 3 separate gold electrodes wire electrodes (50μm diameter, A-M systems). Electrochemical Impedance Spectroscopy (EIS) was measured from 1Hz to 100kHz. Cyclic voltammetry was measured from -0.9 to 0.5V at 100mV s<sup>-1</sup>. Charge storage capacity was calculated as the integral of the 3<sup>rd</sup> scan of the CV, where I is the current and A is the area of the electrode.

$$CSC = \frac{\int |I| dt}{A} \quad (6-1)$$

Charge injection limit is defined as the amount of injectable charge prior to a voltage transient exceeding -0.6V divided by the area of the electrode. An anodic leading biphasic pulse of 1ms per phase with a 200 $\mu$ s interphase delay was used. Charge injection was then calculated as:

$$CIL = \left| \frac{I \times \tau}{A} \right| \quad (6-2)$$

such that  $|V|$  resulting from  $I$  is less than 0.6V. Access voltage was subtracted from the calculation.

### 6.2.6 Biocompatibility

Highly aggressive proliferating Immortalized (HAPI) microglia cells were used as a model for testing the biocompatibility of PEDOT/SNP. Gold electrodes were prepared by sputter-coating 100nm of gold onto a polypropylene sheet with an adhesive mask. The mask was removed to create circular electrodes of 7.5mm diameter. Samples were prepared by electropolymerizing SNP or polystyrene sulfonate doped PEDOT under constant current to a charge density of 75mC cm<sup>-2</sup>. Polymerized electrodes were trimmed to fit into a 48-well plate (Falcon). Samples were sterilized by soaking in 70% ethanol for 15 minutes followed by drying and exposure to UV for 15 minutes. HAPI cells were plated over the polymer samples at a density of 15,000 cells per well. Control cells were grown on tissue culture polystyrene (TCPS). Cells were grown for 2 days (semi-confluent), positive controls were treated with 0.2% Triton-X 4 hours prior to measuring the viability with an XTT assay. 5 samples each of PEDOT/SNP, PEDOT/PSS, and positive and

negative controls were prepared for testing, and the assay repeated 3 times to ensure reproducibility.

XTT assay was performed as directed by the distributor. In brief, 2,3-Bis-(2-Methoxy-4-Nitro-5-Sulfophenyl)-2H-Tetrazolium-5-Carboxanilide (XTT, Invitrogen) was added to culture media at  $1\text{ mg ml}^{-1}$ .  $10\mu\text{l}$  of  $10\text{mM}$  phenazine methosulfate (PMS) was added to  $4\text{ml}$  XTT/media solution just prior to the addition of  $50\mu\text{L}$  of XTT solution per well. Cells were incubated for 3 hours and the absorbance of the supernatant was measured at  $450\text{nm}$ . HAPI cells were imaged with a Live/Dead assay (Invitrogen). Supernatant solution was removed and replaced with  $1/1000$  dilutions for Propidium Iodide and Calcein AM in PBS. Cells were incubated for 1 hour and imaged with fluorescence microscopy.

### **6.2.7 Drug loading**

Drug compounds were dissolved at  $25\text{ mg ml}^{-1}$  in water (for rhodamine, fluorescein, dox, and DNQX) or ethanol (melatonin).  $5\text{mg}$  of mesoporous SNP were sonicated with  $200\mu\text{l}$  of drug solution for 20 minutes prior to the particles being collected by centrifuge and dried under vacuum.

### **6.2.8 Electropolymerization and Drug Release**

$5\text{mg}$  of drug loaded particles were suspended in  $3\text{ml}$  of  $0.01\text{M}$  EDOT solution in water. Electropolymerization was carried out for 200 seconds on  $2\text{mm}$  diameter gold electrodes or  $70\mu\text{m}$  diameter Pt/Ir wires (A-M systems, 90/10 Pt/Ir). Electrodes were then washed with PBS on an orbital shaker for 2 hours then soaked overnight to remove any adsorbed drugs. Drug release was performed with cyclic voltammetry between  $-0.6\text{V}$  and  $0.8\text{V}$  at  $1\text{V s}^{-1}$  for dye release,  $-0.6$  to  $0.8\text{V}$

at  $100\text{mV s}^{-1}$  for DOX and DNQX release, or from  $-0.6$  to  $0.3\text{V}$  at  $100\text{mV s}^{-1}$  for melatonin, into  $3\text{ml}$  of PBS or the animal model.

### **6.2.9 *In Vitro* Activity**

Dox was loaded and released from PEDOT/SNP films as described above. 3T3 cells were cultured in 48 well plates for 2 days to reach semi-confluency, at which point the culture media was removed and replaced with serum-free media containing stock dox, released dox, or no dox. Cells were culture for 72h, at which point the media was aspirated and the viability of the cells measured with XTT assay as described above.

Released melatonin was examined for antioxidant capabilities through a Prussian blue assay. PBS containing released melatonin ( $1\text{mL}$ ) was added to  $1\text{mL}$  of  $1\%$   $\text{K}_3[\text{Fe}(\text{CN})_6]$  and incubated at  $50^\circ\text{C}$  for 20 minutes.  $1\text{mL}$  of solution was removed and added to  $0.8\text{mL}$  of water, followed by the addition of  $200\mu\text{L}$  of  $0.01\%$   $\text{FeCl}_3$ , creating a deep blue dye. The absorbance of the resulting solution was measured at  $700\text{nm}$ .

### **6.2.10 *In Vivo* Drug Release**

Platinum iridium wires electrodes were created by cutting  $8\text{ cm}$  sections of  $70\mu\text{m}$  diameter Pt/Ir (90/10) wire and de-insulating  $1\text{mm}$  at the tip. The tip was cut at a  $30^\circ$  angle to sharpen. The opposite end was connected to a gold pin via silver epoxy to facilitated interfacing with electronic equipment. Carbon fiber electrodes were constructed by pulling a  $7\mu\text{m}$  carbon fiber through a glass capillary which was then filled with mercury to form the electrical connection. Drug loading was

performed as described above, adjusting current to match the exposed surface area. Polymer was deposited at a density of  $100 \text{ mC cm}^{-2}$ .

Wildtype C57-BL6 mice were used to observe fluorescein release, while Thy1-GCaMP mice were used to visualize neural activity during DNQX release. Animals were anesthetized under 2% isoflurane in  $\text{O}_2$ . A cranial window was created above the region of interest, following which the animal was placed under the two-photon microscope for imaging and insertion. Insertion and imaging were performed on awake animals to maximize the GCaMP activity. The electrode was inserted at  $30^\circ$  from parallel to the table, with care taken to minimize bleeding. Release was performed in 3 steps. First, a 2-minute baseline was recorded. This was followed by 10 drug release stimulations with a 30 second delay between subsequent stimulations. *In vivo* drug release was performed by cyclic voltammetry scans from 0.8V to -0.6V vs a Ag/AgCl reference electrode. Following 10 cycles of stimulation, a final 2-minute baseline recording was performed.

Calculations of fluorescence are made by first masking the electrode itself. Following which, the inter-pulse fluorescence was determined by averaging the fluorescent intensity during the reducing voltage, and comparing this to the fluorescent intensity during the prior oxidative voltage ( $V > -0.2$ ).

### **6.2.11 Statistics**

Unless otherwise stated, statistical significance was measured via one-way ANOVA with Tukey's post hoc. Significance of Figure 36B and Figure 37I were determined via two-way ANOVA. Significance of Figure 42E,F was determined via two-tailed paired T-Test. Statistical analysis was performed in GraphPad Prism 7.03.

## 6.2.12 Acknowledgements and Conflicts of Interests

The works presented here are in part due to the assistance of others. We would like to acknowledge Dr. Alberto Vasquez and his lab members for their assistance in two-photon imaging as well as use of the equipment. This work was funded by the NIH NINDS R01NS062019 and R01NS089688. We the authors do not have any conflicts of interest in this work to declare.

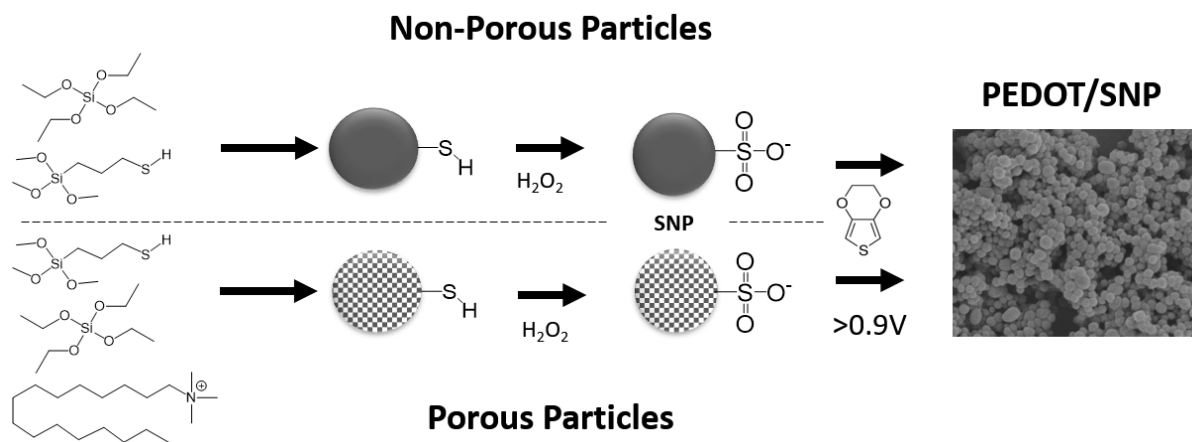


Figure 35 Particle synthesis and polymerization of PEDOT/SNP.

Thiol modified silica nanoparticles are synthesized from tetraethyl orthosilicate and mercaptopropyl trimethoxysilane, with the inclusion of hexadecyl trimethylammonium bromide producing a porous particle structure. The thiol groups are then oxidized to sulfonate under hydrogen peroxide, allowing the particle to serve as a conducting polymer dopant. The particles are then mixed with 3,4-ethylenedioxythiophene (EDOT), and polymerized to form a conducting-polymer/nanoparticle composite for stimulation, recording, and drug delivery.

## 6.3 Results and Discussions

### 6.3.1 Synthesis of Nanoparticle Dopants

In order to create a nanoparticle capable of doping a conductive polymer film, sulfonate modified silica nanoparticles (SNPs) were developed (Figure 35). Silica was chosen due to its known biocompatibility, and the sulfonate functionalization gives silica a permanent negative charge required to balance the positive charge of the oxidized PEDOT film. Two distinct SNPs have been created and examined for their unique properties, non-porous SNP and mesoporous SNP, which are both synthesized from their respective thiol-modified precursors. Non-porous thiol modified nanoparticles were synthesized from TEOS and MTS under basic conditions. Mesoporous particles were synthesized in the same manner, with the inclusion of CTAB as the surfactant template. After washing, Ellman's reagent was used to verify the presence of thiols, resulting in a distinct color change of the solution from clear to straw yellow. Thiolated nanoparticles (TNP) were subsequently oxidized to SNP under hydrogen peroxide and sulfuric acid. During oxidation, the TNP first aggregate together due to the formation of di-sulfide bonds, but subsequently separate into a homogenous suspension after further oxidation. The resulting SNP did not have an effect when exposed to Ellman's reagent, indicating the absence of the thiol groups and suggesting oxidation to sulfonate. The diameter (Figure 36A) and zeta potential (Figure 36B) of the non-porous and mesoporous particles were measured with DLS. SNP possessed significantly greater negative zeta potential than their precursor thiolated particles, further indicating the conversion of the thiol to sulfonate. Similarly, the SNP were more negative than the bare silica, indicating that the SNP possess a permanent negatively charged functional group absent on the bare silica. Non-porous particles had a smaller diameter and more negative zeta

potential than the equivalent porous particles. The discrepancy in the zeta potential may be attributed to the difference in the surface density of the functional groups. While the sulfonate groups are expected to be evenly distributed along the surface of both particles, mesoporous particles have a large area removed due to the pores. While the surface area of the porous particles is likely magnitudes larger than the non-porous counterparts, the outer surface charge density is lower, resulting in the seemingly diminished zeta potential. Similar findings and conclusions were drawn by Slowing et al when examining mesoporous and amorphous silica.[299] These particles are further examined under TEM (Figure 36C,D). The non-porous particles display a smooth surface as expected, while the surfactant template left radial pores in the mesoporous particles. These images show a distinct pore structure similar to what was previously reported.[167]

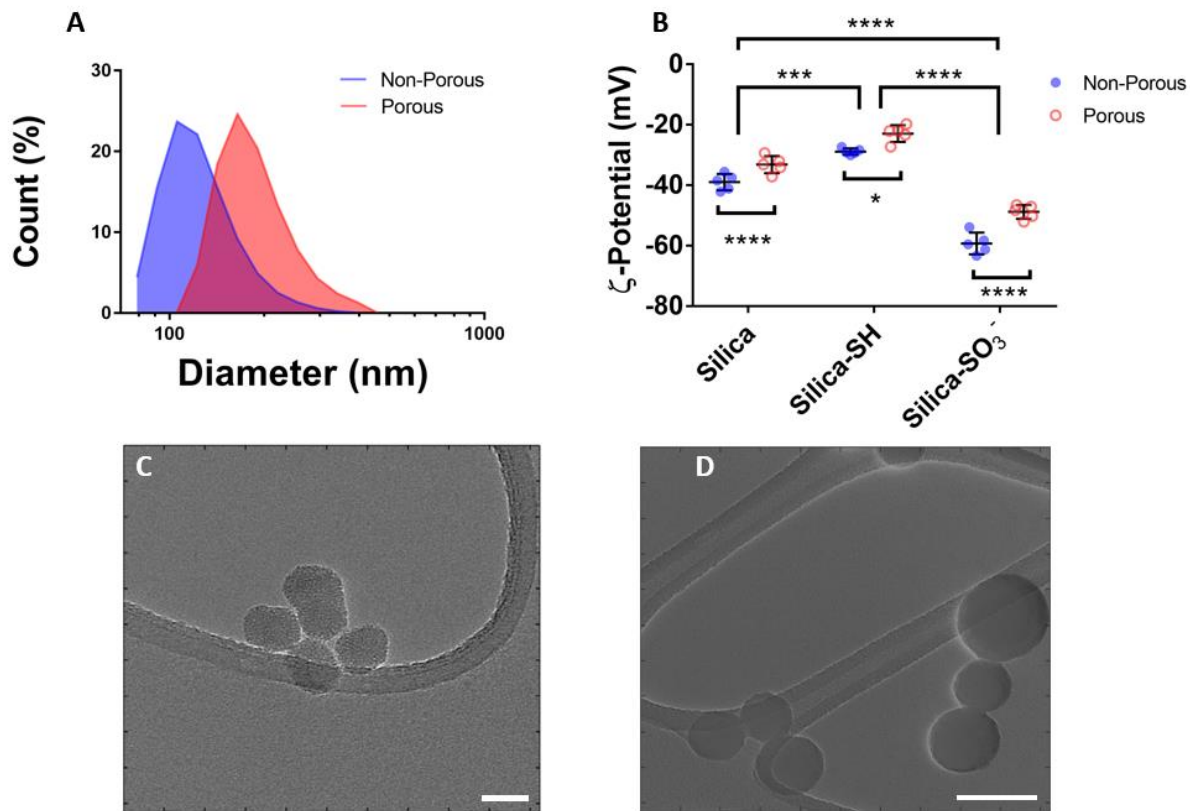


Figure 36. Particle Characterization.

Non-porous and mesoporous nanoparticles were synthesized and characterized by DLS and TEM. The diameter of the mesoporous particles is larger than the non-porous particles, while the zeta potential of the mesoporous particles is significantly lower in magnitude. Mesoporous particles have radial porous observable through TEM, while nonporous particles appear smooth. \* $p < 0.05$  \*\*\* $p < 0.001$  \*\*\*\* $p < 0.0001$ .

### 6.3.2 Electropolymerization and Electrochemical Properties of the PEDOT/SNP

The synthesized SNP were used as a dopant for PEDOT films via electropolymerization. SNPs were suspended in EDOT and electropolymerization was carried out under constant current density of  $320\mu\text{A cm}^{-2}$ . The resulting film was distinctly blue in color, yet notably lighter than films polymerized with common dopants polystyrene-sulfonate or functionalized carbon nanotubes (CNT), most likely due to the translucence of the SNP. Examining the structure of the coating under SEM reveals a unique morphology. The particles appear to stack on each other forming a forest-like effect, with individual particles imparting their own geometry to the film (Figure 37B). Similar observations have been made with very large dopants such as graphene oxide[71] or CNT[182].

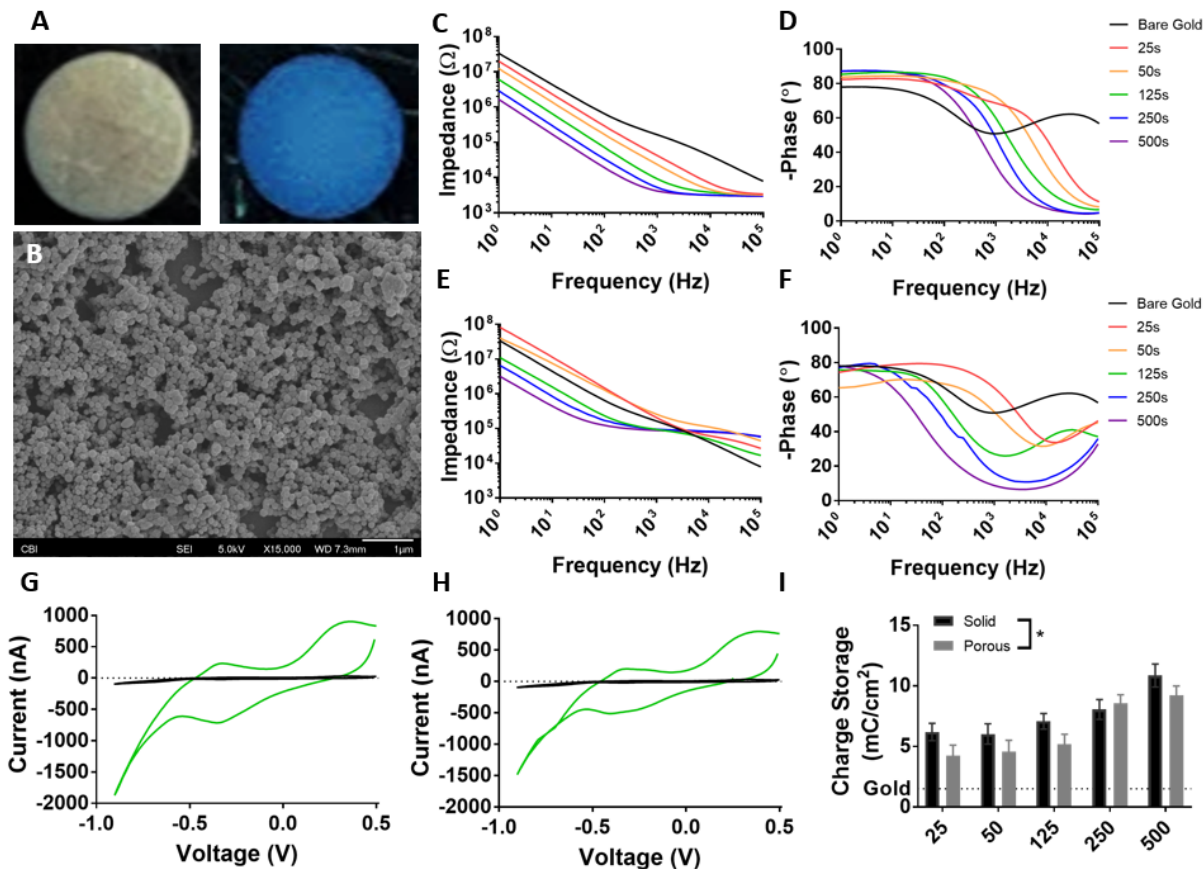


Figure 37. PEDOT/SNP Characterization

(A) An image of the PEDOT/SNP polymer before and after polymerizing on a 2mm gold electrode. (B) SEM was taken of the PEDOT/SNP surface, displaying a forest-like morphology. The electrochemical properties of PEDOT/SNP polymerized on 50 $\mu$ m diameter gold electrodes for solid (C,D) and porous (E,F) SNP with increasing polymer deposition times. (C) and (E) Impedance and phase (D) and (F) of the electrodes was measured in PBS from 1 to 100,000Hz, with a characteristic decrease in impedance at lower frequencies and leftward shift of phase with increasing polymerization time. (G) and (H) Cyclic voltammetry sweeps of 125s coated electrodes (green) and bare gold (black) taken at 1 V s<sup>-1</sup> to show redox peaks. (I) Charge storage capacity of the films from both solid and porous SNP calculated from 0.1V s<sup>-1</sup> CV plots. Solid particles produced significantly higher overall charge storage among all groups, but no significant differences were present within individual groups when comparing solid vs porous particles with the same polymer deposition time. \*p<0.05

The electrochemical properties of PEDOT/SNP Films were examined utilizing a variety of methods. Directly in line with previous studies concerning conduction polymers, increasing polymerization times of PEDOT/SNP led to decreasing impedance magnitudes (Figure 37C,E) and leftward-shifts in the cut-off frequency of the EIS (Figure 37D,F). The cyclic voltammetry plots demonstrated the characteristic shapes of PEDOT coated electrodes, namely a reduction potential of approximately -0.3V vs Ag/AgCl (Figure 37G,H). Of note, an interesting difference can be observed between PEDOT/SNP films with solid or porous particles in terms of their respective capacitive and resistive nature. Charge storage capacity (CSC) was derived from the area of the CV plot, which indicates both redox-activity and capacitance of the film. As expected, CSC of the coatings increases with increasing polymerization time as the film grows thicker. Both particles exhibit an increase in CSC with thicker films, although the CSC is significantly higher for solid particles. While both films display dramatically reduced impedances at low frequencies, porous particle films appear to have a higher resistive nature, increasing impedance at higher frequencies above the bare gold electrode. The changes in impedance were likely caused by the decrease in surface charge of the porous particles relative to the solid. However, the porous particle film maintained a high CSC, being only slightly lower than the solid particles and significantly larger than bare gold electrodes ( $1.5\text{mC cm}^{-2}$ ).

Charge injection limit is an important property for electrical stimulation materials. It is defined as the amount of charge that can be passed from the electrode into solution/tissue without causing irreversible electrochemical reactions. Here, charge injection limit was determined by increasing the amplitude of the stimulation current pulses and measuring the voltage transients. Electrode potential was determined by subtracting the access voltage from the peak of the voltage transient, and the current that result in electrode potential of -0.6V was used to deduce the charge

injection limit (charge injected per pulse per surface area[300]). Due to their superior electrochemical properties, solid SNP films were used for CIL measurements. A sample current pulse and resulting voltage transient for bare gold and gold coated with PEDOT/SNP are shown (Figure 38A). Increasing the thickness and amount of deposited polymer results in a near linear increase in the CIL (Figure 38B). CIL of films polymerized for 800s (a polymer deposition density of  $254 \text{ mc cm}^{-2}$ ) have CILs ( $4.8 \text{ mc cm}^{-2}$ ) in the realm of other advanced coatings such as activated iridium oxide ( $3.9 \text{ mC cm}^{-2}$ ,  $0.4 \text{ ms}$  pulse),[300] hydrophilic CNT ( $1.6 \text{ mC cm}^{-2}$ ,  $1 \text{ ms}$  pulse),[301] and PEDOT/CNT ( $2.5 \text{ mC cm}^{-2}$ ,  $1 \text{ ms}$  pulse).[182] hydrophilic CNT ( $1.6 \text{ mC cm}^{-2}$ ,  $1 \text{ ms}$  pulse),[301] and PEDOT/CNT ( $2.5 \text{ mC cm}^{-2}$ ,  $1 \text{ ms}$  pulse).[182]

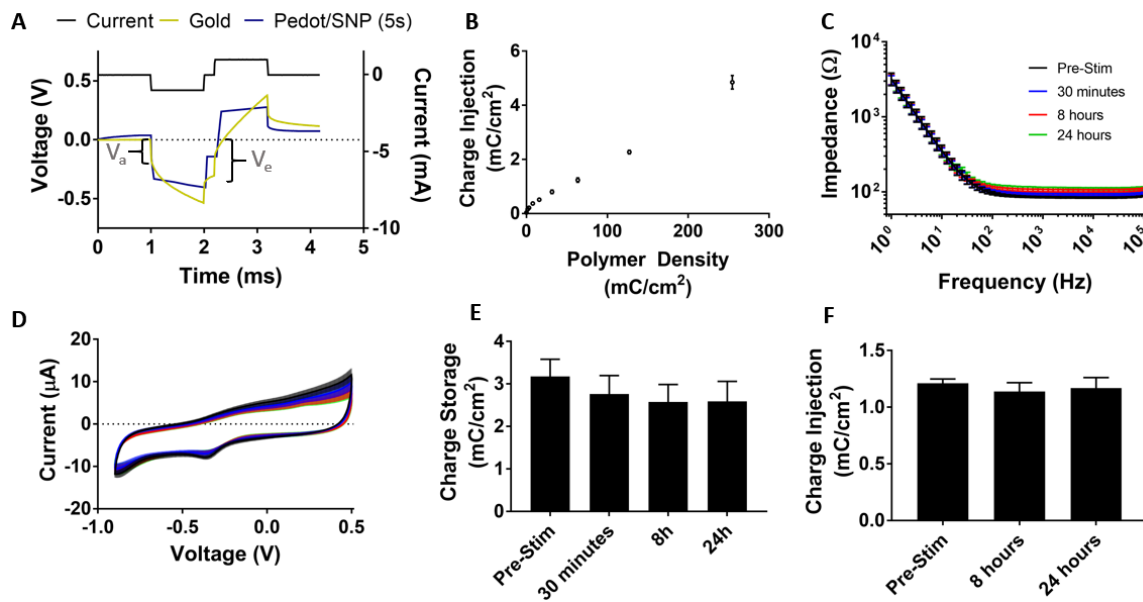


**Figure 38 Charge injection and stimulation stability.**

(A) Sample waveform used for charge injection and corresponding voltage transients for gold and PEDOT/SNP. Labeled is the access voltage ( $V_a$ ) and electrode voltage ( $V_e$ ) for the bare gold electrode. (B) Charge injection calculated for multiple polymer depositions on a 2mm diameter gold electrode. (C-E) Impedance, cyclic voltammograms, and charge storage capacity measurements taken before chronic stimulation, at 30 minutes, 8 hours, and 24 hours on a 2mm diameter gold electrode, respectively. (F) Charge injection limits measured at 0, 8, and 24 hours of chronic stimulation.

To test the stability of the coating under stimulation, the coating was subjected to a pulsatile current waveform at 85% of the calculated CIL at 50Hz for 24 hours ( $4.32 \times 10^6$  stimulations). We expect that any changes in electrical properties of the film would be due to either over-oxidation of the PEDOT, leaching of the dopant, or mechanical cracking and delamination of the coating. After stimulation, we did not observe significant changes in the impedance (Figure 38C), CV scan (Figure 38D), charge storage capacity (Figure 38E), or the charge injection limit (Figure 38F), demonstrating the electrochemical stability of the coating. A similar observation could be made when performing multiple subsequent CV scans on the coating. Following the first scans, the coating has no noticeable change in the CV traces of the 50<sup>th</sup>, 100<sup>th</sup>, or 300<sup>th</sup> scan. Examining the coating before and after subsequent CV scans shows minimal changes in the morphology of the coating without any visible cracking or delamination. This stability is at least in part due to the size of the dopant particles. Small molecule dopants have a tendency to leach from the conducting polymer matrix,[302] reliably enough to become the basis of conducting polymer based drug release. Large dopants such as SNP are effectively entrapped by the PEDOT network, incapable of diffusing out into solution even when PEDOT undergoes reduction. Additionally, the van der Waals interaction between NPs and substrate may help to improve adhesion while the interaction between NPs could also improve the cohesiveness of the coating. Similar observations have been made for other large dopants, such as CNT which improve coating adhesion and stability.[182] Taking the sizable charge injection limits together with the stability of the coating, we show that the PEDOT/SNP polymer is a viable option for chronic stimulation applications.

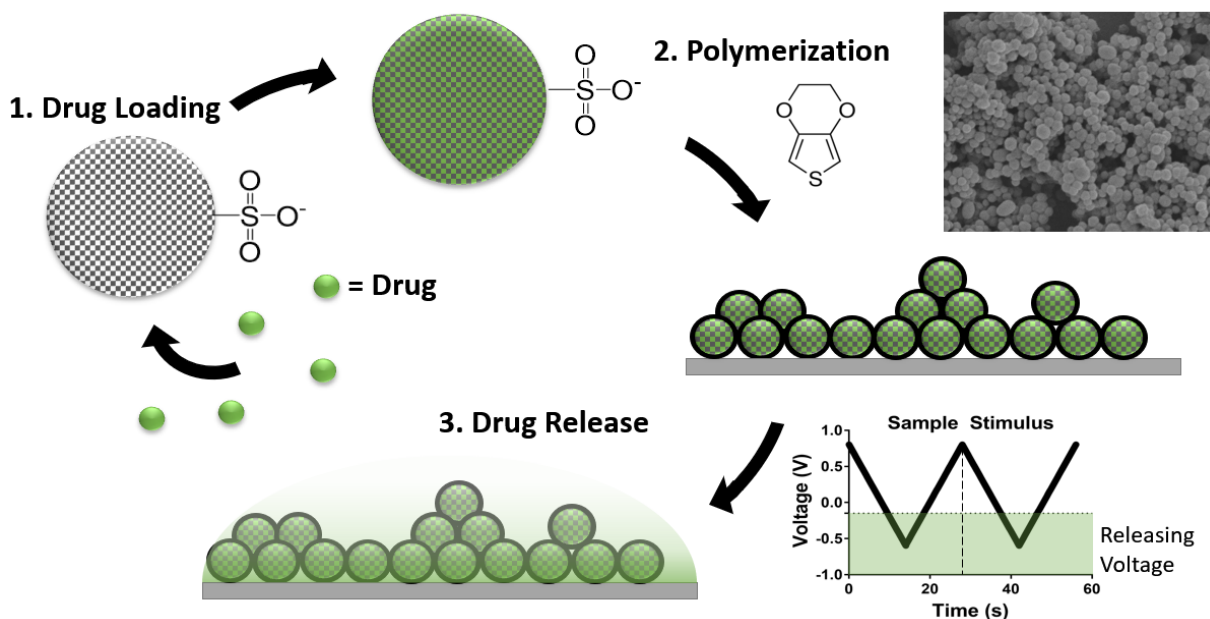


Figure 39 Drug loading into SNP and Drug Release.

Drugs are loaded into the porous nanoparticles via sonication. Loaded sulfonate nanoparticles are collected from solution by centrifuge then resuspended in an aqueous solution of EDOT. PEDOT/SNP films are polymerized under constant current, producing a film of polymer gated silica nanoparticles. Drug release is performed by triangular voltage pulses (cyclic voltammetry). Application of a sufficient reducing voltage results in drug release from the drug loaded PEDOT/SNP film.

Further discussed in the supplemental, a cytotoxicity assessment was performed on the PEDOT/SNP composite. To confirm that the novel PEDOT/SNP composite is biocompatible, we cultured microglia cells directly on PEDOT/SNP films using the commonly used PEDOT/Polystyrene Sulfonate (PEDOT/PSS) for comparison. No differences in metabolic activity and viability were observed by either XTT or Live/Dead assay.

### **6.3.3 Electrically Controlled Drug Release**

Drug loading and release from conducting polymers with electrical control offers a precise method for pharmacological delivery directly to the site of implantation on demand. Mesoporous SNP are employed for drug delivery due to their exceptionally high loading volume (Scheme 2). Rhodamine and fluorescein are used as model drugs for quantifying drug release profile. Fluorescein has a native negative charge while rhodamine-b is positively charged, and the combination of rhodamine and fluorescein allow for a better understanding of how oppositely charged compounds can be released from PEDOT/SNP films. An immediate observation made was the ease of polymerization when the dye was loaded into SNPs prior to polymerization vs without SNPs, with voltages being substantially lower for polymerization of drug loaded SNP. After polymerization, electrodes coated with the dye-loaded composite were examined under a fluorescent microscope to observe the release in PBS in real time. A cyclic voltage sweep from 0.8 to -0.6 was used to trigger drug release from the coatings. We observed a halo of fluorescence surrounding the electrode upon stimulation, which dissipates within seconds of the end of stimulation. The quantified fluorescent intensity of the image was significantly higher during release than after for both rhodamine and fluorescein indicating that both compounds were able to be loaded and released from the PEDOT/SNP film.

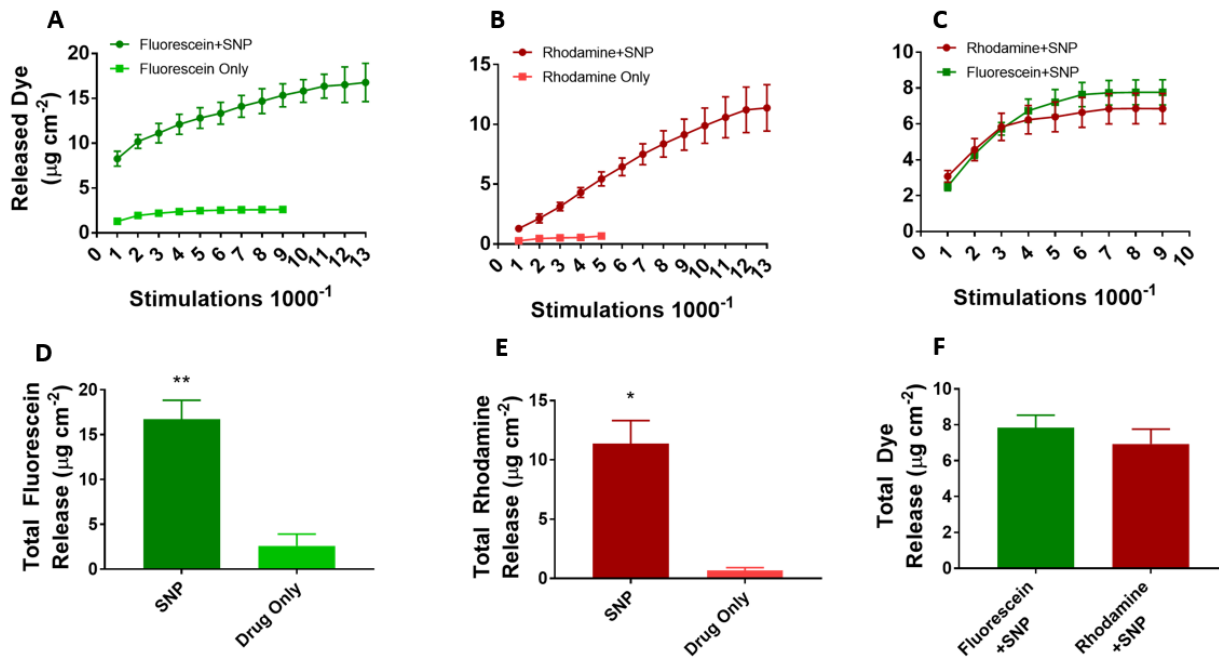


Figure 40. Dye Release.

Dyes were loaded into SNP and released via cyclic voltammetry from a 2mm gold electrode. Fluorescein (A) and rhodamine (B) loaded PEDOT/SNP films were compared to their respective drug only analog. (C) Both Rhodamine and Fluorescein were loaded into the same particles for stimulated co-release of the two oppositely charged compounds under the same conditions as (A) and (B). The total drug loaded was determined by repetitive stimulation until the film was exhausted and solution produced no detectable dye. D-F are the total drug loaded into the films of A-C, respectively. \* $p < 0.05$  \*\* $p < 0.01$ .

We further quantified the amount of release over number of stimuli from PEDOT/SNP composite and compared the performance to a control group of PEDOT loaded with the dye directly without the mesoporous SNP. Control and SNP dopant groups were polymerized to the same charge density. For both fluorescein and rhodamine, we could observe a substantial increase in dye release over 9,000 and 5,000 stimulations relative to their respective control samples (Figure 40A,B), and the SNP doped polymers continued to release for up to 13,000 stimulations. Overall drug loading was increased overall for both fluorescein (6.4x) and rhodamine (16.8x) when SNP were used as a reservoir (Figure 40D,E). This result indicates that SNP doping not only improve drug loading and release capacity, but also broaden the drug choice as majority of the previous conducting polymer drug release work focused on negatively charged drugs.

We account for the changes in drug loading and release by examining the published mechanisms of conducting polymer-based drug delivery[183]. In traditional conducting polymer-based drug deliver, negatively charged compounds are required to balance the positive charge formed by polymerization, and therefore anionic drugs can be loaded into the matrix during polymerization. Positively charged compounds may also be loaded, instead relying on entrapment or interactions with other dopants. Controlled release from these films by alternating oxidative and reductive potentials proceeds through two mechanisms. First, reducing the film eliminates the charge-based interaction, allowing the trapped anionic compounds to exit of the conducting polymer matrix. Second, reduction and re-oxidation changes are accompanied with movement of ions and water in and out of the film, resulting in swelling/shrinking cycles of the polymer[183], which further increases the diffusion of the drug out of the polymer. We speculate that the fluorescein release from the PEDOT/SNP coating occurs first when the film is reduced and the fluorescein exits the particle into the film and solution through diffusion and repulsion by the

negative potential at the electrode. Rhodamine has a stronger electrostatic interaction with the negatively charged particle, slowing the release per stimulus. When the film is reduced, the volume change of the polymer and water influx encourages rhodamine to enter the neutral matrix, where it is then expelled during the subsequent oxidation as the film and dye repel each other.

Traditionally, each electrochemically controlled drug release experiment has been limited to one compound. This may be problematic if a drug therapy requires the use of 2 oppositely charged compounds. For example, co-administration of negatively charged acetylsalicylic acid (Aspirin), and the salts of ticlopidine[303, 304] and clopidogrel[304] have shown to reduce the occurrence of cardiac events following stenting. By loading a combination of fluorescein and rhodamine into SNP prior to polymerization, we could effectively load the film with 2 oppositely charged compounds (Figure 40C,F). Following CV stimulation, we observed a co-release of both compounds, albeit at slightly lower individual release of the compounds per stimulation, in addition to modified release profiles due to interactions between the two compounds. We demonstrated that through the use of SNP, we could load two oppositely charged compounds into one film for simultaneous release. With further optimization of the stimulation parameters for each compound, it may be possible to achieve selective release of co-loaded compounds.

#### **6.3.4 Bioactivity of the Released Drug**

Electrochemical methods of drug release may alter the activity of a compound due to the applied potentials, and it is therefore important to verify that the loading and release process doesn't compromise the drug's bioactivity. In order to assess the biological activity of released components, we loaded and released two bioactive compounds: Doxorubicin (Dox) and Melatonin. For Dox, a potent chemotherapeutic, release was performed for 0 (passive diffusion for 24hours),

20, or 200 cycles into serum free DMEM. A small amount of diffusion release was observed from Dox loaded electrodes, as measured by absorbance at 280 nm. Electrical stimulation triggered significantly more release, with higher number of stimuli releasing more drug (Figure 41A, 20 stimulations release  $1.44\mu\text{g cm}^{-2}$  and 200 stimulations release  $7.4\mu\text{g cm}^{-2}$ ). Released Dox was introduced to cultured 3T3 mouse fibroblast cells (Figure 41B) and the toxicity was compared to freshly prepared Dox solution at the same concentration. After a 3-day incubation period, the viability of the 3T3 cells was evaluated with the XTT assay. No significant difference was observed between cells grown in standard culture media and the diffusion control group. Although we detected a minute amount of Dox in the diffusion control, this quantity is either below the toxic level or a misattributed EDOT monomer which may not have fully reacted during polymerization. Released Dox from 20 and 200 stimulations significantly reduced the viability of cells from control, with the 200 stimulated release leading to higher toxicity compared to 20 stimulations. There was no difference in the effect of released Dox and the concentration-matched stock Dox, demonstrating the complete retainment of the bioactivity after electrochemical loading and release. Through this examination, we have demonstrated that not only does electrochemical release retain the viability of the drug, the drug quantity and effects can be tailored by the release parameters (stimulations) to impart predictable and scalable effects.

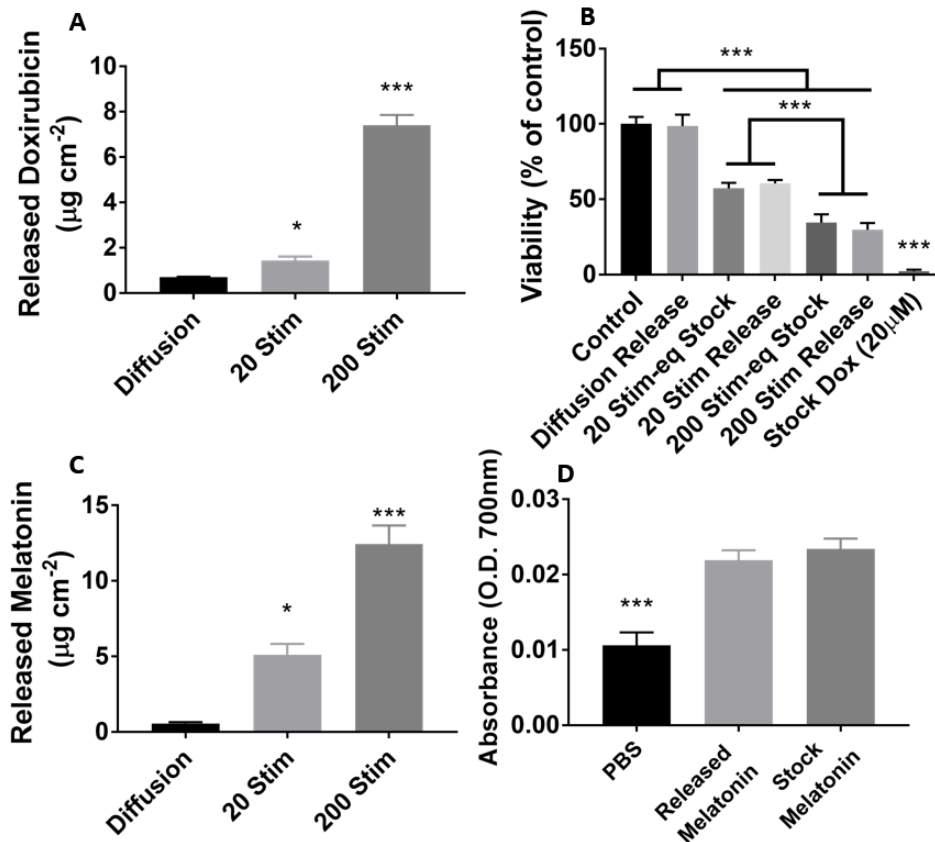


Figure 41. *in vitro* activity of released compounds.

(A) Dox was successfully released from the PEDOT/SNP film. (B) Released Dox was delivered to 3T3 fibroblasts to examine the activity vs a concentration matched stock solution, an untreated negative control condition, or a high-Dox positive control. A high concentration (20µM) Dox sample was used to ensure the activity of the drug and that there was no impact of Dox on the XTT assay. (C) Melatonin was successfully loaded and released from the PEDOT/SNP film. (D) Released melatonin was examined to determine if antioxidant activity remained after release by reducing  $K_3[Fe(III)(CN)_6]$ . This reduction results in a measurable color change. \* $p < 0.05$  \*\*\* $p < 0.001$ .

Melatonin is an antioxidant and signaling molecule shown to minimize inflammation after injury. Recent work has demonstrated that melatonin is capable of preserving neuronal health around implanted neural electrodes and maintain high recording quality over time when systemically administered daily[121]. This finding highly motivates the development of local delivery of melatonin from neural electrodes. However, melatonin presents additional difficulties for electrochemically driven drug delivery in that the compound is not electrochemically stable. With an oxidation potential at 0.65V vs Ag/AgCl[305], melatonin is irreversibly deactivated by the oxidative potential required to polymerize PEDOT, which is generally larger than 0.8V. Here, we present a method of shielding the melatonin from the highly oxidative electropolymerization by first loading the melatonin into porous SNPs. Melatonin loading was performed by sonicating the SNP in an ethanol solution of melatonin, and after drug loading the particles were thoroughly dried under vacuum to eliminate any remaining ethanol. Melatonin's solubility in water is substantially lower than the solubility in ethanol, this allowed for a high degree of loading into the SNP with minimal leakage during the short period of polymerization. The antioxidant capacity of the released melatonin was evaluated by  $K_3[Fe(CN)_6]$  reduction assay.[306] This reduction produced a dramatic color change, which was recorded at 700nm (Figure 41D). We demonstrate here that released melatonin and stock melatonin were both capable of producing a significant change in the absorbance of the solution at 700nm, and demonstrate that the released melatonin had maintained its antioxidant capacity. The retention of melatonin's antioxidant abilities might be attributed to the non-conductive nature of the silica nanoparticles, minimizing electrochemically driven reactions to the loaded drug.

### 6.3.5 In Vivo Proof of Concept Drug Release Demonstration

Different types of microelectrodes, either a platinum iridium microwire or carbon fiber, were coated with PEDOT/SNP for *in vivo* release testing. A craniotomy was performed on a wild-type mouse which was then placed under a two-photon microscope for imaging. A bone screw counter and Ag/AgCl reference were placed in contact with the brain. A fluorescein loaded PEDOT/SNP coated Pt/Ir electrodes was inserted and used to visualize drug release in brain tissue in real time (Figure 42A). CV was performed to initiate the release of the dye, and the peak change in fluorescence was calculated (Figure 42B). After release, the dye dissipated into the surrounding tissues within several seconds. The release and dispersal of the fluorescein dye demonstrates controllable release and the diffusion profile of released compounds *in vivo*.

Next, we aim to modulate cellular activity by release of the glutamate AMPA/Kainate receptor antagonist 6,7-dinitroquinoxaline-2,3-dione (DNQX). DNQX is a small, negatively charged compound that blocks glutamate transmission. We have previously observed that DNQX may be loaded and electrically released from PEDOT/CNT films *in vivo* and produce a transient (<6 second) inhibition of sensory evoked neural activity recorded in barrel cortex of rats.[135] In this study, DNQX release from PEDOT/SNP was assessed using a GCaMP mouse model. The GCaMP fluorescence is tied directly to intracellular calcium activity, such that when neurons fire action potentials, the calcium influx cause GCaMP to produce a bright green fluorescence.

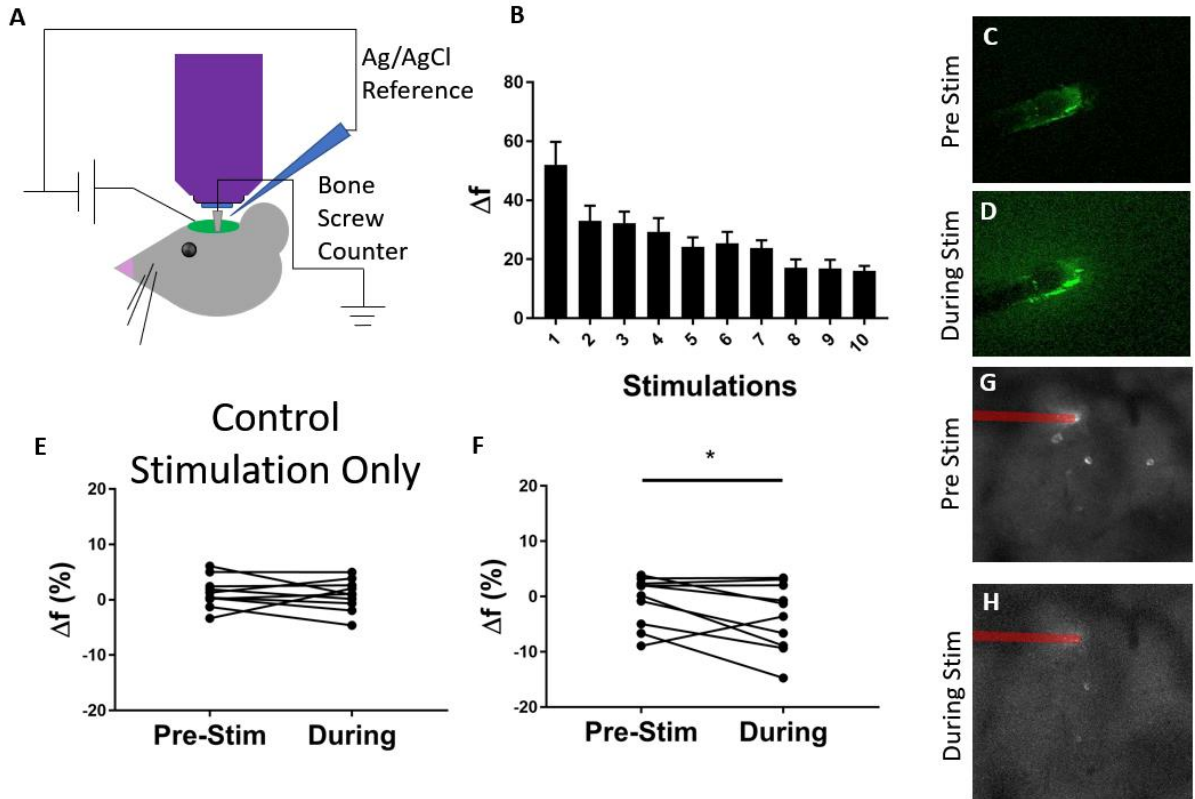


Figure 42. *In vivo* release from PEDOT/SNP polymer.

(A) Experimental set-up. A cranial window was created in the skull of the animal and a bone screw inserted to serve as a counter. The animal was then placed under the two-photon microscope for imaging. A Ag/AgCl reference electrode was placed in contact with the brain, and the working electrode inserted. A fluorescein loaded Pt/Ir electrode was used to visualize the *in vivo* drug release. CV stimulation was used to eject fluorescein into the brain tissue of a wild-type mouse. (B) fluorescence was quantified for each pulse compared to baseline. (C) and (D) are representative images of the fluorescence before and during stimulation of the fluorescein loaded electrode, respectively. An unloaded or DNQX loaded carbon fiber electrode was inserted into a Thy1-GCaMP animal to visualize the effects of drug delivery on neural activity in the brain. (E) quantification of GCaMP activity before and during stimulation through an unloaded electrode. (F) Quantification of GCaMP activity before and during activity of a DNQX loaded electrode. (G) and (H), pixel standard deviations were taken for pre and during stimulation frames for a DNQX loaded electrode, respectively. Note the lack of cellular firing during stimulation. \* $p < 0.05$

In order to minimize tissue damage during insertion, a carbon fiber electrode (D=7 mm) was used for DNQX release. DNQX loaded PEDOT/SNP was polymerized on a carbon fiber electrode and implanted in the mouse brain, proximal to the midline and motor cortex, and CV stimulation was performed to release DNQX from the polymer. We then compared the fluorescence intensity of the tissues prior to and during DNQX release (Figure 42F), and observed a significant decrease in the fluorescence intensity when the electrode was receiving a reducing potential. A control experiment was performed by inserting a PEDOT/SNP electrode without DNQX loading. No change in fluorescent activity was observed in the absence of DNQX (Figure 42E). Qualitatively, a difference in neural firing was noted by examining the standard deviation of Z-projection prior to and during stimulation. This projection examines how pixels deviate over time, displaying pixels with higher deviations as brighter. Cell firing events produce greater deviations in pixel intensity, and the compression allows for a single frame representation of the GCaMP activity over the course of the imaging. We observed a higher number of active cells during the pre-stimulation period (Figure 42G) than during the DNQX release (Figure 42H), with only small amounts or residual GCaMP activity present during release. From these experiments, we can conclude that PEDOT/SNP was able to release DNQX upon electrical stimulation and the released DNQX was capable of modulating neural activity localized to the electrode, demonstrating the feasibility and potential of the PEDOT/SNP based drug delivery platform.

## 6.4 Conclusions

Conducting polymers are at the forefront of biomaterials research with applications in biosensors, bioelectronics, tissue engineering scaffolds and drug delivery systems. Through the

use of nanoparticle-based dopants, we have demonstrated the synthesis of a novel class of conducting polymer composites. The material properties can be fine-tuned by adjusting the nanoparticle dopants. Solid nanoparticle doped PEDOT possesses impressive electrochemical characteristics, including low impedance, high charge storage capacity and charge injection limit among the best reported in advanced electrode coatings. This polymer demonstrates its potential as a stimulating electrode coating by maintaining stability for over 4.3 million stimulations. By exchanging the solid nanoparticles for mesoporous particles, we can effectively incorporate a reservoir for drug delivery. Unlike many other electrochemical drug delivery platforms, we have demonstrated that multiple oppositely charge compounds can be loaded into a single film, and that electroactive compounds can be electrochemically loaded and released while maintaining their bioactivity *in vitro* and *in vivo*. Taken together, the nanoparticle dopant approach offers endless new opportunities for designing new conducting polymers composite to suite the need of various biomedical applications.

## **7.0 Controlled Delivery of Vasodilators from PEDOT/SNP**

Vascular damage and decreases in tissue perfusion are expected to be major factors contributing to the loss of neurons around implanted electrodes. However, there are few methods of controlling and modulating the vascular dynamics in the tissues surrounding these implants. We have utilized a mesoporous silica nanoparticle loaded with the vasodilator sodium nitroprusside with drug release controlled via the conducting polymer poly(ethylenedioxythiophene) to controllably dilate the vasculature around a carbon fiber electrode implanted into the mouse cortex. The vascular dynamics were monitored in real time with two photon microscopy, while changes in vessel diameters and blood flow were examined before, during, and after the release of the vasodilator into the tissues. We observed significant changes in vessel diameters only when the drug was present, while also evaluating the effects of the drug on vessels of difference sizes.

## 7.1 Chapter Introduction

Electrode implantation is inherently traumatic to the sensitive central nervous system (CNS) tissues. The electrode inevitably severs blood vessels, lowering perfusion of blood in the tissues[307], interfering with the delivery of oxygen and nutrients to CNS cells and leading to a reduction in blood oxygen level dependent signaling[308]. Following implantation, remodeling of vascular networks occurs to mitigate the loss of tissue perfusion[51, 94, 309], but this process takes days to weeks and leaves the tissues around the electrode in an oxygen deprived environment. Anoxic environments directly affect neurons, changing their resting membrane potential[310, 311] and leading to excitotoxicity[312-314]. Following neural electrode implantation, the lack of sufficient tissue perfusion may be a principal component of acute cell death or neuronal silencing. However, controlling the vascular dynamics following electrode insertion has not been well studied.

Much like the rest of the body, the CNS vasculature responds to compounds such as nitroglycerin[315-317] and sodium nitroprusside[318, 319], causing rapid vessel dilation. However, direct investigation of the effects of local modulation of blood flow on the CNS tissues is difficult to achieve. This is largely due to the necessity of spatially and temporally constrained drug delivery. Fortunately, drug delivery methods have been heavily investigated in the field of neural engineering which may be employed to control vascular dynamics while recording neural activity. These controlled drug delivery systems can employ numerous techniques, including microfluidics[142-144, 147, 149, 197], degradable polymers[120, 156, 320], nanoparticles and liposomes,[298, 321-324] and conducting polymers.[53, 191, 295, 296, 325] Conducting polymers can be electropolymerized on neural electrode sites to reduce site impedance and increase neural

recording yield.[189, 199] Further, the electroactivity of the conducting polymer created the basis for electrochemically controlled drug loading and release[118, 130, 135, 183, 193, 295, 325].

The first generation of conducting polymer based electrochemical drug delivery system directly load drug molecules into the film during electro-polymerization and release the drug by electrochemically reducing the polymer and dissociating the drug. One limitation of such approach is its in-compatibility with many compounds. Compounds that are positively charged are poorly integrated into the film, while electroactive compounds such as antioxidants can be destroyed during the electro-polymerization of the polymer. Another limitation is drug loading capacity. To address these limitations, we synthesized a mesoporous sulfonate modified silica nanoparticle that serves both as a dopant for the conducting polymer and a drug reservoir that can not load more drug but also shield the compounds from the oxidative polymerization potentials. This methods has demonstrated success in allowing for the enhanced loading and release of negatively charged, positively charges, and electrochemically active compounds.[53, 326]

In this work we have adapted the silica nanoparticle doped conducting polymer polyethylenedioxythiophene (PEDOT/SNP) to locally deliver the vasodilator sodium nitroprusside (NaNP). Cyclic voltammetry was used to reduce and oxidize the polymer, driving the release of NaNP, which was characterized with mass spectrometry. We then implanted PEDOT/SNP/NaNP coated carbon fiber electrodes into the cortical tissue and utilized two-photon microscopy to monitor the dilation of vessels following the drug release in ketamine anesthetized mice.

## **7.2 Methods**

### **7.2.1 Materials and Reagents**

All reagents were purchased from Sigma Aldrich unless otherwise specified. Double deionized water was used for all experiments.

### **7.2.2 Nanoparticle Synthesis**

Mesoporous sulfonate modified silica nanoparticles (SNP) were fabricated as previously described.[53] In brief, mesoporous thiol modified silica nanoparticles were fabricated from a base catalyzed condensation reaction between tetraethyl orthosilicate and mercaptopropyl trimethoxysilane with cetyltrimethylammonium bromide as the surfactant template. Particles were collected by centrifugation, the surfactant template removed, and then the particles were oxidized to sulfonate modified mesoporous silica nanoparticles (SNP) with 20% H<sub>2</sub>O<sub>2</sub>. Following oxidation and washing of the particles, the SNP were stored dry at 4°C until used.

### **7.2.3 Drug loading and Electropolymerization**

Drug loading was performed by dissolving 200mg NaNP into 1mL water, followed by the addition of 10mg SNP. The suspension was sonicated for 20 minutes to encourage the drug to enter the small pores, and the nanoparticles were collected by centrifuge. The supernatant was removed, and the particles dried under N<sub>2</sub> stream.

Electrochemical experiments were performed with an Autolab PGSTAT128N potentiostat (Metrohm Autolab B.V.) Electropolymerization was performed in a 0.01M solution of ethylenedioxythiophene (EDOT\_ in water. 3ml of EDOT solution was added to a small vial followed by the 10mg of drug loaded SNP. The solution was gently triturated prior to polymerization. The polymerization took place under current control with a 3-electrode set up with an Ag/AgCl reference and Pt counter electrode. Polymerization was performed at a current density of 1.5mA cm<sup>-2</sup> for 1000s.

#### **7.2.4 Drug Release and Detection**

Mass spectrometry was used to measure the release of NaNP from the drug loaded PEDOT/SNP films from 3mm diameter glassy carbon electrodes. Release was performed in 1ml of 0.009wt% tetrabutylammonium chloride solution with cyclic voltammetry (CV) scanning from 0.6V to -0.3V vs Ag/AgCl at a rate of 0.1V s<sup>-1</sup> for 200 scans. Quantification of released compounds was performed with a mass spectrometer (Shimadzu LCMS-2020), electrospray ionization with a 10m gradient of 10%-90% 0.1% formic acid in acetonitrile and 0.1%formic acid in water. Concentration and mass were determined by comparing the peak counts to a set of calibration data.

#### **7.2.5 Animal Experiments with 2 Photon Microscopy**

All animal experiments were approved by the University of Pittsburgh Institutional Animal Care and Use Committee. CX3CR1-GFP mice were anesthetized with Ketamine/xylazine (65mg kg<sup>-1</sup> and 7mg kg<sup>-1</sup>) and anesthesia was confirmed by the lack of a toe-pinch response. Breathing and heartrate were monitored throughout the surgery and the animal's body temperature was

controlled with a heating pad. Once anesthesia was achieved, the scalp was removed and a 2mm x 2mm section of the skull was removed. A small amount of dental acrylic was placed around the cranial window to form a well which would hold the saline required for the water immersion lens of the microscope. The mouse was then moved to the imaging platform and an 18g steel needle was inserted into the back to act as the counter electrode. An Ag/AgCl reference was then placed in contact with the saline well on the brain surface. A PEDOT/SNP coated carbon fiber electrode (7 $\mu$ m diameter and 400 $\mu$ m long) was then gradually inserted into the cortex at a 30° angle from the horizontal plane. This ensured that the electrode would not contact the lens during imaging. The mouse was then given a 0.03ml IP injection of sulforhodamine 101 (1mg ml<sup>-1</sup> in saline) to label blood vessels. 2 photon microscopy imaging was performed with an OPO laser (Insight DS+; Spectraphysics, Menlo Park, Ca) tuned to 920nm, photomultiplier tubes (Hamamatsu Photonics KK, Hamamatsu, Shizuoka, Japan), and a 16x 0.8 numerical aperture water immersion lens (Nikon Inc. Milville, Ny). Images were collected with Prairie View software. Z-stacks were taken of the region surrounding the electrode prior to, during, and after drug release. Z-stacks were taken every 20 minutes. Drug release was performed with CV as described above. Vessel diameter was measured with the 'diameter' plugin on ImageJ. 5 animals were used for both drug delivery and control experiments.

### **7.2.6 Statistics**

Statistics were performed in GraphPad Prism 8. Statistical comparisons for released NaNP and vessel diameters were made with Student's T-test. Changes in vessel diameter relative to the initial images were made with a Wilcoxon test, without assuming normally distributed data.

### 7.3 Results

In order to controllably release NaNP into the cortex, we have employed a conducting polymer gated electrochemically controlled drug delivery platform. The NaNP was loaded into the sulfonate functionalized mesoporous silica nanoparticles which were then used to dope the conducting polymer during its electropolymerization. The validation of the drug loading and release was performed with 3mm diameter glassy carbon electrodes. The electrodes were coated for 1000s using either drug loaded SNP or non-loaded SNP which served as a control. The release was performed with cyclic voltammetry for 200 cycles in a dilute solution of tetrabutylammonium chloride, and samples were collected after release to measure the NaNP concentration with mass spectroscopy.

NaNP has a molar mass of approximately  $262 \text{ g M}^{-1}$ , and a reduction potential of approximately  $-0.5\text{V}$  vs Ag/AgCl (Figure 43B). Mass spectroscopy measurements demonstrated significantly higher NaNP concentrations were present in the release samples, with no detected NaNP in the control samples. These concentrations were then converted to released masses and demonstrate that the PEDOT/SNP was capable of releasing  $3.96 \pm 1.7 \text{ }\mu\text{g}$  (mean  $\pm$  SD) of NaNP, or  $56.1 \pm 24.1 \mu\text{g cm}^{-2}$  after 200 stimulations (Figure 43C).

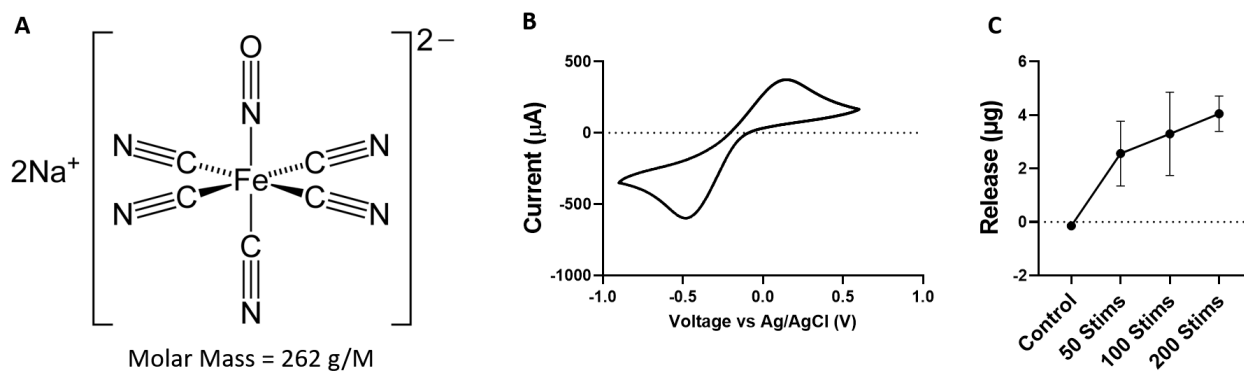
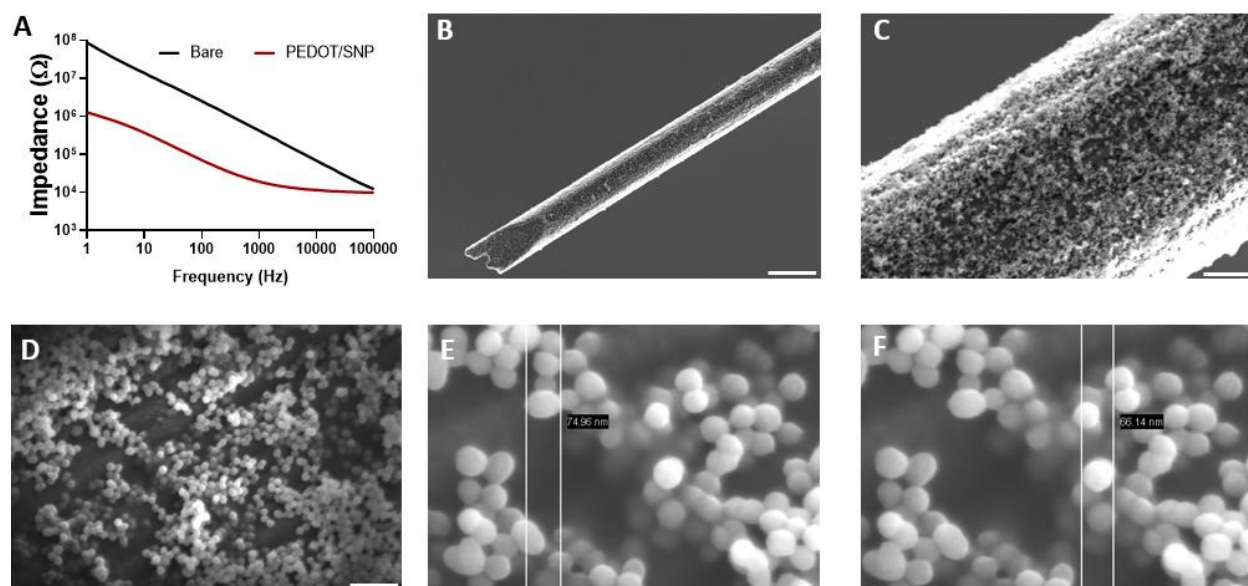


Figure 43. *In Vitro* release of NaNP.

(A) The structure of NaNP, including its charge and molar mass. *In vitro* release experiments were performed in a dilute solution of tetrabutylammonium chloride to minimize noise in the mass spec readings due to excess salt. (B) Cyclic voltammogram of the 100 $\mu\text{M}$  NaNP in water, showing the reduction peak at -0.5V and the oxidation peak at 0.15V (C) Mass spec readings were calibrated and concentrations were calculated for each trial. Significant differences in NaNP were observed when release was performed with NaNP loaded into the nanoparticles compared to PEDOT/SNP without preloaded NaNP \*\*\* $p < 0.001$  students t-test.

Following the validation of the drug release, we performed *in vivo* experiments to examine the effects of controlled release of NaNP on the vasculature and microglia present in the cortex. We used a 400 $\mu$ m long 7 $\mu$ m diameter carbon fiber electrode to perform the release experiments to minimize the insertion injury and maximize the electrochemical surface area. The electrode was coated for 1000s under current controlled polymerization, then washed with water and saline prior to insertion into the animal. Following the polymerization of PEDOT/SNP, we observed the characteristic drop in the electrode impedance across all frequencies (Figure 44A), indicating that the PEDOT/SNP coating was successfully applied to the CFE. Samples were taken for SEM imaging to examine the nature and topography of the coating (Figure 44B-F). The PEDOT/SNP coating appears to have occurred uniformly over the surface of the CFE. Higher magnification images reveal the topography and minute structure of the PEDOT/SNP. The nanoparticles are visible within the polymer, and although there are some areas of nanoparticle aggregation, overall, the film and SNPs are qualitatively uniform in size and distribution (Figure 44E,F).

Vessels were visualized following an injection of SR101. Following the surgical preparations, the animal was moved to the two-photon microscope and the electrode inserted into the cortex. Z-stack images were taken prior to drug release (Stack 0), during release (Stacks 1 and 2), and following the end of release (Stacks 3 and 4). Z stacks took approximately 20 minutes each.



**Figure 44. Characterization of NaNP loaded PEDOT/SNP coated CFE.**

(A) Impedance measurements were taken for the bare CFE and the PEDOT/SNP coated CFE, demonstrating the characteristic decrease in impedance of the CFE following PEDOT polymerization. (B-D) SEM images of the NaNP loaded PEDOT/SNP coated CFE. Images were taken at increasing magnification to visualize the coating uniformity and microstructure. Scale bars (B) 10  $\mu\text{m}$  (C) 1  $\mu\text{m}$  (D) 300 nm. (E,F) diameters of SNP within the PEDOT/SNP polymer, values are 74.96 (E) and 66.14 (F).

Changes in vessel diameter were visualized by overlaying the cortical blood vessels before (yellow) and after (magenta) stimulation (Figure 45A,B). Small translations in the images in the x, y, and z directions were often necessary to directly compare vasculature. The representative control image shows that there is nearly perfect overlap between the pre and post stimulation vessels, indicating that there were no dramatic changes in the vessel diameters. However, during NaNP release, there are prominent magenta borders on many large vessels, indicating that the vessel diameter increased following stimulation and release of NaNP.

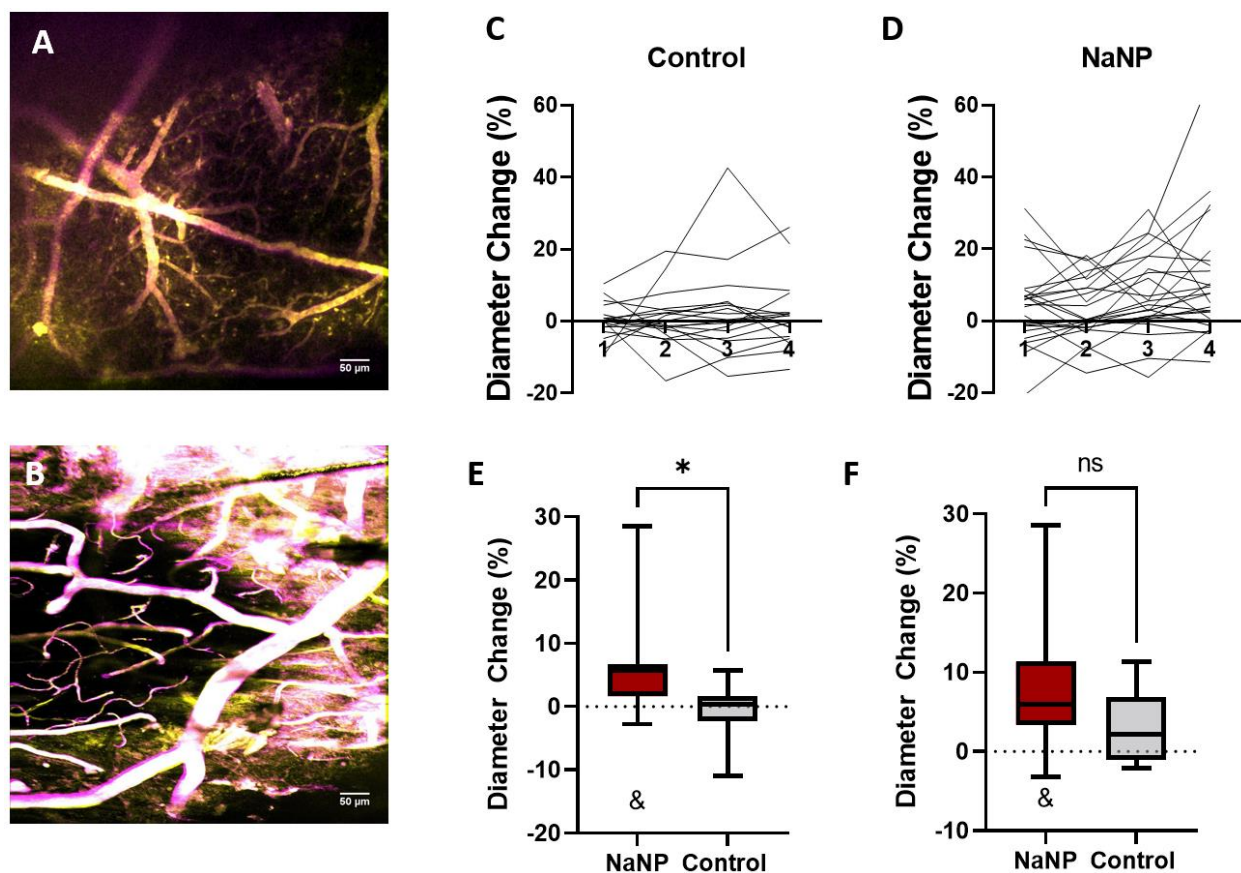


Figure 45. Vessel dynamics after NaNP release.

(A,B) Overlays of cortical vessels before (yellow) and after (magenta) stimulation for control (a) and NaNP loaded (b) PEDOT/SNP coated carbon fibers. Images were produced from Z-Stacks 0 and 2. (C,D) Changes in vessel diameters over time compared to the initial Z-Stack for control and NaNP loaded PEDOT/SNP, respectively. Z-Stack 1 and 2 were taken during stimulation and Z-Stack 3 and 4 immediately following stimulation. (E) Changes in vessel diameter were measured between the pre-stimulation Z-Stack and Z-Stack 2. (F) Changes in vessel diameter were measured between the pre-stimulation Z-Stack and Z-Stack 4. \* $p < 0.05$  with unpaired students t-test, &  $p < 0.05$  relative to 0% change with wilcoxon test. 20 vessels were analyzed for control release, 25 for NaNP release.

Changes in the vessel diameters were mapped over time (Figure 46C,D). Small fluctuations in the diameters of the control vessels were observed, attributed to natural physiological changes in addition to noise from captured images. The experimental group experienced much larger and more positive changes than the control group, and a general upwards trend can be observed. The percent change in vessel diameter was measured between stacks 0 and 2, and 0 and 4 (Figure 46E,F). The first notable difference was that there were significant changes in the diameters of vessels when NaNP was released relative to the pre-release diameters both during release and approximately 20 minutes following the end of release. This change in diameter was not present in the control animals. Additionally, there were significant differences in the % change in vessel diameter between the release and control groups during stimulation.

Next, we examined how vessels of different diameters responded to the local release of NaNP. Vessels were grouped based on their initial diameters, with large vessels having diameters  $> 60$  pixels, medium vessels having diameters  $60 \leq D < 30$  pixels and the remaining vessels  $> 5$  pixels in diameter were categorized as small vessels. It was apparent that small vessels have much greater variation in diameter changes than larger vessels, predominantly due to lower signal to noise ratios. Significant differences were observed following NaNP release for both large ( $p < 0.01$ , Wilcoxon test) and medium vessels ( $p < 0.05$  Wilcoxon test), but not for the smallest vessels measured. No significant changes were observed for controls, regardless of vessel diameter.

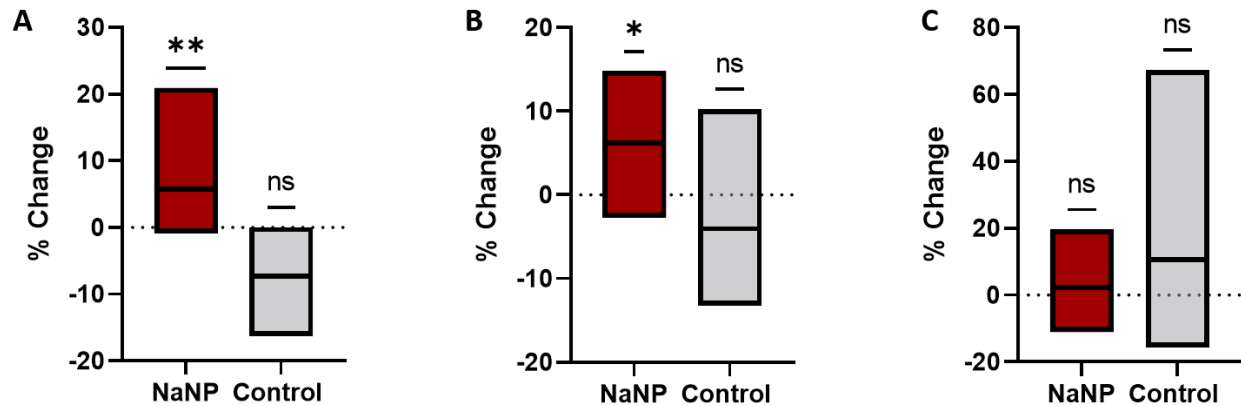


Figure 46 Changes in vessel diameter grouped by vessel size.

(A) Large vessels were selected as having diameters greater than 80 pixels. (B) Medium vessels were selected as having diameters between 30 and 60 pixels. (C) Small vessels were selected as having diameters between 30 and 5 pixels. \* $p < 0.05$  wilcoxon test \*\* $p < 0.01$  Wilcoxon test.

## 7.4 Discussion

Vascular dynamics are thought to play a major role in the health of neural tissues in their native states and following injury. Changes in blood flow and blood oxygenation are the driving principles behind fMRI, and lack of blood flow can result in rapid death of host cells. However, there are very few methods of controllably modulating cerebral vascular dynamics on the scales of neural electrodes. There are fewer still that enable simultaneous electrical recording and stimulation.

We have utilized mesoporous silica nanoparticles functionalized with negatively charge sulfonate groups as drug reservoirs for conducting polymers. The drug of choice was NaNP, known to rapidly affect local blood vessels by the release of nitric oxide. We then validated our drug delivery platform *in vitro*, measuring the concentrations of released NaNP with mass

spectroscopy. Release was performed in a dilute solution of tetrabutylammonium chloride, which greatly increase our signal to noise ratio over standard saline. Traditionally, drug loading and release from conducting polymers is limited, however the released masses of NaNP are impressive for conducting polymer based platforms, on par with previously examined compounds such as fluorescein, rhodamine, and melatonin released from PEDOT/SNP[53].

We then validated that the PEDOT/SNP NaNP releasing coating was capable of controlling vascular dynamics *in vivo*. Drug release was performed after baseline measurements of the vasculature were taken, followed by additional measurement after the end of release. Mice which were implanted with NaNP loaded PEDOT/SNP exhibited prominent changes in vessel diameter, corresponding with the start of stimulation. Mice implanted with control electrodes did not have any significant vascular responses to the cyclic voltammetry stimulation, indicating that any changes in vessel diameters was likely driven by the release of NaNP, not the electrical stimulation.

Measurements taken at different time points appear to indicate that the effects of NaNP release take place during the 20 minutes of stimulation and last for at least 40 minutes following the end of stimulation. Significant differences in the vessel diameters of NaNP treated animals were apparent after stimulation and were significantly higher than the control animals, and after resting for 40 minutes, the vessel diameters were still significantly greater than the baseline diameters. These results are in line with the rapid onset of action of NaNP,[318, 327] which is known to cause vasodilation within seconds of systemic administration through the release of nitric oxide. Interestingly, there was no longer a significant difference in the vessel diameters of NaNP treated animals and control animals at 60 min post stimulation. This may be due to natural fluctuations in the vessel diameters or diffusion of the NaNP from the site of release.

Vessels were then grouped by size to isolate capillaries from arterioles and venules. We observe that the larger vessels have far greater capacity for dilation, while smaller capillaries did not respond to the NaNP. The mechanism of action of NaNP is through the release of nitric oxide, which in turn affects only smooth muscle cells through a signaling cascade originating with guanylate cyclase and the end result of which is the relaxation of myosin light chains in the muscle cells[328]. Capillaries do not contain smooth muscle cells, and as such are not affected by the released nitric oxide.

Our experiments have also demonstrated a reliable method of modulating the vasculature dynamics of the brain, which may find applications in the field of neurovascular coupling and functional magnetic resonance imaging (fMRI). Changes in the energy, oxygen, and nutrient demands in the brain are managed by the central nervous system (CNS) vasculature through neurovascular coupling and is the principal component of fMRI. However, the exact relationships between cortical blood flow and neural activity are debated.[329-334] In addition, many animal studies are performed under anesthesia, and anesthetics often impact blood flow in unique ways.[335-338] The lack of experimental methods of modulating local blood flow complicates the direct examination of neurovascular coupling. While the body of research utilizing fMRI to examine changes in neural activity is large, there has been less effort directed at studying how local changes in blood flow affect CNS cells.

## **7.5 Conclusions**

We were able to achieve fine temporal control of vascular dynamics by utilizing a carbon fiber electrode coated with NaNP loaded PEDOT/SNP. The polymer coating served as both a gate

to the drug release and drug carrier. Release was achieved by cyclically oxidizing and reducing the PEDOT, alternative between drawing the drug from the nanoparticle reservoir into the polymer and expelling the drug from the polymer into the tissues. Changes in vascular dynamics were evident within 20 minutes of stimulation. These findings present a novel tool that can be used to control tissue perfusion following the implantation of a neural electrode.

## 8.0 Conclusions

### 8.1 Summary of Findings

In this dissertation we have investigated two novel methods of modulating cellular and tissue reactions in the central nervous system. The first of these methods employed a novel biomimetic surface modification that utilized silica nanoparticles as a topographical modification. The second employed silica nanoparticles as a drug reservoir for conducting polymer mediated controlled drug delivery.

In chapters 2-5, we sequentially investigated the effects of topographical surface modifications on the bioactivity of L1 and its utility as a biomimetic coating. In chapter 2, we developed a novel thiol-modified silica nanoparticle that can be immobilized to silicon and glass substrates. We then demonstrated that these TNP modified substrates were capable of binding substantially more L1 than unmodified smooth surfaces. Subsequent *in vitro* assessment of the surface determined that the enhanced binding of L1, in addition to the topography of the TNP modified substrate, resulted in heightened neurite extension without evoking additional astrocytic activation. In chapter 3, we investigated the stability of the L1 modified substrates under physiological conditions and then examined the *in vivo* response of cortical tissues to electrodes following surface modification. We observed that the TNP+L1 coating was able to maintain the bioactivity of the L1 protein for 4-weeks in saline, and that the TNP+L1 coating was able to reduce foreign body reactions for 4-weeks *in vivo*. We expanded on this investigation in chapters 4 and 5. In chapter 4, we found that L1 could be immobilized to the TNP modified substrate and then dried and re-hydrated up to 8-weeks later with no notable loss in bioactivity. Functional electrodes were

then coated with the TNP+L1 modification and implanted in mice for 16 weeks. A subset of electrodes were coated with TNP+L1 3-days prior to implantation and stored dry to examine whether the TNP+L1 coating could be fabricated prior to the day of implantation without losing bioactivity. The electrophysiological recording performance of the TNP+L1 electrodes was not adversely altered by drying. We then performed long-term testing of the ability of the electrodes to be stored for up to 28 days after drying with functional 32 channel electrodes in chapter 5.

In chapters 6 and 7, we developed and investigated a method of controlled drug delivery from conducting polymers with mesoporous sulfonate modified silica nanoparticles serving as a drug reservoir. The silica nanoparticle dopants were fabricated by oxidation of thiol-modified nanoparticles with  $H_2O_2$ , and the resulting PEDOT/SNP films demonstrated highly favorable electrochemical properties for neural engineering applications, including lowering the impedance of electrodes while increasing the charge injection limits by more than 100x relative to the uncoated site and on par with other advanced stimulation materials. The PEDOT/SNP films were superior to PEDOT films without drug reservoirs in terms of drug release quantities and number of compatible compounds capable of being loading and released from the films. For example, by first loading melatonin into the SNP, we were able to use the SNP to shuttle melatonin into the PEDOT/SNP films and then release the drug without any significant losses in its redox activity. PEDOT/SNP films coated onto carbon fiber electrodes were used to demonstrate *in vivo* drug release. Fluorescein was the first compound released due to our ability to detect the drug release in real time with two photon microscopy. We then utilized the PEDOT/SNP coatings to directly affect the CNS cells and vasculature. First, DNQX was released and we observed a transient decrease in neural activity as the compound blocked glutamate reception. Next, we use the PEDOT/SNP coating to load and release the vasodilator NaNP. The released NaNP rapidly elicited

dilation of the CNS vessels that was size specific. These *in vivo* experiments serve to demonstrate the utility of the PEDOT/SNP coating as a method of modulating tissue reactions with a high degree of spatial and temporal control.

## **8.2 Future Directions**

Complete control over the tissue reactions following electrode insertion is likely an impossible goal. However, by minimizing/eliminating local inflammatory reactions following the implantation of the device, we can work towards developing truly stable long term neural recording. The research presented here offers two potential tools that may be employed towards this goal, but further research and investigation will be required to maximize the potential benefits posited by these methods.

### **8.2.1 Topographical Modification of Electrodes**

In this work we demonstrated that topographical modification of electrodes with silica nanoparticles resulted in enhanced protein binding and stability. Yet we are unlikely to have reached the ultimate potential of nanoparticle-derived topography. This may require investigating different nanoparticles for topographical modification, including metal and ceramic nanoparticles. Further, investigations into the effects of nanoparticle size, distribution, stacking, and even the method of protein immobilization should be performed to test the boundaries of nanoparticle derived topography. In addition, many of our studies were limited to immobilizing L1. We must

expand the list of compounds to include other proteins and peptide or other active surface modifications such as catalytic antioxidants.

#### **8.2.1.1 Modification of Additional Substrates**

Silicon and silicon dioxide are common insulation materials found in neural electrodes and are easily modifiable with silane chemistry. However, other insulation materials are present on many types of electrodes, including polymers and ceramics. These substrates will require their own unique methods of modification and may not be immediately compatible with the methods described here. Parylene-C, the insulation material found on Utah style electrodes in addition to many others, may require additional steps to ensure that the immobilization on the nanoparticles is effective.

#### **8.2.1.2 Potential Molecular Modifications**

Although L1 has repeatedly demonstrated itself to be a fantastic biomimetic surface modification, we should not limit ourselves to one individual protein. A separate protein, laminin, has been successfully employed by labs to control the foreign body reactions following device implantation[209]. Other proteins derived from the CNS extracellular matrix should be investigated. Peptide sequences such as p20 and IKVAV sequences are far smaller than L1 or laminin and may be able to make more efficient use of the elevated surface area provided by the nanoparticle-modified surface. Other proteins derived from the CNS extracellular matrix should be investigated. Peptide sequences are far smaller than L1 or laminin and may be able to make more efficient use of the elevated surface area provided by the nanoparticle-modified surface.

Other compounds, such as the immobilizable superoxide dismutase mimic iSODm have been investigated in the work *in vitro* but have not been validated *in vivo*. Catalytic antioxidants

may greatly benefit from the enhanced surface area provided by the topographical modification and may even provide long term protection to the device itself.

### **8.2.2 PEDOT/SNP Drug Delivery**

Drug administration is one of the most effective methods available to control the inflammatory reactions observed following the implantation of neural electrodes. In addition, the PEDOT/SNP coating is immediately compatible with virtually all electrically interfacing devices. We have demonstrated that PEDOT/SNP films are capable of loading and releasing a wide library of compounds, including many that are not compatible with traditional methods of conducting polymer mediated drug delivery. However, the extent to which drug delivery from PEDOT/SNP coating can enhance the long-term electrode performance must be further investigated. In order to achieve this, we must examine both the drug loaded into the PEDOT/SNP film and the methods/timescales of release *in vivo*. These experiments must be performed while also measuring the electrophysiology of the tissues to ensure that the compounds are producing the desired reactions in the tissues.

#### **8.2.2.1 Drug Selection**

Numerous compounds have been studied for controlling inflammation and improving long term electrode performance. Antioxidants are one such category of compounds. These include melatonin,[121] resveratrol,[123] MnTBAP,[339], and iSODm.[240] These studies have consistently demonstrated that antioxidants are effective at increasing neuron survival and decreasing glial activation. This is believed to be because of the destruction of dangerous free radical species such as superoxide and nitric oxide. The loading and release of these compounds

from PEDOT/SNP directly at the site of implantation may further enhance their effects by increasing the local concentration and providing precise control over the timing and duration.

Other compounds are known to have rapid and dramatic effects on CNS cells and vasculature. Following electrode implantation, CNS vessels are inherently damaged and the transport of oxygen and nutrients to the cells around the electrode are likely inhibited. We have demonstrated that NaNP can be used to control the local blood flow around the carbon fiber electrode. PEDOT/SNP coated electrode sites that are loaded with NaNP may be able to restore some of the local blood flow following implantation, reducing or eliminating cell death due to hypoxic conditions. Microglia are another potential target for drugs released by PEDOT/SNP. Drug which inhibit the P2Y<sub>12</sub> receptor also inhibit microglial motion, and are therefore great candidates for local delivery. Compounds such as ticagrelor or clopidogrel may eliminate the initial microglial responses to the implant, preventing the characteristic inflammatory signaling cascade and producing dramatic long term effects in the tissues.

#### **8.2.2.2 Timing and Method of Release**

The works here demonstrate that cyclic voltammetry was capable of triggering drug release without impacting local cellular activity. However, these experiments were limited to acute studies and did not investigate other methods of release or the most effective duration of release for producing long term effects.

PEDOT/SNP coatings are not refillable and will eventually be exhausted. The timing of drug release is likely crucial to ensure that the maximum effect can be obtained from the coating. It remains to be examined whether drug release should be concentrated during the initial hours following implantation, or if multiple day or even weeks of administration at lower concentrations

would provide superior treatment. Further, the timing of release is likely to depend heavily on the choice of drug.

Although CV appears to produce highly favorable release profiles without eliciting unwanted reactions in the tissues, other methods of release should be examined to maximum temporal control of release in addition to completely exhausting the drug reservoir. Fast stimulations, either by quickly cycling the voltage or by using biphasic pulses, may provide further control over the timing of the release while also allowing for smaller amounts of drug to be delivered in each individual pulse. It also remains to be seen how the shape of the waveform impacts drug delivery, and investigating the differences caused by triangular waveform (as seen in CV release), rectangular waveforms, and sinusoidal stimuli may reveal unique and useful characteristics.

## Bibliography

- [1] K. Woepfel, Q. Yang, X.T. Cui, Recent advances in neural electrode–tissue interfaces, *Current Opinion in Biomedical Engineering* 4(Supplement C) (2017) 21-31.
- [2] A.B. Schwartz, X.T. Cui, Douglas J. Weber, D.W. Moran, Brain-Controlled Interfaces: Movement Restoration with Neural Prosthetics, *Neuron* 52(1) (2006) 205-220.
- [3] J.C. Barrese, N. Rao, K. Paroo, C. Triebwasser, C. Vargas-Irwin, L. Franquemont, J.P. Donoghue, Failure mode analysis of silicon-based intracortical microelectrode arrays in non-human primates, *Journal of neural engineering* 10(6) (2013) 066014-066014.
- [4] P. Abhishek, X. Qing-Shan, S. Viswanath, N. Toshikazu, S. Gerry, J.S. Wolfgang, C.S. Justin, Comprehensive characterization and failure modes of tungsten microwire arrays in chronic neural implants, *Journal of Neural Engineering* 9(5) (2012) 056015.
- [5] T.D.Y. Kozai, K. Catt, X. Li, Z.V. Gugel, V.T. Olafsson, A.L. Vazquez, X.T. Cui, Mechanical failure modes of chronically implanted planar silicon-based neural probes for laminar recording, *Biomaterials* 37 (2015) 25-39.
- [6] A. Prasad, Q.-S. Xue, R. Dieme, V. Sankar, R.C. Mayrand, T. Nishida, W.J. Streit, J.C. Sanchez, Abiotic-biotic characterization of Pt/Ir microelectrode arrays in chronic implants, *Frontiers in Neuroengineering* 7 (2014) 2.
- [7] S. Zhao, X. Liu, Z. Xu, H. Ren, B. Deng, M. Tang, L. Lu, X. Fu, H. Peng, Z. Liu, X. Duan, Graphene Encapsulated Copper Microwires as Highly MRI Compatible Neural Electrodes, *Nano Letters* 16(12) (2016) 7731-7738.
- [8] S. Ahn, P.S. Spuhler, M. Chiari, M. Cabodi, M. Selim Ünlü, Quantification of surface etching by common buffers and implications on the accuracy of label-free biological assays, *Biosensors and Bioelectronics* 36(1) (2012) 222-229.
- [9] P.V. Brady, J.V. Walther, Kinetics of quartz dissolution at low temperatures, *Chemical Geology* 82 (1990) 253-264.
- [10] W. Zhou, X. Dai, T.-M. Fu, C. Xie, J. Liu, C.M. Lieber, Long Term Stability of Nanowire Nanoelectronics in Physiological Environments, *Nano Letters* 14(3) (2014) 1614-1619.
- [11] S.B. Brummer, L.S. Robblee, F.T. Hambrecht, CRITERIA FOR SELECTING ELECTRODES FOR ELECTRICAL STIMULATION: THEORETICAL AND PRACTICAL CONSIDERATIONS, *Annals of the New York Academy of Sciences* 405(1) (1983) 159-171.
- [12] D.R. Merrill, M. Bikson, J.G.R. Jefferys, Electrical stimulation of excitable tissue: design of efficacious and safe protocols, *Journal of Neuroscience Methods* 141(2) (2005) 171-198.

- [13] P. Takmakov, M.K. Zachek, R.B. Keithley, P.L. Walsh, C. Donley, G.S. McCarty, R.M. Wightman, Carbon Microelectrodes with a Renewable Surface, *Analytical Chemistry* 82(5) (2010) 2020-2028.
- [14] D.E. Arreaga-Salas, A. Avendaño-Bolívar, D. Simon, R. Reit, A. Garcia-Sandoval, R.L. Rennaker, W. Voit, Integration of High-Charge-Injection-Capacity Electrodes onto Polymer Softening Neural Interfaces, *ACS Applied Materials & Interfaces* 7(48) (2015) 26614-26623.
- [15] Y. Lu, H. Lyu, A.G. Richardson, T.H. Lucas, D. Kuzum, Flexible Neural Electrode Array Based-on Porous Graphene for Cortical Microstimulation and Sensing, *Scientific Reports* 6 (2016) 33526.
- [16] S.B. Brummer, M.J. Turner, Electrochemical Considerations for Safe Electrical Stimulation of the Nervous System with Platinum Electrodes, *IEEE Transactions on Biomedical Engineering* BME-24(1) (1977) 59-63.
- [17] F.C. Stuart, A.L. Kip, G.W. Cristin, T. Pavel, Tissue damage thresholds during therapeutic electrical stimulation, *Journal of Neural Engineering* 13(2) (2016) 021001.
- [18] F.C. Stuart, Neural Stimulation and Recording Electrodes, *Annual Review of Biomedical Engineering* 10 (2008) 275-309.
- [19] X. Cui, J. Wiler, M. Dzaman, R.A. Altschuler, D.C. Martin, In vivo studies of polypyrrole/peptide coated neural probes, *Biomaterials* 24(5) (2003) 777-787.
- [20] P.A. Cody, J.R. Eles, C.F. Lagenaur, T.D.Y. Kozai, X.T. Cui, Unique electrophysiological and impedance signatures between encapsulation types: An analysis of biological Utah array failure and benefit of a biomimetic coating in a rat model, *Biomaterials* 161 (2018) 117-128.
- [21] K. Woepfel, C. Hughes, A.J. Herrera, J.R. Eles, E.C. Tyler-Kabara, R.A. Gaunt, J.L. Collinger, X.T. Cui, Explant Analysis of Utah Electrode Arrays Implanted in Human Cortex for Brain-Computer-Interfaces, *Frontiers in Bioengineering and Biotechnology* 9 (2021).
- [22] P.A. Tresco, B.D. Winslow, The challenge of integrating devices into the central nervous system, *Crit Rev Biomed Eng* 39(1) (2011) 29-44.
- [23] V.S. Polikov, P.A. Tresco, W.M. Reichert, Response of brain tissue to chronically implanted neural electrodes, *J Neurosci Methods* 148(1) (2005) 1-18.
- [24] T.D.Y. Kozai, A.L. Vazquez, C.L. Weaver, S.-G. Kim, X.T. Cui, In vivo two-photon microscopy reveals immediate microglial reaction to implantation of microelectrode through extension of processes, *Journal of neural engineering* 9(6) (2012) 066001.
- [25] K. Nakajima, S. Honda, Y. Tohyama, Y. Imai, S. Kohsaka, T. Kurihara, Neurotrophin secretion from cultured microglia, *Journal of neuroscience research* 65(4) (2001) 322-331.
- [26] J.A. Smith, A. Das, S.K. Ray, N.L. Banik, Role of pro-inflammatory cytokines released from microglia in neurodegenerative diseases, *Brain Res Bull* 87(1) (2012) 10-20.

- [27] J. Turner, W. Shain, D. Szarowski, M. Andersen, S. Martins, M. Isaacson, H. Craighead, Cerebral astrocyte response to micromachined silicon implants, *Experimental neurology* 156(1) (1999) 33-49.
- [28] T. Kozai, T. Marzullo, F. Hooi, N. Langhals, A. Majewska, E. Brown, D. Kipke, Reduction of neurovascular damage resulting from microelectrode insertion into the cerebral cortex using in vivo two-photon mapping, *Journal of neural engineering* 7(4) (2010) 046011.
- [29] T. Saxena, L. Karumbaiah, E.A. Gaupp, R. Patkar, K. Patil, M. Betancur, G.B. Stanley, R.V. Bellamkonda, The impact of chronic blood–brain barrier breach on intracortical electrode function, *Biomaterials* 34(20) (2013) 4703-4713.
- [30] L. Karumbaiah, S.E. Norman, N.B. Rajan, S. Anand, T. Saxena, M. Betancur, R. Patkar, R.V. Bellamkonda, The upregulation of specific interleukin (IL) receptor antagonists and paradoxical enhancement of neuronal apoptosis due to electrode induced strain and brain micromotion, *Biomaterials* 33(26) (2012) 5983-96.
- [31] C.L. Kolarcik, S.D. Luebben, S.A. Sapp, J. Hanner, N. Snyder, T.D. Kozai, E. Chang, J.A. Nabity, S.T. Nabity, C.F. Lagenaur, Elastomeric and soft conducting microwires for implantable neural interfaces, *Soft matter* 11(24) (2015) 4847-4861.
- [32] H.S. Sohal, G.J. Clowry, A. Jackson, A. O’Neill, S.N. Baker, Mechanical flexibility reduces the foreign body response to long-term implanted microelectrodes in rabbit cortex, *PLoS One* 11(10) (2016) e0165606.
- [33] J.K. Nguyen, D.J. Park, J.L. Skousen, A.E. Hess-Dunning, D.J. Tyler, S.J. Rowan, C. Weder, J.R. Capadona, Mechanically-compliant intracortical implants reduce the neuroinflammatory response, *Journal of neural engineering* 11(5) (2014) 056014.
- [34] L. Karumbaiah, Saxena, T., Carlson, D., Patil, K., Patkar, R., Gaupp, E. A., ... & Bellamkonda, R. V, Relationship between intracortical electrode design and chronic recording function, *Biomaterials* 34(33) (2013) 8061-8074.
- [35] B.D. Winslow, M.B. Christensen, W.K. Yang, F. Solzbacher, P.A. Tresco, A comparison of the tissue response to chronically implanted Parylene-C-coated and uncoated planar silicon microelectrode arrays in rat cortex, *Biomaterials* 31(35) (2010) 9163-72.
- [36] J.L. Skousen, S.M. Merriam, O. Srivannavit, G. Perlin, K.D. Wise, P.A. Tresco, Reducing surface area while maintaining implant penetrating profile lowers the brain foreign body response to chronically implanted planar silicon microelectrode arrays, *Prog Brain Res* 194 (2011) 167-80.
- [37] J.L. Skousen, M.J. Bridge, P.A. Tresco, A strategy to passively reduce neuroinflammation surrounding devices implanted chronically in brain tissue by manipulating device surface permeability, *Biomaterials* 36 (2015) 33-43.
- [38] S.M. Gutowski, K.L. Templeman, A.B. South, J.C. Gaulding, J.T. Shoemaker, M.C. LaPlaca, R.V. Bellamkonda, L.A. Lyon, A.J. Garcia, Host response to microgel coatings on neural electrodes implanted in the brain, *J Biomed Mater Res A* 102(5) (2014) 1486-99.

- [39] S.M. Gutowski, J.T. Shoemaker, K.L. Templeman, Y. Wei, R.A. Latour, Jr., R.V. Bellamkonda, M.C. LaPlaca, A.J. Garcia, Protease-degradable PEG-maleimide coating with on-demand release of IL-1Ra to improve tissue response to neural electrodes, *Biomaterials* 44 (2015) 55-70.
- [40] E. Azemi, C.F. Lagenaur, X.T. Cui, The surface immobilization of the neural adhesion molecule L1 on neural probes and its effect on neuronal density and gliosis at the probe/tissue interface, *Biomaterials* 32(3) (2011) 681-692.
- [41] T.D. Kozai, X. Li, L.M. Bodily, E.M. Caparosa, G.A. Zenonos, D.L. Carlisle, R.M. Friedlander, X.T. Cui, Effects of caspase-1 knockout on chronic neural recording quality and longevity: insight into cellular and molecular mechanisms of the reactive tissue response, *Biomaterials* 35(36) (2014) 9620-9634.
- [42] A.J. Sawyer, W. Tian, J.K. Saucier-Sawyer, P.J. Rizk, W.M. Saltzman, R.V. Bellamkonda, T.R. Kyriakides, The effect of inflammatory cell-derived MCP-1 loss on neuronal survival during chronic neuroinflammation, *Biomaterials* 35(25) (2014) 6698-6706.
- [43] L.B. Moore, A.J. Sawyer, A. Charokopos, E.A. Skokos, T.R. Kyriakides, Loss of monocyte chemoattractant protein-1 alters macrophage polarization and reduces NF $\kappa$ B activation in the foreign body response, *Acta biomaterialia* 11 (2015) 37-47.
- [44] E. Patrick, M.E. Orazem, J.C. Sanchez, T. Nishida, Corrosion of Tungsten Microelectrodes used in Neural Recording Applications, *Journal of neuroscience methods* 198(2) (2011) 158-171.
- [45] T. Pavel, R. Kiersten, K.S. Phillips, S.I. Irada, K. Victor, G.W. Cristin, Rapid evaluation of the durability of cortical neural implants using accelerated aging with reactive oxygen species, *Journal of Neural Engineering* 12(2) (2015) 026003.
- [46] T.D.Y. Kozai, X. Li, L.M. Bodily, E.M. Caparosa, G.A. Zenonos, D.L. Carlisle, R.M. Friedlander, X.T. Cui, Effects of caspase-1 knockout on chronic neural recording quality and longevity: Insight into cellular and molecular mechanisms of the reactive tissue response, *Biomaterials* 35(36) (2014) 9620-9634.
- [47] E. Azemi, W.R. Stauffer, M.S. Gostock, C.F. Lagenaur, X.T. Cui, Surface immobilization of neural adhesion molecule L1 for improving the biocompatibility of chronic neural probes: In vitro characterization, *Acta Biomaterialia* 4(5) (2008) 1208-1217.
- [48] E. Azemi, C. Lagenaur, X.T. Cui, The Surface Immobilization of the Neural Adhesion Molecule L1 on Neural Probes and its Effect on Neuronal Density and Gliosis at the Probe/Tissue Interface, *Biomaterials* 32(3) (2011) 681-692.
- [49] J.R. Eles, A.L. Vazquez, N.R. Snyder, C. Lagenaur, M.C. Murphy, T.D. Kozai, X.T. Cui, Neuroadhesive L1 coating attenuates acute microglial attachment to neural electrodes as revealed by live two-photon microscopy, *Biomaterials* 113 (2017) 279-292.

- [50] Q. Yang, B. Wu, J.R. Eles, A.L. Vazquez, T.D.Y. Kozai, X.T. Cui, Zwitterionic Polymer Coating Suppresses Microglial Encapsulation to Neural Implants In Vitro and In Vivo, *Adv Biosyst* 4(6) (2020) e1900287.
- [51] S. Krystyna, Y. Meijun, G. Yu-Rong, R. Harmain, X.H. Daniel, Longitudinal multimodal assessment of neurodegeneration and vascular remodeling correlated with signal degradation in chronic cortical silicon microelectrodes, *Neurophotonics* 7(1) (2020) 1-28.
- [52] S.M. Wellman, F. Cambi, T.D. Kozai, The role of oligodendrocytes and their progenitors on neural interface technology: A novel perspective on tissue regeneration and repair, *Biomaterials* 183 (2018) 200-217.
- [53] K.M. Woepfel, X.S. Zheng, Z.M. Schulte, N.L. Rosi, X.T. Cui, Nanoparticle Doped PEDOT for Enhanced Electrode Coatings and Drug Delivery, *Advanced Healthcare Materials* 8(21) (2019) 1900622.
- [54] S. Bovetti, C. Moretti, T. Fellin, Mapping brain circuit function in vivo using two-photon fluorescence microscopy, *Microscopy Research and Technique* 77(7) (2014) 492-501.
- [55] Q. Chen, J. Cichon, W. Wang, L. Qiu, S.-Jin R. Lee, Nolan R. Campbell, N. DeStefino, Michael J. Goard, Z. Fu, R. Yasuda, Loren L. Looger, Benjamin R. Arenkiel, W.-B. Gan, G. Feng, Imaging Neural Activity Using Thy1-GCaMP Transgenic Mice, *Neuron* 76(2) (2012) 297-308.
- [56] R.P. Paras, Z. Huanan, T.R. Matthew, B.N. Justin, P.M. Shaun, J.K. Michael, D.Y.K. Takashi, A.K. Nicholas, A.C. Cynthia, Chronic in vivo stability assessment of carbon fiber microelectrode arrays, *Journal of Neural Engineering* 13(6) (2016) 066002.
- [57] R.P. Paras, N. Kyoungwan, Z. Huanan, D.Y.K. Takashi, A.K. Nicholas, Y. Euisik, A.C. Cynthia, Insertion of linear 8.4  $\mu$  m diameter 16 channel carbon fiber electrode arrays for single unit recordings, *Journal of Neural Engineering* 12(4) (2015) 046009.
- [58] T.D.Y. Kozai, K. Catt, Z. Du, K. Na, O. Srivannavit, R.-u.M. Haque, J. Seymour, K.D. Wise, E. Yoon, X.T. Cui, Chronic in vivo evaluation of PEDOT/CNT for stable neural recordings, *IEEE transactions on bio-medical engineering* 63(1) (2016) 111-119.
- [59] L. Luan, X. Wei, Z. Zhao, J.J. Siegel, O. Potnis, C.A. Tuppen, S. Lin, S. Kazmi, R.A. Fowler, S. Holloway, A.K. Dunn, R.A. Chitwood, C. Xie, Ultraflexible nanoelectronic probes form reliable, glial scar-free neural integration, *Science Advances* 3(2) (2017) e1601966.
- [60] C. Xie, J. Liu, T.-M. Fu, X. Dai, W. Zhou, C.M. Lieber, Three-dimensional macroporous nanoelectronic networks as minimally invasive brain probes, *Nat Mater* 14(12) (2015) 1286-1292.
- [61] C. Xie, Z. Lin, L. Hanson, Y. Cui, B. Cui, Intracellular Recording of Action Potentials by Nanopillar Electroporation, *Nature nanotechnology* 7(3) (2012) 185-190.
- [62] M. Kang, S. Jung, H. Zhang, T. Kang, H. Kang, Y. Yoo, J.-P. Hong, J.-P. Ahn, J. Kwak, D. Jeon, N.A. Kotov, B. Kim, Subcellular Neural Probes from Single-Crystal Gold Nanowires, *ACS Nano* 8(8) (2014) 8182-8189.

- [63] T.D. Kozai, N.B. Langhals, P.R. Patel, X. Deng, H. Zhang, K.L. Smith, J. Lahann, N.A. Kotov, D.R. Kipke, Ultrasmall implantable composite microelectrodes with bioactive surfaces for chronic neural interfaces, *Nat Mater* 11(12) (2012) 1065-73.
- [64] P.R. Patel, H. Zhang, M.T. Robbins, J.B. Nofar, S.P. Marshall, M.J. Kobylarek, T.D. Kozai, N.A. Kotov, C.A. Chestek, Chronic in vivo stability assessment of carbon fiber microelectrode arrays, *J Neural Eng* 13(6) (2016) 066002.
- [65] G. Guitchounts, J.E. Markowitz, W.A. Liberti, T.J. Gardner, A carbon-fiber electrode array for long-term neural recording, *J Neural Eng* 10(4) (2013) 046016.
- [66] T.M. Fu, G.S. Hong, T. Zhou, T.G. Schuhmann, R.D. Viveros, C.M. Lieber, Stable long-term chronic brain mapping at the single-neuron level, *Nature Methods* 13(10) (2016) 875-+.
- [67] H. Fang, J. Zhao, K.J. Yu, E. Song, A.B. Farimani, C.-H. Chiang, X. Jin, Y. Xue, D. Xu, W. Du, K.J. Seo, Y. Zhong, Z. Yang, S.M. Won, G. Fang, S.W. Choi, S. Chaudhuri, Y. Huang, M.A. Alam, J. Viventi, N.R. Aluru, J.A. Rogers, Ultrathin, transferred layers of thermally grown silicon dioxide as biofluid barriers for biointegrated flexible electronic systems, *Proceedings of the National Academy of Sciences* 113(42) (2016) 11682-11687.
- [68] X. Xie, L. Rieth, L. Williams, S. Negi, R. Bhandari, R. Caldwell, R. Sharma, P. Tathireddy, F. Solzbacher, Long-term reliability of Al<sub>2</sub>O<sub>3</sub> and Parylene C bilayer encapsulated Utah electrode array based neural interfaces for chronic implantation, *J Neural Eng* 11(2) (2014) 026016.
- [69] X. Cui, Lee, V. A., Raphael, Y., Wiler, J. A., Hetke, J. F., Anderson, D. J. and Martin, D. C., Surface modification of neural recording electrodes with conducting polymer/biomolecule blends, *J. Biomed. Mater. Res.* 56 (2001) 261-272.
- [70] K.A. Ludwig, J.D. Uram, J. Yang, D.C. Martin, D.R. Kipke, Chronic neural recordings using silicon microelectrode arrays electrochemically deposited with a poly(3,4-ethylenedioxythiophene) (PEDOT) film, *J Neural Eng* 3(1) (2006) 59-70.
- [71] C.L. Weaver, J.M. LaRosa, X. Luo, X.T. Cui, Electrically Controlled Drug Delivery from Graphene Oxide Nanocomposite Films, *ACS Nano* 8(2) (2014) 1834-1843.
- [72] L. Ouyang, C.-c. Kuo, B. Farrell, S. Pathak, B. Wei, J. Qu, D.C. Martin, Poly[3,4-ethylene dioxythiophene (EDOT)-co-1,3,5-tri[2-(3,4-ethylene dioxythienyl)]-benzene (EPh)] copolymers (PEDOT-co-EPh): optical, electrochemical and mechanical properties, *Journal of Materials Chemistry B* 3(25) (2015) 5010-5020.
- [73] B. Wei, L. Ouyang, J. Liu, D.C. Martin, Post-polymerization functionalization of poly(3,4-propylenedioxythiophene) (PProDOT) via thiol-ene "click" chemistry, *Journal of Materials Chemistry B* 3(25) (2015) 5028-5034.
- [74] N. Bhagwat, K.L. Kiick, D.C. Martin, Electrochemical deposition and characterization of carboxylic acid functionalized PEDOT copolymers, *Journal of Materials Research* 29(23) (2014) 2835-2844.

- [75] L.K. Povlich, J.C. Cho, M.K. Leach, J.M. Corey, J. Kim, D.C. Martin, Synthesis, copolymerization and peptide-modification of carboxylic acid-functionalized 3,4-ethylenedioxythiophene (EDOTacid) for neural electrode interfaces, *Biochimica et Biophysica Acta (BBA) - General Subjects* 1830(9) (2013) 4288-4293.
- [76] Y.W. Fan, F.Z. Cui, S.P. Hou, Q.Y. Xu, L.N. Chen, I.S. Lee, Culture of neural cells on silicon wafers with nano-scale surface topography, *Journal of Neuroscience Methods* 120(1) (2002) 17-23.
- [77] C.D. Johnson, A.R. D'Amato, D.L. Puhl, D.M. Wich, A. Vesperman, R.J. Gilbert, Electrospun fiber surface nanotopography influences astrocyte-mediated neurite outgrowth, *Biomedical Materials* 13(5) (2018) 054101.
- [78] J. Xie, M.R. MacEwan, X. Li, S.E. Sakiyama-Elbert, Y. Xia, Neurite Outgrowth on Nanofiber Scaffolds with Different Orders, Structures, and Surface Properties, *ACS Nano* 3(5) (2009) 1151-1159.
- [79] H.S. Yoo, T.G. Kim, T.G. Park, Surface-functionalized electrospun nanofibers for tissue engineering and drug delivery, *Advanced Drug Delivery Reviews* 61(12) (2009) 1033-1042.
- [80] V. Mahairaki, S.H. Lim, G.T. Christopherson, L. Xu, I. Nasonkin, C. Yu, H.-Q. Mao, V.E. Koliatsos, Nanofiber Matrices Promote the Neuronal Differentiation of Human Embryonic Stem Cell-Derived Neural Precursors In Vitro, *Tissue Engineering Part A* 17(5-6) (2010) 855-863.
- [81] E. Migliorini, G. Greci, J. Ban, A. Pozzato, M. Tormen, M. Lazzarino, V. Torre, M.E. Ruaro, Acceleration of neuronal precursors differentiation induced by substrate nanotopography, *Biotechnology and Bioengineering* 108(11) (2011) 2736-2746.
- [82] L. Song, K. Wang, Y. Li, Y. Yang, Nanotopography promoted neuronal differentiation of human induced pluripotent stem cells, *Colloids and Surfaces B: Biointerfaces* 148 (2016) 49-58.
- [83] T. Posati, A. Pistone, E. Saracino, F. Formaggio, M.G. Mola, E. Troni, A. Sagnella, M. Nocchetti, M. Barbalinardo, F. Valle, S. Bonetti, M. Caprini, G.P. Nicchia, R. Zamboni, M. Muccini, V. Benfenati, A Nanoscale Interface Promoting Molecular and Functional Differentiation of Neural Cells, *Sci Rep* 6 (2016) 31226.
- [84] H.K. Kim, E. Kim, H. Jang, Y.-K. Kim, K. Kang, Neuron–Material Nanointerfaces: Surface Nanotopography Governs Neuronal Differentiation and Development, *ChemNanoMat* 3(5) (2017) 278-287.
- [85] E.E. S., S.C. S., M.S. M., C. Keying, F. He, C.J. R., The Neuroinflammatory Response to Nanopatterning Parallel Grooves into the Surface Structure of Intracortical Microelectrodes, *Advanced Functional Materials* 28(12) (2018) 1704420.
- [86] S.P. Khan, G.G. Auner, G.M. Newaz, Influence of nanoscale surface roughness on neural cell attachment on silicon, *Nanomedicine: Nanotechnology, Biology and Medicine* 1(2) (2005) 125-129.

- [87] E.S. Ereifej, H.W. Matthew, G. Newaz, A. Mukhopadhyay, G. Auner, I. Salakhutdinov, P.J. VandeVord, Nanopatterning effects on astrocyte reactivity, *Journal of Biomedical Materials Research Part A* 101A(6) (2013) 1743-1757.
- [88] J. BJKim, SAHara,CDLee1,LYu, C A Gutierrez, T Q Hoang,V Pikov, E Meng, 3D Parylene sheath neural probe for chronic recordings, *JOURNAL OF NEURAL ENGINEERING* 10 (2013).
- [89] L.B.-K. Moshe David-Pur, Giora Beit-Yaakov, Dorit Raz-Prag, Yael Hanein, All-carbon-nanotube flexible multi-electrode array for neuronal recording and stimulation, *Biomed Microdevices* 16 (2014) 43-53.
- [90] F. Vitale, S.R. Summerson, B. Aazhang, C. Kemere, M. Pasquali, Neural Stimulation and Recording with Bidirectional, Soft Carbon Nanotube Fiber Microelectrodes, *ACS Nano* 9(4) (2015) 4465-4474.
- [91] G.S.G. Liang Guo, Xi Liu, Christopher Tuthill, T. Richard Nichols, and Stephen P. DeWeerth, A PDMS-Based Integrated Stretchable Microelectrode Array (isMEA) for Neural and Muscular Surface Interfacing, *IEEE TRANSACTIONS ON BIOMEDICAL CIRCUITS AND SYSTEMS* 7 (2013).
- [92] M.M. Liang Guo , Ning Zhang , Robert Langer , and Daniel G. Anderson, Stretchable Polymeric Multielectrode Array for Conformal Neural Interfacing, *Advanced Materials* 26 (2013) 1427-1433.
- [93] Z.J. Du, C.L. Kolarcik, T.D. Kozai, S.D. Luebben, S.A. Sapp, X.S. Zheng, J.A. Nabity, X.T. Cui, Ultrasoft microwire neural electrodes improve chronic tissue integration, *Acta Biomater* (2017).
- [94] L. Luan, X. Wei, Z. Zhao, J.J. Siegel, O. Potnis, C.A. Tuppen, S. Lin, S. Kazmi, R.A. Fowler, S. Holloway, A.K. Dunn, R.A. Chitwood, C. Xie, Ultraflexible nanoelectronic probes form reliable, glial scar-free neural integration, *Sci Adv* 3(2) (2017) e1601966.
- [95] R. Khilwani, P.J. Gilgunn, T.D. Kozai, X.C. Ong, E. Korkmaz, P.K. Gunalan, X.T. Cui, G.K. Fedder, O.B. Ozdoganlar, Ultra-miniature ultra-compliant neural probes with dissolvable delivery needles: design, fabrication and characterization, *Biomed Microdevices* 18(6) (2016) 97.
- [96] L.W.T. Fan Wu, Member, Fujun Chen, Joshua D. Berke, David L. Kaplan, and Euisik Yoon, Silk-Backed Structural Optimization of High-Density Flexible Intracortical Neural Probes, *JOURNAL OF MICROELECTROMECHANICAL SYSTEMS*, 24 (2015) 62-69.
- [97] M.I. Fan Wu, and Euisik Yoon, A FLEXIBLE FISH-BONE-SHAPED NEURAL PROBE STRENGTHENED BY BIODEGRADABLE SILK COATING FOR ENHANCED BIOCOMPATIBILITY, *Transducers* 11 (2011) 966-969.
- [98] T.D.Y. Kozai, Z. Gugel, X. Li, P.J. Gilgunn, R. Khilwani, O.B. Ozdoganlar, G.K. Fedder, D.J. Weber, X.T. Cui, Chronic tissue response to carboxymethyl cellulose based dissolvable insertion needle for ultra-small neural probes, *Biomaterials* 35(34) (2014) 9255-9268.

- [99] J. Liu, T.-M. Fu, Z. Cheng, G. Hong, T. Zhou, L. Jin, M. Duvvuri, Z. Jiang, P. Kruskal, C. Xie, Z. Suo, Y. Fang, C.M. Lieber, Syringe injectable electronics, *Nature nanotechnology* 10(7) (2015) 629-636.
- [100] S.H. Felix, Shah, K. G., Tolosa, V. M., Sheth, H. J., Tooker, A. C., Delima, T. L., Shantanu P. Jadhav, Loren M. Frank, Satinderpall S. Pannu, Neural Probes Using Rigid Stiffeners Attached with Biodissolvable Adhesive, *J. Vis. Exp.* 79 (2013).
- [101] T. Zhou, G. Hong, T.M. Fu, X. Yang, T.G. Schuhmann, R.D. Viveros, C.M. Lieber, Syringe-injectable mesh electronics integrate seamlessly with minimal chronic immune response in the brain, *Proc Natl Acad Sci U S A* 114(23) (2017) 5894-5899.
- [102] I.D. Dryg, M.P. Ward, K.Y. Qing, H. Mei, J.E. Schaffer, P.P. Irazoqui, Magnetically Inserted Neural Electrodes: Tissue Response and Functional Lifetime, *IEEE Transactions on Neural Systems and Rehabilitation Engineering* 23(4) (2015) 562-571.
- [103] M. Jorfi, J.L. Skousen, C. Weder, J.R. Capadona, Progress Towards Biocompatible Intracortical Microelectrodes for Neural Interfacing Applications, *Journal of neural engineering* 12(1) (2015) 011001-011001.
- [104] T. Ware, D. Simon, R.L. Rennaker, W. Voit, Smart Polymers for Neural Interfaces, *Polymer Reviews* 53(1) (2013) 108-129.
- [105] J.S. Neil T. Markwardt, Robert L. Rennaker II, Sub-meninges Implantation Reduces Immune Response to Neural Implants, *J Neurosci Method* 214(2) (2013) 119–125.
- [106] J.M.C. Dongjin Seo, Jan M. Rabaey, Elad Alon, Michel M. Maharbiz, Neural Dust: An Ultrasonic, Low Power Solution for Chronic Brain-Machine Interfaces, (2013).
- [107] D. Seo, J.M. Carmena, J.M. Rabaey, M.M. Maharbiz, E. Alon, Model validation of untethered, ultrasonic neural dust motes for cortical recording, *Journal of Neuroscience Methods* 244 (2015) 114-122.
- [108] P. Yeon, S. Mirbozorgi, B. Ash, H. Eckhardt, M. Ghovanloo, Fabrication and Microassembly of a mm-Sized Floating Probe for a Distributed Wireless Neural Interface, *Micromachines* 7(9) (2016) 154.
- [109] K.A. Potter, M. Jorfi, K.T. Householder, E.J. Foster, C. Weder, J.R. Capadona, Curcumin-releasing mechanically adaptive intracortical implants improve the proximal neuronal density and blood–brain barrier stability, *Acta Biomaterialia* 10(5) (2014) 2209-2222.
- [110] Y. Zhong, R.V. Bellamkonda, Controlled release of anti-inflammatory agent  $\alpha$ -MSH from neural implants, *Journal of Controlled Release* 106(3) (2005) 309-318.
- [111] S.-C.L. Bo Zhu, Haichao Zhao, Hsing-An Lin, Jun Sekine, Aiko Nakao, Chi Chen, Yoshiro Yamashita, & Hsiao-hua Yu, Large enhancement in neurite outgrowth on a cell membrane-mimicking conducting polymer, *Nature Communications* (2014).

- [112] C.L. Kolarcik, D. Bourbeau, E. Azemi, E. Rost, L. Zhang, C.F. Lagenaur, D.J. Weber, X.T. Cui, In vivo effects of L1 coating on inflammation and neuronal health at the electrode/tissue interface in rat spinal cord and dorsal root ganglion, *Acta biomaterialia* 8(10) (2012) 3561-3575.
- [113] T.D.Y. Kozai, A.S. Jaquins-Gerstl, A.L. Vazquez, A.C. Michael, X.T. Cui, Dexamethasone retrodialysis attenuates microglial response to implanted probes in vivo, *Biomaterials* 87 (2016) 157-169.
- [114] K.A. Potter-Baker, W.G. Stewart, W.H. Tomaszewski, C.T. Wong, W.D. Meador, N.P. Ziats, J.R. Capadona, Implications of Chronic Daily Anti-Oxidant Administration on the Inflammatory Response to Intracortical Microelectrodes, *Journal of neural engineering* 12(4) (2015) 046002-046002.
- [115] S. Spieth, A. Schumacher, F. Trenkle, O. Brett, K. Seidl, S. Herwik, S. Kisban, P. Ruther, O. Paul, A.A. Aarts Arno, P. Neves Hercules, P.D. Rich, E. Theobald David, T. Holtzman, W. Dalley Jeffrey, B.-E. Verhoef, P. Janssen, R. Zengerle, Approaches for drug delivery with intracortical probes, *Biomedical Engineering / Biomedizinische Technik*, 2014, p. 291.
- [116] P.M. Ivan R. Minev, Arthur Hirsch, Quentin Barraud, Nikolaus Wenger, Eduardo Martin Moraud, Jérôme Gandar, Marco Capogrosso, Tomislav Milekovic, Léonie Asboth, Rafael Fajardo Torres, Nicolas Vachicouras, Qihan Liu, Natalia Pavlova, Simone Duis, Alexandre Larmagnac, Janos Vörös, Silvestro Micera, Zhigang Suo, Grégoire Courtine, Stéphanie P. Lacour, Electronic dura mater for long-term multimodal neural interfaces, *Science* 347(6218) (2015) 159-163.
- [117] A. Canales, X. Jia, U.P. Frieriep, R.A. Koppes, C.M. Tringides, J. Selvidge, C. Lu, C. Hou, L. Wei, Y. Fink, P. Anikeeva, Multifunctional fibers for simultaneous optical, electrical and chemical interrogation of neural circuits in vivo, *Nat Biotechnol* 33(3) (2015) 277-84.
- [118] X. Luo, C. Matranga, S. Tan, N. Alba, X.T. Cui, Carbon nanotube nanoreservoir for controlled release of anti-inflammatory dexamethasone, *Biomaterials* 32(26) (2011) 6316-6323.
- [119] C.L. Kolarcik, K. Catt, E. Rost, I.N. Albrecht, D. Bourbeau, Z. Du, T.D. Kozai, X. Luo, D.J. Weber, X.T. Cui, Evaluation of poly(3,4-ethylenedioxythiophene)/carbon nanotube neural electrode coatings for stimulation in the dorsal root ganglion, *J Neural Eng* 12(1) (2015) 016008.
- [120] K.M. Woepfel, X.T. Cui, Neural Drug Delivery, in: N.V. Thakor (Ed.), *Handbook of Neuroengineering*, Springer Singapore, Singapore, 2020, pp. 1-41.
- [121] A. Golabchi, B. Wu, X. Li, D.L. Carlisle, T.D.Y. Kozai, R.M. Friedlander, X.T. Cui, Melatonin improves quality and longevity of chronic neural recording, *Biomaterials* 180 (2018) 225-239.
- [122] A.P.-B. Kelsey, G.S. Wade, H.T. William, T.W. Chun, D.M. William, P.Z. Nicholas, R.C. Jeffrey, Implications of chronic daily anti-oxidant administration on the inflammatory response to intracortical microelectrodes, *Journal of Neural Engineering* 12(4) (2015) 046002.

- [123] K.A. Potter, A.C. Buck, W.K. Self, M.E. Callanan, S. Sunil, J.R. Capadona, The effect of resveratrol on neurodegeneration and blood brain barrier stability surrounding intracortical microelectrodes, *Biomaterials* 34(29) (2013) 7001-7015.
- [124] R.L. Rennaker, J. Miller, H. Tang, D.A. Wilson, Minocycline increases quality and longevity of chronic neural recordings, *Journal of Neural Engineering* 4(2) (2007) L1-L5.
- [125] T.D.Y. Kozai, A.S. Jaquins-Gerstl, A.L. Vazquez, A.C. Michael, X.T. Cui, Dexamethasone retrodialysis attenuates microglial response to implanted probes in vivo, *Biomaterials* 87(Supplement C) (2016) 157-169.
- [126] A. Jaquins-Gerstl, Z. Shu, J. Zhang, Y. Liu, S.G. Weber, A.C. Michael, Effect of Dexamethasone on Gliosis, Ischemia, and Dopamine Extraction during Microdialysis Sampling in Brain Tissue, *Analytical Chemistry* 83(20) (2011) 7662-7667.
- [127] K.A. Potter-Baker, J.R. Capadona, Reducing the “Stress”: Antioxidative Therapeutic and Material Approaches May Prevent Intracortical Microelectrode Failure, *ACS Macro Letters* 4(3) (2015) 275-279.
- [128] P. Takmakov, K. Ruda, K. Scott Phillips, I.S. Isayeva, V. Krauthamer, C.G. Welle, Rapid evaluation of the durability of cortical neural implants using accelerated aging with reactive oxygen species, *Journal of Neural Engineering* 12(2) (2015) 026003.
- [129] K. Park, Controlled drug delivery systems: Past forward and future back, *Journal of Controlled Release* 190 (2014) 3-8.
- [130] K. Catt, H. Li, V. Hoang, R. Beard, X.T. Cui, Self-powered therapeutic release from conducting polymer/graphene oxide films on magnesium, *Nanomedicine: Nanotechnology, Biology and Medicine* 14(7) (2018) 2495-2503.
- [131] S. Carli, C. Trapella, A. Armirotti, A. Fantinati, G. Ottonello, A. Scarpellini, M. Prato, L. Fadiga, D. Ricci, Biochemically Controlled Release of Dexamethasone Covalently Bound to PEDOT, *Chemistry – A European Journal* 24(41) (2018) 10300-10305.
- [132] S. Yang, D. Zhang, Z. Yang, X. Hu, S. Qian, J. Liu, B. Wilson, M. Block, J.-S. Hong, Curcumin Protects Dopaminergic Neuron Against LPS Induced Neurotoxicity in Primary Rat Neuron/Glia Culture, *Neurochemical Research* 33(10) (2008) 2044-2053.
- [133] K.A. Potter-Baker, J.K. Nguyen, K.M. Kovach, M.M. Gitomer, T.W. Srail, W.G. Stewart, J.L. Skousen, J.R. Capadona, Development of superoxide dismutase mimetic surfaces to reduce accumulation of reactive oxygen species for neural interfacing applications, *Journal of Materials Chemistry B* 2(16) (2014) 2248-2258.
- [134] J.E. John, S.L. Baptiste, L.G. Sheffield, H. von Gizycki, R.I. Kuzniecky, O. Devinsky, N. Ludvig, Transmeningeal delivery of GABA to control neocortical seizures in rats, *Epilepsy Research* 75(1) (2007) 10-17.

- [135] J. Du Zhanhong, G.Q. Bi, T. Cui Xinyan, Electrically Controlled Neurochemical Release from Dual-Layer Conducting Polymer Films for Precise Modulation of Neural Network Activity in Rat Barrel Cortex, *Advanced Functional Materials* 28(12) (2017) 1703988.
- [136] L. Tian, S.A. Hires, T. Mao, D. Huber, M.E. Chiappe, S.H. Chalasani, L. Petreanu, J. Akerboom, S.A. McKinney, E.R. Schreiter, C.I. Bargmann, V. Jayaraman, K. Svoboda, L.L. Looger, Imaging neural activity in worms, flies and mice with improved GCaMP calcium indicators, *Nature Methods* 6 (2009) 875.
- [137] E. Shigetomi, E.A. Bushong, M.D. Haustein, X. Tong, O. Jackson-Weaver, S. Kracun, J. Xu, M.V. Sofroniew, M.H. Ellisman, B.S. Khakh, Imaging calcium microdomains within entire astrocyte territories and endfeet with GCaMPs expressed using adeno-associated viruses, *The Journal of General Physiology* 141(5) (2013) 633.
- [138] C. Van den Haute, K. Eggermont, B. Nuttin, Z. Debyser, V. Baekelandt, Lentiviral Vector-Mediated Delivery of Short Hairpin RNA Results in Persistent Knockdown of Gene Expression in Mouse Brain, *Human Gene Therapy* 14(18) (2003) 1799-1807.
- [139] Z. Hassani, G.F. Lemkine, P. Erbacher, K. Palmier, G. Alfama, C. Giovannangeli, J.-P. Behr, B.A. Demeneix, Lipid-mediated siRNA delivery down-regulates exogenous gene expression in the mouse brain at picomolar levels, *The Journal of Gene Medicine* 7(2) (2005) 198-207.
- [140] S.T. Retterer, K.L. Smith, C.S. Bjornsson, J.N. Turner, M.S. Isaacson, W. Shain, Constant pressure fluid infusion into rat neocortex from implantable microfluidic devices, *Journal of Neural Engineering* 5(4) (2008) 385-391.
- [141] Y.C. Michael, R.L. Russell, F.M. Paul, S.G. Lance, H.O. Edward, Variables affecting convection-enhanced delivery to the striatum: a systematic examination of rate of infusion, cannula size, infusate concentration, and tissue—cannula sealing time, *Journal of Neurosurgery* 90(2) (1999) 315-320.
- [142] I.R. Mineev, P. Musienko, A. Hirsch, Q. Barraud, N. Wenger, E.M. Moraud, J. Gandar, M. Capogrosso, T. Milekovic, L. Asboth, R.F. Torres, N. Vachicouras, Q. Liu, N. Pavlova, S. Duis, A. Larmagnac, J. Vörös, S. Micera, Z. Suo, G. Courtine, S.P. Lacour, Electronic dura mater for long-term multimodal neural interfaces, *Science* 347(6218) (2015) 159.
- [143] S. Takeuchi, D. Ziegler, Y. Yoshida, K. Mabuchi, T. Suzuki, Parylene flexible neural probes integrated with microfluidic channels, *Lab on a Chip* 5(5) (2005) 519-523.
- [144] K. Seidl, S. Spieth, S. Herwik, J. Steigert, R. Zengerle, O. Paul, P. Ruther, In-plane silicon probes for simultaneous neural recording and drug delivery, *Journal of Micromechanics and Microengineering* 20(10) (2010) 105006.
- [145] I. Kalus, B. Schnegelsberg, N.G. Seidah, R. Kleene, M. Schachner, The proprotein convertase PC5A and a metalloprotease are involved in the proteolytic processing of the neural adhesion molecule L1, *J Biol Chem* 278 (2003).

- [146] D.L. Hunt, C. Lai, R.D. Smith, A.K. Lee, T.D. Harris, M. Barbic, Multimodal in vivo brain electrophysiology with integrated glass microelectrodes, *Nature Biomedical Engineering* (2019).
- [147] K. Gao, G. Li, L. Liao, J. Cheng, J. Zhao, Y. Xu, Fabrication of flexible microelectrode arrays integrated with microfluidic channels for stable neural interfaces, *Sensors and Actuators A: Physical* 197 (2013) 9-14.
- [148] A. Canales, X. Jia, U.P. Froriep, R.A. Koppes, C.M. Tringides, J. Selvidge, C. Lu, C. Hou, L. Wei, Y. Fink, P. Anikeeva, Multifunctional fibers for simultaneous optical, electrical and chemical interrogation of neural circuits in vivo, *Nature Biotechnology* 33 (2015) 277.
- [149] H.J. Lee, Y. Son, J. Kim, C.J. Lee, E.-S. Yoon, I.-J. Cho, A multichannel neural probe with embedded microfluidic channels for simultaneous in vivo neural recording and drug delivery, *Lab on a Chip* 15(6) (2015) 1590-1597.
- [150] C. Dagdeviren, K.B. Ramadi, P. Joe, K. Spencer, H.N. Schwerdt, H. Shimazu, S. Delcasso, K.-i. Amemori, C. Nunez-Lopez, A.M. Graybiel, M.J. Cima, R. Langer, Miniaturized neural system for chronic, local intracerebral drug delivery, *Science Translational Medicine* 10(425) (2018) eaan2742.
- [151] L. Erdmann, B. Macedo, K.E. Uhrich, Degradable poly(anhydride ester) implants: effects of localized salicylic acid release on bone, *Biomaterials* 21(24) (2000) 2507-2512.
- [152] A. Göpferich, Mechanisms of polymer degradation and erosion, *Biomaterials* 17(2) (1996) 103-114.
- [153] A. Göpferich, J. Tessmar, Polyanhydride degradation and erosion, *Advanced Drug Delivery Reviews* 54(7) (2002) 911-931.
- [154] N. Kamaly, B. Yameen, J. Wu, O.C. Farokhzad, Degradable Controlled-Release Polymers and Polymeric Nanoparticles: Mechanisms of Controlling Drug Release, *Chemical Reviews* 116(4) (2016) 2602-2663.
- [155] M. Westphal, Z. Ram, V. Riddle, D. Hilt, E. Bortey, G. On behalf of the Executive Committee of the Gliadel® Study, Gliadel® wafer in initial surgery for malignant glioma: long-term follow-up of a multicenter controlled trial, *Acta Neurochirurgica* 148(3) (2006) 269-275.
- [156] J. Perry, A. Chambers, K. Spithoff, N. Laperriere, Gliadel wafers in the treatment of malignant glioma: a systematic review, *Curr Oncol* 14(5) (2007) 189-194.
- [157] X. Hu, S. Liu, G. Zhou, Y. Huang, Z. Xie, X. Jing, Electrospinning of polymeric nanofibers for drug delivery applications, *Journal of Controlled Release* 185 (2014) 12-21.
- [158] M. Elsbahy, K.L. Wooley, Design of polymeric nanoparticles for biomedical delivery applications, *Chemical Society Reviews* 41(7) (2012) 2545-2561.

- [159] K.C. Spencer, J.C. Sy, K.B. Ramadi, A.M. Graybiel, R. Langer, M.J. Cima, Characterization of Mechanically Matched Hydrogel Coatings to Improve the Biocompatibility of Neural Implants, *Scientific Reports* 7(1) (2017) 1952.
- [160] D. Macaya, M. Spector, Injectable hydrogel materials for spinal cord regeneration: a review, *Biomedical Materials* 7(1) (2012) 012001.
- [161] D.-H. Kim, D.C. Martin, Sustained release of dexamethasone from hydrophilic matrices using PLGA nanoparticles for neural drug delivery, *Biomaterials* 27(15) (2006) 3031-3037.
- [162] M.R. Abidian, D.C. Martin, Multifunctional Nanobiomaterials for Neural Interfaces, *Advanced Functional Materials* 19(4) (2009) 573-585.
- [163] Y. Zhong, R.V. Bellamkonda, Dexamethasone-coated neural probes elicit attenuated inflammatory response and neuronal loss compared to uncoated neural probes, *Brain Research* 1148 (2007) 15-27.
- [164] S.J. Park, Y.J. Lee, D.N. Heo, I.K. Kwon, K.-S. Yun, J.Y. Kang, S.H. Lee, Functional nerve cuff electrode with controllable anti-inflammatory drug loading and release by biodegradable nanofibers and hydrogel deposition, *Sensors and Actuators B: Chemical* 215 (2015) 133-141.
- [165] D.N. Heo, S.-J. Song, H.-J. Kim, Y.J. Lee, W.-K. Ko, S.J. Lee, D. Lee, S.J. Park, L.G. Zhang, J.Y. Kang, S.H. Do, S.H. Lee, I.K. Kwon, Multifunctional hydrogel coatings on the surface of neural cuff electrode for improving electrode-nerve tissue interfaces, *Acta Biomaterialia* 39 (2016) 25-33.
- [166] S.J. Jhaveri, M.R. Hynd, N. Dowell-Mesfin, J.N. Turner, W. Shain, C.K. Ober, Release of Nerve Growth Factor from HEMA Hydrogel-Coated Substrates and Its Effect on the Differentiation of Neural Cells, *Biomacromolecules* 10(1) (2009) 174-183.
- [167] K. Möller, J. Kobler, T. Bein, Colloidal Suspensions of Nanometer-Sized Mesoporous Silica, *Advanced Functional Materials* 17(4) (2007) 605-612.
- [168] F. Tang, L. Li, D. Chen, Mesoporous Silica Nanoparticles: Synthesis, Biocompatibility and Drug Delivery, *Advanced Materials* 24(12) (2012) 1504-1534.
- [169] V. Cauda, A. Schlossbauer, T. Bein, Bio-degradation study of colloidal mesoporous silica nanoparticles: Effect of surface functionalization with organo-silanes and poly(ethylene glycol), *Microporous and Mesoporous Materials* 132(1) (2010) 60-71.
- [170] Q. He, Z. Zhang, F. Gao, Y. Li, J. Shi, In vivo Biodistribution and Urinary Excretion of Mesoporous Silica Nanoparticles: Effects of Particle Size and PEGylation, *Small* 7(2) (2011) 271-280.
- [171] J. Kobler, K. Möller, T. Bein, Colloidal Suspensions of Functionalized Mesoporous Silica Nanoparticles, *ACS Nano* 2(4) (2008) 791-799.

- [172] K.M. Woepfel, X.S. Zheng, X.T. Cui, Enhancing surface immobilization of bioactive molecules via a silica nanoparticle based coating, *Journal of Materials Chemistry B* 6(19) (2018) 3058-3067.
- [173] M. Benezra, O. Penate-Medina, P.B. Zanzonico, D. Schaer, H. Ow, A. Burns, E. DeStanchina, V. Longo, E. Herz, S. Iyer, J. Wolchok, S.M. Larson, U. Wiesner, M.S. Bradbury, Multimodal silica nanoparticles are effective cancer-targeted probes in a model of human melanoma, *The Journal of Clinical Investigation* 121(7) (2011) 2768-2780.
- [174] F. Yan, Y. Wang, S. He, S. Ku, W. Gu, L. Ye, Transferrin-conjugated, fluorescein-loaded magnetic nanoparticles for targeted delivery across the blood-brain barrier, *Journal of Materials Science: Materials in Medicine* 24(10) (2013) 2371-2379.
- [175] D.C. Martin, Molecular design, synthesis, and characterization of conjugated polymers for interfacing electronic biomedical devices with living tissue, *MRS Communications* 5(2) (2015) 131-153.
- [176] J.-W. Lee, F. Serna, J. Nickels, C.E. Schmidt, Carboxylic Acid-Functionalized Conductive Polypyrrole as a Bioactive Platform for Cell Adhesion, *Biomacromolecules* 7(6) (2006) 1692-1695.
- [177] G. Oyman, C. Geyik, R. Ayranci, M. Ak, D. Odaci Demirkol, S. Timur, H. Coskunol, Peptide-modified conducting polymer as a biofunctional surface: monitoring of cell adhesion and proliferation, *RSC Advances* 4(96) (2014) 53411-53418.
- [178] B. Wei, J. Liu, L. Ouyang, C.-C. Kuo, D.C. Martin, Significant Enhancement of PEDOT Thin Film Adhesion to Inorganic Solid Substrates with EDOT-Acid, *ACS Applied Materials & Interfaces* 7(28) (2015) 15388-15394.
- [179] N. Bhagwat, R.E. Murray, S.I. Shah, K.L. Kiick, D.C. Martin, Biofunctionalization of PEDOT films with laminin-derived peptides, *Acta Biomaterialia* 41 (2016) 235-246.
- [180] B. Wu, B. Cao, I.M. Taylor, K. Woepfel, X.T. Cui, Facile Synthesis of a 3,4-Ethylene-Dioxythiophene (EDOT) Derivative for Ease of Bio-Functionalization of the Conducting Polymer PEDOT, *Frontiers in chemistry* 7 (2019) 178-178.
- [181] X. Cui, D.C. Martin, Electrochemical deposition and characterization of poly(3,4-ethylenedioxythiophene) on neural microelectrode arrays, *Sensors and Actuators B: Chemical* 89(1) (2003) 92-102.
- [182] X. Luo, C.L. Weaver, D.D. Zhou, R. Greenberg, X.T. Cui, Highly stable carbon nanotube doped poly(3,4-ethylenedioxythiophene) for chronic neural stimulation, *Biomaterials* 32(24) (2011) 5551-5557.
- [183] D. Svirskis, J. Travas-Sejdic, A. Rodgers, S. Garg, Electrochemically controlled drug delivery based on intrinsically conducting polymers, *Journal of Controlled Release* 146(1) (2010) 6-15.

- [184] C. Boehler, F. Oberueber, M. Asplund, Tuning drug delivery from conducting polymer films for accurately controlled release of charged molecules, *Journal of Controlled Release* 304 (2019) 173-180.
- [185] C. Boehler, C. Kleber, N. Martini, Y. Xie, I. Dryg, T. Stieglitz, U.G. Hofmann, M. Asplund, Actively controlled release of Dexamethasone from neural microelectrodes in a chronic in vivo study, *Biomaterials* 129 (2017) 176-187.
- [186] K. Krukiewicz, J.K. Zak, Conjugated polymers as robust carriers for controlled delivery of anti-inflammatory drugs, *Journal of Materials Science* 49(16) (2014) 5738-5745.
- [187] P.M. George, D.A. LaVan, J.A. Burdick, C.Y. Chen, E. Liang, R. Langer, Electrically Controlled Drug Delivery from Biotin-Doped Conductive Polypyrrole, *Advanced Materials* 18(5) (2006) 577-581.
- [188] W.R. Stauffer, X.T. Cui, Polypyrrole doped with 2 peptide sequences from laminin, *Biomaterials* 27(11) (2006) 2405-2413.
- [189] X. Cui, Lee, V. A., Raphael, Y., Wiler, J. A., Hetke, J. F., Anderson, D. J. and Martin, D. C., Surface modification of neural recording electrodes with conducting polymer/biomolecule blends, *Journal of biomedical materials research* 56 (2001) 261-272.
- [190] R.T. Richardson, B. Thompson, S. Moulton, C. Newbold, M.G. Lum, A. Cameron, G. Wallace, R. Kapsa, G. Clark, S. O'Leary, The effect of polypyrrole with incorporated neurotrophin-3 on the promotion of neurite outgrowth from auditory neurons, *Biomaterials* 28(3) (2007) 513-523.
- [191] R.T. Richardson, A.K. Wise, B.C. Thompson, B.O. Flynn, P.J. Atkinson, N.J. Fretwell, J.B. Fallon, G.G. Wallace, R.K. Shepherd, G.M. Clark, S.J. O'Leary, Polypyrrole-coated electrodes for the delivery of charge and neurotrophins to cochlear neurons, *Biomaterials* 30(13) (2009) 2614-2624.
- [192] B.C. Thompson, S.E. Moulton, R.T. Richardson, G.G. Wallace, Effect of the dopant anion in polypyrrole on nerve growth and release of a neurotrophic protein, *Biomaterials* 32(15) (2011) 3822-3831.
- [193] X. Luo, X.T. Cui, Electrochemically controlled release based on nanoporous conducting polymers, *Electrochemistry Communications* 11(2) (2009) 402-404.
- [194] T.D.Y. Kozai, K. Catt, Z. Du, K. Na, O. Srivannavit, R.u.M. Haque, J. Seymour, K.D. Wise, E. Yoon, X.T. Cui, Chronic *In Vivo* Evaluation of PEDOT/CNT for Stable Neural Recordings, *IEEE Transactions on Biomedical Engineering* 63(1) (2016) 111-119.
- [195] J. Isaksson, P. Kjäll, D. Nilsson, N. Robinson, M. Berggren, A. Richter-Dahlfors, Electronic control of Ca<sup>2+</sup> signalling in neuronal cells using an organic electronic ion pump, *Nature Materials* 6 (2007) 673.

- [196] D.T. Simon, S. Kurup, K.C. Larsson, R. Hori, K. Tybrandt, M. Goiny, E.W.H. Jager, M. Berggren, B. Canlon, A. Richter-Dahlfors, Organic electronics for precise delivery of neurotransmitters to modulate mammalian sensory function, *Nature Materials* 8 (2009) 742.
- [197] C.M. Proctor, A. Slézia, A. Kaszas, A. Ghestem, I. del Agua, A.-M. Pappa, C. Bernard, A. Williamson, G.G. Malliaras, Electrophoretic drug delivery for seizure control, *Science Advances* 4(8) (2018) eaau1291.
- [198] J.L. Collinger, B. Wodlinger, J.E. Downey, W. Wang, E.C. Tyler-Kabara, D.J. Weber, A.J.C. McMorland, M. Velliste, M.L. Boninger, A.B. Schwartz, High-performance neuroprosthetic control by an individual with tetraplegia, *The Lancet* 381(9866) (2013) 557-564.
- [199] X. Cui, J.F. Hetke, J.A. Wiler, D.J. Anderson, D.C. Martin, Electrochemical deposition and characterization of conducting polymer polypyrrole/PSS on multichannel neural probes, *Sensors and Actuators A: Physical* 93(1) (2001) 8-18.
- [200] P.A. Hårdhammar, H.M.M. van Beusekom, H.U. Emanuelsson, S.H. Hofma, P.A. Albertsson, P.D. Verdouw, E. Boersma, P.W. Serruys, W.J. van der Giessen, Reduction in Thrombotic Events With Heparin-Coated Palmaz-Schatz Stents in Normal Porcine Coronary Arteries, *Circulation* 93(3) (1996) 423-430.
- [201] Q. Han, W. Jin, Z. Xiao, H. Ni, J. Wang, J. Kong, J. Wu, W. Liang, L. Chen, Y. Zhao, B. Chen, J. Dai, The promotion of neural regeneration in an extreme rat spinal cord injury model using a collagen scaffold containing a collagen binding neuroprotective protein and an EGFR neutralizing antibody, *Biomaterials* 31(35) (2010) 9212-9220.
- [202] I.M. Taylor, Z. Du, E.T. Bigelow, J.R. Eles, A.R. Horner, K.A. Catt, S.G. Weber, B.G. Jamieson, X.T. Cui, Aptamer-functionalized neural recording electrodes for the direct measurement of cocaine in vivo, *Journal of Materials Chemistry B* 5(13) (2017) 2445-2458.
- [203] N.C. Foulds, C.R. Lowe, Enzyme entrapment in electrically conducting polymers. Immobilisation of glucose oxidase in polypyrrole and its application in amperometric glucose sensors, *Journal of the Chemical Society, Faraday Transactions 1: Physical Chemistry in Condensed Phases* 82(4) (1986) 1259-1264.
- [204] X. Kang, J. Wang, H. Wu, I.A. Aksay, J. Liu, Y. Lin, Glucose Oxidase-graphene-chitosan modified electrode for direct electrochemistry and glucose sensing, *Biosensors and Bioelectronics* 25(4) (2009) 901-905.
- [205] P.J. Conroy, S. Hearty, P. Leonard, R.J. O’Kennedy, Antibody production, design and use for biosensor-based applications, *Seminars in Cell & Developmental Biology* 20(1) (2009) 10-26.
- [206] D.T. Arazawa, J.D. Kimmel, W.J. Federspiel, Kinetics of CO<sub>2</sub> exchange with carbonic anhydrase immobilized on fiber membranes in artificial lungs, *Journal of Materials Science: Materials in Medicine* 26(6) (2015) 193.
- [207] J.D. Kimmel, D.T. Arazawa, S.H. Ye, V. Shankarraman, W.R. Wagner, W.J. Federspiel, Carbonic anhydrase immobilized on hollow fiber membranes using glutaraldehyde activated

chitosan for artificial lung applications, *Journal of Materials Science: Materials in Medicine* 24(11) (2013) 2611-2621.

[208] K. Matsumoto, K. Ohnishi, T. Kiyotani, T. Sekine, H. Ueda, T. Nakamura, K. Endo, Y. Shimizu, Peripheral nerve regeneration across an 80-mm gap bridged by a polyglycolic acid (PGA)-collagen tube filled with laminin-coated collagen fibers: a histological and electrophysiological evaluation of regenerated nerves, *Brain Research* 868(2) (2000) 315-328.

[209] H. Wei, C.M. George, V.B. Ravi, Nanoscale laminin coating modulates cortical scarring response around implanted silicon microelectrode arrays, *Journal of Neural Engineering* 3(4) (2006) 316.

[210] I.I. Slowing, J.L. Vivero-Escoto, C.-W. Wu, V.S.Y. Lin, Mesoporous silica nanoparticles as controlled release drug delivery and gene transfection carriers, *Advanced Drug Delivery Reviews* 60(11) (2008) 1278-1288.

[211] C.-Y. Lin, W.-P. Li, S.-P. Huang, C.-S. Yeh, C.-M. Yang, Hollow mesoporous silica nanosphere-supported FePt nanoparticles for potential theranostic applications, *Journal of Materials Chemistry B* (2017).

[212] C.-H. Lee, S.-H. Cheng, I.P. Huang, J.S. Souris, C.-S. Yang, C.-Y. Mou, L.-W. Lo, Intracellular pH-Responsive Mesoporous Silica Nanoparticles for the Controlled Release of Anticancer Chemotherapeutics, *Angewandte Chemie* 122(44) (2010) 8390-8395.

[213] J. Lee, Y. Lee, J.K. Youn, H.B. Na, T. Yu, H. Kim, S.-M. Lee, Y.-M. Koo, J.H. Kwak, H.G. Park, H.N. Chang, M. Hwang, J.-G. Park, J. Kim, T. Hyeon, Simple Synthesis of Functionalized Superparamagnetic Magnetite/Silica Core/Shell Nanoparticles and their Application as Magnetically Separable High-Performance Biocatalysts, *Small* 4(1) (2008) 143-152.

[214] C.-Y. Lai, B.G. Trewyn, D.M. Jeftinija, K. Jeftinija, S. Xu, S. Jeftinija, V.S.Y. Lin, A Mesoporous Silica Nanosphere-Based Carrier System with Chemically Removable CdS Nanoparticle Caps for Stimuli-Responsive Controlled Release of Neurotransmitters and Drug Molecules, *Journal of the American Chemical Society* 125(15) (2003) 4451-4459.

[215] Z. Wang, P. Wu, Z. He, H. He, W. Rong, J. Li, D. Zhou, Y. Huang, Mesoporous silica nanoparticles with lactose-mediated targeting effect to deliver platinum(IV) prodrug for liver cancer therapy, *Journal of Materials Chemistry B* (2017).

[216] V.S. Polikov, P.A. Tresco, W.M. Reichert, Response of brain tissue to chronically implanted neural electrodes, *Journal of Neuroscience Methods* 148(1) (2005) 1-18.

[217] S.J. Cheryl Miller, Surya Mallapragada, Synergistic effects of physical and chemical guidance cues on neurite alignment and outgrowth on biodegradable polymer substrates, *Tissue Engineering* 8(3) (2004).

[218] N. Snyder, X.T. Cui, NOVEL METHODS FOR THE PREVENTION OF NEURODEGENERATION AROUND NEURAL IMPLANTS (Doctoral Dissertation), (2015).

- [219] J.R. Eles, A.L. Vazquez, N.R. Snyder, C. Lagenaur, M.C. Murphy, T.D.Y. Kozai, X.T. Cui, Neuroadhesive L1 coating attenuates acute microglial attachment to neural electrodes as revealed by live two-photon microscopy, *Biomaterials* 113 (2017) 279-292.
- [220] C. Lagenaur, V. Lemmon, An L1-like molecule, the 8D9 antigen, is a potent substrate for neurite extension, *Proceedings of the National Academy of Sciences of the United States of America* 84(21) (1987) 7753-7757.
- [221] D. Salvemini, C. Muscoli, D.P. Riley, S. Cuzzocrea, Superoxide Dismutase Mimetics, *Pulmonary Pharmacology & Therapeutics* 15(5) (2002) 439-447.
- [222] M. Pool, J. Thiemann, A. Bar-Or, A.E. Fournier, NeuriteTracer: A novel ImageJ plugin for automated quantification of neurite outgrowth, *Journal of Neuroscience Methods* 168(1) (2008) 134-139.
- [223] C.A. Orr, J.J. Cernohous, P. Guegan, A. Hirao, H.K. Jeon, C.W. Macosko, Homogeneous reactive coupling of terminally functional polymers, *Polymer* 42(19) (2001) 8171-8178.
- [224] K. Raeyoung, N. Yoonkey, Electrochemical layer-by-layer approach to fabricate mechanically stable platinum black microelectrodes using a mussel-inspired polydopamine adhesive, *Journal of Neural Engineering* 12(2) (2015) 026010.
- [225] Y. Li, D.S. Galileo, Soluble L1CAM promotes breast cancer cell adhesion and migration in vitro, but not invasion, *Cancer Cell International* 10(1) (2010) 34.
- [226] H.R. R Timpl, P G Robey, S I Rennard, J M Foidart and G R Martin, Laminin-a glycoprotein from basement membranes, *Journal of biological chemistry* 254 (1979) 9933-9937.
- [227] E.C.T. Peter D. Yurchenco, Aristidis S. Charonis, Heinz Furthermayr, Laminin Polymerization *in Vitro*, *The Journal of Biological Chemistry* 260(12) (1985) 7636-7644.
- [228] K. Webb, E. Budko, T.J. Neuberger, S. Chen, M. Schachner, P.A. Tresco, Substrate-bound human recombinant L1 selectively promotes neuronal attachment and outgrowth in the presence of astrocytes and fibroblasts, *Biomaterials* 22(10) (2001) 1017-1028.
- [229] M. Dihne, C. Bernreuther, M. Sibbe, W. Paulus, M. Schachner, A new role for the cell adhesion molecule L1 in neural precursor cell proliferation, differentiation, and transmitter-specific subtype generation, *J Neurosci* 23(16) (2003) 6638-50.
- [230] A. Golabchi, K.M. Woepfel, X. Li, C.F. Lagenaur, X.T. Cui, Neuroadhesive protein coating improves the chronic performance of neuroelectronics in mouse brain, *Biosensors and Bioelectronics* 155 (2020) 112096.
- [231] K.M. Woepfel, X.T. Cui, Nanoparticle and Biomolecule Surface Modification Synergistically Increases Neural Electrode Recording Yield and Minimizes Inflammatory Host Response, *Advanced Healthcare Materials* 10(16) (2021) 2002150.

- [232] Z.-Z. Wu, Y. Zhao, W.S. Kisaalita, Interfacing SH-SY5Y human neuroblastoma cells with SU-8 microstructures, *Colloids and Surfaces B: Biointerfaces* 52(1) (2006) 14-21.
- [233] M.-H. Kim, M. Park, K. Kang, I.S. Choi, Neurons on nanometric topographies: insights into neuronal behaviors in vitro, *Biomaterials Science* 2(2) (2014) 148-155.
- [234] H. Amin, M. Dipalo, F. De Angelis, L. Berdondini, Biofunctionalized 3D Nanopillar Arrays Fostering Cell Guidance and Promoting Synapse Stability and Neuronal Activity in Networks, *ACS Appl Mater Interfaces* 10(17) (2018) 15207-15215.
- [235] C.C. Gertz, M.K. Leach, L.K. Birrell, D.C. Martin, E.L. Feldman, J.M. Corey, Accelerated neuritogenesis and maturation of primary spinal motor neurons in response to nanofibers, *Dev Neurobiol* 70(8) (2010) 589-603.
- [236] C.A.R. Chapman, H. Chen, M. Stamou, J. Biener, M.M. Biener, P.J. Lein, E. Seker, Nanoporous Gold as a Neural Interface Coating: Effects of Topography, Surface Chemistry, and Feature Size, *ACS Applied Materials & Interfaces* 7(13) (2015) 7093-7100.
- [237] D. Brüggemann, Nanoporous Aluminium Oxide Membranes as Cell Interfaces, *Journal of Nanomaterials* 2013 (2013) 460870.
- [238] E.S. Ereifej, G.M. Rial, J.K. Hermann, C.S. Smith, S.M. Meade, J.M. Rayyan, K. Chen, H. Feng, J.R. Capadona, Implantation of Neural Probes in the Brain Elicits Oxidative Stress, *Frontiers in Bioengineering and Biotechnology* 6(9) (2018).
- [239] X. Yu, H. Biedrzycki Adam, S. Khalil Andrew, D. Hess, M. Umhoefer Jennifer, D. Markel Mark, L. Murphy William, Nanostructured Mineral Coatings Stabilize Proteins for Therapeutic Delivery, *Advanced Materials* 29(33) (2017) 1701255.
- [240] X.S. Zheng, N.R. Snyder, K. Woeppel, J.H. Barengo, X. Li, J. Eles, C.L. Kolarcik, X.T. Cui, A superoxide scavenging coating for improving tissue response to neural implants, *Acta Biomaterialia* 99 (2019) 72-83.
- [241] K.J. Yu, D. Kuzum, S.-W. Hwang, B.H. Kim, H. Juul, N.H. Kim, S.M. Won, K. Chiang, M. Trumpis, A.G. Richardson, H. Cheng, H. Fang, M. Thompson, H. Bink, D. Talos, K.J. Seo, H.N. Lee, S.-K. Kang, J.-H. Kim, J.Y. Lee, Y. Huang, F.E. Jensen, M.A. Dichter, T.H. Lucas, J. Viventi, B. Litt, J.A. Rogers, Bioresorbable silicon electronics for transient spatiotemporal mapping of electrical activity from the cerebral cortex, *Nature Materials* 15(7) (2016) 782-791.
- [242] P. Ariano, O. Budnyk, S. Dalmazzo, D. Lovisolo, C. Manfredotti, P. Rivolo, E. Vittone, On diamond surface properties and interactions with neurons, *The European Physical Journal E* 30(2) (2009) 149.
- [243] V. Raffa, V. Pensabene, A. Menciassi, P. Dario, Design criteria of neuron/electrode interface. The focused ion beam technology as an analytical method to investigate the effect of electrode surface morphology on neurocompatibility, *Biomedical Microdevices* 9(3) (2007) 371-383.

- [244] W. Liao, B.A. Randall, N.A. Alba, X.T. Cui, Conducting polymer-based impedimetric aptamer biosensor for in situ detection, *Analytical and Bioanalytical Chemistry* 392(5) (2008) 861-864.
- [245] G. Buzsáki, Large-scale recording of neuronal ensembles, *Nature Neuroscience* 7(5) (2004) 446-451.
- [246] S. Suzuki, J. Namiki, S. Shibata, Y. Mastuzaki, H. Okano, The neural stem/progenitor cell marker nestin is expressed in proliferative endothelial cells, but not in mature vasculature, *J Histochem Cytochem* 58(8) (2010) 721-30.
- [247] M.S. Rao, A.K. Shetty, Efficacy of doublecortin as a marker to analyse the absolute number and dendritic growth of newly generated neurons in the adult dentate gyrus, *Eur J Neurosci* 19(2) (2004) 234-46.
- [248] X. Yang, T. Zhou, T.J. Zwan, G. Hong, Y. Zhao, R.D. Viveros, T.-M. Fu, T. Gao, C.M. Lieber, Bioinspired neuron-like electronics, *Nature Materials* 18(5) (2019) 510-517.
- [249] G. Xu, D.-y. Nie, W.-z. Wang, P.-h. Zhang, J. Shen, B.-t. Ang, G.-h. Liu, X.-g. Luo, N.-l. Chen, Z.-c. Xiao, Optic nerve regeneration in polyglycolic acid–chitosan conduits coated with recombinant L1-Fc, *NeuroReport* 15(14) (2004).
- [250] M. Hortsch, The L1 family of neural cell adhesion molecules: old proteins performing new tricks, *Neuron* 17 (1996).
- [251] H. Kamiguchi, V. Lemmon, Neural cell adhesion molecule L1: signaling pathways and growth cone motility, *J Neurosci Res* 49 (1997).
- [252] Yang ML, Li Y, Chilukuri K, Boulos MI, Kappes JC, Galileo DS: L1 stimulation of human glioma cell motility correlates with FAK activation. Submitted for publication.
- [253] A. Rosengren, L. Wallman, N. Danielsen, T. Laurell, L.M. Bjursten, Tissue reactions evoked by porous and plane surfaces made out of silicon and titanium, *IEEE Transactions on Biomedical Engineering* 49(4) (2002) 392-399.
- [254] J.C. Pickup, G.W. Shaw, D.J. Claremont, In vivo molecular sensing in diabetes mellitus: an implantable glucose sensor with direct electron transfer, *Diabetologia* 32(3) (1989) 213-217.
- [255] L. Hsiung, A.N. Barclay, M.R. Brandon, E. Sim, R.R. Porter, Purification of human C3b inactivator by monoclonal-antibody affinity chromatography, *Biochem J* 203(1) (1982) 293-298.
- [256] R. Zhuang, Y. Zhang, R. Zhang, C. Song, K. Yang, A. Yang, B. Jin, Purification of GFP fusion proteins with high purity and yield by monoclonal antibody-coupled affinity column chromatography, *Protein Expression and Purification* 59(1) (2008) 138-143.
- [257] T.I. Valdes, F. Moussy, In Vitro and In Vivo Degradation of Glucose Oxidase Enzyme Used for an Implantable Glucose Biosensor, *Diabetes Technology & Therapeutics* 2(3) (2000) 367-376.

- [258] F. Moussy, Implantable glucose sensor: progress and problems, *SENSORS*, 2002 IEEE, 2002, pp. 270-273 vol.1.
- [259] J.M. Harris, C. Reyes, G.P. Lopez, Common Causes of Glucose Oxidase Instability in In Vivo Biosensing: A Brief Review, *Journal of Diabetes Science and Technology* 7(4) (2013) 1030-1038.
- [260] S. Zhang, Z. Zhang, Y. Lu, M. Rostam-Abadi, A. Jones, Activity and stability of immobilized carbonic anhydrase for promoting CO<sub>2</sub> absorption into a carbonate solution for post-combustion CO<sub>2</sub> capture, *Bioresource Technology* 102(22) (2011) 10194-10201.
- [261] J. Hou, G. Dong, B. Xiao, C. Malassigne, V. Chen, Preparation of titania based biocatalytic nanoparticles and membranes for CO<sub>2</sub> conversion, *Journal of Materials Chemistry A* 3(7) (2015) 3332-3342.
- [262] A. Dankwardt, J. Muller, B. Hock, Stabilization of enzyme immunoassays for atrazine, *Anal Chim Acta* 362(1) (1998) 35-45.
- [263] G. Grasso, M. Fragai, E. Rizzarelli, G. Spoto, K.J. Yeo, A new methodology for monitoring the activity of cdMMP-12 anchored and freeze-dried on Au(111), *J Am Soc Mass Spectr* 18(5) (2007) 961-969.
- [264] N. Nath, R. Hurst, B. Hook, P. Meisenheimer, K.Q. Zhao, N. Nassif, R.F. Bulleit, D.R. Storts, Improving protein array performance: Focus on washing and storage conditions, *J Proteome Res* 7(10) (2008) 4475-4482.
- [265] R. Seetharam, Y. Wada, S. Ramachandran, H. Hess, P. Satir, Long-term storage of bionanodevices by freezing and lyophilization, *Lab Chip* 6(9) (2006) 1239-1242.
- [266] A. Stabenau, G. Winter, Application and drying of protein drug microdroplets on solid surfaces, *Pharm Dev Technol* 12(1) (2007) 61-70.
- [267] H. W., M.G. C., S.T. M., B.R. V., A Novel Anti-inflammatory Surface for Neural Electrodes, *Advanced Materials* 19(21) (2007) 3529-3533.
- [268] M. Rogers, C.L. Leong, S. Gowers, X. Niu, A. De Mello, M.G. Boutelle, A Biosensor-Based Microfluidic Analysis System for Monitoring Brain Injury, *PITTCON 2014, Chicago, USA, 2014*.
- [269] J. Hou, M.Y. Zulkifli, M. Mohammad, Y. Zhang, A. Razmjou, V. Chen, Biocatalytic gas-liquid membrane contactors for CO<sub>2</sub> hydration with immobilized carbonic anhydrase, *Journal of Membrane Science* 520 (2016) 303-313.
- [270] J.L. Scoggin, C. Tan, N.H. Nguyen, U. Kansakar, M. Madadi, S. Siddiqui, P.U. Arumugam, M.A. DeCoster, T.A. Murray, An enzyme-based electrochemical biosensor probe with sensitivity to detect astrocytic versus glioma uptake of glutamate in real time in vitro, *Biosensors and Bioelectronics* 126 (2019) 751-757.

- [271] A. Domínguez-Bajo, B.L. Rodilla, I. Calaresu, A. Arché-Núñez, A. González-Mayorga, D. Scaini, L. Pérez, J. Camarero, R. Miranda, E. López-Dolado, M.T. González, L. Ballerini, M.C. Serrano, Interfacing Neurons with Nanostructured Electrodes Modulates Synaptic Circuit Features, *Advanced Biosystems* 4(9) (2020) 2000117.
- [272] J.W. Salatino, K.A. Ludwig, T.D.Y. Kozai, E.K. Purcell, Glial responses to implanted electrodes in the brain, *Nature Biomedical Engineering* 1(11) (2017) 862-877.
- [273] D.H. Szarowski, M.D. Andersen, S. Retterer, A.J. Spence, M. Isaacson, H.G. Craighead, J.N. Turner, W. Shain, Brain responses to micro-machined silicon devices, *Brain Research* 983(1) (2003) 23-35.
- [274] C.M. George, D.R. Howard, I.L. Allan, G. Claire-Anne, E.G. Robert, V.B. Ravi, Implanted neural electrodes cause chronic, local inflammation that is correlated with local neurodegeneration, *Journal of Neural Engineering* 6(5) (2009) 056003.
- [275] K. Wang, R.-Y. Tang, X.-B. Zhao, J.-J. Li, Y.-R. Lang, X.-X. Jiang, H.-J. Sun, Q.-X. Lin, C.-Y. Wang, Covalent bonding of YIGSR and RGD to PEDOT/PSS/MWCNT-COOH composite material to improve the neural interface, *Nanoscale* 7(44) (2015) 18677-18685.
- [276] A.H. Taub, R. Hogri, A. Magal, M. Mintz, Y. Shacham-Diamand, Bioactive anti-inflammatory coating for chronic neural electrodes, *Journal of Biomedical Materials Research Part A* 100A(7) (2012) 1854-1858.
- [277] A.M. Montgomery, J.C. Becker, C.H. Siu, V.P. Lemmon, D.A. Cheresch, J.D. Pancook, X. Zhao, R.A. Reisfeld, Human neural cell adhesion molecule L1 and rat homologue NILE are ligands for integrin alpha v beta 3, *J Cell Biol* 132 (1996).
- [278] T. Brummendorf, S. Kenwrick, F.G. Rathjen, Neural cell recognition molecule L1: from cell biology to human hereditary brain malformations, *Curr Opin Neurobiol* 8 (1998).
- [279] W. Chen, S. Cai, Q.-Q. Ren, W. Wen, Y.-D. Zhao, Recent advances in electrochemical sensing for hydrogen peroxide: a review, *Analyst* 137(1) (2012) 49-58.
- [280] S.N. Flesher, J.L. Collinger, S.T. Foldes, J.M. Weiss, J.E. Downey, E.C. Tyler-Kabara, S.J. Bensmaia, A.B. Schwartz, M.L. Boninger, R.A. Gaunt, Intracortical microstimulation of human somatosensory cortex, *Science Translational Medicine* 8(361) (2016) 361ra141.
- [281] N.K. Guimard, N. Gomez, C.E. Schmidt, Conducting polymers in biomedical engineering, *Progress in Polymer Science* 32(8) (2007) 876-921.
- [282] A.L. Kip, B.L. Nicholas, D.J. Mike, M.R.-B. Sarah, L.H. Jeffrey, R.K. Daryl, Poly(3,4-ethylenedioxythiophene) (PEDOT) polymer coatings facilitate smaller neural recording electrodes, *Journal of Neural Engineering* 8(1) (2011) 014001.
- [283] T.D.Y. Kozai, N.B. Langhals, P.R. Patel, X. Deng, H. Zhang, K.L. Smith, J. Lahann, N.A. Kotov, D.R. Kipke, Ultrasmall implantable composite microelectrodes with bioactive surfaces for chronic neural interfaces, *Nature Materials* 11 (2012) 1065.

- [284] S. Chen, W. Pei, Q. Gui, R. Tang, Y. Chen, S. Zhao, H. Wang, H. Chen, PEDOT/MWCNT composite film coated microelectrode arrays for neural interface improvement, *Sensors and Actuators A: Physical* 193 (2013) 141-148.
- [285] S. Venkatraman, J. Hendricks, Z.A. King, A.J. Sereno, S. Richardson-Burns, D. Martin, J.M. Carmena, In Vitro and In Vivo Evaluation of PEDOT Microelectrodes for Neural Stimulation and Recording, *IEEE Transactions on Neural Systems and Rehabilitation Engineering* 19(3) (2011) 307-316.
- [286] Y. Lu, T. Li, X. Zhao, M. Li, Y. Cao, H. Yang, Y.Y. Duan, Electrodeposited polypyrrole/carbon nanotubes composite films electrodes for neural interfaces, *Biomaterials* 31(19) (2010) 5169-5181.
- [287] X. Zheng, K.M. Woepfel, A.Y. Griffith, E. Chang, M.J. Looker, L.E. Fisher, B.J. Clapsaddle, X.T. Cui, Soft Conducting Elastomer for Peripheral Nerve Interface, *Advanced Healthcare Materials* 0(0) (2019) 1801311.
- [288] Y. Vlamidis, M. Lanzi, E. Salatelli, I. Gualandi, B. Fraboni, L. Setti, D. Tonelli, Electrodeposition of PEDOT perchlorate as an alternative route to PEDOT:PSS for the development of bulk heterojunction solar cells, *Journal of Solid State Electrochemistry* 19(6) (2015) 1685-1693.
- [289] Z.A. King, C.M. Shaw, S.A. Spanninga, D.C. Martin, Structural, chemical and electrochemical characterization of poly(3,4-Ethylenedioxythiophene) (PEDOT) prepared with various counter-ions and heat treatments, *Polymer* 52(5) (2011) 1302-1308.
- [290] R.M. Hernández, L. Richter, S. Semancik, S. Stranick, T.E. Mallouk, Template Fabrication of Protein-Functionalized Gold-Polypyrrole-Gold Segmented Nanowires, *Chemistry of Materials* 16(18) (2004) 3431-3438.
- [291] M.C. Kum, K.A. Joshi, W. Chen, N.V. Myung, A. Mulchandani, Biomolecules-carbon nanotubes doped conducting polymer nanocomposites and their sensor application, *Talanta* 74(3) (2007) 370-375.
- [292] J. Serra Moreno, S. Panero, S. Materazzi, A. Martinelli, M.G. Sabbieti, D. Agas, G. Materazzi, Polypyrrole-polysaccharide thin films characteristics: Electrosynthesis and biological properties, *Journal of Biomedical Materials Research Part A* 88A(3) (2009) 832-840.
- [293] T.E. Campbell, A.J. Hodgson, G.G. Wallace, Incorporation of Erythrocytes into Polypyrrole to Form the Basis of a Biosensor to Screen for Rhesus (D) Blood Groups and Rhesus (D) Antibodies, *Electroanalysis* 11(4) (1999) 215-222.
- [294] N. Gomez, C.E. Schmidt, Nerve growth factor-immobilized polypyrrole: Bioactive electrically conducting polymer for enhanced neurite extension, *Journal of Biomedical Materials Research Part A* 81A(1) (2007) 135-149.

- [295] R. Wadhwa, C.F. Lagenaur, X.T. Cui, Electrochemically controlled release of dexamethasone from conducting polymer polypyrrole coated electrode, *Journal of Controlled Release* 110(3) (2006) 531-541.
- [296] M.R. Abidian, D.-H. Kim, D.C. Martin, Conducting-Polymer Nanotubes for Controlled Drug Release, *Advanced Materials* 18(4) (2006) 405-409.
- [297] P. Gupta, V. Kumar, S. Paul, Silica functionalized sulfonic acid catalyzed one-pot synthesis of 4,5,8a-triarylhex-ahydropyrimido[4,5-d]pyrimidine-2,7(1H,3 H)-diones under liquid phase catalysis, *Journal of the Brazilian Chemical Society* 21 (2010) 349-354.
- [298] Q. He, J. Shi, Mesoporous silica nanoparticle based nano drug delivery systems: synthesis, controlled drug release and delivery, pharmacokinetics and biocompatibility, *Journal of Materials Chemistry* 21(16) (2011) 5845-5855.
- [299] I.I. Slowing, C.-W. Wu, J.L. Vivero-Escoto, V.S.-Y. Lin, Mesoporous Silica Nanoparticles for Reducing Hemolytic Activity Towards Mammalian Red Blood Cells, *Small* 5(1) (2009) 57-62.
- [300] S.F. Cogan, P.R. Troyk, J. Ehrlich, T.D. Plante, In vitro comparison of the charge-injection limits of activated iridium oxide (AIROF) and platinum-iridium microelectrodes, *IEEE Transactions on Biomedical Engineering* 52(9) (2005) 1612-1614.
- [301] K. Wang, H.A. Fishman, H. Dai, J.S. Harris, Neural Stimulation with a Carbon Nanotube Microelectrode Array, *Nano Letters* 6(9) (2006) 2043-2048.
- [302] S. Harish, D. Sridharan, S. Senthil Kumar, J. Joseph, K.L.N. Phani, Barrier films to control loss of 9,10-anthraquinone-2-sulphonate dopant from PEDOT films during electrochemical transitions, *Electrochimica Acta* 54(13) (2009) 3618-3622.
- [303] M.B. Leon, D.S. Baim, J.J. Popma, P.C. Gordon, D.E. Cutlip, K.K.L. Ho, A. Giambartolomei, D.J. Diver, D.M. Lasorda, D.O. Williams, S.J. Pocock, R.E. Kuntz, A Clinical Trial Comparing Three Antithrombotic-Drug Regimens after Coronary-Artery Stenting, *New England Journal of Medicine* 339(23) (1998) 1665-1671.
- [304] M.E. Bertrand, H.-J. Rupprecht, P. Urban, A.H. Gershlick, f.t.C. Investigators, Double-Blind Study of the Safety of Clopidogrel With and Without a Loading Dose in Combination With Aspirin Compared With Ticlopidine in Combination With Aspirin After Coronary Stenting, *Circulation* 102(6) (2000) 624-629.
- [305] W. Xiao-Ping, Z. Lan, L. Wen-Rong, D. Jian-Ping, C. Hong-Qing, C. Guo-Nan, Study on the Electrochemical Behavior of Melatonin with an Activated Electrode, *Electroanalysis* 14(23) (2002) 1654-1660.
- [306] I. Gulcin, M.E. Buyukokuroglu, M. Oktay, O.I. Kufrevioglu, On the in vitro antioxidative properties of melatonin, *Journal of Pineal Research* 33(3) (2002) 167-171.

- [307] T.D. Kozai, A.L. Vazquez, C.L. Weaver, S.G. Kim, X.T. Cui, In vivo two-photon microscopy reveals immediate microglial reaction to implantation of microelectrode through extension of processes, *J Neural Eng* 9(6) (2012) 066001.
- [308] N.J. Michelson, A.L. Vazquez, J.R. Eles, J.W. Salatino, E.K. Purcell, J.J. Williams, X.T. Cui, T.D.Y. Kozai, Multi-scale, multi-modal analysis uncovers complex relationship at the brain tissue-implant neural interface: new emphasis on the biological interface, *Journal of neural engineering* 15(3) (2018) 033001-033001.
- [309] X.H. Daniel, L. Andrea, A. Erkinay, G. Noah, P.T. Kevin, T.J. Pfefer, A. Anant, K. Victor, G.W. Cristin, Optical coherence microscopy of mouse cortical vasculature surrounding implanted electrodes, *Proc.SPIE*, 2014.
- [310] C. Jiang, G.G. Haddad, Effect of anoxia on intracellular and extracellular potassium activity in hypoglossal neurons in vitro, *Journal of Neurophysiology* 66(1) (1991) 103-111.
- [311] A.E. Schramm, A. Carton-Leclercq, S. Diallo, V. Navarro, M. Chavez, S. Mahon, S. Charpier, Identifying neuronal correlates of dying and resuscitation in a model of reversible brain anoxia, *Progress in Neurobiology* 185 (2020) 101733.
- [312] H. Zhu, James E. Cottrell, Ira S. Kass, The Effect of Thiopental and Propofol on NMDA- and AMPA-mediated Glutamate Excitotoxicity *Anesthesiology* 87(4) (1997) 944-951.
- [313] S. Rothman, Synaptic release of excitatory amino acid neurotransmitter mediates anoxic neuronal death, *J Neurosci* 4(7) (1984) 1884-91.
- [314] S.M. Rothman, J.W. Olney, Glutamate and the pathophysiology of hypoxic--ischemic brain damage, *Ann Neurol* 19(2) (1986) 105-111.
- [315] J.M. Schulz, B.K. Al-Khazraji, J.K. Shoemaker, Sodium nitroglycerin induces middle cerebral artery vasodilatation in young, healthy adults, *Experimental Physiology* 103(8) (2018) 1047-1055.
- [316] M.E. Moir, T.D. Vermeulen, S.O. Smith, E. Woehrle, B.J. Matuszewski, M. Zamir, J.K. Shoemaker, Vasodilatation by carbon dioxide and sodium nitroglycerin reduces compliance of the cerebral arteries in humans, *Experimental Physiology* 106(8) (2021) 1679-1688.
- [317] A. Dahl, D. Russell, R. Nyberg-Hansen, K. Rootwelt, Effect of nitroglycerin on cerebral circulation measured by transcranial Doppler and SPECT, *Stroke* 20(12) (1989) 1733-1736.
- [318] D.G. Hottinger, D.S. Beebe, T. Kozhimannil, R.C. Prielipp, K.G. Belani, Sodium nitroprusside in 2014: A clinical concepts review, *J Anaesthesiol Clin Pharmacol* 30(4) (2014) 462-71.
- [319] N.D. Olesen, M. Fischer, N.H. Secher, Sodium nitroprusside dilates cerebral vessels and enhances internal carotid artery flow in young men, *The Journal of Physiology* 596(17) (2018) 3967-3976.

- [320] S.M. Willerth, S.E. Sakiyama-Elbert, Approaches to neural tissue engineering using scaffolds for drug delivery, *Advanced Drug Delivery Reviews* 59(4) (2007) 325-338.
- [321] K.S. Soppimath, T.M. Aminabhavi, A.R. Kulkarni, W.E. Rudzinski, Biodegradable polymeric nanoparticles as drug delivery devices, *Journal of Controlled Release* 70(1) (2001) 1-20.
- [322] J.M. Koziara, R.J. Mumper, D.D. Allen, Nanoparticle Surface Charges Alter Blood–Brain Barrier Integrity and Permeability AU - Lockman, Paul R, *Journal of Drug Targeting* 12(9-10) (2004) 635-641.
- [323] K. Gao, X. Jiang, Influence of particle size on transport of methotrexate across blood brain barrier by polysorbate 80-coated polybutylcyanoacrylate nanoparticles, *International Journal of Pharmaceutics* 310(1) (2006) 213-219.
- [324] K. Ulbrich, T. Knobloch, J. Kreuter, Targeting the insulin receptor: nanoparticles for drug delivery across the blood–brain barrier (BBB), *Journal of Drug Targeting* 19(2) (2011) 125-132.
- [325] B. Massoumi, A. Entezami, Electrochemically Controlled Binding and Release of Dexamethasone from Conducting Polymer Bilayer Films, *Journal of Bioactive and Compatible Polymers* 17(1) (2002) 51-62.
- [326] C. Tan, N. Kushwah, X.T. Cui, Electrically Controlled Neurochemical Delivery from Microelectrodes for Focal and Transient Modulation of Cellular Behavior, *Biosensors* 11(9) (2021) 348.
- [327] J.N. Cohn, L.P. Burke, Nitroprusside, *Annals of Internal Medicine* 91(5) (1979) 752-757.
- [328] F. Murad, Cyclic guanosine monophosphate as a mediator of vasodilation, *J Clin Invest* 78(1) (1986) 1-5.
- [329] R. Mukamel, H. Gelbard, A. Arieli, U. Hasson, I. Fried, R. Malach, Coupling Between Neuronal Firing, Field Potentials, and fMRI in Human Auditory Cortex, *Science* 309(5736) (2005) 951-954.
- [330] M.E. Raichle, M.A. Mintun, Brain work and brain imaging, *Annual review of neuroscience* 29 (2006) 449-76.
- [331] A. Viswanathan, R.D. Freeman, Neurometabolic coupling in cerebral cortex reflects synaptic more than spiking activity, *Nature neuroscience* 10(10) (2007) 1308-12.
- [332] Y. Nir, I. Dinstein, R. Malach, D.J. Heeger, BOLD and spiking activity, *Nature neuroscience* 11(5) (2008) 523-4; author reply 524.
- [333] Z.P. Infantolino, K.R. Luking, C.L. Sauder, J.J. Curtin, G. Hajcak, Robust is not necessarily reliable: From within-subjects fMRI contrasts to between-subjects comparisons, *NeuroImage* 173 (2018) 146-152.

- [334] A. Ekstrom, How and when the fMRI BOLD signal relates to underlying neural activity: The danger in dissociation, *Brain Research Reviews* 62(2) (2010) 233-244.
- [335] K. Masamoto, M. Fukuda, A. Vazquez, S.-G. Kim, Dose-dependent effect of isoflurane on neurovascular coupling in rat cerebral cortex, *Eur J Neurosci* 30(2) (2009) 242-250.
- [336] J.E. Bryant, M. Frölich, S. Tran, M.A. Reid, A.C. Lahti, N.V. Kraguljac, Ketamine induced changes in regional cerebral blood flow, interregional connectivity patterns, and glutamate metabolism, *Journal of Psychiatric Research* 117 (2019) 108-115.
- [337] H.-J. Shim, W.B. Jung, F. Schlegel, J. Lee, S. Kim, J. Lee, S.-G. Kim, Mouse fMRI under ketamine and xylazine anesthesia: Robust contralateral somatosensory cortex activation in response to forepaw stimulation, *NeuroImage* 177 (2018) 30-44.
- [338] M. Ueki, G. Mies, K.A. Hossmann, Effect of alpha-chloralose, halothane, pentobarbital and nitrous oxide anesthesia on metabolic coupling in somatosensory cortex of rat, *Acta Anaesthesiologica Scandinavica* 36(4) (1992) 318-322.
- [339] I. Batinić-Haberle, S. Cuzzocrea, J.S. Rebouças, G. Ferrer-Sueta, E. Mazzon, R. Di Paola, R. Radi, I. Spasojević, L. Benov, D. Salvemini, Pure MnTBAP selectively scavenges peroxynitrite over superoxide: Comparison of pure and commercial MnTBAP samples to MnTE-2-PyP in two models of oxidative stress injury, an SOD-specific *Escherichia coli* model and carrageenan-induced pleurisy, *Free Radical Biology and Medicine* 46(2) (2009) 192-201.